Search for CP violation in τ decays at Belle II

Dissertation
zur Erlangung des Doktorgrades
an der Fakultät für Mathematik, Informatik und Naturwissenschaften
Fachbereich Physik
der Universität Hamburg

vorgelegt von
Paolo Leo
aus Copertino (Italien)

Hamburg
2025

Gutachter/innen der Dissertation:	Prof. Dr. Kerstin Tackmann Dr. Armine Rostomyan
Zusammensetzung der Prüfungskommission:	Prof. Dr. Kerstin Tackmann Dr. Armine Rostomyan Prof. Dr. Jochen Liske Prof. Dr. Markus Diehl Prof. Dr. Johannes Haller
Vorsitzende/r der Prüfungskommission:	Prof. Dr. Jochen Liske
Datum der Disputation:	22.07.2025
Vorsitzender des Fach-Promotionsausschusses PHYSIK:	Prof. Dr. Wolfgang J. Parak
Leiter des Fachbereichs PHYSIK:	Prof. Dr. Markus Drescher
Dekan der Fakultät MIN:	Prof. Dr.-Ing. Norbert Ritter

Abstract

This thesis presents a search for direct Charge-Parity (CP) violation in the decay $\tau^- \to \pi^- K^0_S \nu_\tau (\geq 0\pi^0)$ using data collected by the Belle II experiment, corresponding to an integrated luminosity of 365 fb^{-1}. The analysis is motivated by a previous BABAR measurement, which reported a 2.8σ deviation from the Standard Model prediction. A CP asymmetry measurement is performed using a similar method, with improved control over detector and background-induced asymmetries through dedicated corrections.

The observed decay-rate asymmetry between τ^- and τ^+ decays is corrected for detection effects, background biases, and known $K^0/\bar{K}^0$ nuclear interaction asymmetries. These corrections are derived from control samples, and a dilution factor is applied to suppress contributions from background modes such as $\tau^- \to K^- K^0_S \nu_\tau$ and $\tau^- \to \pi^- K^0 \bar{K}^0 \nu_\tau$.

The analysis is conducted separately for electron- and muon-tagged τ decays, totaling approximately 262×10^3 signal events, and statistically combined assuming uncorrelated systematic uncertainties.

In parallel, this thesis contributes to a theoretical study evaluating the Standard Model assumption that the CP-violating term from $\tau^- \to \pi^- K^0 \bar{K}^0 \nu_\tau$ decays vanishes. The K^0_S efficiency functions developed here are essential for estimating the A_3 contribution, enabling comparison between theoretical predictions and Monte Carlo simulations.

For the main measurement, the dominant uncertainty is statistical, followed by systematics from detection-induced asymmetry corrections. At the time of writing, the CP asymmetry result remains blinded pending internal Belle II review; however, the associated statistical and systematic uncertainties are presented. This work highlights Belle II's sensitivity to CP violation in τ decays and lays the groundwork for more precise future measurements.

Zusammenfassung

Diese Arbeit präsentiert eine Suche nach direkter CP-Verletzung im Zerfall $\tau^- \to \pi^- K^0_S \nu_\tau (\geq 0\pi^0)$ unter Verwendung von Daten des Belle-II-Experiments, entsprechend einer integrierten Luminosität von 365 fb^{-1}. Die Analyse ist motiviert durch eine frühere Messung der BABAR-Kollaboration, die eine Abweichung vom Standardmodell auf dem Niveau von 2.8σ berichtete. Eine Messung der CP-Asymmetrie wird unter Anwendung einer ähnlichen Methode durchgeführt, wobei durch gezielte Korrekturen eine verbesserte Kontrolle über detektor- und hintergrundbedingte Asymmetrien erreicht wird.

Die beobachtete Zerfallsratenasymmetrie zwischen τ^-- und τ^+-Zerfällen wird für Effekte bei der Detektion, Hintergrundeinflüsse sowie bekannte Asymmetrien in den Kernwechselwirkungen von K^0 und $\bar{K}^0$ korrigiert. Diese Korrekturen werden mithilfe spezieller Kontrollproben abgeleitet, und ein Dämpfungsfaktor wird angewendet, um Beiträge von Hintergrundprozessen wie $\tau^- \to K^- K^0_S \nu_\tau$ und $\tau^- \to \pi^- K^0 \bar{K}^0 \nu_\tau$ zu unterdrücken.

Die Analyse wird getrennt für τ-Zerfälle mit Elektronen- bzw. Myon-Tagging durchgeführt und umfasst insgesamt etwa 262×10^3 ausgewählte Signalereignisse. Die beiden Stichproben werden statistisch kombiniert, wobei unkorrelierte systematische Unsicherheiten angenommen werden.

Parallel zur Hauptmessung trägt diese Arbeit zu einer theoretischen Studie bei, welche die Standardmodell-Annahme prüft, dass der CP-verletzende Term aus dem Zerfall $\tau^- \to \pi^- K^0 \bar{K}^0 \nu_\tau$ verschwindet. Die in dieser Arbeit entwickelten K^0_S-Effizienzfunktionen sind entscheidend für die zuverlässige Abschätzung des A_3-Beitrags und ermöglichen den Vergleich theoretischer Vorhersagen mit Monte-Carlo-Simulationen.

Für die Hauptmessung wird festgestellt, dass die dominante Unsicherheit statistischer Natur ist, gefolgt von systematischen Unsicherheiten, die aus den Korrekturen für detektionsbedingte Asymmetrien resultieren. Zum Zeitpunkt der Erstellung dieser Arbeit ist das finale Ergebnis der CP-Asymmetrie noch geblindet und befindet sich in interner Überprüfung durch die Belle-II-Kollaboration; jedoch werden die zugehörigen statistischen und systematischen Unsicherheiten präsentiert. Diese Arbeit zeigt die Empfindlichkeit von Belle II gegenüber CP-Verletzung in τ-Zerfällen und bildet die Grundlage für präzisere Messungen in der Zukunft bei Verfügbarkeit größerer Datensätze.

Contents

Chapter 1

Introduction

The Standard Model (SM) of particle physics stands as one of the most successful frameworks in understanding the fundamental building blocks of the universe and their interactions. It categorizes elementary particles into two primary groups: fermions, which include quarks and leptons, and bosons, which mediate fundamental forces. Through this framework, the interactions governed by electromagnetism, the weak nuclear force, and the strong nuclear force are described with remarkable precision, leading to profound theoretical insights and extensive experimental confirmations.

Despite its extraordinary success, the SM is not a complete theory of nature. It leaves several fundamental questions unanswered, highlighting the need for new physics beyond its scope. One of its most notable limitations is its inability to incorporate gravity within its structure, as it lacks a quantum theory of gravitation. Additionally, the nature and composition of dark matter, which constitutes a significant fraction of the universe's total mass-energy, remain elusive. The origin of neutrino masses, which suggests physics beyond the SM, is another open problem. Furthermore, the hierarchy problem, which pertains to the unexplained disparity between the weak scale and the Planck scale, challenges our understanding of fundamental interactions.

Addressing these unresolved issues requires probing the SM's boundaries with high-precision experiments and novel theoretical approaches. Current and future efforts in particle physics, such as collider experiments, neutrino observatories, and astrophysical studies, aim to uncover possible deviations from the SM predictions. Such investigations have the potential to guide us toward more comprehensive theories, including possible grand unification models, supersymmetry, or other extensions that provide deeper insights into the fabric of the universe.

By exploring these frontiers, physicists seek not only to refine our current understanding but also to uncover the underlying principles that govern the universe at its most fundamental level. The search for new physics is an ongoing endeavor, and every experimental breakthrough brings us closer to answering some of the most profound mysteries of nature.

In this context, this thesis contributes to the search for Charge-Parity (CP) violation in τ lepton decays, specifically in the process $\tau^- \to \pi^- K^0_S \nu_\tau (\geq 0\pi^0)$, studied at the Belle II experiment. CP violation is a fundamental phenomenon with significant implications for understanding matter-antimatter asymmetry in the universe. The measurement is performed using data collected by the Belle II detector, located at the KEK laboratory in Tsukuba, Japan. Belle II records electron-positron collisions provided by the SuperKEKB accelerator, producing $\Upsilon(4S)$ resonances that

decay into pairs of B mesons. However, this analysis focuses on τ leptons produced in these collisions, whose pair-production cross section is of the same order as that of B mesons at Belle II energies, seeking possible signs of CP violation in their decay dynamics.
The structure of this thesis is as follows:

- Chapter 2 introduces the theoretical background of CP violation in τ decays, its significance, and possible extensions beyond the SM.
- Chapter 3 presents the experimental setup, detailing the Belle II detector, SuperKEKB accelerator, and data collection techniques relevant to this analysis.
- Chapter 4 describes the CDC calibration method in Belle II and discusses a key feature that affects the main analysis.
- Chapter 5 describes the analysis and the event selection strategy, employed to extract CP-violating asymmetries in $\tau^- \to \pi^- K^0_S \nu_\tau (\geq 0\pi^0)$ decays.
- Chapter 6 details the corrections applied to account for detector and physics-induced asymmetries, including detection asymmetry, neutral kaon interaction effects, and background-induced biases.
- Chapter 7 discusses the evaluation of systematic uncertainties, and reports on consistency checks performed to validate the robustness of the result.
- Chapter 8 describes a collaborative work between the main analysts and a theoretical group to address one of the main assumptions in the analysis strategy.
- Chapter 9 presents the analysis results, compares with previous measurements, and outlines prospects for future CP violation studies in τ decays.

Chapter 2

Theory of Particle-Antiparticle Asymmetries

This chapter presents the theoretical framework for studying CP violation in τ lepton decays, with a particular focus on the process $\tau^- \to \pi^- K^0_S \nu_\tau$. It begins with a brief overview of the SM, emphasizing the role of weak interactions and charged currents, which are central to the mechanism of CP violation. The discussion then turns to well-established CP-violating effects in meson systems – particularly in the kaon, B meson, and more recently, D meson sectors – which provide valuable context and motivation for exploring similar phenomena in τ decays.
While CP violation is firmly established in meson physics, its presence in τ decays remains an open question. This gap motivates dedicated investigations into potential CP-violating signatures in τ processes. To this end, the chapter introduces the concepts of direct and indirect CP violation, along with theoretical expectations both within and beyond the SM.
Particular attention is given to hadronic final-state interactions in $\tau^- \to \pi^- K^0_S \nu_\tau$ decays, which may give rise to observable CP asymmetries. Moreover, the potential of τ decays to uncover new sources of CP violation and offer insights into physics beyond the SM is explored.
Finally, possible experimental signatures of CP violation in τ decays at Belle II are outlined, setting the stage for the subsequent chapters, which describe the experimental methodology and analysis techniques used in this thesis.

2.1 The SM of particle physics

The SM of particle physics is the most successful and extensively tested theory describing the fundamental particles and their interactions. It encompasses the elementary constituents of matter – quarks and leptons – which are fermions with half-integer spin. These particles are organized into three generations, each forming weak isospin doublets, as illustrated in Fig. 2.1. Quarks are never found in isolation due to the strong interaction; instead, they combine to form hadrons, such as protons and neutrons. They can group in triplets to form baryons, or in quark-antiquark pairs to form mesons. Leptons, on the other hand, can exist as free particles and include the electron, muon, and tau, along with their corresponding neutrinos.
The SM is a renormalizable quantum field theory based on the gauge symmetry group

$$SU(3)_C \otimes SU(2)_L \otimes U(1)_Y. \tag{2.1}$$

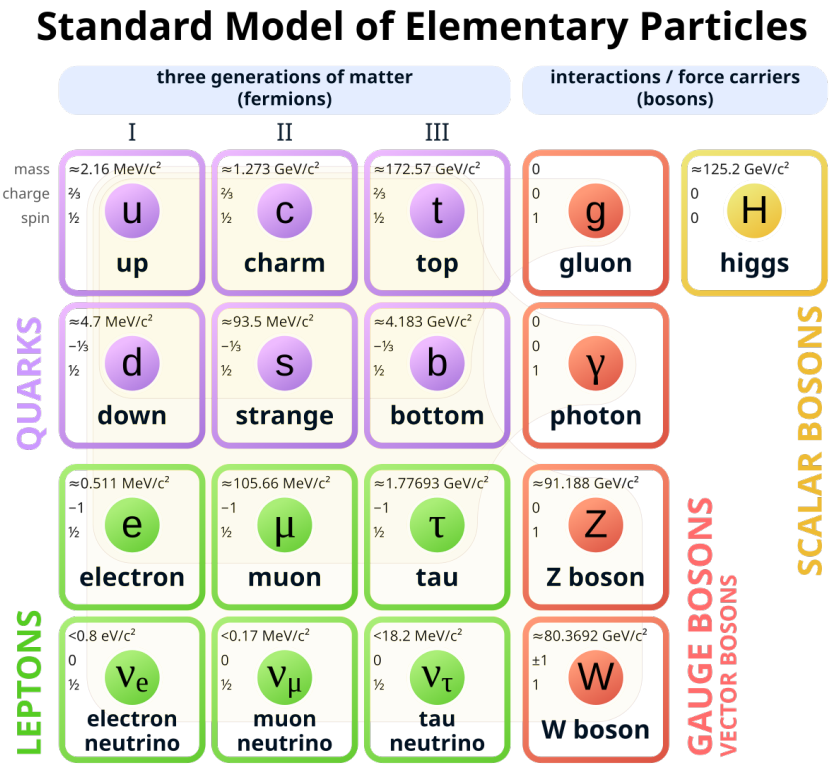

Figure 2.1: The fundamental particles of the SM. Quarks and leptons, both classified as fermions, are organized into three generations (columns). The four force carriers include the photon (electromagnetic interaction), W and Z bosons (weak interaction), and the gluon (strong interaction). The Higgs boson arises from the Higgs field, responsible for the mechanism of mass generation.

The matter fields are represented by spin-1/2 fermions, arranged into weak isospin doublets for each generation:

$$\begin{pmatrix} u \\ d \end{pmatrix}, \quad \begin{pmatrix} c \\ s \end{pmatrix}, \quad \begin{pmatrix} t \\ b \end{pmatrix}, \qquad \begin{pmatrix} \nu_e \\ e^- \end{pmatrix}, \quad \begin{pmatrix} \nu_\mu \\ \mu^- \end{pmatrix}, \quad \begin{pmatrix} \nu_\tau \\ \tau^- \end{pmatrix}. \tag{2.2}$$

Each particle has a corresponding antiparticle with the same mass and opposite electric charge and quantum numbers. For instance, the positron is the antiparticle of the electron, and each quark has a corresponding antiquark. When a particle and its antiparticle meet, they can annihilate, producing energy typically in the form of photons.

The interactions among these particles are mediated by bosons with integer spin, shown in Fig. 2.1. The strong interaction, described by the $SU(3)_C$ symmetry of quantum chromodynamics (QCD), is mediated by eight massless gluons. It is responsible for binding quarks together to form hadrons, such as protons and neutrons. In the context of hadronic τ decays – like $\tau^- \to \pi^- K^0_S \nu_\tau$ – the strong interaction governs the formation and dynamics of mesons such as K^0_S, making an understanding of QCD effects essential for precise measurements of CP violation.

The electromagnetic interaction is mediated by the photon (γ) and binds electrons to nuclei, forming atoms. It plays a central role in a wide range of physical phenomena, from atomic transitions to the propagation of light.

The weak interaction, governed by the $SU(2)_L \otimes U(1)_Y$ symmetry, is mediated by the $W^\pm$ and Z bosons. It is unique in enabling flavour-changing processes among both quarks and neutrinos. This interaction is responsible for β decay, neutrino oscillations, and various particle decays, including those of the τ lepton. In particular, $W^\pm$ bosons mediate charged-current interactions, allowing transitions between up- and down-type quarks, as well as between charged leptons and their corresponding neutrinos. This mechanism underlies decays like $\tau^- \to \pi^- K^0_S \nu\tau$, which are studied to probe CP violation at Belle II.

The Higgs boson, also included in Fig. 2.1, originates from the Higgs field, whose spontaneous symmetry breaking provides mass to the W and Z bosons and to the fermions via Yukawa couplings. The Higgs mechanism is essential for explaining the mass spectrum of SM particles and has direct implications for decay rates and kinematic distributions observed in experiments.

2.1.1 Open questions

Despite its predictive power and experimental successes, the SM leaves several fundamental questions unanswered. One major issue is its inability to incorporate gravity, as there is no quantum field theoretical description of gravitation within the SM framework. Additionally, dark matter and dark energy, which together make up about 95% of the universe's energy content, remain unexplained.

Another unresolved mystery is the origin of neutrino masses. The discovery of neutrino oscillations implies that neutrinos have mass, contradicting the original formulation of the SM. Extensions such as the seesaw mechanism suggest new physics beyond the SM.

Furthermore, the observed matter-antimatter asymmetry in the universe requires additional sources of CP violation beyond those currently included in the SM. The study of CP violation

in τ decays, such as the $\tau^- \to \pi^- K^0_S \nu_\tau$ process analyzed in this thesis, contributes to understanding this asymmetry and could provide hints of new physics.
Other open questions include the strong CP problem, the hierarchy problem, and the possibility of unifying the fundamental forces under a Grand Unified Theory or a framework such as Supersymmetry. Future experiments, including those at Belle II, aim to shed light on these mysteries and potentially lead to a more complete theory of fundamental interactions.

2.1.2 The CP violation problem

CP symmetry is a fundamental concept in particle physics, which states that the laws of physics should remain invariant if particles are replaced by their corresponding antiparticles (charge conjugation, C) and if their spatial coordinates are inverted (parity transformation, P). If CP were conserved, particles and antiparticles would exhibit identical behavior under all interactions.
We know that the atoms in our local part of the Universe are composed of electrons, protons, and neutrons, not their corresponding antiparticles. Astronomical searches for photons produced by the e^+e^- annihilation process at the boundaries between matter and antimatter regions of the Universe have ruled out the existence of galaxies or areas dominated by antimatter. The dominance of matter is thought to have emerged during the early stages of the Universe's evolution. In the early Universe, when the thermal energy $k_B T$ significantly exceeded the masses of hadrons, baryons and antibaryons were produced in equal numbers and remained in thermal equilibrium with the high-energy photon bath through processes such as

$$\gamma + \gamma \longleftrightarrow p + \bar{p} \; . \tag{2.3}$$

As the Universe expanded and cooled, the mean photon energy dropped below the threshold required for baryon-antibaryon pair production, rendering the forward reaction in Eq. 2.3 ineffective. Annihilation between baryons and antibaryons continued for a time, reducing their number densities, until the remaining baryons could no longer find antibaryons to annihilate with, effectively "freezing out" the baryon number. However, observations show that a small excess of baryons over antibaryons survived this annihilation epoch. The origin of this asymmetry is attributed to a mechanism known as baryogenesis, a process that occurred earlier in the Universe's evolution and generated a tiny imbalance between matter and antimatter. This asymmetry is essential for the existence of the observable matter-dominated Universe. If CP is not violated, equal number densities of baryons and antibaryons are predicted, $n_B = n_{\bar{B}}$, and a baryon to photon number n_γ density ratio of

$$n_B = n_{\bar{B}} \sim 10^{-18} n_\gamma \tag{2.4}$$

This prediction contradicts the observed matter-dominated Universe, where the baryon–antibaryon asymmetry, deduced from the relative abundances of light isotopes formed during Big Bang nucleosynthesis, is

$$\frac{n_B - n_{\bar{B}}}{n_\gamma} \sim 10^{-9}. \tag{2.5}$$

To explain the observed matter–antimatter asymmetry in the Universe, three conditions, which were originally formulated by Sakharov in 1967, must be satisfied. In the early Universe, there must have been:

- Baryon number non-conservation: There must be processes that do not conserve baryon number. At the beginning, there was no matter in the Universe, and the total baryon number was zero. However, the total baryon number is no longer zero in the present-day Universe, as shown by galaxies and stellar structures that are formed by baryons.

- Matter-antimatter asymmetric processes: There must be processes in nature that proceed at a different rate for matter and antimatter; otherwise, there should be equal amounts of matter and antimatter in the current Universe. Alternatively, matter and antimatter could have annihilated with each other, leaving no matter to form galactic structures.

- Non-equilibrium thermal conditions: There must be a time early in the early Universe when it was not in thermal equilibrium. If baryogenesis had occurred under conditions of thermal equilibrium, then it would have been equally likely to proceed backwards. More specifically, any process that creates a net baryon number will be cancelled out by the corresponding reverse process. An inflationary expansion stage of the Universe, for example, can provide the environment where non-equilibrium thermal conditions can be found.

In the SM, CP violation arises solely from a complex phase in the Cabibbo-Kobayashi-Maskawa (CKM) matrix, which governs quark mixing. In extensions of the SM that incorporate neutrino masses, an analogous phase appears in the Pontecorvo-Maki-Nakagawa-Sakata (PMNS) matrix, potentially leading to CP violation in the lepton sector [1]. Although CP violation has been experimentally observed in the decays of neutral K and B mesons, the magnitude of CP violation predicted by the SM is insufficient, by several orders of magnitude, to account for the observed matter–antimatter asymmetry of the Universe. This discrepancy strongly suggests the existence of additional sources of CP violation beyond the SM. Searching for such effects, for example in τ decays as investigated in this thesis, is therefore a crucial step toward understanding the origin of the baryon asymmetry and probing physics beyond the SM.

2.2 Charged weak currents and CKM matrix

The $W^{\pm}$ bosons mediate the charged currents of the weak interaction. They change the flavor of particles, enabling transitions between different generations of quarks and leptons. For example, a charged lepton radiating a W^{-} boson transforms into its corresponding neutrino, while a down-type quark can transition into an up-type quark via the exchange of a $W^{\pm}$ boson. These transitions are governed by the V-A (vector minus axial-vector) structure of the weak interaction, meaning that the charged weak current couples only to left-handed fermions. In the quark sector, such transitions are modulated by the Cabibbo-Kobayashi-Maskawa (CKM) matrix, which determines the strength of flavor-changing processes.
Mathematically, the interaction Lagrangian describing the coupling of the $W\pm$ bosons to fermions is given by:

$$\mathcal{L} = -\frac{g_2}{2\sqrt{2}}(J^{\mu}_{W} W^{-}_{\mu} + J^{\mu\dagger}_{W} W^{+}_{\mu}) \tag{2.6}$$

The factor g_2 is the weak coupling constant, related to the Fermi constant G_F via electroweak symmetry breaking. While $J_W^{\mu\dagger}$ represents the charged-raising weak current that contains contributions from both quark and lepton interactions. It can be written as

$$J_W^{\mu\dagger} = \begin{pmatrix} \bar{\nu_e} & \bar{\nu_\mu} & \bar{\nu_\tau} \end{pmatrix} \gamma^\mu (1-\gamma^5) \begin{pmatrix} e^- \\ \mu^- \\ \tau^- \end{pmatrix} + \begin{pmatrix} \bar{u} & \bar{c} & \bar{t} \end{pmatrix} \gamma^\mu (1-\gamma^5) V_q \begin{pmatrix} d \\ s \\ b \end{pmatrix} \tag{2.7}$$

where V_q is a unitary matrix, the quark fields are given in their mass eigenstates and the leptons in their flavour eigenstates. The matrices γ^μ and γ^5 are the Dirac matrices, which are fundamental to the description of fermions in quantum field theory and the weak interaction. The γ^μ matrices are a set of four 4×4 matrices that form the basis of the Dirac algebra. They satisfy the Clifford algebra relation,

$$\{\gamma^\mu \gamma^\nu\} = \gamma^\mu \gamma^\nu + \gamma^\nu \gamma^\mu = 2\eta^{\mu\nu} I, \tag{2.8}$$

where $\eta^{\mu\nu}$ is the Minkowski metric with signature $(+,-,-,-)$, and I is the 4×4 identity matrix. The γ^μ matrices can be represented in a variety of forms, with the most commonly used being the Dirac representation (or standard representation), where

$$\gamma^0 = \begin{pmatrix} I & 0 \\ 0 & I \end{pmatrix}, \quad \begin{pmatrix} 0 & \sigma^i \\ \sigma^i & 0 \end{pmatrix} \quad (i = 1,2,3), \tag{2.9}$$

with σ^i being the Pauli matrices. These matrices encode the relativistic structure of fermions and describe how they interact with gauge bosons.
The γ^5 matrix, defined as

$$\gamma^5 = i\gamma^0\gamma^1\gamma^2\gamma^3, \tag{2.10}$$

is another important matrix in the Dirac algebra. The operator $\frac{1}{2}(1 \mp \gamma^5)$ projects onto the left(right)-handed component of a Dirac-spinor.
Interactions of the form $\bar{\psi}\gamma^\mu\psi$ are called vector interactions because they transform as vectors under a parity transformation, P, given by:

$$P\vec{x} = -\vec{x} \tag{2.11}$$

On the other hand, interactions involving $\bar{\psi}\gamma^\mu\gamma^5\psi$ transform as axial vectors, denoted as $\vec{L}$, which remain unchanged under parity transformations:

$$P\vec{L} = \vec{L} \tag{2.12}$$

Thus, the weak interaction Lagrangian exhibits a V-A structure, meaning it maximally violates parity symmetry.
A similar analysis applies to the charge conjugation operator, C, which reverses the charge quantum numbers of particles. For example, under charge conjugation:

$$C\,|e^-\rangle = |e^+\rangle \tag{2.13}$$

The transformation of Dirac spinors under C is given by:

$$C\psi = i\gamma^2\psi. \tag{2.14}$$

Figure 2.2: The Feynman diagrams for $s \to u$ (left) and $\bar{s} \to \bar{u}$ (right) transitions.

Since the matrices γ^5 and γ^u anti-commute (i.e., $\gamma^5, \gamma^\mu = \gamma^5\gamma^\mu + \gamma^\mu\gamma^5 = 0$), the charge conjugation of the term $\bar{\psi}\gamma^\mu\gamma^5\psi$ introduces an additional minus sign. Therefore, the weak interaction also maximally violates C symmetry.
One direct consequence of this violation is that charged currents couple exclusively to left-handed particles and right-handed antiparticles. In the context of the weak interaction, the relevant particle-antiparticle transformation involves the combined CP transformation.
As already indicated, the fermion fields in Eq. 2.7 are expressed in their mass eigenstates. These mass eigenstates are the result of diagonalizing the Yukawa interaction terms in the SM Lagrangian, which are responsible for generating the masses of quarks. The mass terms take the form

$$m_q = \bar{q}_L q_R + \bar{q}_R q_L \ , \tag{2.15}$$

where m_1 represents the quark mass, and q_L and q_R denote the left- and right-handed components of a quark spinor, respectively. In this context, the mass eigenstates q are the physical states that diagonalize the quark mass terms. Importantly, the mass eigenstates q are not necessarily the same as the weak eigenstates q', which correspond to the quark states before accounting for their masses.
The unitary matrix V_q is used to relate the two sets of eigenstates. This matrix defines the transformation between the weak and mass eigenstates of quarks:

$$\begin{pmatrix} d' \\ s' \\ b' \end{pmatrix} = V_q \begin{pmatrix} d \\ s \\ b \end{pmatrix} , \tag{2.16}$$

where d, s, b represent the weak eigenstates, and d', s', b' are the mass eigenstates. The unitary matrix V_q is the CKM matrix V_{CKM} and it is defined as

$$V_{\text{CKM}} \equiv V_q = \begin{pmatrix} V_{ud} & V_{us} & V_{ub} \\ V_{cd} & V_{cs} & V_{cb} \\ V_{td} & V_{ts} & V_{tb} \end{pmatrix} . \tag{2.17}$$

The CKM matrix encodes the mixing between the different quark flavors and plays a crucial role in weak decays involving quarks.
As an illustration, the Feynman diagram for a $s \to u$ quark transition is depicted in Fig. 2.2. Feynman diagrams serve as visual representations of the rules used to calculate the transition matrix element for fundamental interactions. In the case of a $s \to u$ transition, the corresponding matrix element is proportional to V_{us}, while for the reverse transition $\bar{s} \to \bar{u}$ the matrix element is proportional to the complex conjugate V_{us}^*. These diagrams provide a convenient way to encode the dynamics of weak decays and quark flavor transitions. A commonly used approximation for

the CKM matrix is the Wolfenstein parameterization, which expresses the matrix elements in terms of four parameters: λ, A, ρ, and η. These parameters provide an intuitive understanding of quark mixing and CP violation. The CKM matrix in this form is written as:

$$V_{\mathrm{CKM}} = \begin{pmatrix} 1 - 1/2\lambda^2 & \lambda & A\lambda^3(\rho - i\eta) \\ -\lambda & 1 - 1/2\lambda^2 & A\lambda^2 \\ A\lambda^3(1 - \rho - i\eta) & -A\lambda^2 & 1 \end{pmatrix} + \mathcal{O}(\lambda^4). \tag{2.18}$$

Here:

- $\lambda \simeq 0.225$ serves as an expansion parameter and reflects the hierarchical structure of quark mixing. It approximately corresponds to $\sin\theta_C$, the sine of the Cabibbo angle [2].
- A influences the mixing elements V_{ts}, V_{tb}, V_{td}, and V_{ct}, which correspond to transitions involving the top quark.
- ρ and η parameterize the CP-violating phase in the CKM matrix, with η playing the dominant role, while ρ has a lesser effect. This CP-violating phase governs CP violation in weak interactions.

The Wolfstein parameterization is particularly useful because it clearly shows the hierarchical structure of quark mixing, where transitions between different generations are suppressed by increasing powers of λ.

2.3 Kaon phenomenology

The weak interaction discussed in the previous section leads to neutral meson mixing and CP violation in the SM. Here, the phenomenology of mixing and CP violation is discussed with a focus on strange mesons.

2.3.1 Neutral meson mixing

The charged currents couple a meson, K^0, and its anti-meson, $\bar{K}^0$, to a two-state system. The effective Schroedinger equation with the Hamiltonian $\mathbf{H} = (\mathbf{M} - \frac{i}{2}\mathbf{\Gamma})$ is

$$\begin{aligned} i\frac{\mathrm{d}}{\mathrm{d}t}\begin{pmatrix} |K^0(t)\rangle \\ |\bar{K}^0(t)\rangle \end{pmatrix} &= \left(\mathbf{M} - \tfrac{i}{2}\mathbf{\Gamma}\right)\begin{pmatrix} |K^0(t)\rangle \\ |\bar{K}^0(t)\rangle \end{pmatrix} \\ &= \left(\begin{pmatrix} M_{11} & M_{12} \\ M_{12}^* & M_{22} \end{pmatrix} - i\begin{pmatrix} \Gamma_{11} & \Gamma_{12} \\ \Gamma_{12}^* & \Gamma_{22} \end{pmatrix}\right)\begin{pmatrix} |K^0(t)\rangle \\ |\bar{K}^0(t)\rangle \end{pmatrix}, \end{aligned} \tag{2.19}$$

where $\mathbf{M}$ is the mass matrix with $\mathbf{M} = \mathbf{M}^\dagger$ and $\mathbf{\Gamma}$ the decay matrix with $\mathbf{\Gamma} = \mathbf{\Gamma}^\dagger$.
CPT symmetry requires that $m = M_{11} = M_{22}$ and $\Gamma = \Gamma_{11} = \Gamma_{22}$. Off-diagonal elements of the mass matrix $\mathbf{M}$ are related to the box diagrams shown in Fig. 2.3. The off-diagonal elements of the decay matrix $\mathbf{\Gamma}$ arise due to the possibility that both K^0 and $\bar{K}^0$ can decay into common final states via weak interactions. These shared decay channels lead to interference effects that

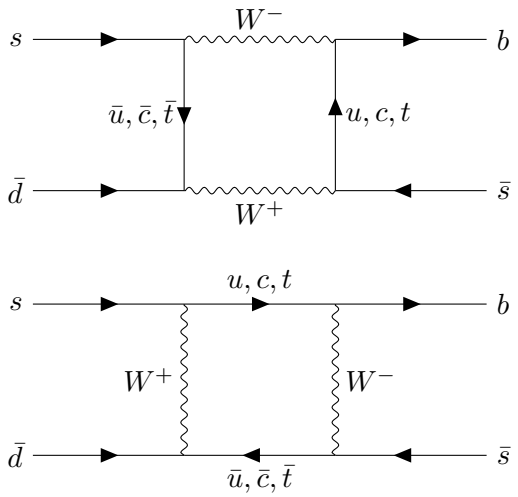

Figure 2.3: Two box diagrams describing K^0–$\bar{K}^0$ mixing.

contribute to Γ_{12} and Γ_{12}^*.
The mass eigenstates of Hamiltonian $\mathbf{H}$, K_S and K_L, obey the exponential decay,

$$\begin{aligned} |K_\mathrm{L}(t)\rangle &= e^{-iM_\mathrm{L}t}e^{-\Gamma_\mathrm{L}t/2}\,|K_\mathrm{L}\rangle\,, \\ |K_\mathrm{S}(t)\rangle &= e^{-iM_\mathrm{S}t}e^{-\Gamma_\mathrm{S}t/2}\,|K_\mathrm{S}\rangle\,, \end{aligned} \tag{2.20}$$

where the masses and lifetimes are given by:

$$\begin{aligned} m = \frac{M_\mathrm{L}+M_\mathrm{S}}{2}\,, \quad \Gamma = \frac{\Gamma_\mathrm{L}+\Gamma_\mathrm{S}}{2} = \frac{1}{\tau}\,, \\ \Delta m = M_\mathrm{L}-M_\mathrm{S}\,, \quad \Delta\Gamma = \Gamma_\mathrm{L}-\Gamma_\mathrm{S}\,. \end{aligned} \tag{2.21}$$

The mass difference Δm is always chosen to be positive, $\Delta\Gamma$ can have both signs. The combinations $x \equiv \Delta m/\Gamma$ and $y \equiv \Delta\Gamma/(2\Gamma)$ are commonly used to describe the mixing parameters.
The mass eigenstates, K_L and K_S, can be written in terms of the strong interaction eigenstates, K^0 and $\bar{K}^0$, as

$$\begin{aligned} |K_S\rangle &= p\,|K^0\rangle + q\,|\bar{K}^0\rangle\,, \\ |K_L\rangle &= p\,|K^0\rangle - q\,|\bar{K}^0\rangle\,, \end{aligned} \tag{2.22}$$

where p and q are complex parameters with the normalisation requirement $|p^2| + |q^2| = 1$.
The ratio $\frac{p}{q}$ is given by

$$\left(\frac{p}{q}\right)^2 = \frac{2M_{12}^* - i\Gamma_{12}^*}{2M_{12} - i\Gamma_{12}}. \tag{2.23}$$

The time evolution of the states K^0 and $\bar{K}^0$ can be obtained by combining Equations 2.20 and 2.22:

$$|K^0(t)\rangle = g_+(t)\,|K^0\rangle + \frac{q}{p}g_-(t)\,|\bar{K}^0\rangle\,, \tag{2.24}$$

$$|\bar{K}^0(t)\rangle = \frac{p}{q}g_-(t)\,|K^0\rangle + g_+(t)\,|\bar{K}^0\rangle\,. \tag{2.25}$$

where the functions $g_+(t)$ and $g_-(t)$are given by

$$g_+(t) = e^{-imt}e^{-\Gamma t/2}\left[\cosh\frac{\Delta\Gamma t}{4}\cos\frac{\Delta m t}{2} - i\sinh\frac{\Delta\Gamma t}{4}\sin\frac{\Delta m t}{2}\right], \tag{2.26}$$

$$g_-(t) = e^{-imt}e^{-\Gamma t/2}\left[\sinh\frac{\Delta\Gamma t}{4}\cos\frac{\Delta m t}{2} + i\cosh\frac{\Delta\Gamma t}{4}\sin\frac{\Delta m t}{2}\right], \tag{2.27}$$

Equations 2.24 and 2.25 are not symmetric under CP transformation if $|\frac{q}{p}|$ is different from 1. This defines CP violation in mixing.
Table 2.1 summarises the mixing parameters of K^0 mesons. Neutral kaons have a very large lifetime splitting. The lifetime of the long-lived state, $K^0_{\rm L}$, is about 500 times larger than that of the short-lived state, $K^0_{\rm S}$.

Meson	**Mass**	**Lifetime**
K^0	$m = (497.614 \pm 0.024)$ MeV/c^2	
$K^0_{\rm S}$	$\Delta m = (0.5293 \pm 0.0009) \times 10^{10}\hbar$ s^{-1}	$\tau_{\rm S} = (0.8954 \pm 0.0004) \times 10^{-10}$ s
$K^0_{\rm L}$		$\tau_{\rm L} = (5.116 \pm 0.0021) \times 10^{-8}$ s
	$x \simeq 0.9$	$y \simeq 1$

Table 2.1: The mixing parameters of K^0 mesons. Approximate numbers are calculated from the measured values in the table.

2.4 The CP violation

Given the definition of the mass eigenstates as in Eq. 2.22, an asymmetry parameter ϵ can be defined as

$$\epsilon = \frac{p-q}{p+q}. \tag{2.28}$$

Note that when $\epsilon = 0$, there is no CP violation. Furthermore, the two eigenstates are no longer orthogonal; rather, the inner product of the two eigenstates is proportional to the real part of ϵ to first order of ϵ:

$$\langle K^0_{\rm L}|K^0_{\rm S}\rangle = |p^2| + |q^2| \simeq 2{\rm Re}(\epsilon). \tag{2.29}$$

The parameter ϵ is related to the processes represented in Fig. 2.3. The matrix element (M_{fi}) for the transition of K^0 to $\bar{K}^0$ by an exchange of quarks q and q' is proportional to $G_F^2 V_{qd}V_{qs}^* V_{q'd}V_{q's}^*$. Conversely, the matrix element for the transition of $\bar{K}^0$ to K^0 is proportional to the complex conjugate M_{fi}^*. the difference in transition rates between $K^0 \to \bar{K}^0$ and $\bar{K}^0 \to K^0$ is then proportional to the imaginary part of M_{fi}:

$$\Gamma(K^0 \to \bar{K}^0) - \Gamma(\bar{K}^0 \to K^0) = 2{\rm Im}(M_{fi}). \tag{2.30}$$

In other words, the non-zero complex phase in the CKM matrix is a necessary condition for a non-zero ϵ, which represents the mixture of different CP eigenstates in $K^0_{\rm L}$ and $K^0_{\rm S}$.
In Section ... it will be shown that the asymmetry measured in this work is proportional to the

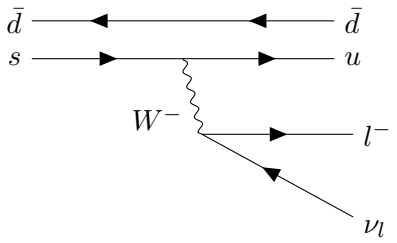

Figure 2.4: Feynman diagram for $\bar{K}^0 \to \pi^+ l^- \nu_l$. The strangeness changes from -1 ($\bar{K}^0$) to 0 (π^+) during the process, so the charge changes from 0 ($\bar{K}^0$) to 1 (π^+).

real part of ϵ ($\mathcal{R}(\epsilon)$). One can measure Re(ϵ) by noting that only K^0_{L} component remains at a time sufficiently long after production of the neutral kaon:

$$|K^0_{\mathrm{L}}\rangle = \frac{1}{\sqrt{2}\sqrt{1+|\epsilon|^2}} \left[(1+\epsilon)\,|K^0\rangle + (1-\epsilon)\,|\bar{K}^0\rangle\right]. \tag{2.31}$$

Due to the $\Delta Q = \Delta S$ rule [3], that states that the change in the electric charge Q of the hadron is equal to the change in its strangeness quantum number S, the semileptonic decay $K^0_{\mathrm{L}} \to \pi^+ l^- \bar{\nu}_l$ primarily comes from the $\bar{K}^0$ component of the K^0_{L} [4]. Fig 2.4 shows that as $\bar{K}^0$ meson decays to a π^+ meson, the strangeness changes from -1 to 0, and the charge increases by 1. Similarly, $K^0_{\mathrm{L}} \to \pi^- l^+ \nu_l$ primarily comes from the K^0 component. The semileptonic decay rates for the K^0_{L} are proportional to the components of the K^0 and the $\bar{K}^0$:

$$\Gamma(K^0_{\mathrm{L}} \to \pi^+ l^- \bar{\nu}_l) \propto |\,\langle \bar{K}^0 | K^0_{\mathrm{L}}\rangle\,|^2 \propto |1+\epsilon|^2 \simeq 1 + 2\mathrm{Re}(\epsilon), \tag{2.32}$$

$$\Gamma(K^0_{\mathrm{L}} \to \pi^- l^+ \nu_l) \propto |\,\langle K^0 | K^0_{\mathrm{L}}\rangle\,|^2 \propto |1-\epsilon|^2 \simeq 1 - 2\mathrm{Re}(\epsilon), \tag{2.33}$$

where the approximations are good to the first order of ϵ. Thus, by comparing the decay rates for $K^0_{\mathrm{L}} \to \pi^+ l^- \bar{\nu}_l$ and $K^0_{\mathrm{L}} \to \pi^- l^+ \nu_l$, one can measure Re($\epsilon$) (the approximation is accurate to the first order of ϵ). Experimental results find $2\mathrm{Re}(\epsilon) = (3.27 \pm 0.12) \times 10^{-3}$ [5].
Other than in kaon decays, the CP violation has also been observed in B meson decays, with significant contributions from experiments at B factories such as Belle II and LHCb. The decays of B_d mesons, for example, help constrain some of the parameters in the CKM matrix [4]. In addition, CP violation has been explored in D meson decays, although no significant evidence has been found to date. Another manifestation of CP violation in the B meson sector is the mixing of B^0 and $\bar{B}^0$ mesons [4].

2.5 The τ lepton

τ leptons are fundamental particles and belong to the third generation of leptons. Being leptons, they do not interact via the strong interaction and decay only via the weak interaction, which makes them valuable probes of weak-interaction dynamics within the SM [6], as well as sensitive tools for exploring potential signals of physics beyond the SM.
The τ has a relatively short lifetime ($\tau_\tau = 290$ fs) compared to other leptons ($\tau_\mu = 2.2$ μs), which makes them almost decay immediately, and usually only their decay products can be detected. They are the heaviest of the three leptons, with a mass of 1776.86 ± 0.12 MeV [7], which allows them to decay into not only electrons and muons, but also hadrons.

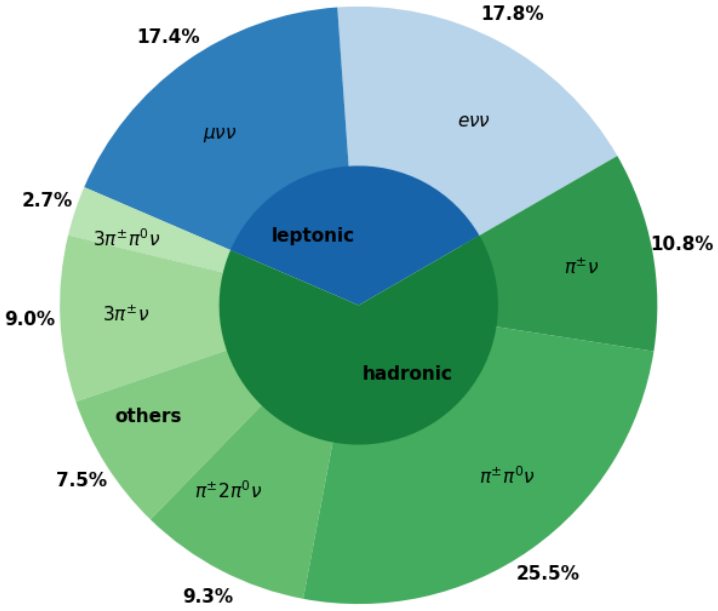

Figure 2.5: A pie chart of τ branching fractions.

Fig 2.5 shows a pie chart of the most common τ lepton decay modes and their relative branching fractions. Although the τ can decay to both pions and kaons, decays to kaons are Cabibbo-suppressed relative to pion modes due to the smaller value of the CKM matrix element $|V_{us}|$ compared to $|V_{ud}|$ (see Section 2.2). This suppression is approximately of order $\lambda^2 \simeq 0.05$, where λ is the Wolfenstein parameter introduced earlier. The hadronic decays of τ leptons are of great interest since they also provide a unique way to study the strong interaction responsible for binding quarks together to form hadrons [8, 9]. The leptonic decays of the τ can instead be used to test the Lorentz structure of the charged current in the theory of weak interaction. The observable parameters are called Michel parameters, which are bilinear combinations of coupling constants that arise in the most general expression for the decay matrix element [8].
In the SM, the only non-zero coupling due to the V-A nature of the weak interaction is the left-handed vector coupling g^V_{LL}.
The leptonic decays of the τ make up about 35.2% of all decays. In Fig 2.6 Feynamn diagrams are shown for a generic hadronic decay and a leptonic decay, where l denotes either an electron or a muon.

2.5.1 CP Violation in the τ Leptons Sector

CP violation has so far been firmly established only in the quark sector, particularly in the decays of K and B mesons. In the lepton sector, no direct observation of CP violation has been made yet. However, the discovery of neutrino oscillations has opened the possibility of

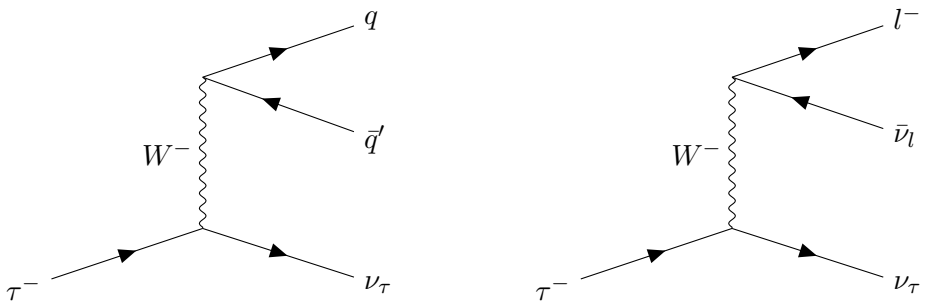

Figure 2.6: Feynman diagrams for a hadronic decay (left) and a leptonic decay (right) of the τ lepton.

CP violation in the neutrino sector, governed by a complex phase in the PMNS matrix. Recent results from experiments such as T2K and NOvA provide hints of such effects [10], but no conclusive evidence has been reported to date.
In charged lepton decays, CP violation is highly suppressed in the SM. Nevertheless, Bigi and Sanda have shown that small but nonzero CP-violating effects can arise in certain τ decays, such as $\tau^- \to \bar{K}^0\pi^-\nu_\tau$, due to the K^0–$\bar{K}^0$ mixing and associated interference effects [5]. According to the SM, the following transition amplitudes are equal:

$$T(\tau^- \to \bar{K}^0\pi^-\nu) = T(\tau^+ \to K^0\pi^+\nu) \tag{2.34}$$

However, observations are made with the mass eigenstates K_L and K_S, not the flavour eigenstates K^0 and $\bar{K}^0$. The mixing of the eigenstates is the same as what is presented in Section 2.3.1. Since K_L and K_S are not orthogonal, both $K_L \to 2\pi$ and $K_S \to 2\pi$ are possible. The asymmetry for the $\tau^- \to K_S\pi^-\nu_\tau$ is then [5]:

$$A = \frac{\Gamma(\tau^+ \to \text{“}K_S\text{”}\pi^+\bar{\nu}_\tau) - \Gamma(\tau^- \to \text{“}K_S\text{”}\pi^-\nu_\tau)}{\Gamma(\tau^+ \to \text{“}K_S\text{”}\pi^+\bar{\nu}_\tau) + \Gamma(\tau^- \to \text{“}K_S\text{”}\pi^-\nu_\tau)} = |p^2| + |q^2| \simeq 2\text{Re}(\epsilon) \tag{2.35}$$

where “K_S” (in quotation marks) represents both K_S and K_L decays to the $\pi^+\pi^-$ final state. The approximation is accurate to the first order of ϵ. The description given above does not specify the dynamics that generate $|q| \neq |p|$; rather, it only relies on the assumption that the τ decay is described by SM dynamics.
A measured deviation of the asymmetry from the SM prediction would indicate the presence of additional underlying dynamics. One potential source of such new physics is CP violation resulting from the interference of amplitudes, one of which involves the exchange of supersymmetric (SUSY) particles [11], as illustrated in Fig. 2.7. In Fig. 2.8, for example, the SM amplitude (left) and the amplitude of a charged Higgs exchange (right) can interfere. Namely, the charged Higgs diagram will contribute to both s- and p-wave states [12]. However, while this effect is apparent in an angular distribution analysis, a study on the overall asymmetry should not be affected, barring any detector-induced effect. There are, however, no explicit predictions of the impact of new physics effects on CP violation in τ decays.

2.5.2 Goal of the Study

The goal of the study is to measure the asymmetry presented by Bigi and Sanda in τ lepton decays [5]. The τ lepton decays provide a clean laboratory for studies, which is desirable in the

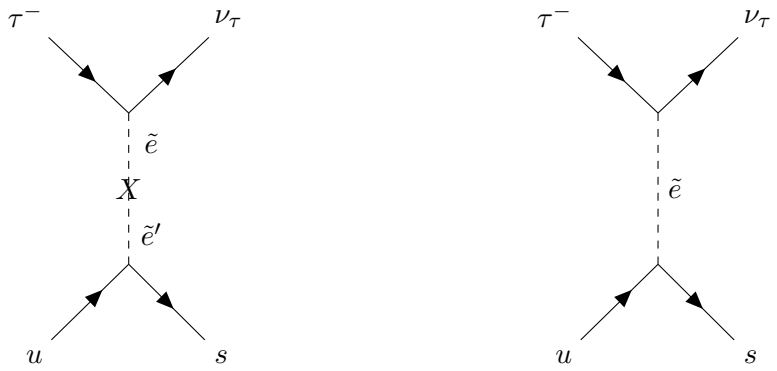

Figure 2.7: Non-SM contributions to $\tau^- \to \bar{u}s\nu_\tau$ in supersymmetric scenarios.

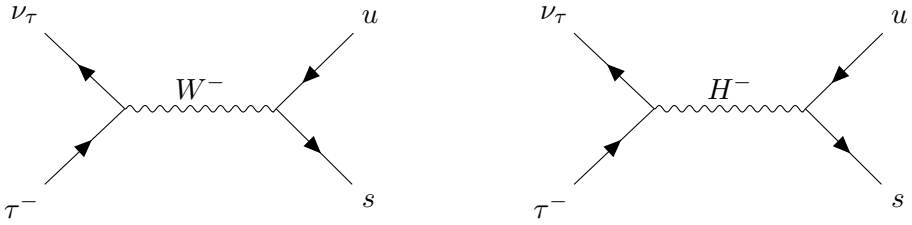

Figure 2.8: τ decaying via a W boson (left) and a charged Higgs boson (right).

investigations of new physics effects. Namely, hadronic backgrounds will be low, and detector inefficiencies arising from a high number of charged tracks in the detector can be avoided. If the CP asymmetry is found to deviate from the SM prediction, then it is a signal for new physics. The measured CP asymmetry may also be used as a constraint to rule out some new physics models in particular.

The number of decays observed is proportional to the decay rate. By counting the numbers of decays for the modes $\tau^- \to \pi^- K^0_{\rm S}(\geq 0\pi^0)\nu_\tau$ and $\tau^+ \to \pi^+ K^0_{\rm S}(\geq 0\pi^0)\bar{\nu}_\tau \to$ separately, one can then compute the asymmetry:

$$A_Q = \frac{N(\tau^+ \to \pi^+ K^0_{\rm S}(\geq 0\pi^0)\bar{\nu}_\tau) - N(\tau^- \to \pi^- K^0_{\rm S}(\geq 0\pi^0)\nu_\tau)}{N(\tau^+ \to \pi^+ K^0_{\rm S}(\geq 0\pi^0)\bar{\nu}_\tau) + N(\tau^- \to \pi^- K^0_{\rm S}(\geq 0\pi^0)\nu_\tau)} \,. \tag{2.36}$$

The Belle II experiment provides a large sample of τ lepton decays, which is instrumental in reducing the statistical uncertainty in the final result and in turn, can increase the sensitivity to new physics, should there be any. The Belle II detector, as well as the strategy of selecting the dataset, will be described in the next chapters.

2.6 Analysis Overview

This analysis aims to search for direct CP violation in the decay $\tau^- \to \pi^- K^0_{\rm S}(\geq 0\pi^0)\nu_\tau$, where $K^0_{\rm S} \to \pi^+\pi^-$.

CP violation has been observed in the K and B meson decays. Within the SM, there is no asymmetry expected in the lepton decays, and in particular in the $\tau^- \to \pi^-\bar{K}^0\nu_\tau$ and $\tau^+ \to \pi^+ K^0\bar{\nu}_\tau$ decays.

However, following the arguments of Bigi and Sanda [5], since experimentally, we observe K^0_S

and K_L^0, the decay of the lepton to final states containing a K_S^0, will also have a non-zero decay-rate asymmetry due to CP violation in the kaon sector. The reason is that K_S^0 and K_L^0 are linear combinations of K^0 and $\bar{K}^0$ states,

$$|K_S^0\rangle = p|K^0\rangle + q|\bar{K}^0\rangle$$
$$|K_L^0\rangle = p|K^0\rangle - q|\bar{K}^0\rangle,$$

and those are not exact CP eigenstates. As a result, the charge asymmetry (A_Q):

$$A_Q = \frac{\Gamma(\tau^+ \to \pi^+ K^0 \bar{\nu}_\tau) - \Gamma(\tau^- \to \pi^- \bar{K}^0 \nu_\tau)}{\Gamma(\tau^+ \to \pi^+ K^0 \bar{\nu}_\tau) + \Gamma(\tau^- \to \pi^- \bar{K}^0 \nu_\tau)}, \tag{2.37}$$

where the K^0 and $\bar{K}^0$ are identified as K_{S}^0, with Γ being the decay rate, is expected to be non-zero.

The charge asymmetry in Eq. 2.37 is computed for short (proper) decay times of the kaon, t_K, of the order of the K_{S} lifetime, $\mathcal{O}(\Gamma_S^{-1})$.

Bigi and Sanda predict that $A_Q = (3.27 \pm 0.12) \times 10^{-3}$ and its measurement would provide a valuable calibration point in CP searches. Any deviation from the SM prediction would be evidence for new physics.

2.7 Previous measurements

Previously, two experiments, BABAR at PEP II and Belle at KEKB, have already searched for direct CP violation in $\tau^\pm \to K_{\mathrm{S}}^0 \pi^\pm \nu_\tau$ decays, using two different analysis methods and obtaining different results.

The Belle collaboration [13] searched for CP violation, A_{CP}, in angular observables of this decay and found the measurement to be compatible with zero with a precision of $O \sim 10^{-3}$.

The BABAR collaboration [14] searched for CP violation by measuring the decay-rate asymmetry A_Q (see Eq. (2.37)) using $\tau^- \to \pi^- K_{\mathrm{S}}^0 (\geq 0\pi^0)\nu_\tau$, and the corresponding charge conjugate decays. The decay-rate asymmetry was measured to be $(-0.36 \pm 0.23_{\mathrm{stat.}} \pm 0.11_{\mathrm{syst.}})\%$. This measurement is 2.8σ away from the SM prediction of $(0.36 \pm 0.01)\%$ [5].

For this reason, in the recent years, the theory community has been looking for a result from Belle II, that could confirm or invalidate the discrepancy observed by BABAR.

In this context, Belle II provides an opportunity to revisit this measurement with improved detector performance and analysis techniques, even though the current dataset is of comparable size to that used by BABAR. The work presented in this thesis focuses on a new measurement of CP violation in $\tau^- \to \pi^- K_S^0 \nu_\tau (\geq 0\pi^0)$ decays using a datset with an integrated luminosity of 365 fb^{-1}. Following a similar approach to that of BABAR, this analysis measures the decay-rate asymmetry between τ^+ and τ^- decays, with corrections applied for detector-induced asymmetries and background contributions.

The measurement is performed separately for electron- and muon-tagged events. Contributions from $\tau^- \to K^- K_{\mathrm{S}}^0 \nu_\tau$ and $\tau^- \to \pi^- K^0 \bar{K}^0 \nu_\tau$ decays are treated as background and removed through a dilution correction. The objective is to provide an independent and more robust cross-check of the BABAR result, benefiting from improved control of systematic uncertainties.

2.8 Summary

The main messages of this chapter are:

- CP violation is one of the processes that can explain the origins of the matter-antimatter asymmetry in the Universe.
- The flavour-changing currents of the weak interaction induce CP violation and neutral meson mixing.
- CP violation was never observed in τ sector. If the CP asymmetry is found to deviate from the SM prediction, then it is a signal for new physics.
- A dedicated measurement strategy using the Belle II dataset is designed to improve upon previous analyses by BABAR and Belle, aiming to clarify the observed discrepancy with the SM prediction and enhance sensitivity to potential new physics.

Chapter 3

The Belle II Experiment

3.1 Introduction

The Belle II experiment [15] is a high-energy physics experiment hosted at the High Energy Accelerator Research Organisation (KEK) in Tsukuba, Japan. Belle II began construction in 2010 and took approximately seven years to complete, with its commissioning phase starting in 2018. It was constructed as an upgrade to its predecessor, the Belle experiment, which operated from 1999 to 2010.

The experiment operates at the SuperKEKB accelerator [16], an asymmetric beam energy electron-positron collider designed to produce large amounts of B mesons, hence the frequent use of the term "B-factory" to qualify such experiments. The collision data is collected at the interaction point (IP) by the Belle II detector. Belle II's primary goals are to search for new physics (NP) and to improve the measurements of SM parameters. But, like its predecessor, it also focuses on exploring CP violation (CPV) and rare decays in B mesons to better understand the universe's matter-antimatter asymmetry.

In fact, notable discoveries from Belle include the observation of rare B meson decays [17], contributions to our understanding of CPV [18] and precision measurements of SM parameters [19]. Belle II's physics program encompasses a wide range of topics, including, among others, B, D and τ physics, and investigations into dark matter and dark energy phenomena [15]. As it continues its operation, the Belle II experiment holds the potential to make further discoveries.

3.2 The SuperKEKB accelerator

SuperKEKB is a circular electron-positron accelerator. As depicted in Fig. 3.1, it consists first of a linear injection system (linac) that accelerates the electrons e^- and positrons e^+. As positrons are produced with higher emittance than electrons, they have to go through an additional stage, the damping ring. This dedicated positron damping ring prepares the positron beam by reducing its emittance and stabilizing its trajectory. Once the beam is sufficiently conditioned, it is injected, like the electron beam is, into the main accelerator rings. This last part includes two rings, one for each particle, and has a circumference of 3 km. The Belle II detector, that will be detailed in Section 3.3, is situated at the interaction point of both beams.

As mentioned earlier, SuperKEKB is an asymmetric beam energy accelerator, which means that

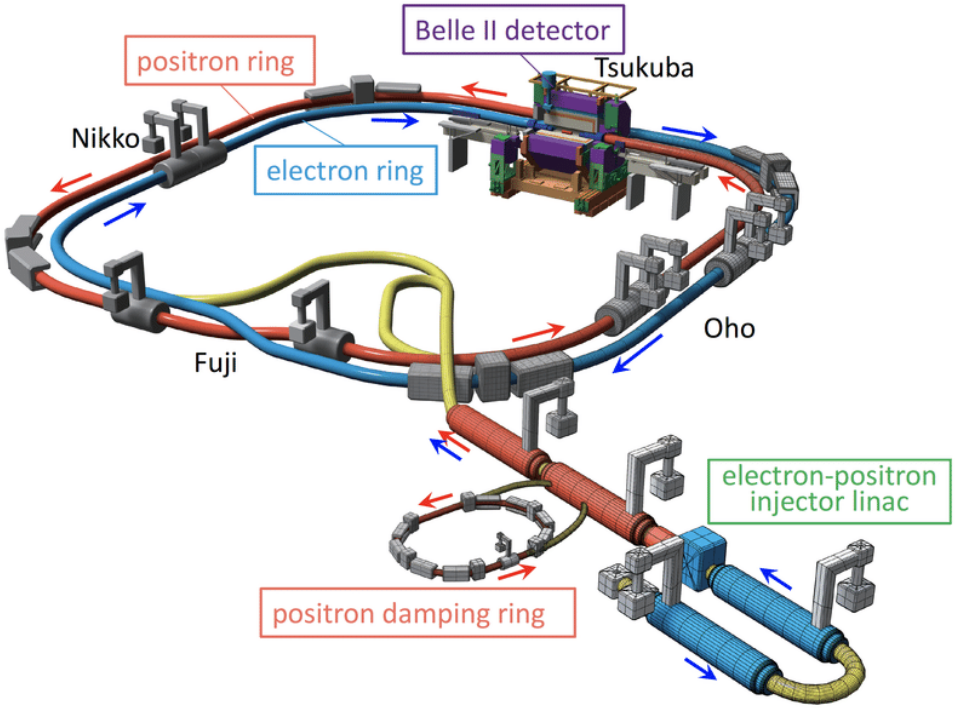

Figure 3.1: An overview of the SuperKEKB accelerator, taken from "SuperKEKB collider" [20].

electrons and positrons are not accelerated with the same energy. The electron ring is a high-energy ring (HER) of 7 GeV, and the positron ring is a low-energy ring (LER) of 4 GeV. The asymmetry is a key element to allow for time-dependent CP measurements. In comparison, Belle had a LER of 3.5 GeV and a HER of 8 GeV. This change of Lorentz boost from $\beta\gamma = 0.42$ to $\beta\gamma = 0.28$ enables measurement improvements. Even if it reduces the beam loss due to Touschek scattering in the lower energy beam, explained later in Section 3.2.1, which, in turns, reduces the spatial separation between B mesons, it leads to improvements in solid angle acceptance for missing energy decays, and therefore is advantageous for analysis with neutrinos in the final state.

The beam energies are chosen not only to get boosted collision products, but also such that the resulting center of mass system (CMS) energy is 10.58 GeV. This energy corresponds to the $\Upsilon(4S)$ resonance, depicted in Fig. 3.2. This resonance maximises the production of the B mesons through the decay $e^+e^- \to (\Upsilon(4S) \to B\bar{B})$, as the branching fraction of $\Upsilon(4S) \to B\bar{B}$ itself is higher than 96% [7]. As shown in Fig. 3.2, even though the majority of the data is collected at the $\Upsilon(4S)$ resonance, the beam energies are flexible enough to cover other resonances as well, from $\Upsilon(1S)$ at 9.46 GeV to $\Upsilon(6S)$ at 11.24 GeV. These resonances do not necessarily decay into the same final products, allowing further analysis to be undertaken. The CMS energy is confined within this specific resonance range; the upper limit is set by the constrained power of the linear injector, and even if this limit could be circumvented, the beam transport limit due to magnet strength would only allow a restricted increase. The lower limit is due to the current lattice design not being sufficient to accommodate lower energies.

It must also be mentioned that the data sets that can be collected at B-factories are not made only of B mesons. As illustrated by the chart in Fig. 3.3, and detailed in Section 3.6, at

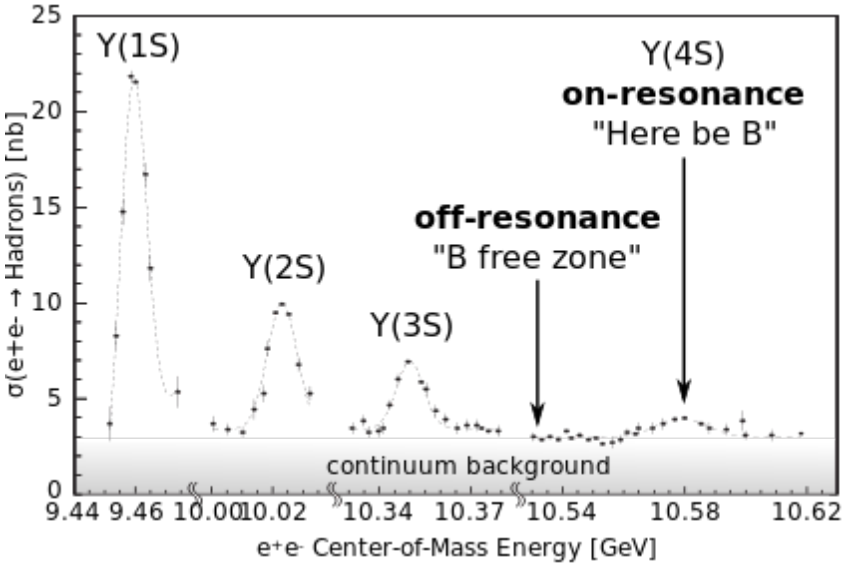

Figure 3.2: $e^+e^- \rightarrow$ hadrons cross section as a function of the center-of-mass energy. The "off-resonance" arrow at 60 MeV below the $\Upsilon(4S)$ resonance indicates the energy where no B mesons can be produced, allowing to collect a pure sample of continuum events [21].

$\sqrt{s} = 10.58$ GeV the production cross sections of $e^+e^- \rightarrow \tau^+\tau^-$ and $e^+e^- \rightarrow c\bar{c}$ events are comparable to $e^+e^- \rightarrow \Upsilon(4S)$. Hence, B-factories are also τ-charm factories, allowing to study with high precision the charm and τ production and decays. The performance of an accelerator can be expressed by the luminosity it is capable of delivering. The luminosity, denoted as $\mathcal{L}$, is a measure of the number of events N that are produced in a certain amount of time t, which takes into account their cross-section σ, as:

$$\mathcal{L} = \frac{1}{\sigma}\frac{\mathrm{d}N}{\mathrm{d}t} \tag{3.1}$$

It is expressed in the units of $\mathrm{cm}^{-2}\mathrm{s}^{-1}$ or $\mathrm{b}^{-1}\mathrm{s}^{-1}$, where 1 b = 10^{-24} cm^2. A useful related quantity is the integrated luminosity $\mathcal{L}_{\mathrm{int}}$, which is:

$$\mathcal{L}_{\mathrm{int}} = \int \mathcal{L}\ \mathrm{d}t \tag{3.2}$$

The luminosity can be estimated by different methods that mainly relies on counting the number of events of a very specific type of controlled events produced in great quantities.

3.2.1 Beam-induced backgrounds

The Belle II detector has to deal with many beam-induced backgrounds that can potentially affect its performance. Beam-induced backgrounds arise from imperfections or intrinsic dynamics of the stored beams themselves, often related to beam stability, vacuum quality, or injection mechanics. They exist even without actual collisions. The most significant are Touschek scattering, beam-gas scattering, synchrotron radiation, and injection background. Single-beam backgrounds can be avoided or reduced to some degree with beam-steering, collimators, vacuum-scrubbing, shielding, or a well-designed interaction region (IR).

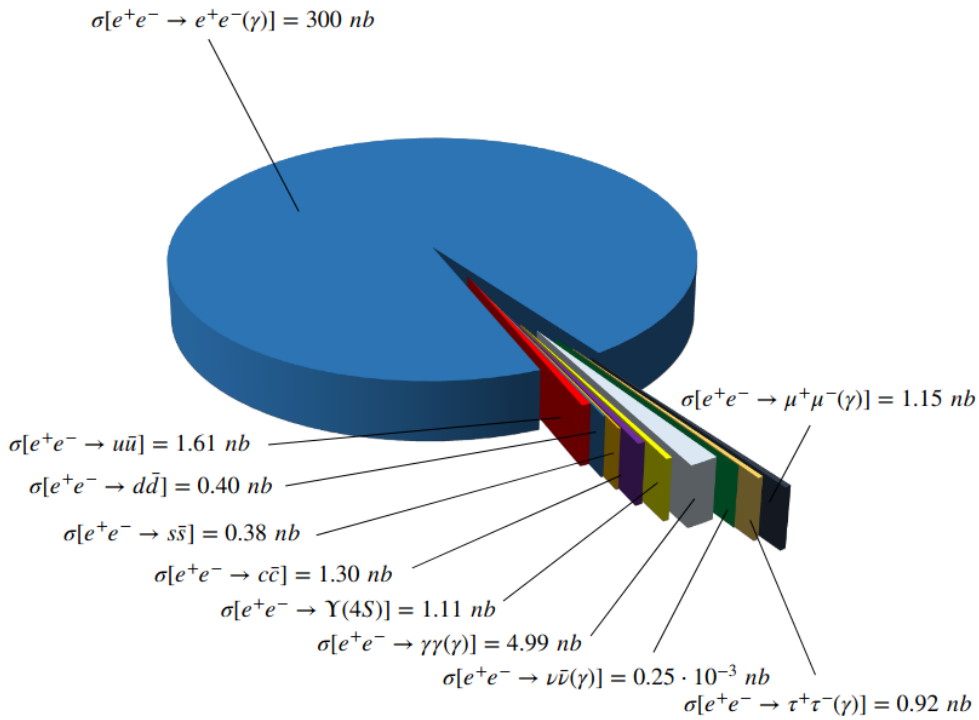

Figure 3.3: Cross sections of the main final states produced in e^+e^- collision at the $\Upsilon(4S)$ center-of-mass energy. Credit: Ref. [22].

- **Touschek scattering**: Touschek scattering occurs when particles within a bunch collide and subsequently strike the beam pipe. This results in a particle shower that may hit the Belle II detector. The rate of Touschek scattering depends on the beam current, the total number of bunches, and is inversely proportional to the beam size [23]. Because of the small beam sizes in SuperKEKB, Touschek scattering is a major background source. However, it is only relevant for the LER since the scattering rate is also proportional to $1/E^3$ with E being the beam energy, and the HER also has a lower beam current [24].

- **Beam-gas scattering**: Beam-gas scattering occurs when the beams interact with residual gas in the vacuum tubes and then hit the wall of the vacuum chamber, producing a shower of particles. The beams can interact with the gas molecules via Coulomb scattering and Bremsstrahlung. The beam-gas rate depends on the beam current, the number of gas molecules (determined by the vacuum pressure), and the magnetic field strength of the focusing magnets [24]

- **Synchrotron radiation**: Synchrotron radiation results from the radial acceleration of charged particles in the magnetic field of bending and focusing magnets. The synchrotron photons can have energies on the order of keV and potentially impact the inner detectors. This can be substantially mitigated by specially designing the IR to counteract such effects. The intensity of synchrotron radiation increases with the square of the beam energy, which means that it occurs predominantly in the HER [15]

- **Injection background**: The injection background is due to the continuous injection of charge into the storage rings, which modifies the beam bunch. During injection, a veto

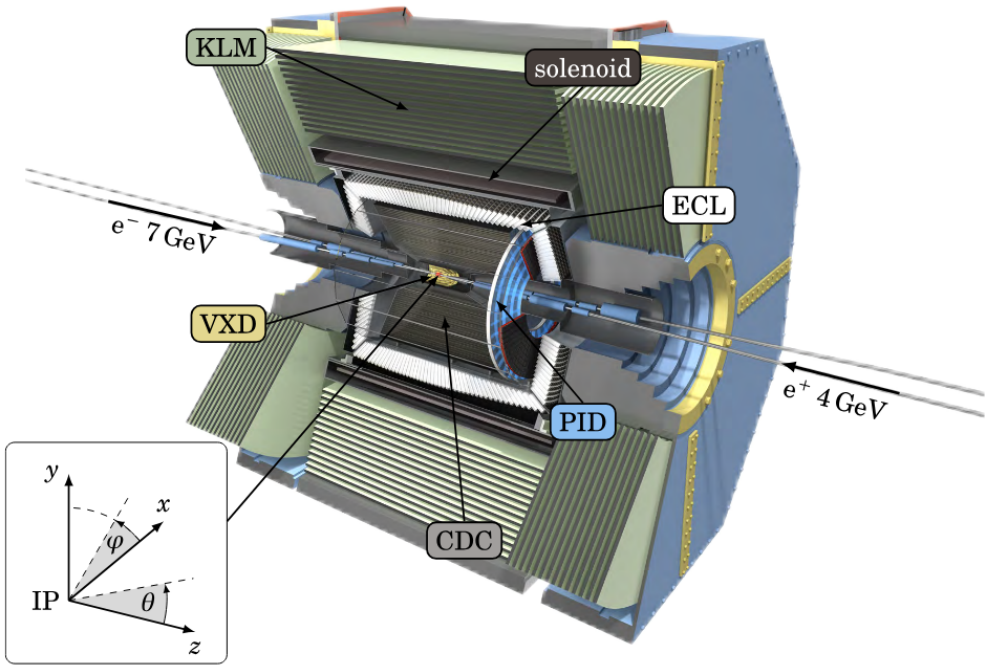

Figure 3.4: 3D rendering of the Belle II detector and sub-detector systems. The different sub-detector systems are indicated and the interaction point (IP) is detailed with its coordinate system. The rendering is coming from [25].

signal is sent that prevents Belle II from recording data, but studies have shown that the background conditions increase shortly after an injection.

3.3 The Belle II Detector

The Belle II detector [24] surrounds the interaction point where electrons and positrons collide in SuperKEKB. Belle II is 7×7.5 m^2 in size and weighs 1400 tons.
As depicted on Fig. 3.4, the Belle II detector is composed of several sub-detector systems, each responsible for detecting a specific property of a given group of particles, thereby defining their location within the detection system. These sub-detectors undertake various tasks together, encompassing the measurement of particle passage, position, time, momentum, energy, and identity. To this end, they capitalise on diverse physical effects such as ionisation in gases, liquids, and solids, deflection in magnetic fields, electromagnetic showers, and Cherenkov radiations. Despite their fundamental differences, all sub-detector systems have one thing in common: their detection principle is based on the particle's passage through matter, hence their strong dependence on the type of particle they have to detect. The seven sub-detectors comprise an inner part that reconstructs vertices and tracks (PXD, SVD and CDC), a hadron identification system (TOP and ARICH), an electromagnetic calorimeter (ECL), a solenoid to deflect charged particles trajectories, and an outer K_L^0 and μ chamber (KLM), all mentioned from the nearest to the farthest from the ee interaction point. The position of all sub-detectors are detailed in Fig. 3.5, on which the Belle II detector is shown from the side. Before introducing all sub-detectors mentioned previously in greater detail, it is worth mentioning the upgrades that have

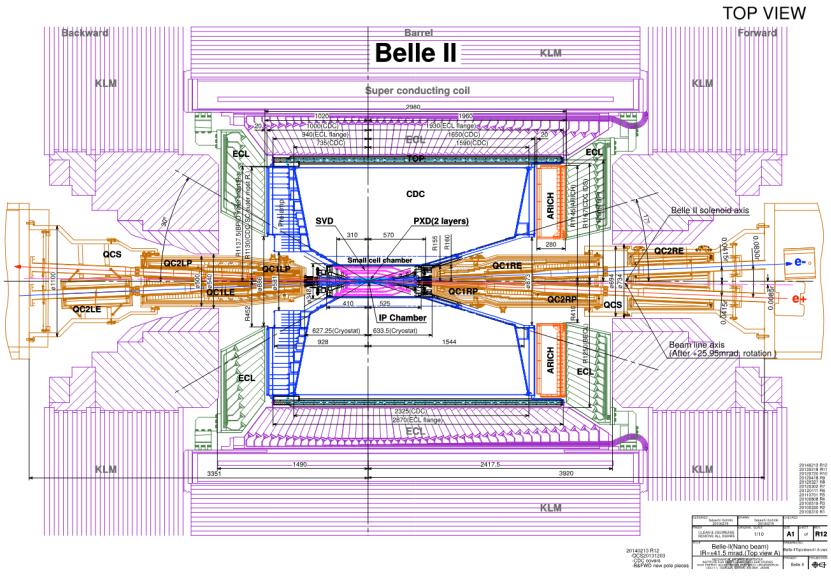

Figure 3.5: An overhead view of a slice of the Belle II detector, illustrating the interaction region and the different sub-detector systems. The drawing is taken from "The Belle II Physics Book" [15]

been introduced by the change from the Belle to the Belle II detector, as well as the improvements undertaken during the long shutdown (LS1).
The changes from the Belle detector include the readjustment of the PXD detector at a smaller distance from the IP, a larger SVD acceptance, an improved K/π separation from the TOP and ARICH detectors, improved trigger systems adapted to a higher event rate, an improved coverage of almost the full solid angle, a higher reconstruction efficiencies for charged particles, a better momentum resolution and a more precise measurement of photons energy and direction [15,24]. During LS1, the full two-layer pixel detector was installed and the photo-multiplier tubes (PMTs) of the time-of-propagation (TOP) detector were replaced.

3.3.1 The coordinate system

Belle II adopts a Cartesian, right-handed, coordinate system, Fig. 3.6, with origin at the nominal interaction point and axes as follows: the z axis is defined as the symmetry axis of the solenoid, and the positive direction is approximately given by the incoming electron beam; the y axis points upwards, in the direction of the detector-hall roof; the x axis points along the radial direction towards the outside of the accelerator ring. With respect to the z axis, ϕ is the azimuthal angle and θ is the zenith angle, with $\phi = \theta$ defined for (x, y, z) = (1, 0, 0) and $\theta = 0$ for (x, y, z) = (0, 0, 1). In addition, ρ is defined as the radius in the x - y plane ($\rho = \sqrt{p_x^2 + p_y^2}$) and r in three dimensions ($r = \sqrt{p_x^2 + p_y^2 + p_z^2}$), such that $sin\theta = \frac{\rho}{r}$, $cos\theta = \frac{z}{r}$ and $cos\phi = \frac{x}{\rho}$.

3.3.2 The Pixel Detector

The PXD [26] represents the two innermost layers of the vertex detector. It has been developed using the DEpleted P-channel Field Effect Transistor (DEPFET) technology [27], which combines low power consumption in the active pixel area, and low intrinsic noise, with a small

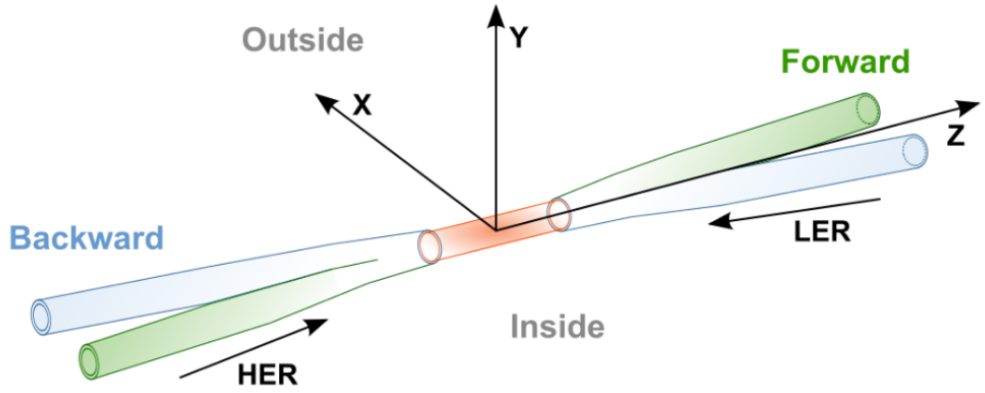

Figure 3.6: The Belle II coordinate system.

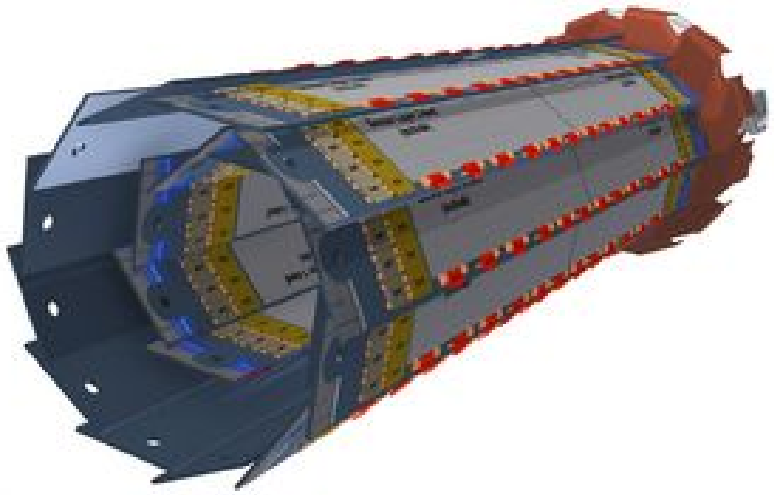

Figure 3.7: Schematic view of the geometrical arrangement of the PXD. Only two ladders of the second layer are installed in the current setup. Credit: Belle II PXD Group.

material budget. The setup and the operating principle of a DEPFET pixel are schematically illustrated in Fig. 3.8 The PXD layers are situated directly outside of the 20 mm beam pipe, at radial distances $r_1 = 14$ mm and $r_2 = 22$ mm, and they consist of 8 and 12 ladders, respectively. An illustration of this structure is provided in Fig. 3.7 The structure is extremely light with the thickness of a PXD layer equivalent to less than 0.2% radiation length per layer. The active area of each module is segmented into 250 $\times$ 768 pixels with sizes ranging from (50 $\times$ 55) μm^2 in the center of the inner layer to (50 $\times$ 85) μm^2 in the outer layer.
The PXD position makes it exposed to large QED background, hence the modules are designed to resist to 20 Mrad radiation dose, which is expected to be accumulated in 10 years of Belle II operation. The PXD performance in data taking observed since 2019 is optimal. The hit-efficiency of most of the modules is measured to be greater than 98%, and the detector ensures vertex reconstruction with an average spatial resolution of approximately 14 μm [28].

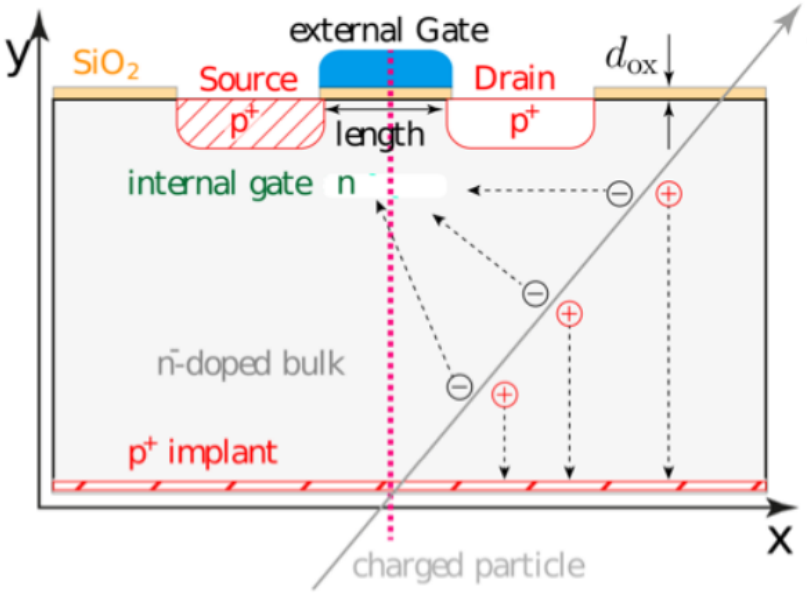

Figure 3.8: A DEPFET pixel and its operating principle. Credit: Belle II PXD Group.

3.3.3 The Silicon Vertex Detector

The SVD [29] represents a major upgrade of the Belle vertex detector. It is composed of four layers of double-sided silicon-strip sensors arranged in the structure illustrated in Fig. 3.9. The layers radii range from 39 mm to 135 mm and the acceptance of the detector covers polar angles between 17° and 150° and the full azimuthal angle. The layers have 7 to 16 ladders, with 2 to 5 sensors per ladder: rectangular sensors in the barrel-shaped part of the layers and trapezoidal in the forward section of the outermost three layers. The sensors have 768 read-out strips per side: long strips on the p-side parallel to the beam axis (z direction) and short strips on the n-side along r-ϕ, as illustrated in Fig. 3.10 When a charged particle passes through a sensor, electron-hole pairs are created along its path by ionisation. Electrons are collected by n^- strips and holes by the p^+ strips, so that two coordinates of the particle position can be read. In total there are 172 SVD sensors and about 220 thousand strips. All the sensors are connected to fast APV25 front-end chips providing good signal-to-noise ratio for all the layers. The optimised ladder design and support structures result in a material budget per ladder equivalent to only 0.7% radiation length at normal incidence. The SVD performance observed in data taking since 2019 is excellent. The average hit efficiency is greater than 99.5% and the spatial resolution ranges from 18μm to 35 μm (reference).

3.3.4 The Central Drift Chamber

The Belle II CDC [30] is an upgrade of the Belle central drift chamber. The detector is used for multiple purposes. Primarily, it is a tracking detector designed to reconstruct charged tracks and to measure their momenta. It provides particle identification information by measuring the charged-particle energy loss within its gas volume, which is particularly useful for low momentum tracks not reaching the outer detectors dedicated to particle identification. In addition, the CDC generates reliable trigger signals for charged particles. The volume of the chamber is contained

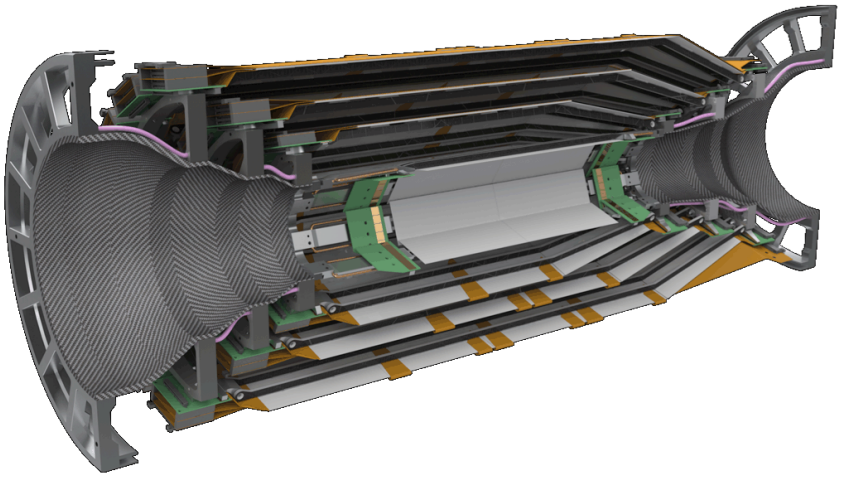

Figure 3.9: chematic view of the geometrical arrangement of the SVD. Credit: Belle II SVD Group

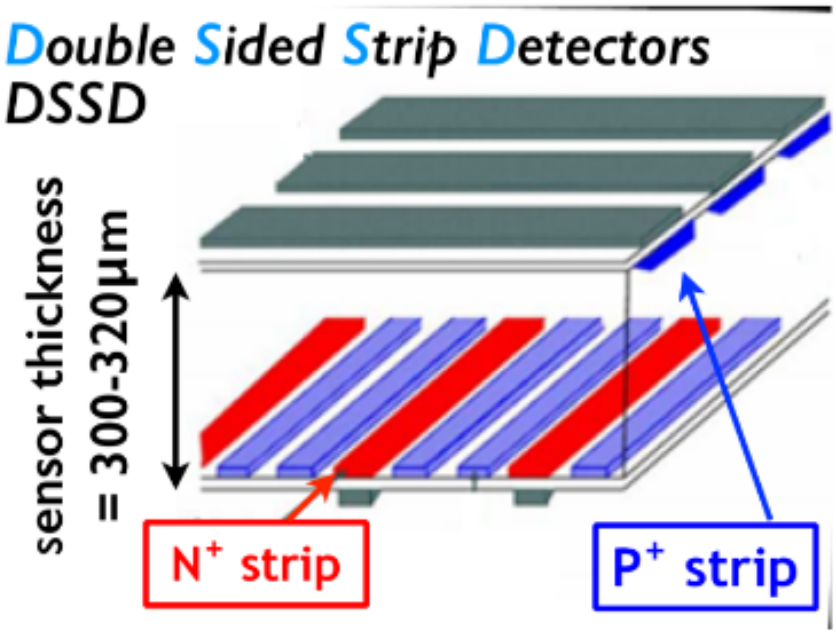

Figure 3.10: Setup of a double-sided silicon-strip sensor in the SVD. Credit: Belle II SVD Group.

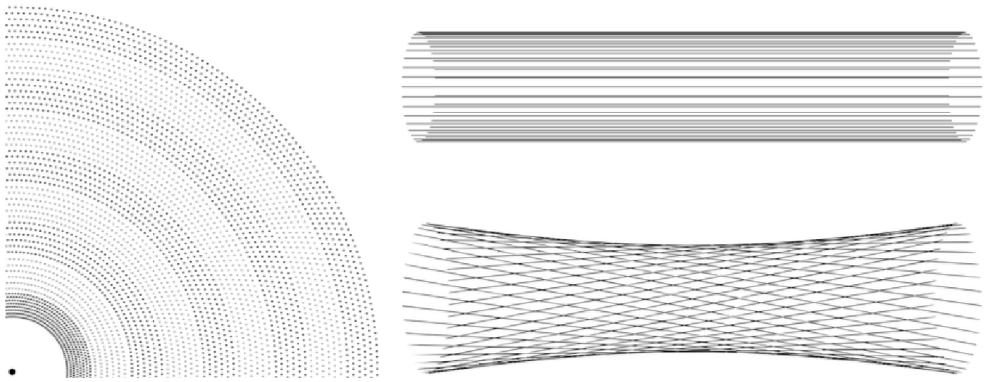

Figure 3.11: Left: a quadrant of a slice of the CDC $r - \phi$ projection. Right: a visualisation of stereo wires (bottom) relative to axial wires (top). The skew is exaggerated. Credit: Belle II Tracking Group

between an inner cylinder having radius of 160 mm and an outer cylinder with radius of 1130 mm, and it is occupied by about 50000 sense and field wires. The wires define drift cells with a size of about 2 cm, where the electric field is approximately cylindrical. The sense wires are arranged in layers, and six or eight adjacent layers correspond to a so-called superlayer. The outer eight superlayers consist of six layers of 160 to 384 wires. The innermost superlayer is made of eight layers having 160 wires, defining smaller (half-size) drift cells, in order to cope with the increase of background at smaller radial distances from the the IP. The superlayers alternate between axial (A) orientation, aligned with the solenoidal magnetic field, and stereo (U, V) orientation, skewed with respect to the axial wires. The direction changes sign between U and V superlayers, producing an AUAVAUAVA configuration. An illustration of the CDC wire configuration is provided in Fig. 3.11 Combining information from axial and stereo superlayers it is possible to reconstruct a full three-dimensional helix track. The gas mixture used in the chamber is He-C_2H_6 50:50. The average drift velocity is 3.3 cm/μs and the maximum drift time is about 350 ns [15]. The spatial resolution is approximately 120 μm [31].

3.3.5 Particle Identification (TOP and ARICH)

In the barrel region of the Belle II detector, charged particle identification, and in particular K/π discrimination, relies on the TOP counter [32]. This subdetector is installed on the CDC outer cover, and it consists of 16 modules composed of four parts glued together: two fused quartz bars (refractive index n = 1.44 for photons of 405 nm wavelength) of dimensions (125 $\times$ 45 $\times$ 2) cm, a mirror located at the forward end of the bars, and a 10 cm long prism that couples the bar with an array of micro-channel-plate photomultiplier (MCP-PMT) tubes [33]. An illustration of a TOP module is provided in Fig. 3.12 The operating principle of the counter is shown in Fig. 3.13 A charged particle traversing a quartz radiator emits Cherenkov photons in a cone with an opening angle θ_C , depending on the particle velocity. Part of the photons is internally reflected inside the quartz bar. The time of propagation of each photon from the emission point to the photomultiplier surface is related to θ_C.
Moreover, photon arrival times are measured using the time of the collision as a reference, thus

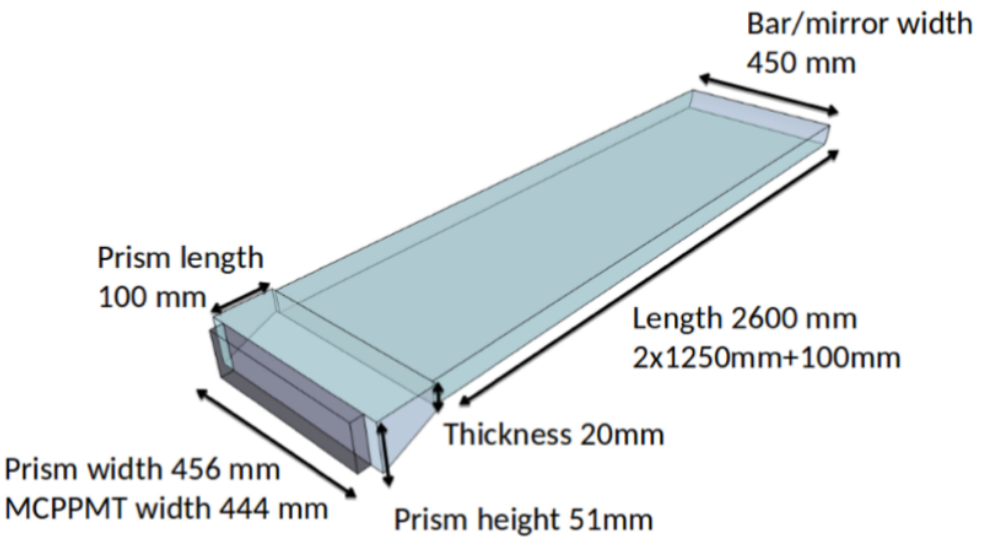

Figure 3.12: Sketch of one module of the TOP detector. Credit: Belle II TOP Group.

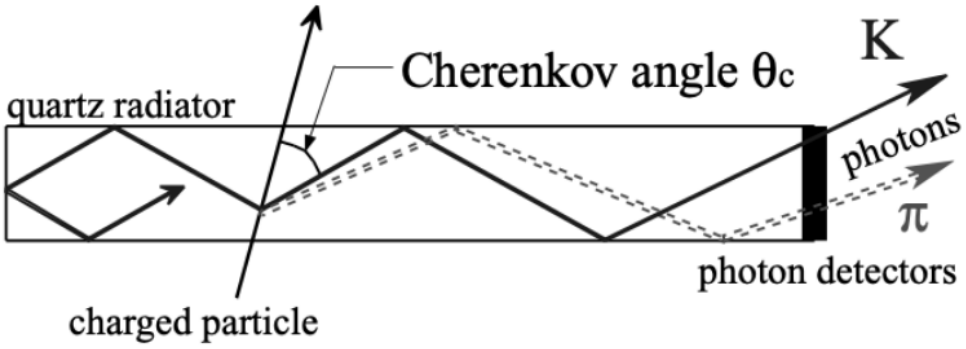

Figure 3.13: Illustration of the operating principle of the TOP detector. Credit: Belle II TOP Group.

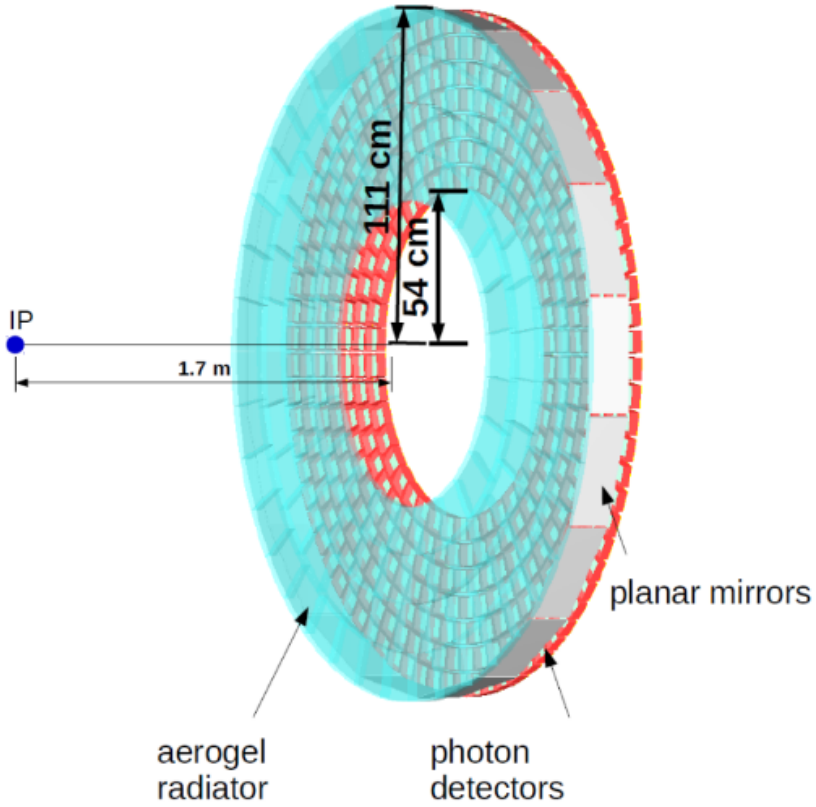

Figure 3.14: Illustration of the ARICH detector with its main components. Credit: Belle II ARICH Group.

photons are further separated in time based on the time of flight of the corresponding charged particle. Arrival time differences between photons from kaons and pions are $\sim$ 100 ps at 2 GeV/c in momentum, and the time resolution of the TOP is smaller than this separation. The PID information is extracted by comparing the time distribution of the photons in one of the modules with the probability density functions (PDFs) describing the expected distributions for six particle hypotheses: e, μ, π, K, p, d. The performance of the TOP detector evaluated in terms of K/π separation is good: 85% kaon identification efficiency at a 10% pion misidentification rate [34].

In the forward endcap, the ARICH is used to separate kaons from pions over most of their momentum spectrum and to provide discrimination between pions, muons and electrons below 1 GeV/c [35]. The ARICH is a proximity-focusing ring-imaging Cherenkov (RICH) detector with aerogel as a radiator. An illustration of this subdetector is shown in Fig. 3.14 It has a toroidal shape with an outside radius of 1145 mm, an inside radius of 420 mm and a length of 280 mm. The detector components along the beamline, starting with the closest to the collision point, are a 40 mm thick radiator, made of 248 silica aerogel tiles arranged in 2 layers, an expansion space of 160 mm, and an 80 mm thick photon detection system consisting of 420 Hybrid Avalanche Photo Detectors (HAPD) [36]. The operating principle of the ARICH is shown in Fig. 3.15 The type of charged particle traversing the detector can be determined by measuring the emission angle of the Cherenkov photons. The particle identification information is based on the comparison between the observed pattern of photons and the PDFs describing

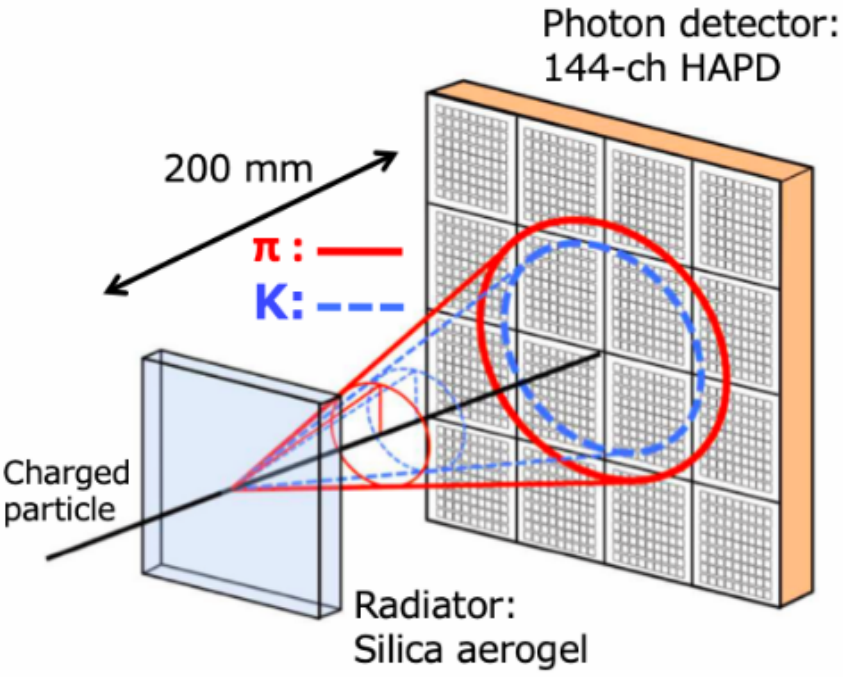

Figure 3.15: Operating principle of the ARICH counter. Credit: Belle II ARICH Group

the expected distribution of Cherenkov photons on the photodetector plane for different particle hypotheses. The ARICH counter is capable of separating kaon from pions with an identification efficiency of 93% at a pion misidentification rate of 10% [37].

3.3.6 The Electromagnetic Calorimeter

The ECL is utilized to measure the energy of γ and e^- in a range of 20 MeV and 4 GeV. Especially for the reconstruction of π^0 decaying into two γ, the ECL is essential for the γ detection and energy measurement. It consists of 6624 CsI(TI) scintillation crystals pointing in direction to the IP3. Each crystal has the shape of a truncated pyramid with an average size of 6 cm $\times$ 6 cm $\times$ 30 cm. The radiation length amounts to $X_0 = 16.1$ along the long crystal edge. Fig. 3.16 shows a schematic cross-section of the crystal arrangement in the barrel and end-cap regions. The ECL can detect $e^{\pm}$, hadrons (h) or, γ due to their interactions with the crystal nuclei, which generate electromagnetic (EM) and/or hadronic showers. Within an EM shower, more and more photons are created until the lower energy threshold is reached. The number of created photons is proportional to the energy of the initial particle. Photodiodes are mounted on the end of the crystals to detect the created photon showers.
In addition to the energy, the angular coordinates can be determined. Furthermore, the ECL signals enter the L1 global decision logic (GDL) for triggering.

3.3.7 Superconducting magnet

A superconducting solenoid generates a 1.5 T magnetic field parallel to the beam axis in a cylindrical volume of 3.4 m in diameter and 4.4 m in length. The superconductor used to build the coil is NbTi/Cu. It is supplied with a 4400 A current and it operates with a liquid helium

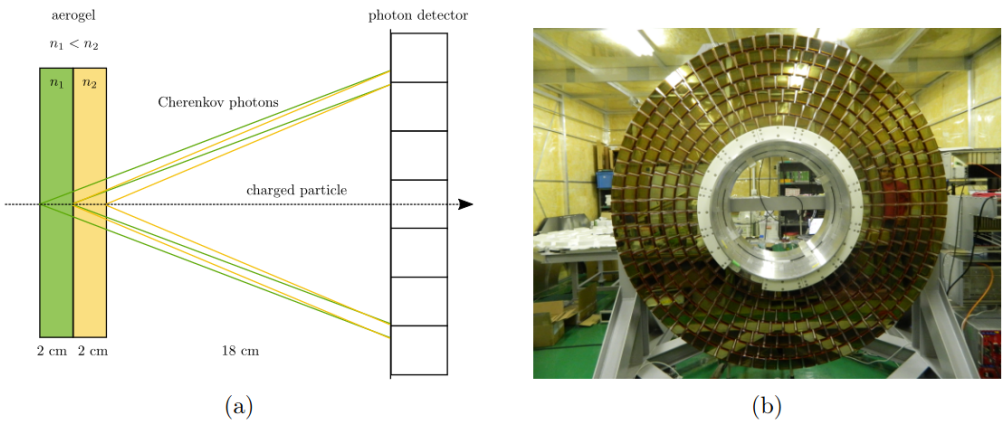

Figure 3.16: (a) Schematic working principle of the proximity focusing ARICH (Figure adapted from [24]). (b) HAPAD photon detector disk (Figure taken from [15]).

cryogenic system. The magnetic field has been mapped with Hall sensors with a precision of 0.1% [38]. Inhomogeneities of the field are related to edge effects and to the presence of the final focus magnets system of SuperKEKB.

3.3.8 K_L^0 and μ detection

The KLM is an upgrade of the Belle KLM [24,39]. It is a detector dedicated to K_L^0 and μ identification, consisting of an alternating sandwich of 4.7 cm thick iron plates and active detector elements, located outside of the superconducting solenoid. The iron plates serve as the magnetic flux return for the solenoid and provide 3.9 interaction lengths where the K_L^0 mesons can shower hadronically [38]. Muons and non-showering charged hadrons with momentum larger than ~ 0.6 GeV/c traverse the KLM until they escape the detector or they are stopped because of energy loss due to electromagnetic interaction with the detector material. K_L^0 mesons that interact in the ECL or in the iron plates of the KLM create a hadronic shower which allows their detection using both detectors or the individual detector information only. The KLM has an octagonal shape in the barrel section, covering the polar angle region $45° < \theta < 125°$. Two end caps (forward and backward) extend the angular acceptance of the detector to $20° < \theta < 155°$. The outermost layers of the barrel section are made of modules consisting of two coupled Resistive Plate Chambers (RPC) (proportional gas chambers used in streamer mode), with independent power supplies, as illustrated in Fig. 3.17 In the end caps and in the two innermost barrel layers of the KLM, where the background flux is higher, the RPCs are replaced by two layers of scintillators strips coupled with a silicon photomultiplier.
The muon detection efficiency reaches 89% for tracks with momentum above 1 GeV/c, with hadron fake rate of $\sim 1.3\%$. The K_L^0 detection efficiency increases almost linearly with momentum to a plateau of 80% at 3 GeV/c [24].

3.4 Reconstruction Software

The Belle II analysis software framework (basf2) [40, 41], is an open-source project developed by the Belle II collaboration to support both online and offline data processing in a modular

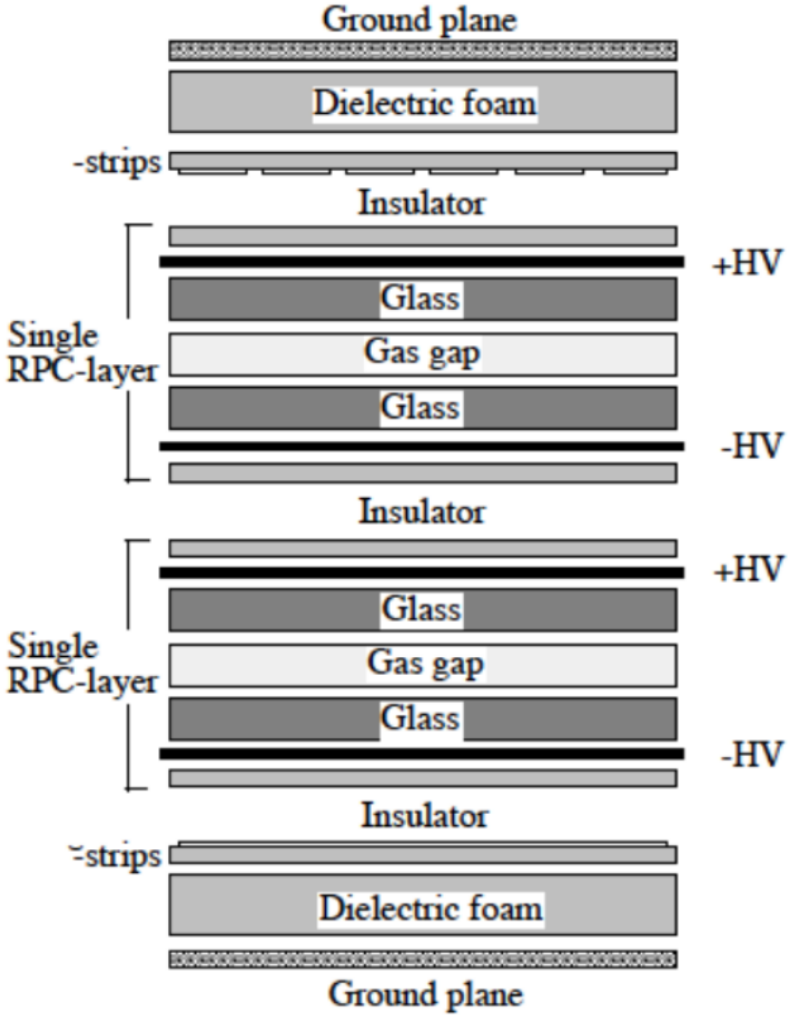

Figure 3.17: Schematic depiction of a module in the barrel section of the KLM. Credit: Belle II KLM Group.

and efficient manner. It employs a structure in which small, dedicated modules execute sequentially, exchanging information through a shared object store. The module execution sequence and configuration are defined in Python-based steering files, while the modules themselves are primarily written in C++. A sequence of modules is referred to as a path, and multiple paths can be run in parallel within the same job.
The framework handles the full data processing chain—from low-level detector signals to high-level physics objects. It begins by constructing intermediate entities such as track hits (from the vertex detectors and the CDC) or calorimeter clusters (from the ECL). These are subsequently used to reconstruct higher-level objects, such as charged particle tracks or decay vertices, often using complex algorithms that must contend with significant background noise. To manage data volume, basf2 stores primarily these high-level objects in the output, while lower-level data is archived separately. This strategy reduces event size by approximately a factor of 40.
The reduced data still retains sufficient detail for physics analyses, enabling the extraction of quantities like particle four-momenta and identification variables. Even more abstract descriptors—such as event-level variables or outputs from machine learning classifiers—can also be computed within the framework. The final analysis data are saved in so-called mini Data Summary Tables (mDST files), where each event is characterized by a defined set of features. These features primarily relate to the reconstructed energy and momentum of observed particles, but may also include more sophisticated analysis variables as needed. Analysts choose which variables to compute and store, balancing detail with storage constraints. Given the vast volume of data produced by Belle II, it is impractical for individual analysts to access all available information. As such, careful data reduction and selection strategies are critical. One commonly used method is event skimming [19], which filters the dataset to retain only events relevant to a particular analysis. For instance, in τ physics studies, skims are used to isolate $e^+e^- \to \tau^+\tau^-$ events while removing unrelated processes. These skims are designed to maintain high signal efficiency, even if the resulting samples are not highly pure, ensuring that very few relevant events are lost. Skims can be defined and applied directly within basf2, allowing multiple researchers to begin their analyses from a reduced dataset without needing to reprocess the full data sample.
Development of basf2 is ongoing, with continual improvements in algorithms, performance, and feature set.

3.5 Trigger System

The Belle II trigger system is designed to efficiently select and record the physics events of interest while suppressing the events induced from beam backgrounds and high cross-section processes, such as Bhabha scattering.
All this is done under the constraints of limited storage capabilities and bandwidth of the DAQ system. Efficient trigger system is essential for low-multiplicity processes such as $e^+e^- \to \tau^+\tau^-$ or dark sector searches that can have a single high energy photon in the final state. The trigger system comprises two main stages: the hardware-based trigger system, or level 1 (L1), and the software-based high level trigger (HLT).
The L1 trigger system is required to make a retention decision for an event in under 5 μs and still must also be capable of distinguishing between two consecutive events spaced as closely as

200 ns. The maximum output rate of the L1 trigger system is 30 kHz. At the design luminosity of SuperKEKB, the frequency of events for a process with a cross-section of 1 nb will be around 800 Hz [15]. For comparison, radiative Bhabha scattering, which is one of the most prominent physics backgrounds for many low-multiplicity processes, has a cross-section of 74 nb in the acceptance region of ECL. Therefore, the L1 trigger system must be incredibly efficient and still provide good discrimination of background sources.
Several sub-detectors provide information to the L1, most notably the CDC and the ECL. The detector signals are processed using Field Programmable Gate Arrays (FPGAs), which allows for fast low-level particle and event reconstruction. The CDC is used to reconstruct tracks from charged particles, which are either 2D or 3D tracks. A 2D track is a reconstructed track that uses only information from its projection to the $r - \phi$ plane, allowing a faster reconstruction. Novel 3D tracking algorithms using neural networks have been developed for the L1 trigger [42,43], to also provide information about the z coordinate of tracks. This helps to distinguish background tracks not starting from the IP. The associated tracks on the trigger level are called Neuro 3D. These 3D tracks can also match with ECL or KLM clusters, resulting in a better classification of the events. The ECL provides information on the position of the cluster and the energy deposited to the L1. This is especially important for vetoing Bhabha events, for which a special logic based on back-to-back ECL clusters was developed (this is a separate trigger called 3D Bhabha). Unfortunately, this Bhabha veto also removes some of the interesting low-multiplicity processes, so there is always a trade-off which can be controlled by the tightness of the veto.
Following the L1 trigger, events undergo a assessment through the software-driven HLT. In this phase, full event reconstruction is accessible using all sub-detectors, with the exception of the PXD, due to its extremely high data rates. The HLT is also responsible for identifying regions of interest for the PXD readout based on reconstructed tracks. Data storage limitations require the HLT to lower the event rates to approximately 10 kHz. To process the rate of 30 kHz acquired by the L1, 6000 CPU cores have to be used [15].
For this work, only a few selected L1 trigger lines will be used. These triggers have specific requirements and names. All trigger lines require the absence of an injection veto from SuperKEKB to avoid data recording during periods of increased noise following beam injections. For CDC triggers, a full track is defined as one that passes through all the CDC layers, whereas a reduced (or "short") track may end or exit the CDC before the last layer. This is especially important for particles with momentum in the forward or backward direction. In general, low-multiplicity events with tracks in the barrel region will have a higher trigger efficiency since the fraction of undesired background events with tracks in the endcap regions is significantly larger. Some trigger lines may have been inactive or prescaled during some data-taking periods. A prescale of n means that only every n^{th} event triggered by the associated trigger line is kept, often used for triggers with a high rate when the overall rate is at its limit. More about the used trigger lines and their efficiency for this analysis will be provided in the Section 5.5.3.

3.6 Data and simulation

This section introduces the current Belle II dataset and the simulated samples used for the analysis.

3.6.1 Data

As of the writing of this thesis in spring 2025, the Belle II run period is divided into three main parts. The first run period Run 1, comprising three different phases, started in February 2016 and lasted until July 2022. LS1 then took place until January 2024 when the second run period Run 2 started, and is meant to continue until 2026 or 2027. The first phase of Run 1 corresponds to the commissioning of SuperKEKB from February to June 2016, without the Belle II detector and aforementioned superconducting magnet system. The second phase then took place, during four months of which the first data was taken, corresponding to an integrated luminosity of 0.5 fb^{-1}. The third and last phase of Run 1 started in March 2019, when the full detector, including the vertex sub-detector, was installed. The dataset collected until the above mentioned period is also called pre-LS1 data.
This data-taking period is divided into several parts, called "Experiment". There is a total of 14 different Experiments, all categorised as "physics runs", i.e., runs during which physical data is acquired. The Experiments correspond to specific run conditions; while the majority of these Experiments translate a production of data at the $\Upsilon(4S)$ resonance, there are two Experiments which solely translate either another resonance, or off-resonance data: Experiment 21 and 25. As for the Experiments 8, 12, 18 and 22, they not only correspond to a production of data at the $\Upsilon(4S)$ resonance, but also a production of data at either another resonance, or by a scan of a certain resonance. Table 3.1 shows the relevant experiments (7 to 26) and the year it was taken, together with the CM energy used in the respective periods and the corresponding integrated luminosities.
After LS1, SuperKEKB was ready to resume operations in January 2024, when Run 2 started. After a few tests, the first collisions were observed in February 20, continuing the data-taking at experiment 30.
Fig. 3.18 shows the weekly integrated recorded luminosity usable for physics analyses and the overall recorded luminosity until now. Data collected with the Belle II detector between 2019 and 2022 at a CM energy corresponding to the $\Upsilon(4S)$ resonance amounts to a total integrated luminosity of

$$\mathcal{L}_{\text{int}} = 361.654 \pm 0.021 \pm 2.170 \text{ fb}^{-1}, \tag{3.3}$$

where the first uncertainty is statistical and the second is systematic. This luminosity measurement, which was obtained using Bhabha events, is provided by Belle II colleagues for the whole collaboration [45] and is used throughout this analysis.

3.6.1.1 Data processing

Collected data undergo two primary processing stages: prompt processing and reprocessing; the distinction between them lies in the extent of calibrations applied during processing.
"Prompt" processing occurs immediately after data collection: Data is gathered over a fixed period, typically two weeks, then calibrated and processed iteratively. The dataset resulting from this operation is referred to as a "Bucket". Prompt data always utilises the latest major software release and undergoes thorough calibration, with quality comparable to reprocessed data. Consequently, most calibrations performed during prompt processing are retained for reprocessing. Reprocessing involves recalibrating and reprocessing all data collected up to a

Period	Exp.	CM Energy	Integrated Luminosity [fb^{-1}]
early 2019	7	$\Upsilon(4S)$	$0.506 \pm 0.002 \pm 0.004$
		$\Upsilon(4S)$	$1.663 \pm 0.003 \pm 0.011$
		off-resonance	$0.808 \pm 0.001 \pm 0.006$
		$\Upsilon(4S)$ scan	$0.038 \pm 0.001 \pm 0.001$
late 2019	10	$\Upsilon(4S)$	$3.655 \pm 0.002 \pm 0.024$
		off-resonance	$8.691 \pm 0.002 \pm 0.056$
early 2020	12	$\Upsilon(4S)$	$54.573 \pm 0.005 \pm 0.350$
		off-resonance	$8.691 \pm 0.002 \pm 0.056$
late 2020	14	$\Upsilon(4S)$	$16.500 \pm 0.006 \pm 0.106$
early 2021	16	$\Upsilon(4S)$	$10.294 \pm 0.004 \pm 0.066$
	17	$\Upsilon(4S)$	$10.715 \pm 0.004 \pm 0.069$
	18	$\Upsilon(4S)$	$89.900 \pm 0.011 \pm 0.576$
		off-resonance	$8.482 \pm 0.004 \pm 0.055$
late 2021	20	$\Upsilon(4S)$	$3.788 \pm 0.003 \pm 0.025$
	21	$\Upsilon(5S)$ scan	$19.750 \pm 0.004 \pm 0.147$
	22	$\Upsilon(4S)$	$32.060 \pm 0.007 \pm 0.206$
		$\Upsilon(5S)$ scan	$0.041 \pm 0.001 \pm 0.001$
early 2022	24	$\Upsilon(4S)$	$85.642 \pm 0.011 \pm 0.549$
	25	off-resonance	$24.574 \pm 0.006 \pm 0.158$
	26	$\Upsilon(4S)$	$54.795 \pm 0.009 \pm 0.351$

Table 3.1: The data-taking periods of Belle II and the corresponding experiment number up to 2022, together with the CM energy at which the data was taken and the corresponding integrated luminosity, where the first uncertainty is statistical while the second is systematic.

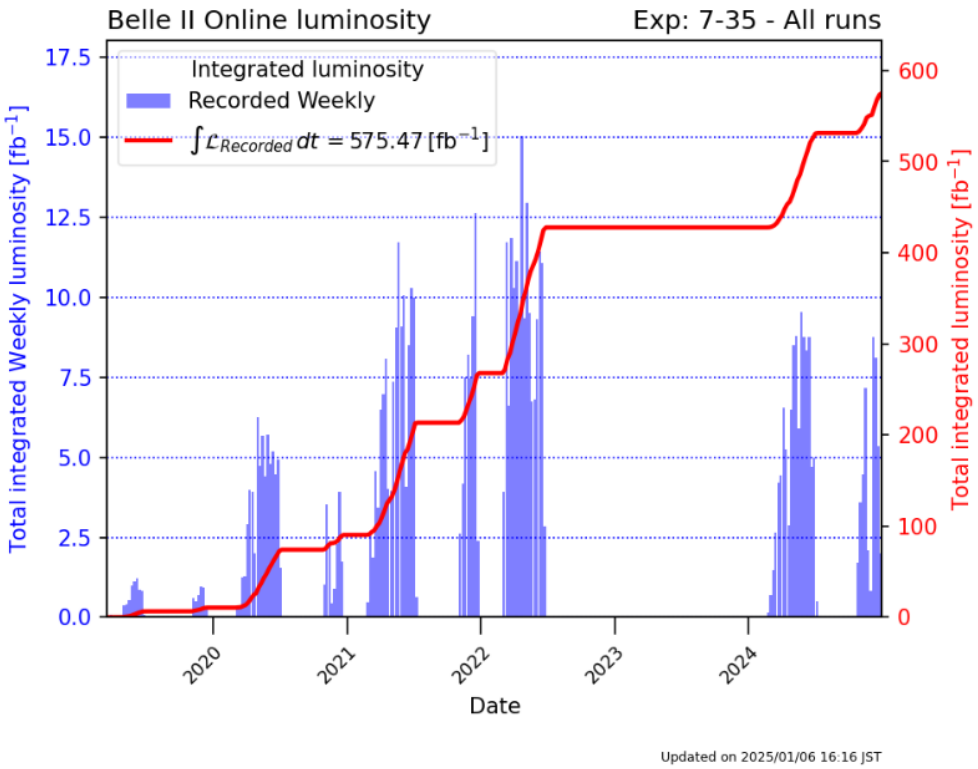

Figure 3.18: The integrated luminosity recorded by the Belle II detector up to now. The histogram shows the weekly luminosity, while the red line shows the total integrated luminosity. After July 2022, Belle II and SuperKEKB entered LS1, only continuing data-taking in February 2024. The image is taken from [44]

	Process	Restriction	Coss-section [nb]
$e^+e^- \to$	$\Upsilon(4S)$		1.110 ± 0.008
	$u\bar{u}(\gamma)$		1.61
	$d\bar{d}(\gamma)$		0.40
	$s\bar{s}(\gamma)$		0.38
	$c\bar{c}(\gamma)$		1.30
$e^+e^- \to$	$\tau^+\tau^-(\gamma)$		0.919
$e^+e^- \to$	$e^+e^-e^+e^-$	$W_{ll} > 0.5$ GeV	39.7 ± 0.1
	$e^+e^-\mu^+\mu^-$	$W_{ll} > 0.5$ GeV	18.9 ± 0.1
$e^+e^- \to$	$e^+e^-\tau^+\tau^-$		0.01836
	$e^+e^+p^+p^-$		0.0117
	$e^+e^+K^+K^-$		0.0798
	$e^+e^+\pi^+\pi^-$		1.895
$e^+e^- \to$	$e^+e^-(\gamma)$	$10^\circ < \theta_e^* < 170^\circ$, $E_e^* > 0.15$ GeV	300 ± 3
		$p_e > 0.5$ GeV and e in ECL	74.4
$e^+e^- \to$	$\gamma\gamma(\gamma)$	$10^\circ < \theta_\gamma^* < 170^\circ$, $E_\gamma^* > 0.15$ GeV	4.99 ± 0.05
		$E_\gamma > 0.5$ GeV in ECL	3.30
$e^+e^- \to$	$\mu^+\mu^-(\gamma)$	None	1.148
		$p_\mu > 0.5$ GeV in CDC	0.831
$e^+e^- \to$	$\mu^+\mu^-\gamma(\gamma)$	$p_\mu > 0.5$ GeV in CDC, $\geq 1\gamma(E_\gamma > 0.5$ GeV) in ECL	0.242
$e^+e^- \to$	$\nu\bar{\nu}(\gamma)$		0.25×10^{-3}
$e^+e^- \to$	$B^0\bar{B}^0$		0.51
	B^+B^-		0.54

Table 3.2: The primary physics processes occurring in e^+e^- collisions at a CM energy of 10.58 GeV, taken from "The Belle II Physics Book" [15]

specific time. Reprocessing, labeled as "Proc" and representing a total of five "Chunks", occurs annually (or biennially from 2023). Recalibration starts from prompt calibration and is refined with improved or new calibration algorithms. Full reprocessing utilises a major software release, ensuring a coherent processing of the entire data set. Both prompt and reprocessed data sets are accessible on the grid via corresponding collections, stored in mDST format.

3.6.2 Cross-sections

The cross-sections for the dominant physics processes in electron-positron collisions at Belle II energies are given in Table 3.2. In some cases, restrictions to the kinematics of the final state particles are applied, such as for their momentum to lie inside the detector acceptance. These selections are often imposed at the generator level when simulating samples to limit their size. The quoted cross-sections are obtained with Monte Carlo simulations using different generators (mentioned in the next section), with the quoted uncertainties only due to the limited size of the produced samples. The cross-section for $q\bar{q}$ finals states or $e^+e^- \to \Upsilon(4S)$ is not very well

known and is sometimes obtained using data [19, 46].

3.6.3 Monte Carlo simulation

Monte Carlo (MC) simulations are critical in order to understand the kinematics and response of the detector for different physics events. It typically involves three steps: event generation, detector interaction simulation, and detector response digitisation.
During the event generation step, the production vertices of particles, their four-momenta, and decays are produced for particular physics processes, either following the SM or a NP model. Several SM physics processes are used in this work to study both signal and background, using different generators that specialise in specific processes.
The $e^+e^- \to \tau^+\tau^-$ events are generated by the KKMC generator [47, 48]. Following this, the decay of τ leptons is modelled using the TAUOLA software package [49–52], and radiative corrections are applied via PHOTOS [53]. In TAUOLA, 92 decay modes are active and initialised with branching fractions following the particle listing from the PDG [7]. They are determined from a global fit to all available branching fraction measurements while considering the unitarity constraint. Depending on the decay channels, these τ decays compose both the signal and the background for this analysis
KKMC is also used for the production of $\mu^+\mu^-(\gamma)$ and $q\bar{q}$, while the fragmentation of the $q\bar{q}$ pairs is handled by the PYTHIA computer program [54]. The event generator BabaYaga.NLO [55–59] is employed for $e^+e^- \to e^+e^-(\gamma)$ events, also known as Bhabha scattering, and EvtGen is utilised for the decay of B and D mesons. For the creation of $e^+e^- \to l^+l^-l^+l^-$ and $e^+e^- \to e^+e^-h'^+h'^-$, AAFH [60–62] and TREPS [63] are employed. During the generation of these events, referred to as two-photon processes, no radiative effects are included due to limitations of the generators. A comprehensive list of all generated samples and details about their size and cross-sections used in generation are provided in Section 5.3 .
The generated particles undergo a complete simulation of their interactions with the detector via the GEANT4 [64] software. This process includes the creation of authentic trajectories, secondary particles, and energy depositions within the detector, also taking into account electronic effects and stochastic noise. The precise geometry and material composition of the Belle II detector are employed for these simulations.
As a last step, the consequent detector signals are used to reconstruct the events using basf2. The detector signals are acquired from the GEANT4 hits by individual modules for each detector. The L1 trigger system is also simulated, which is referred to as trigger simulation (TSIM). Contrary to data, simulated events are not rejected, neither from the L1 nor from the HLT trigger, and only the trigger decision on whether it would keep the event is stored. This is also referred to as trigger "flags".
The resulting simulated samples will be referred to as MC samples. They are used to approximate the distributions of the underlying model, since an analytical description of the whole process is not feasible. However, the simulation will never be perfect and the discrepancies between reality and simulation must be carefully evaluated and, if needed, corrected.
At Belle II there are two types of MC samples: run-dependent and run-independent. Run-dependent MC uses randomly triggered data events to include beam backgrounds and evolving detector conditions that match those present during the different data-taking periods. On the

other hand, run-independent MC uses simulated beam backgrounds and fixed detector conditions.

3.7 Charged particle identification

All Belle II sub-detectors contribute to the particle identification (PID) determination, with the exception of the PXD. Their contribution is more precisely defined by the computation of likelihoods $\mathcal{L}_x^d$, used to assess the identity of a particle. These likelihoods depend on several parameters that vary given the sub-detector $d \in$ SVD, CDC, TOP, ARICH, ECL, KLM $\equiv D$. And is also generated for each long-lived particle $x \in e, \mu, \pi, K, p, d \equiv X$. They are generally further combined into ratios of log likelihoods to consolidate the hypothetical identity of the particle and mitigate floating-point errors.
In the case of the SVD, the likelihood relies on the measurement of the energy loss ($\mathrm{d}E/\mathrm{d}x$) of charged particles traversing its sensors. A track typically provides eight measurements of $\mathrm{d}E/\mathrm{d}x$ (two for each sensor), with their average exhibiting a Landau distribution. The determination of the peak position is further improved by truncation, i.e., eliminating the two highest energy measurements. The likelihoods is measured as

$$\mathcal{L}_x^{\mathrm{SVD}} = \prod_i \mathcal{P}_x \left((\mathrm{d}E/\mathrm{d}x)_i , p \right), \tag{3.4}$$

where the product runs on all the SVD remaining hits, and $\mathcal{P}_x$ is the two-dimensional probability density function (pdf) for particle hypothesis x.
In the CDC, measurements of ($\mathrm{d}E/\mathrm{d}x$) are obtained from individual drift cells, where the pulse signal is digitised, and values surpassing a certain threshold are integrated to create the raw ADC readout. Prior to utilizing these values in an average, various corrections are necessary, including geometrical path length adjustments and disparities among individual electronic channels. Variations in CDC gas gain, arising from fluctuations in pressure, temperature, and gas mixture composition, are monitored, determining a unified scale factor for each data-taking run. To approximate Gaussian behavior, we exclude the lower 5% and higher 25% of the corrected ADC measurements when calculating the average $(\mathrm{d}E/\mathrm{d}x)_m$. The likelihoods is expressed as

$$\mathcal{L}_x^{\mathrm{CDC}} = \exp\left[-\frac{1}{2} \left(\frac{(\mathrm{d}E/\mathrm{d}x)_m - (\mathrm{d}E/\mathrm{d}x)_p}{\sigma_p} \right)^2 \right], \tag{3.5}$$

where $(\mathrm{d}E/\mathrm{d}x)_p$ is the predicted truncated average and σ_p is the expected resolution on the $\mathrm{d}E/\mathrm{d}x$ measurement, which depends on the polar angle, the number of hits on the track and the value $\mathrm{d}E/\mathrm{d}x$ itself.
As for the TOP, it is the Cherenkov photons, produced by the passage of relativistic charged particles and internally reflected through the bar until their detection at one extremity of each bar, that will be used. More precisely, their number, their arrival times and impact positions will serve to compute the likelihood, as

$$\mathcal{L}_x^{\mathrm{TOP}} = \exp\left[\sum_i \log\left(\frac{N_x S_x(c_i, t_i) + N_B B(c_i, t_i)}{N_x + N_B} \right) + \log P_N(N_x + N_B) \right], \tag{3.6}$$

where N_x and N_B are the number of expected signal and background photons, $S_x(c,t)$ and $B(c,t)$ are the signal and background pdf's, which depend on the position of the pixel defined by the index c and on the time of arrival of the photon t, and P is the Poisson probability to detect N photons while expecting $N_x + N_B$.

For the ARICH, the likelihood assessment relies on comparing the observed spatial distribution of photons, i.e., hits, on the photo-detector plane with the pdf describing the anticipated distribution based on the parameters of a track traversing the ARICH and the assumed charged particle hypothesis. Typically, approximately 13 photons per relativistic charged particle are detected on average. The likelihood function for each hypothesis x is formulated by multiplying the probabilities of individual pixels being in the observed state, whether on or off, with no distinction made for pixels hit by single or multiple photons. As the probability of a pixel being hit by photons follows a Poisson distribution, it is given by $(1 - e^{-n_{x,k}})$, where $n_{x,k}$ is the expected average number of photons on pixel k for hypothesis x. The likelihoods is determined by

$$\mathcal{L}_x^{\mathrm{ARICH}} = \exp\left[-N_x + \sum_k (n_{x,k} + \log(1 - e^{-n_{x,k}}))\right], \tag{3.7}$$

where N_x is the expected total number of hits and the sum runs only over the pixels that were hit in an event.

In the case of the ECL, the likelihood is currently based only on the E/p ratio, which is the ratio between the measured energy E_{cluster} of a calorimeter cluster associated to the track connected to the particle hypothesis, and the momentum $p_{\mathrm{lab}} \equiv p$ determined by the tracking system. The likelihood is there given by

$$\mathcal{L}_x^{\mathrm{ECL}} = P_x(E/p), \tag{3.8}$$

where $P_x(E/p)$ is the pdf for particle hypothesis x.

Finally, for the KLM, the likelihood determination is based on the distance traveled by a charged particle within the detector; muons are able to traverse most or all of it, while hadrons are typically stopped within the first layers. The computation of the likelihood involves two main stages. First, the track is extrapolated from the outermost layer of the CDC that registered a hit. Then, the likelihood is computed for each particle hypothesis, but if the extrapolated track fails to intersect with the KLM, the algorithm assigns an identical likelihood to all particle hypotheses. The KLM likelihood comprises two components: the "longitudinal" term evaluates the observed penetration depth against the expected depth, while the "transverse" term is based on transverse shower characteristics. The total likelihood is expressed as:

$$\mathcal{L}_x^{\mathrm{KLM}} = \mathcal{L}_x^{\mathrm{KLM,L}} \cdot \mathcal{L}_x^{\mathrm{KLM,T}} = \left(\prod_k \mathcal{L}_{x,k}^{\mathrm{L}}\right) \cdot \mathcal{L}_x^{\mathrm{KLM,T}} \tag{3.9}$$

where $\mathcal{L}_x^{\mathrm{KLM,L}}$ corresponds to the longitudinal term, $\mathcal{L}_x^{\mathrm{KLM,T}}$ is the transverse term, $\mathcal{L}_{x,k}^{\mathrm{L}}$ represents the probability of hits for a particle of type x in the kth layer of the KLM. $\mathcal{L}_{x,k}^{\mathrm{L}} = p_{x,k}$ if the hit has been recorded, and $\mathcal{L}_{x,k}^{\mathrm{L}} = (1 - p_{x,k}\epsilon_k)$ otherwise, with ϵ_k the measured detection efficiency of the kth layer.

As already mentioned, these likelihoods, detailed now for all sub-detectors participating in the PID determination, are basic ingredients of all PID variables that are employed. In the form of ratios, they define all high-level hID variables today in use at Belle II. There are actually

three main families of variables that have been developed. The default approach relies on the assumption that sub-detectors likelihoods are independent, and thus can be all combined to obtain the full likelihood for a particle hypothesis x as:

$$\log\mathcal{L}_x = \log\left(\prod_{d\in D}\mathcal{L}_x^d\right) = \sum_{d\in D}\log\mathcal{L}_x^d \ . \tag{3.10}$$

In order to discriminate between the hypothesis x and all the other stable particle hypotheses, a ratio considering them all is built, and is given as:

$$P_i = \frac{\exp\left(\sum_{d\in D}\log\mathcal{L}_i^d\right)}{\sum_{x\in X}\exp\left(\sum_{d\in D}\log\mathcal{L}_x^d\right)} = \frac{\prod_{d\in D}\mathcal{L}_i^d}{\sum_{x\in X}\left(\prod_{d\in D}\mathcal{L}_x^d\right)} = \frac{\exp\left(\log\mathcal{L}_i\right)}{\sum_{x\in X}\exp\left(\log\mathcal{L}_x\right)}. \tag{3.11}$$

The ratio presented in Eq. 3.11 is known as the "Global" PID variable and, in the presented analysis in this thesis, this is used to identify muons and will be referred to as P_μ. It is worth noting that if no information is available for a specific particle x and a detector d, i.e. $\mathcal{L}_x^d = \text{NaN}$, this particular likelihood is set to 1 and does not contribute. Another ratio, defined on the same principle, but relying on only two hypotheses, can be also expressed as:

$$P_{i \text{ vs } j} = \frac{\exp(\log\mathcal{L}_i)}{\exp(\log\mathcal{L}_i) + \exp(\log\mathcal{L}_j)} \ . \tag{3.12}$$

As two hypotheses are used, the variable built with the ratio computed in Eq. 3.12 is known as the "Binary" PID variable.

The advantage of this approach, which directly uses the likelihoods, is its simplicity, since combining the information from all the sub-detectors is straightforward. It is also possible to further customise these variables by discarding a sub-detector that was not optimally calibrated in some data taking period, or by adding more particle hypothesis in the likelihood ratio, in case we want to discriminate among additional particle hypotheses.

There are nevertheless significant drawbacks, such as the fact that potential correlations between the sub-detectors likelihoods are not taken into account, or that some detectors might spoil the information provided by the other sub-detectors, or that the discrimination power of a sub-detector between two particle hypotheses x or y may not guarantee equal probabilities favoring x over y. The latter would indeed result in a slightly biased binary or global likelihood ratio as, in the default combination, one of the two sub-detectors might be unfairly weighted compared to the other. These reasons motivated the development of more advanced PID variables, such as the following two approaches. In this second approach, calibration weights are applied to the individual likelihoods to overcome some of the limitations of the default approach. These weights $w_{x,d}$ are defined for each detector d and particle hypothesis x. Using Eq. 3.10, a weighted likelihood can be computed as:

$$\log\mathcal{L}'_x = \log\left(\prod_{d\in D}\left(\mathcal{L}_x^d\right)^{w_{x,d}}\right) = \sum_{d\in D} w_{x,d}\log\mathcal{L}_x^d, \tag{3.13}$$

which gives the following ratio:

$$P'_i = \frac{\exp\left(\sum_{d\in D} w_{i,d}\log\mathcal{L}_i^d\right)}{\sum_{x\in X}\exp\left(\sum_{d\in D} w_{x,d}\log\mathcal{L}_x^d\right)} = \frac{\exp\left(\log\mathcal{L}'_i\right)}{\sum_{x\in X}\exp\left(\log\mathcal{L}'_x\right)}. \tag{3.14}$$

This variable is referred to as the "Reweighted" PID variable. The calibration weights used in Eq. 3.13 and Eq. 3.14 are organised in the form of a 6×6 matrix, expressed as:

$$w = \begin{array}{c} \begin{array}{cccccc} \text{svd} & \text{cdc} & \text{top} & \text{arich} & \text{ecl} & \text{klm} \end{array} \\ \begin{pmatrix} 0.80897 & 2.27021 & 0.43437 & 0.59494 & 2.46420 & 0.15824 \\ 1.36293 & 1.95849 & 0.42866 & 0.61061 & 1.96239 & 0.48289 \\ 1.06375 & 1.43302 & 0.42645 & 0.59816 & 2.01812 & 0.18273 \\ 1.79259 & 1.90825 & 0.42230 & 0.60463 & 1.66284 & 0.21942 \\ 1.71904 & 1.86573 & 0.41388 & 0.64555 & 1.96317 & 0.22059 \\ 1.26471 & 2.02610 & 0.38130 & 0.69305 & 4.08499 & 0.14939 \end{pmatrix} \end{array} \begin{array}{c} e \\ \mu \\ \pi \\ K \\ p \\ d \end{array} \tag{3.15}$$

These weights are obtained after training a neural network (NN) on a sample of simulated single-particle events in which all six categories are equally represented. They are more precisely implemented as in a usual neural network, where the procedure aims at minimizing the cross entropy loss function. An additional binary cross entropy term is added to the loss function, in order to increase the separation between pions and the other particles, as they are the most abundantly produced particle and have a significant probability to be misidentified as leptons, kaons and protons. One observation is that setting all weights to 1 would lead to the default likelihood ratio.

A third and last approach that is employed to improve the default implementation relies on multivariate methods, such as neural networks or boosted decision trees (BDT). In the presented analysis, the BDT approach serves as the criterion for the identification of electrons and is denoted as P_e.

The variable known as the "BDT" or also "MVA" PID variable was developed in a view of improving the separation between electrons, muons and pions [65]. For that, the likelihood of the ECL, depending on the E/p ratio as detailed in Eq. 3.8, is modified. Even if this variable is in general very powerful in discriminating electrons and muons against hadrons, such as pions, it shows a reduction of discriminating power towards low momentum ranges. Indeed, in that specific scenario, electrons have a stronger bending of their trajectory, which leads to longer paths through material and therefore increasing energy losses from Bremsstrahlung, affecting the separation power between muons and electrons. The hadronic inelastic interactions rate is also higher in that case, which impacts the separation power between muons and pions.

To counter these effects, several variables related to the lateral and longitudinal shower shape development, and track penetration depth into the ECL are combined into a BDT to allow further discrimination. As these variables are expected to be highly correlated, the use of a BDT is preferable to provide a better handle at exploiting non-trivial dependencies across inputs to improve classification performance. The BDT is trained in multi-class mode to separate leptons from all other particle hypotheses, but it is also possible to train it in binary lepton vs pion mode. In order to exploit the particle ID capability in its entirety, these inputs are combined with the high-level likelihoods for the electron, muon and pion hypotheses from the other sub-detectors, and gives the following ratio of likelihood:

$$\tilde{P}_i = \frac{\exp(\sum_{d \in D} \log \tilde{\mathcal{L}}_i^d)}{\sum_{x \in X} \exp(\sum_{d \in D} \log \tilde{\mathcal{L}}_x^d)} = \frac{\exp(\log \tilde{\mathcal{L}}_i)}{\sum_{x \in X} \exp(\log \tilde{\mathcal{L}}_x)}, \tag{3.16}$$

θ [rad]	θ [deg]	cosθ	Correspondence
(0.22, 0.56)	(12.61°, 32.09°)	(0.98, 0.85)	①
(0.56, 1.13)	(32.09°, 64.75°)	(0.85, 0.39)	②
(1.13, 1.57)	(64.75°, 90.00°)	(0.39, 0.00)	③
(1.57, 1.88)	(90.00°, 107.71°)	(0.00, -0.31)	④
(1.88, 2.23)	(107.71°, 127.78°)	(-0.31, -0.62)	⑤
(2.23, 2.71)	(127.78°, 155.27°)	(-0.62, -0.91)	⑥

Table 3.3: The polar angle binning used for electron ID corrections. The correspondence between the bins and the detector regions is illustrated in Fig. 3.19

θ [rad]	θ [deg]	cosθ	Correspondence
(0.40, 0.64)	(22.92°, 36.67°)	(0.92, 0.81)	①
(0.64, 0.82)	(36.67°, 46.98°)	(0.81, 0.69)	②
(0.82, 1.16)	(46.98°, 66.46°)	(0.69, 0.40)	③
(1.16, 1.46)	(66.46°, 83.65°)	(0.40, 0.11)	④
(1.46, 1.78)	(83.65°, 101.99°)	(0.11, -0.21)	⑤
(1.78, 2.13)	(101.99°, 122.04°)	(-0.21, -0.53)	⑥
(2.13, 2.22)	(122.04°, 127.20°)	(-0.53, -0.62)	⑦
(2.22, 2.60)	(127.20°, 148.97°)	(-0.62, -0.86)	⑧

Table 3.4: The polar angle binning used for muon ID corrections. The correspondence between the bins and the detector regions is illustrated in Fig. 3.20

where log $\tilde{\mathcal{L}}_x$ is defined using Eq. 3.10. Another emerging variable, called "NN" PID variable, uses neural networks to discriminate pions from kaons. Ongoing advancements aim to extend its capability to discriminate among all particle hypotheses. However, since this feature is still under development, additional details are currently lacking.

3.7.1 Particle identification corrections

Imperfections in the simulation are corrected on the basis of the observed differences between data and MC, measured in several calibration channels. Efficiency measurements utilise decays such as $J/\psi \to l^+l^-$ or the processes $e^+e^- \to l^+l^-\gamma$ and $e^+e^- \to e^+e^-l^+l^-$, where l represents either an electron or a muon. For assessing mis-id rates, decays such as $K^0_S \to \pi^+\pi^-$ and $e^+e^- \to \tau^+\tau^-$ events, with the decay $\tau^\pm \to \pi^\pm\pi^\mp\pi^\pm\nu_\tau$, are used. These correction factors are obtained globally by the Belle II lepton ID performance group and then provided to all analysts. The lepton ID correction factors are binned in momentum, polar angle, and charge. The polar angle binning is different for electron and muon identification variables, the corresponding binning are presented in Table 3.3 and 3.4. The selection of bin edges is influenced by key areas (like gaps or instrumentation) and the segmentation of the sub-detectors. A vertical cross section of the Belle II detector, which highlights the areas belonging to the various bins, is depicted in Fig. 3.19 and Fig. 3.20 The momentum binning differs slightly between electron and muon-related corrections at low momentum. While for electron-related corrections the bin edges are {0.2, 0.4, 0.5, 1.0,

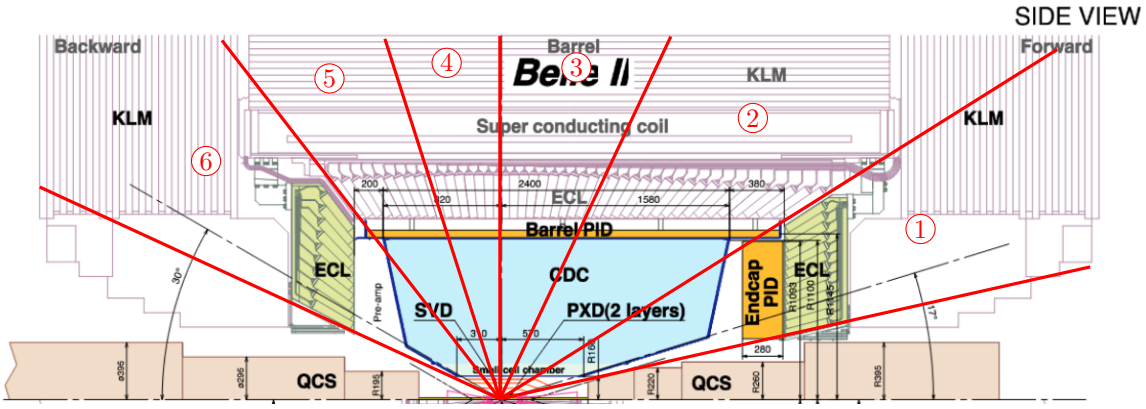

Figure 3.19: A cross section of the Belle II detector viewed from the side, showing the electron ID segments in polar angle. The highlighted edges of the correction bins match those listed in Table 3.3.

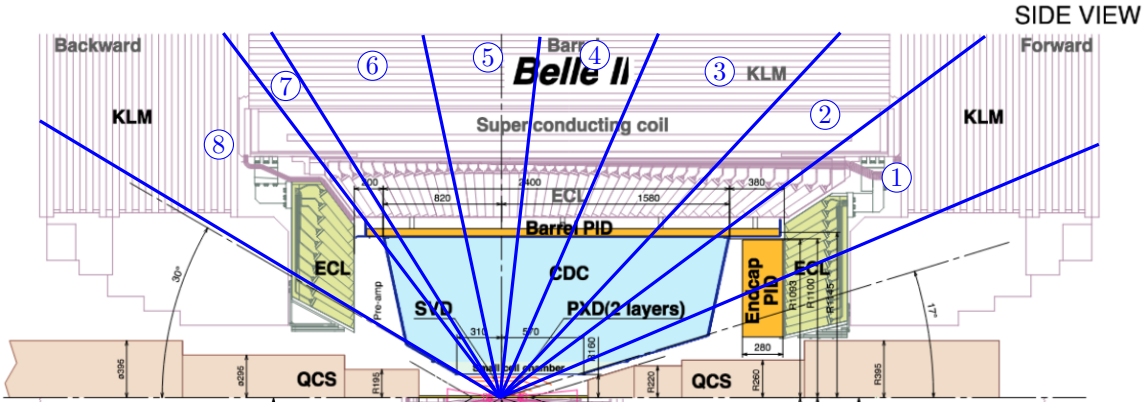

Figure 3.20: A cross section of the Belle II detector viewed from the side, showing the muon ID segments in polar angle. The highlighted edges of the correction bins match those listed in Table 3.4.

1.5, 2.0, 2.5, 3.0, 3.5, 4.0, 4.5, 5.0, 5.5, 6.0, 6.5, 7.0} GeV, for muon-related corrections they are {0.2, 0.4, 0.5, 0.7, 1.0, 1.5, 2.0, 2.5, 3.0, 3.5, 4.0, 4.5, 5.0, 5.5, 6.0, 6.5} GeV. While efficiency corrections are available up to 7 GeV, the $h^{\pm} \to l^{\pm}$ mis-id rate corrections are only available up to 5 GeV, and also only for the polar angle bins in the forward direction. This is due to the limited number of high momentum tracks in the corresponding calibration channels.

Chapter 4

CDC Calibration: Addressing Charge Asymmetry

In the Belle II experiment, cosmic ray data are collected and analyzed, with particle tracks reconstructed through fitting procedures. The resulting fit parameters – such as drift distances and residuals – serve as the basis for detector calibration and alignment. The initial sections of this chapter describe the calibration methodology, both at the level of individual parameters and in a comprehensive context, following the approach outlined in [66]. The concluding sections highlight a central challenge that links this chapter to the broader analysis, along with the strategies employed to address it.

4.1 CDC Readout and Cosmic Ray Data Acquisition

The Central Drift Chamber (CDC) consists of 14,336 sense wires and is equipped with 299 front-end readout electronic boards mounted on the backward side of the detector, as illustrated in the blue-colored region on the left side of Fig. 4.1. Each board handles signals from 48 sense wires, with each signal processed by an amplifier-shaper-discriminator (ASD) chip [67]. The ASD output is digitized by a 10-bit, 31.75-MS/s analog-to-digital converter (ADC) chip. Timing information is processed by a multiple-hit time-to-digital converter (TDC) with a time resolution of 0.98 ns, implemented within a field-programmable gate array (FPGA).
The digitized ADC and TDC signals are temporarily stored in an internal buffer inside the FPGA while awaiting a trigger signal. Once triggered, the data are transmitted to the data acquisition (DAQ) system via optical fibers. The FPGA buffer can store data for up to 8 μs, exceeding the expected maximum trigger latency of 5 μs at design luminosity (corresponding to an event rate of 30 kHz).

4.1.1 Cosmic Ray Data Acquisition

The default calibration procedure combines data from various sources, including cosmic rays, dimuon events, and hadronic collisions. Each data type contributes differently: cosmic rays provide continuous coverage and high-statistics samples independent of beam conditions; dimuon events offer well-understood kinematics and timing from e^+e^- collisions; and hadronic events help to calibrate in conditions closest to physics data-taking.

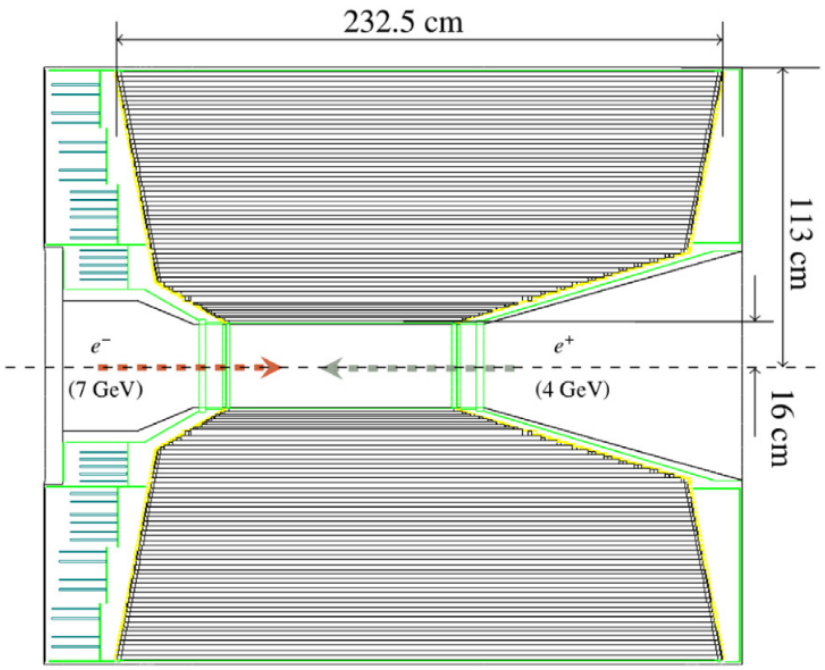

Figure 4.1: Longitudinal cross section of the Belle II CDC.

In this discussion, the focus is placed exclusively on the calibration using cosmic ray data. This approach offers unique advantages in studying time alignment, drift properties, and detector response in a magnetic field-free or controlled environment.
Cosmic ray data are collected both in the absence and presence of a magnetic field:

- **Without magnetic field:** Data are triggered using a plastic scintillator placed near the interaction point (IP) region. In addition, the presence of a track segment (TS) in CDC super-layer 2 is required. A TS is a basic element constructed for the track trigger. In this configuration, the trigger timing is provided by the scintillator.

- **With a magnetic field of 1.5 T:** In this configuration, data are recorded without the use of the plastic scintillator. The trigger requires the presence of a TS in CDC super-layer 2 and signals from at least two channels of the electromagnetic calorimeter (ECL). Additional subdetectors involved in this setup include the time-of-propagation (TOP) counter and the barrel K_L and muon detector. Trigger timing is derived from the ECL signals.

All collected data are analyzed using the basf2 framework [41]. Track reconstruction is performed with the track finder described in [68], where all tracks are assumed to be downward-going (rather than outward-going). This assumption results in negative time-of-flight values for cosmic ray tracks traversing the upper half of the detector. The reconstructed tracks are subsequently fitted using the GENFIT2 toolkit [69, 70], which employs a deterministic annealing filter algorithm to reject outlier hits and resolve the left/right ambiguity in drift time measurements. The fitted parameters are then used for detector calibration and alignment.

4.2 Calibration Procedure

This section outlines both the individual parameter calibration and the overall iterative calibration process applied to the CDC. Calibration is performed through multiple iterations, each consisting of the following steps: track reconstruction, extraction of fitted hit information, application of calibration algorithms, and updating of calibration constants for subsequent iterations.

4.2.1 Time Relation Calibration

Each TDC operates in a common stop mode, where the timing measurement is initiated by the arrival of a signal from a sense wire (start) and terminated by a common trigger signal (stop), which is distributed by the trigger system with a fixed latency of approximately 5 μs. The time relation used in the calibration is expressed as:

$$a \cdot TDC = T_0 - T_{evt} - T_{tof} - T_{drift} - T_{prop.} - T_{tw}. \tag{4.1}$$

In this equation:

- a is the TDC resolution.
- T_0 is a per-channel constant representing the sum of the stop signal latency and an individual channel offset that requires calibration.
- T_{evt} accounts for event-by-event fluctuations in the stop signal timing relative to its nominal value.
- T_{tof} is the time-of-flight of the particle from a reference plane to the ionization point.
- T_{drift} is the drift time of the ionization electrons.
- $T_{prop.}$ is the signal propagation time along the sense wire to the backward end-plate.
- T_{tw} is the delay due to the time walk effect.

The values of T_{tof} and $T_{prop.}$ vary per hit and are calculated based on the reconstructed track information. An example TDC spectrum is shown in Fig. 4.2, where the right-edge reflection point is used to determine the initial value of T_0.

4.2.2 T_0 Correction

The most critical calibration constant is T_0, as it directly impacts the precision of drift time determination. An initial set of raw T_0 values is extracted from the TDC spectra for all readout channels. These values are necessary for performing track reconstruction in the first calibration iteration.
Since the right edge of the TDC spectrum corresponds to zero drift time, and the mean value of T_{evt} is zero by definition, the initial T_0 value for each channel can be estimated from Eq. 4.1 as:

$$T_0^{\text{initial}} = a \cdot TDC_{\text{edge}} + T_{tof} + T_{prop.} + T_{tw}, \tag{4.2}$$

where TDC_{edge} is the position of the right edge of the TDC spectrum, determined by fitting with a Fermi-Dirac-like function. The T_{tof} and $T_{prop.}$ values are computed under the assumption

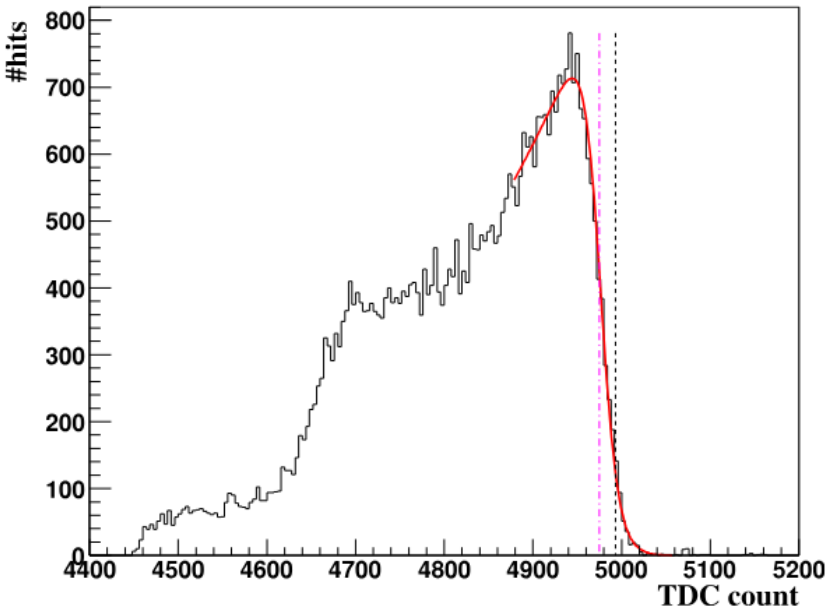

Figure 4.2: TDC count distribution. The red line represents a fit used to identify the right-edge reflection point (magenta dash–dot line). The black dashed line marks the initial value of T_0. The gap between the edge position and T_0 corresponds to the sum of T_{tof}, $T_{prop.}$, and T_{tw}. The image is taken from [66].

that all cosmic muons originate from the interaction point (IP) and travel with a polar angle of 90°. The time walk offsets (T_{tw}) are treated similarly and calibrated as a function of ADC count.

After the initial track fitting, the unbiased fitted drift distances are converted to drift times using the time-to-distance relation, $x(t)$. The residuals – defined as the difference between the measured and fitted drift times – are then calculated for each channel. The distribution of these time residuals is fitted with a Gaussian function, and the mean value, denoted ΔT, is used to correct the T_0 value.

To improve the resolution of ΔT, hits located within 0.7 mm of the sense wires and in cell boundary regions (where resolution is poorest) are excluded from the fit. The T_0 value for each channel is iteratively updated using the corresponding ΔT, and this process is repeated until the condition $|\Delta T| < 0.5$ ns is satisfied.

Fig 4.3 shows the ΔT values for a typical CDC layer (layer 6) before and after the T_0 correction. By the fourth iteration, the residuals are significantly reduced, and most ΔT values are consistent with zero.

4.2.3 Time-to-Space Relations

The time-to-space relation, $x(t)$, is calibrated separately for each CDC layer, for both sides of each sense wire (left/right), and for different track incident angles. The terms “left” and “right” refer to the side on which a particle passes relative to the sense wire. The track incident angle in the r–ϕ plane, denoted as α, is illustrated in Fig. 4.4. It is defined as the angle between the projected track momentum and the sense wire in the r–ϕ plane, and ranges from $-90°$ to $+90°$

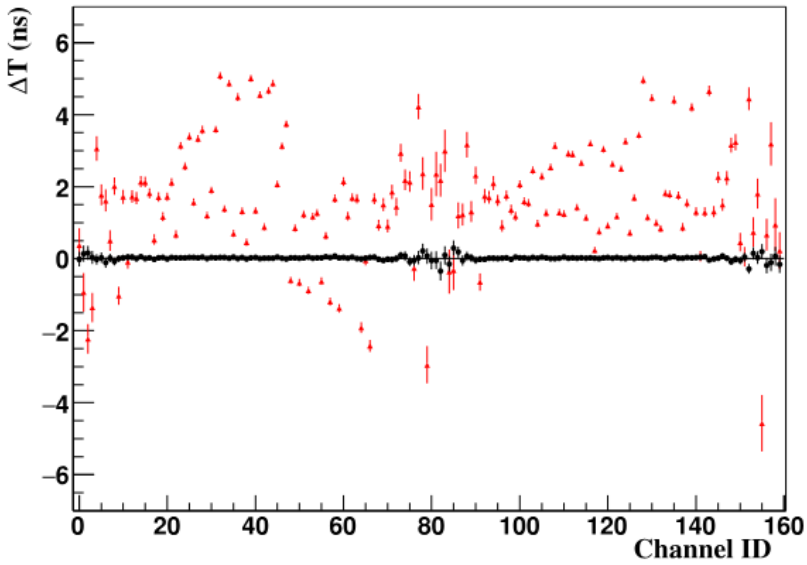

Figure 4.3: Channel-wise ΔT values in CDC layer 6. Red triangles represent the values before the T_0 correction (first iteration), and black circles show the values after the fourth iteration. The T_0 correction reduces the timing offsets, bringing ΔT close to zero for most channels. The image is taken from [66].

in 10° steps. The incident angle in the r–z plane, θ, varies from 0° to 180° and is grouped into seven angular bins. In total, 14,112 distinct $x(t)$ relations must be calibrated. Each $x(t)$ relation is derived from the correlation between the unbiased drift distance and the measured drift time, the latter computed using Eq. 4.1. A representative example of the $x(t)$ relation is shown in Fig. 4.5. The data are fitted using a fifth-order Chebyshev polynomial in the drift time range of 0–350 ns for tracks passing on the left side of the wire, and 0–330 ns for those passing on the right side. In the boundary region, where drift distances are smallest and resolution is poorer, a linear function is used. The polynomial and linear fits are smoothly connected at the transition point to ensure continuity.

4.2.4 Use of $x(t)$ in Monte Carlo Simulation

In the MC simulation of the Belle II CDC, the true hit position of a charged particle is known from the generator-level information. To simulate the detector response, this hit position must be converted into a drift time, which mimics what the electronics would measure in real data. This is achieved by inverting the calibrated $x(t)$ relation to obtain $t(x)$. This inverted function is essential for digitization, the process that emulates the signals recorded by the TDC.
In practice, the fitted $x(t)$ relation from data is inverted numerically or analytically (if the fit allows), and this inverse is embedded into the simulation framework (e.g., in the digitizer module). Therefore, during calibration, care must be taken to ensure that the fitted $x(t)$ relation remains strictly monotonic and well-behaved to allow for a valid inversion. This requirement strongly influences the choice of fitting function—especially in the large drift time region, where sparse statistics and field non-uniformities can distort the shape. It also motivates the use of constrained fits (e.g., low-order Chebyshev polynomials) that preserve monotonicity and yield

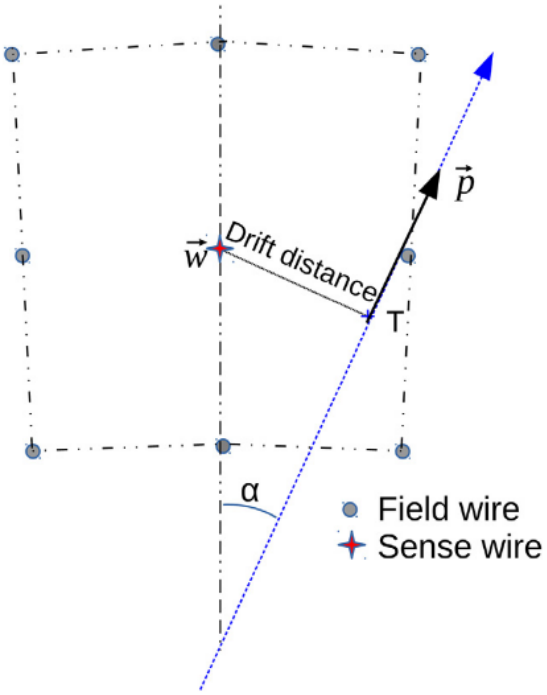

Figure 4.4: Definition of the track incident angle α in the r–ϕ plane. The track momentum vector is denoted by $\vec{p}$, and $\vec{w}$ is the vector from the origin to the position of the sense wire.

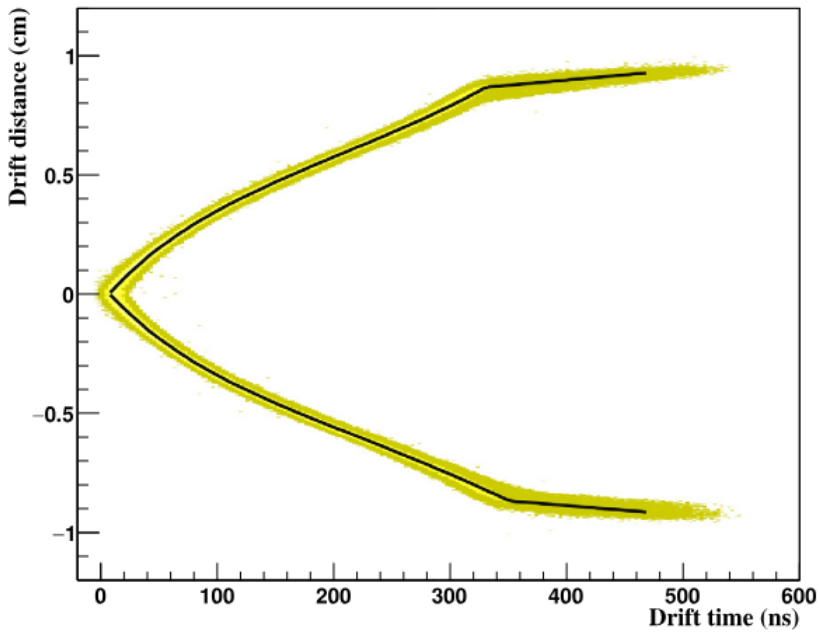

Figure 4.5: Example of a time-to-space relation, $x(t)$, for CDC layer 54 with $10° < \alpha \leq 20°$ and $75° < \theta \leq 105°$. Positive drift distances correspond to tracks passing on the right side of the sense wire, while negative distances indicate left-side passages. The fitted function is shown as a black line. The image is taken from [66].

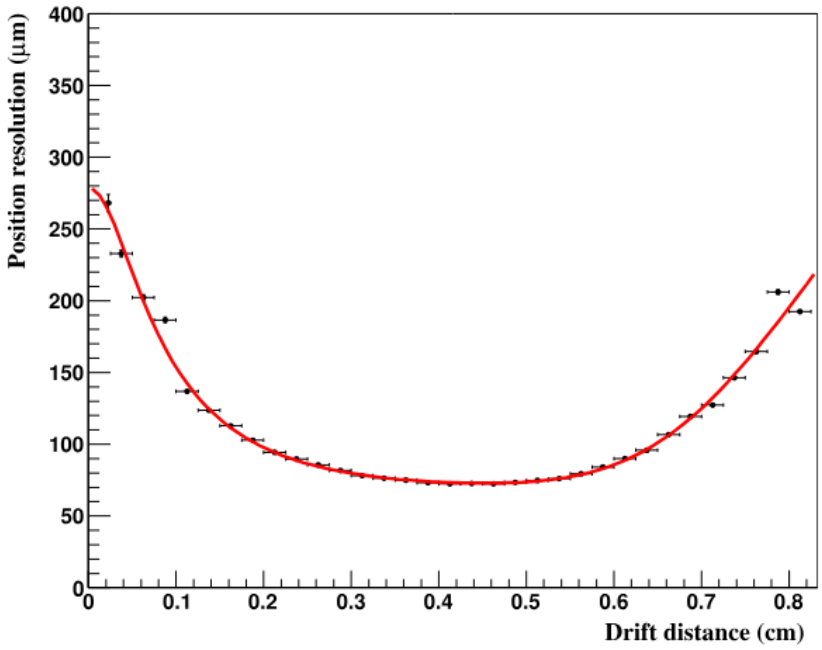

Figure 4.6: Position resolution as a function of drift distance for CDC layer 51, in the angular region $0° < \alpha \leq 10°$ and $50° < \theta \leq 75°$. The data correspond to tracks passing to the right side of the sense wires. The fitted function, described in the text, is superimposed. The image is taken from [66].

stable inverse functions suitable for MC use.

4.2.5 Position Resolution

The intrinsic position resolution, denoted by σ, is evaluated using the geometric mean of the biased and unbiased residual distributions:

$$\sigma = \sqrt{\sigma_{\text{unbiased}} \cdot \sigma_{\text{biased}}}. \tag{4.3}$$

This approach helps mitigate the influence of tracking uncertainties on the resolution estimate. Here, σ_{biased} and σ_{unbiased} are the standard deviations obtained from single-Gaussian fits to the residuals from biased and unbiased track fits, respectively. The σ values are updated concurrently with the $x(t)$ relations in each calibration iteration.
Position resolution is calibrated for each CDC layer, each side of the sense wire (left/right), and across different track incident angles. A representative example of the position resolution as a function of drift distance is shown in Fig. 4.6. In this example, the best resolution achieved is approximately 75 μm, corresponding to a drift distance of 0.45 cm. Across layers and incident angles, the best resolutions range from 50 to 120 μm, with typical values being better than 100 μm. The position resolution, calibrated using cosmic ray data, is essential for both Belle II data analysis and Monte Carlo (MC) simulations. It is parameterised by considering four main contributing factors:

1. **Ionisation statistics**, which dominate at small drift distances;
2. **Electron diffusion** in the gas, which scales as $\sqrt{x}$;

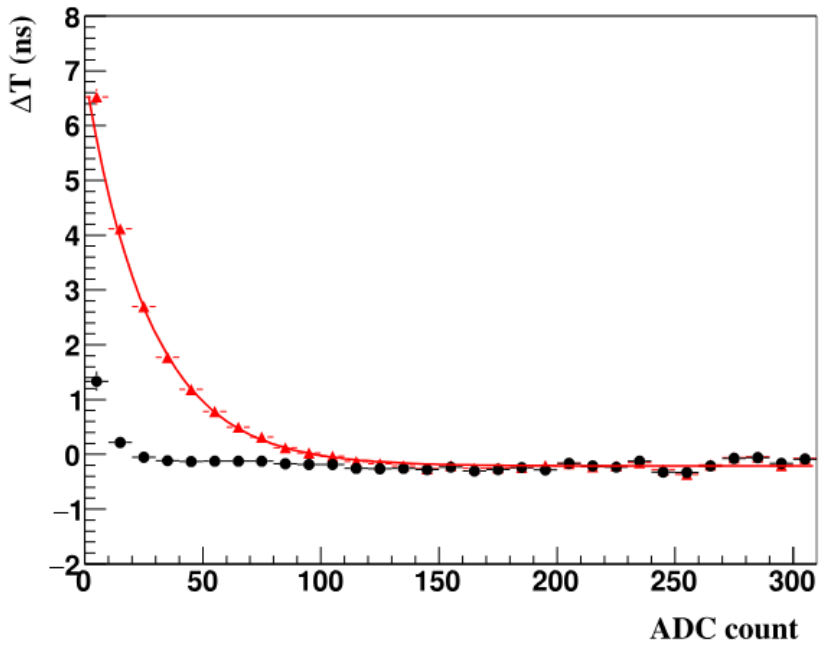

Figure 4.7: Time walk correction for a typical front-end board (Board ID 20). Red triangles indicate the timing residuals before correction, and black circles show the residuals after correction. The image is taken from [66]

3. **Electronic noise**, assumed to be independent of drift distance;

4. **Electric field distortion** near the cell boundary, modeled empirically with an exponential function.

The total position resolution is expressed as the quadratic sum of these four contributions. This composite function provides a good fit to the measured data, as demonstrated in Fig. 4.6.

4.2.6 Time Walk Effect

In the CDC readout system, the signal from each sense wire is split into two processing paths: one for pulse-height measurement via the ADC, and another for timing measurement via the TDC. For timing, a leading-edge discriminator is used, which causes the measured timing to depend on the signal amplitude – an effect known as the *time walk*.
Calibration of the time walk effect is performed after the calibration of T_0, $x(t)$, and the position resolution σ. The correction is based on the dependence of the time residual ΔT on the ADC count for each front-end board. For a representative board, this dependence is shown by the red points in Fig. 4.7, where the systematic shift in timing due to pulse height is clearly observed.
The time walk effect is modeled using an exponential function, which describes the decrease in timing error with increasing pulse height. After applying the correction, the residual timing shifts – represented by the black points in Fig. 4.7 – are reduced to within 0.5 ns of zero for all ADC values, except for the lowest bin (ADC < 10), where the hits are predominantly due to electronic noise.

4.2.7 Calibration Procedure

The full calibration procedure for the CDC is outlined in the flow diagram presented in Fig. 4.8. The first iteration begins with a set of raw T_0 values derived from the TDC spectra, $x(t)$ relations obtained from the Garfield simulation [71], position resolutions from beam test results, and initial null values for the time walk.
The calibration proceeds in the following order:

1. T_0 **Calibration**: The first step is to calibrate T_0, which is iterated until the time residuals ΔT for all channels converge to zero.

2. $x(t)$ **and Position Resolution Calibration**: Once T_0 is stabilized, the $x(t)$ relations and position resolutions are calibrated. During this step, T_0 is also updated alongside the calibration of σ (position resolution).

3. **Convergence**: These three calibrations—T_0, $x(t)$, and σ—are repeated iteratively until they converge.

4. **Time Walk Calibration**: The final step involves the calibration of the time walk effect. This correction affects the drift time estimation and, therefore, requires additional iterations for recalibrating T_0, $x(t)$, and position resolution after the time walk calibration.

The full calibration procedure is performed iteratively, ensuring that all parameters converge to their optimal values. The flow chart in Fig. 4.8 illustrates this process in detail.

4.3 Charge Asymmetry in the CDC

After the calibration and alignment procedures, the performance of the CDC is analyzed using both experimental data and Monte Carlo (MC) simulations. Key track variables examined in these performance studies include the resolutions of d_0, z_0, and $p^*(t)$. One notable anomaly, currently under investigation in Belle II, is the charge asymmetry observed in the mean values of the number of CDC hits (*nCDCHits*), the number of degrees of freedom (*ndf*), and the p-value of the reconstructed tracks. Interestingly, this charge asymmetry shows opposite signs between the data and MC simulations.
Fig 4.9 displays the mean values of *nCDCHits*, *ndf*, and p-value for positive and negative tracks. The mean values from the data are compared with those from the run-independent MC15ri simulated events, indicated by the horizontal lines. This discrepancy poses challenges for analyses involving CP violation and charge asymmetry measurements. Since selection criteria based on variables such as *nCDCHits* may introduce an instrumental asymmetry not reflected in the MC simulations, this issue complicates the accuracy of precision measurements.

4.3.1 Efforts to Resolve the Charge Asymmetry

Recent investigations into the charge asymmetry in the data have revealed that applying a cut for larger drift times eliminates the difference in the number of CDC hits between positive and negative tracks. This observation suggests that the $x(t)$ relations used in the calibration for large drift times need to be refined.

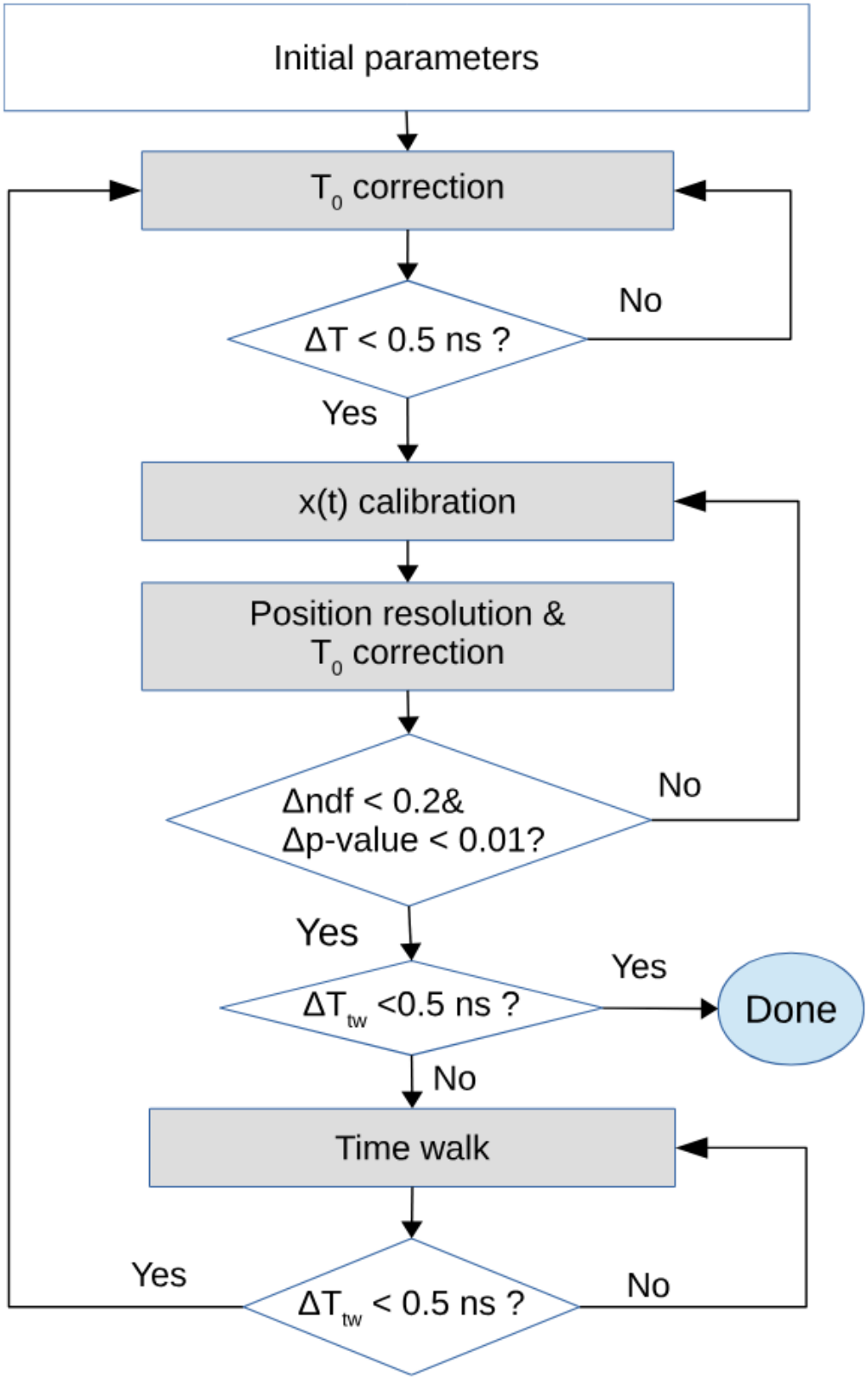

Figure 4.8: Flow chart of the calibration procedure for the Belle II CDC. Here, ΔT represents the mean of the time residuals, and Δndf and Δp-value correspond to the differences in the mean number of degrees of freedom and the probability of the χ^2 distribution of track fitting between two consecutive iterations, respectively.

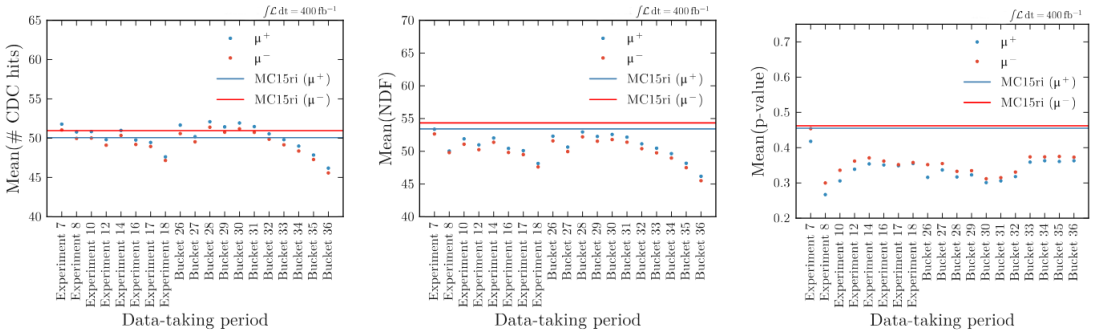

Figure 4.9: Means of the number of CDC hits (left), degrees of freedom (middle), and p-values (right) for positive and negative tracks. Points represent the samples from the pre-LS1 data, while the horizontal lines correspond to the mean values from the run-independent MC15 simulation.

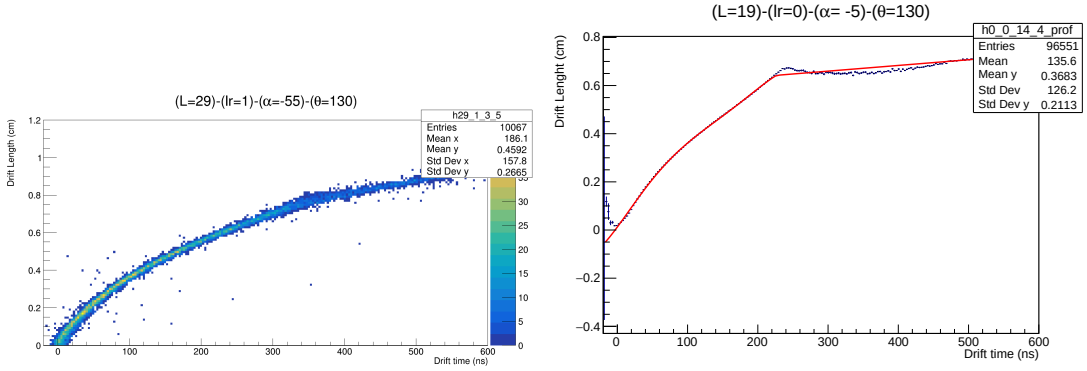

Figure 4.10: Distribution of the 2D drift length and drift time (left) and the $x(t)$ profile with the fit (right). The plot illustrates the reduction in drift length as the drift time approaches approximately 250 ns. The red line represents a fit consisting of a 5th-order Chebyshev polynomial combined with a linear polynomial.

As discussed in Section 4.2.3, the $x(t)$ relation is determined up to a fixed drift time value, t_{cut}, beyond which a linear extrapolation is applied. The fit is based on the x-profile histogram derived from the 2D drift length versus drift time distribution, as shown in Fig. 4.10. Fig. 4.10 highlights the insufficient modeling of the large drift time region. To improve the calibration procedure, the following conditions were set for the new fit relation:

- The improved procedure should not degrade the $x(t)$ relation for $t < t_{cut}$;
- The calibration should remain stable and fully automated;
- The inverse $x(t)$ relation must be a single-valued function, as required by the Monte Carlo (MC) simulations.

Several fitting solutions were tested to better model the large drift time region, including the addition of an N-th order Chebyshev polynomial. While some configurations yielded better results, the challenge was ensuring that the inverse $x(t)$ relation remained single-valued for MC compatibility. After applying parameter constraints, a 2nd-order Chebyshev polynomial was

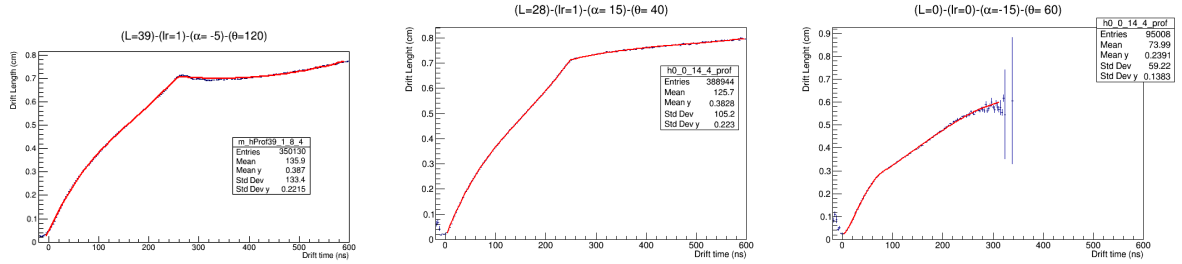

Figure 4.11: Updated $x(t)$ relation using the new fitting function. A 2nd-order Chebyshev polynomial is used to model the large drift time region.

found to be the most effective choice. Example fits are shown in Fig. 4.11. A full calibration was performed and validated using data from "experiment26" within the run range [1410-1970]. This calibration showed a slight improvement in the number of CDC hits, degrees of freedom (ndf), and p-values for the tracks. However, the charge asymmetry issue remains unresolved.

4.4 Discussion

In an effort to resolve the charge asymmetry issue, a new fitting function for the time-to-space relations was introduced into the calibration procedure. While this approach did not fully resolve the issue, it resulted in notable improvements in the overall track quality.
These findings suggest two potential avenues for future work:

- The charge asymmetry may stem from another source, possibly related to tracks with large drift times.
- Additional efforts should focus on further refining the $x(t)$ relation. One potential approach could involve allowing multi-valued functions in the Monte Carlo (MC) simulations.

The charge asymmetry effect was carefully analyzed and addressed throughout the analysis presented in this thesis.

Chapter 5

Physics Analysis

The search for CPV in τ lepton decays is an important probe for physics beyond the SM. In particular, the decay $\tau^- \to \pi^- K^0_S \nu_\tau$ provides a clean laboratory to explore potential CP-violating effects arising from NP, while also allowing for scrutiny of possible SM contributions and hadronic uncertainties.
In this chapter, we present a study of CP violation in the decay $\tau^- \to \pi^- K^0_S \nu_\tau$, which forms the core of this thesis. The measurement is based on the comparison of decay-rate asymmetries between τ^- and τ^+ decays, exploiting the high-statistics dataset collected by the Belle II experiment. Belle II is particularly well-suited for such analyses due to its large τ-pair production rate and its rigorous control of systematic uncertainties, achieved through ongoing detector calibration and data quality efforts.
Charge conjugation is implied throughout unless stated otherwise. Where appropriate, comparisons with previous results, such as those from the BaBar and Belle collaborations, are included for context.

5.1 τ Physics at Belle II

Even though Belle II is mostly known as a B-factory, it is also a τ-factory; the production cross section of τ lepton pairs $\sigma(e^+e^- \to \tau^+\tau^-)$, highlighted in Fig. 5.1, is equal to 0.919 nb, which is approximately the same as B meson pairs $\sigma(e^+e^- \to B\bar{B})$, which is equal to 1.05 nb. The list of all possible measurements in τ physics is wide. It includes the precise determination of its parameters: mass, lifetime, and electric and magnetic dipole moments (EDM and MDM). The study of pure leptonic decays allows for testing lepton flavor universality and determination

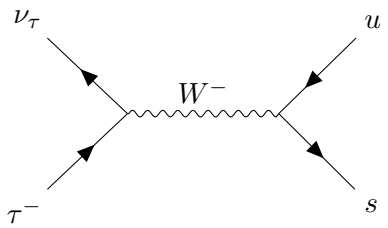

Figure 5.1: Feynman diagram of the process $e^+e^- \to \tau^+\tau^-$. An annihilation diagram (s-channel) is required to get two τ leptons in the final state.

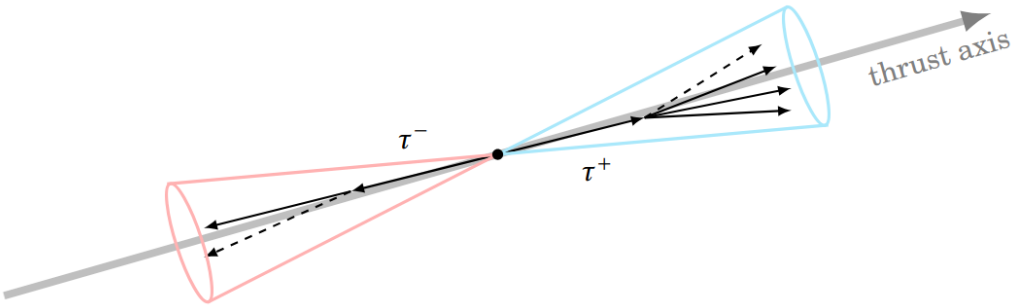

Figure 5.2: "Thrust" axis sketch. Illustration of a case where the τ lepton pair decays into one and three charged particles.

of the Lorentz structure of weak interaction without uncertainties of QCD calculations. The existence of hadronic decay modes opens up an opportunity to study QCD at 1 GeV, test lepton flavor universality, and search for CPV. Any deviations from the SM predictions observed in these studies will indicate the presence of the new physics. In addition, one can directly search for NP in lepton-flavor-violating (LFV) decays of τ lepton or in decays with new invisible particles in the final state.
In the CMS, the τ lepton pairs are produced back-to-back. This particularity allows the definition of two hemispheres in space, which are separated by the plane perpendicular to the so-called "thrust" axis, depicted in Fig. 5.2. The latter corresponds to the maximal momentum projection of all visible particles, from which the thrust value can be further derived as:

$$\text{thrust} \overset{\text{max}}{=} \sum_i \frac{|\vec{p}_i^{\,\text{CMS}} \cdot \hat{n}_{\text{thrust}}|}{\sum |\vec{p}_i^{\,\text{CMS}}|} \ , \tag{5.1}$$

where $\vec{p}_i^{\,\text{CMS}}$ is the momentum in the CMS of the ith particle and $\hat{n}_{\text{thrust}}$ is the unit vector in the direction of the thrust axis. The thrust value, by definition, is dimensionless. Hence, according to Eq. 5.1, τ lepton pairs are expected to exhibit a thrust value nearing 1.
The decay products of one of the two τs are used to select the events (tag side), and we search for signal in the decay products of the other τ (signal side). To suppress background, we reconstruct specific topologies. For example, in the 1×3 topology, we reconstruct 1 charged particle in the signal side and 3 charged particles in the tag side. We use the collected $e^+e^- \to \tau^+\tau^-$ events for precision tests of the SM, and the search for new physics in τ decays.
Finally, thanks to the constrained kinematics, a low background environment, and dedicated triggers, Belle II has excellent reconstruction capabilities for low multiplicity signatures.

5.2 Analysis Strategy

This analysis adopts a strategy similar to that employed by the BaBar collaboration in their previous measurement of CP violation in τ decays [14].
Approximately 1% of the τ leptons have a K^0_S in the final state. The $K^0_S \to \pi^+\pi^-$ decays with a branching fraction of $(69.20 \pm 0.05)\%$ and $K^0_S \to \pi^0\pi^0$ with a branching fraction of $(30.69 \pm 0.05)\%$ [72].
A measurement of A_Q based solely on the exclusive decay $\tau^- \to \pi^- K^0_S \nu_\tau$ would lack the statisti-

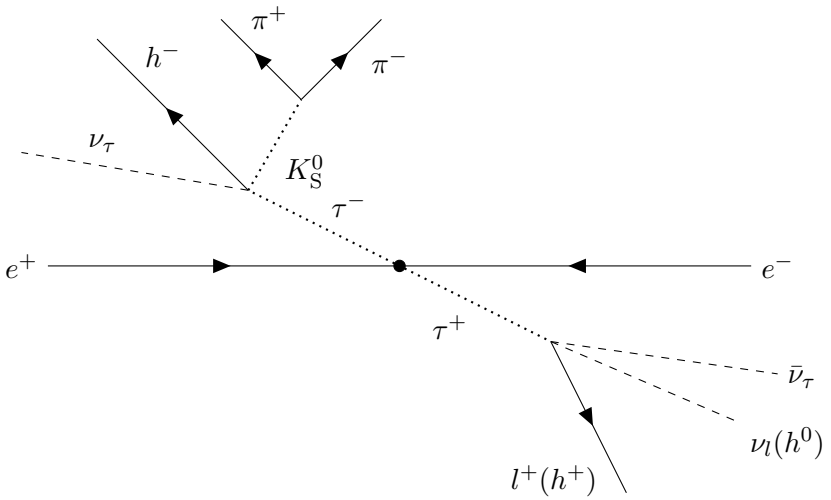

Figure 5.3: Schematic view of the signal decay (additional π^0s in the decay are not shown for clarity).

cal sensitivity required to test the SM prediction, due to the limited branching fraction. To improve the performance of the analysis – particularly in terms of signal efficiency and background rejection – we define the signal to include the broader class of decays $\tau^- \to h^- K^0_S(\geq 0\pi^0)\nu_\tau$ where any number of neutral pions in the final state is allowed. Here, h^- can be either a π^- or a K^-, and the decay $\tau^- \to \pi^- K^0 \bar{K}^0 \nu_\tau$ is included. This inclusive definition is motivated by both the gain in sensitivity and the practical difficulty in experimentally distinguishing $\tau \to \pi K^0_S \nu(\geq 0\pi^0)$ from the other two channels. As discussed later, the contributions from these additional modes are accounted for and removed under SM assumptions about their decay rate asymmetries relations.

The other τ produced in the event is constrained to decay to 1 prong, specifically to an electron or a muon (tag side). See Fig. 5.3 for the schematic of the topology. After suppressing the background via a Multi Variate Analysis (MVA) method, we intend to measure the decay rate asymmetry A of the signal decay modes described above.

The measured asymmetry A is defined as:

$$A = \frac{f_1 A_1 + f_2 A_2 + f_3 A_3}{f_1 + f_2 + f_3}, \tag{5.2}$$

where:

- A_1, A_2 and A_3 are the decay rate asymmetry of $\tau^- \to \pi^- K^0_S(\geq 0\pi^0)\nu_\tau$, $\tau^- \to K^- K^0_S(\geq 0\pi^0)\nu_\tau$ and $\tau^- \to \pi^- K^0 \bar{K}^0 \nu_\tau$ decay modes, respectively.
- f_1, f_2 and f_3 are the fractions of $\tau^- \to \pi^- K^0_S(\geq 0\pi^0)\nu_\tau$, $\tau^- \to K^- K^0_S(\geq 0\pi^0)\nu_\tau$ and $\tau^- \to \pi^- K^0 \bar{K}^0 \nu_\tau$ decay modes, respectively, of the total selected sample, and are estimated from MC.

According to the SM prediction, $A_1 = -A_2$. This is because the K^0_S in $\tau^- \to \pi^- K^0_S(\geq 0\pi^0)\nu_\tau$ is produced only via $\bar{K}^0$, whereas the K^0_S in $\tau^- \to K^- K^0_S(\geq 0\pi^0)\nu_\tau$ is produced only via a K^0. Furthermore, $A_3 \simeq 0$ in the SM because the asymmetries originating from the τ decays

containing K^0 and $\bar{K}^0$, cancel each other almost completely (This is discussed in detail in Chapter 8). Hence, A_1 is obtained from the measured asymmetry A by applying a scale factor:

$$A_1 = \left(\frac{f_1 + f_2 + f_3}{f_1 - f_2} \right) A. \tag{5.3}$$

5.3 Monte Carlo and Data Samples

The analysis described in this note relies on `MC15rd` (15^{th} campaign of the run dependent MC) and the full LS1 dataset.
For the reconstruction of the events, we use a steering file using basf2 release `light-2303-iriomote` [73] on `mDSTs` files produced centrally with release version `r`elease-06-00-10 [74].

5.3.1 Monte Carlo samples

MC simulations are essential in high-energy physics experiments like Belle II to model the expected detector response and physics processes, allowing for the estimation of signal efficiencies, background contributions, and systematic uncertainties.
The following generic and low multiplicity samples were reconstructed:

- $\tau\tau$ samples. These are generated by performing two steps: 1) the process $e^+e^- \to \tau\tau(\gamma)$ is generated using KKMC [75, 76] and 2) the subsequent decay of the τ is handled by the latest version of TAUOLA [77, 78] (called `TauolaBelle2`) and PYTHIA8 [79] generators;

- $q\bar{q}$ background samples: $u\bar{u}$, $d\bar{d}$, $s\bar{s}$, and $c\bar{c}$ generated with KKMC, the subsequent the fragmentation handled by PYTHIA8 [79];

- $B\bar{B}$ background samples: mixed ($B^0\bar{B}^0$) and charged (B^+B^-);

- radiative dilepton ($ll(\gamma)$) background samples: $ee(\gamma)$ and $\mu\mu(\gamma)$;

- two photon and other low-multiplicity background samples: $eell$, $llXX$, and $hhISR$. These samples include $eeee$, $ee\mu\mu$, $eeKK$, $ee\pi\pi$, $eepp$, $ee\tau\tau$, $\mu\mu\tau\tau$, $\mu\mu\tau\tau$, $\mu\mu\mu\mu$, $K^+K^-\gamma$, $K^0\bar{K}^0\gamma$, $\pi^+\pi^-\gamma$ and $\pi^+\pi^-\pi^0\gamma$.

Details on the cross-section σ, integrated luminosity $\int \mathcal{L}dt$ and number of events N of these MC samples can be found in Table 5.1.

5.3.2 Data samples

We only use the on-resonance data, which corresponds to a total integrated luminosity of

$$\mathcal{L}_{\text{int}} = 365.293 \text{ fb}^{-1}. \tag{5.4}$$

This consists of the reprocessing `proc13` and the prompt processing `bucket26-36` (as explained in Section 3.6.1.1). More details, as well as the integrated luminosity per period, is given Table 5.2.

	Process	σ[nb]	$\int \mathcal{L}dt$ [fb^{-1}]	N [10^6]
$\tau\tau$	$ee \to \tau\tau$	0.919	1455.052	1337.19
$q\bar{q}$	$ee \to c\bar{c}$	1.329	1455.052	1933.76
	$ee \to d\bar{d}$	0.401	1455.052	583.48
	$ee \to s\bar{s}$	0.383	1455.052	557.28
	$ee \to u\bar{u}$	1.605	1455.052	2335.36
$b\bar{b}$	$ee \to B^+B^-$	0.54	1455.052	785.73
	$ee \to B^0\bar{B}^0$	0.51	1455.052	742.08
$ll(\gamma)$	$ee \to ee(\gamma)$	295.8	36.3731	10759.16
	$ee \to \mu\mu(\gamma)$	1.148	1455.052	1670.40
$eell$	$ee \to eeee$	39.55	363.767	14386.98
	$ee \to ee\mu\mu$	18.83	363.767	6849.73
$llXX$	$ee \to eeKK$	0.0798	363.767	29.03
	$ee \to ee\pi\pi$	1.895	363.767	689.34
	$ee \to eepp$	0.0117	363.767	4.26
	$ee \to ee\tau\tau$	0.01836	363.767	6.68
	$ee \to \mu\mu\tau\tau$	1.441×10^{-4}	363.767	5.24×10^{-2}
	$ee \to \tau\tau\tau\tau$	2.114×10^{-7}	363.767	7.69×10^{-5}
$hhISR$	$ee \to K^+K^-\gamma$	0.0163	363.767	5.93
	$ee \to K^0\bar{K}^0\gamma$	0.008864	363.767	3.22
	$ee \to K^+K^-\gamma$	0.1667	363.767	60.64
	$ee \to K^+K^-\gamma$	0.02378	363.767	8.65

Table 5.1: The simulated processes with their cross section σ, their integrated luminosity $\int \mathcal{L}dt$ and the number of events N. If not suggested otherwise all particles are to be understood as charged particles such that the overall charge sums to zero.

5.4 Event topology

In e^+e^- annihilation data, the τ leptons are produced in pairs from the process $e^+e^- \to \tau^+\tau^-$. The event is divided into two opposite hemispheres, the tag and the signal hemispheres, defined by the plane perpendicular to the thrust axis, as defined in Eq.5.1.
The signal hemisphere contains the $\tau^- \to h^- K^0_S \nu_\tau$ decay with a τ_{sig} decaying into a single track, originating near the interaction point (IP), and the K^0_S candidate, while the other one is the tag hemisphere where the τ decays leptonically (See Fig. 5.3). The latter is inclusive of all the 1 prong decays of τ (τ_{tag}), that contain one leptonic charged particle (e, μ).
Only photon candidates that pass the tighter selection criteria (defined in next Section 5.5) are used to compute event shape and kinematics variables via the buildEventShape and buildEventKinematics modules [73].

Sample	Experiment	Buckets	$\int \mathcal{L}dt$ [fb^{-1}]		
			Value	Stat.	Syst.
Chunk 1	7	-	0.509	0.002	0.004
	8	-	1.663	0.003	0.011
	10	-	3.666	0.003	0.024
Chunk 2	12	-	54.772	0.005	0.348
Chunk 3	14	16, 16b	16.509	0.006	0.105
Chunk 4	16	17	10.306	0.004	0.066
	17	18	10.730	0.005	0.069
Chunk 5	18	19a, 20, 21, 22, 23, 24, 25	90.172	0.011	0.575
Prompt	20	26	3.792	0.003	0.024
	22	28, 29	32.177	0.007	0.205
	24	30, 31, 32, 33	85.992	0.011	0.547
	26	35, 36	55.005	0.009	0.351
Total			365.29	0.021	2.297

Table 5.2: `Proc13` and `Prompt` data set. Samples are defined with chunks, experiment and buckets numbers. Their luminosity is indicated in the last three columns, where the central value, the statistical and systematic uncertainties are indicated. The bucket label is usually used for `Prompt` productions, while the processing number, `Proc`, is used for the official data production

5.5 Event selection

To accurately measure decay rates yields and therefore the charge asymmetry, the signal events have to be selected.
The variables selected for this measurement must efficiently separate the signal from background, while accurately representing real data. To accurately identify the signal decay $\tau \to \pi K^0_S \nu_\tau (\geq 0\pi^0)$, it is essential to reconstruct both charged and neutral particles in the event. Precise charged particle identification allows us to differentiate pions from kaons, which is crucial to suppress backgrounds such as $\tau \to K K^0_S \nu_\tau$. Neutral particle reconstruction, including photons from initial- and final-state radiation (ISR/FSR) as well as π^0 decays, is also necessary to correctly model the event topology and improve background rejection.

5.5.1 Event reconstruction

We apply the following requirements to reconstruct a signal-like event. Neutral particles are divided into π^0 candidates and photon candidates not coming from a π^0 decay.

- **Neutral pions**
  To reconstruct $\pi^0 \to \gamma\gamma$ candidates, we implemented the π^0 reconstruction according to the studies done in [80] (see Tab.5.3), optimizing the selection for four different types of neutral pions depending on whether the photons are reconstructed in the forward endcap (FWD), barrel region (BRL) or backward endcaps (BWD). This selection imposes requirements on:

- The energies of the leading and sub-leading photons coming from the π^0 candidate,
- The angle between the two photons,
- The π^0 momentum,

The invariant mass of all pairs of neutral clusters in the signal hemisphere is calculated. Any photon pair with an invariant mass between 0.115 GeV/c^2 and 0.152 GeV/c^2 is considered a π^0 candidate. In the reconstruction, we require zero π^0 candidates in the tag hemisphere to reduce background contamination, primarily arising from $q\bar{q}$ events.

- **Photons**
  To reduce the contamination coming from the beam-induced background, remaining photons not identified as coming from a π^0 have tighter criteria before being stored as photon candidates in the event:
  - $E > 0.1$ GeV, where E is the photon's energy.
  - |cluster timing| $<$ 200 ns, where the cluster timing is defined as the time of the electromagnetic calorimeter (ECL) cluster, and it is calculated as the photon timing minus the event t0.
  - $-0.8660 < \cos(\theta) < 0.9565$, corresponding to the CDC acceptance, where θ is the photon's polar angle.
  - clusterNHits > 1.5, where clusterNHits is the sum of all crystals in an ECL cluster. For non-overlapping clusters, this is an integer value, while in case of energy splitting among nearby clusters, this can be a non-integer value.
  - minimum cluster-to-track distance $>$ 40cm or $E > 0.4$ GeV. This can reject hadronic split-offs and single tracks having unmatched ECL clusters.

- **Tracks**
  For the charged particle in the $\tau^- \to h^- K^0_S \nu_\tau$ decay and the track of the other τ decaying leptonically we require the distance of the point of closest approach (POCA) to the interaction point in the $r - \phi$ plane (dr) is less than 1 and the relative distance in the z-direction (dz) is between -3 and 3 are considered (this is what is called a "good track").

- **Pions**
  - EoverP < 0.8, where EoverP is defined as the energy of the track over its momentum. If no energy is deposited in ECL, a value of -1 is assigned to energy. This cut is applied on the charged particle candidate in the signal hemisphere. This selection exploits the distinct energy deposition patterns of different particle species: electrons typically deposit nearly all their energy in the ECL, resulting in EoverP $\simeq 1$, whereas charged pions generally deposit only a fraction of their momentum as electromagnetic energy, leading to significantly lower EoverP values. By imposing this cut, electron contamination in the signal sample is effectively suppressed.
    This requirement is particularly important because electrons in the signal hemisphere can mimic the signal topology through processes such as radiative Bhabha scattering

($e^+e^- \to e^+e^-\gamma$, with photon conversions producing additional e^+e^- pairs) or radiative tau decays ($\tau \to e\nu\nu\gamma$), which can complicate the reconstruction and bias the CP violation measurement. Therefore, rejecting candidates with EoverP $\simeq 1$ helps to reduce these electron-induced backgrounds and enhances the purity of the pion signal.

- **Electrons and Muons**
  PID variables are used on the 1-prong track to identify electrons or muons.
  - pidChargedBDTScore_e > 0.99 for electrons, where pidChargedBDTScore_e is the multiclass-BDT-based electron ID, defined as P_e and detailed in Section 3.7.
  - muonID_no_SVD > 0.99 for muons, where muonID_no_SVD is the global-likelihood-based muon ID, defined as P_μ and detailed in Section 3.7.

- **K_S**
  - There is at least 1 $K^0_S \to \pi^+\pi^-$ in the signal hemisphere, defined as in the stdKshorts list [73].
  - The reconstructed K^0_S mass is between 0.45 GeV/c^2 and 0.55 GeV/c^2.

- **Event cuts**
  - Both the charged particle candidate in the signal hemisphere and the 1-prong track have to be "good tracks" to ensure they originate from the primary collision vertex.
  - The number of total tracks has to be equal to 4, corresponding to the expected decay topology: one charged hadron and two pions from the K^0_S decay on the signal side, and one charged lepton from the tag side. This requirement helps suppress background events with additional charged particles and maintains a clean signal sample.
  - The direction of particles from the two τs is pointing to opposite hemispheres. This condition exploits the back-to-back production of $\tau^+\tau^-$ pairs in the center-of-mass frame of the e^+e^- collision, ensuring that decay products from each τ are spatially separated. This separation reduces combinatorial background and improves the accuracy of assigning tracks and clusters to the correct τ decay, thereby enhancing the purity of the selected events.
  - All tracks have their charges adding up to zero. This charge conservation requirement reflects the fact that $\tau^+\tau^-$ pairs are produced without net charge, and their decay products collectively conserve electric charge

5.5.2 Preselection cuts

A preliminary set of selection cuts is commonly applied in $e^+e^- \to \tau^+\tau^-$ analyses to mitigate an observed excess of data. Previous studies have shown that this excess typically concentrates in regions of low visible center-of-mass energy and low thrust, and is attributed to hadronic two-photon processes, $e^+e^- \to e^+e^-n(h^+h^-)$ with $n \geq 4$, which are not accurately modeled in the Monte Carlo (MC) simulations. The visible center-of-mass energy is defined as the sum of

Region	$E_{\gamma-lead}$ [GeV]	$E_{\gamma-sub}$ [GeV]	π^0 cos($\gamma\gamma$ angle)	p_{π^0} [GeV]
whole detector	> 0.3375	> 0.0875	> 0.8792	> 0.6111
$\gamma\gamma$ FWD	> 0.5625	> 0.1625	> 0.9458	> 0.9444
$\gamma\gamma$ BRL	> 0.4125	> 0.0625	> 0.8875	> 0.6333
$\gamma\gamma$ BWD	> 0.4125	> 0.1125	> 0.8708	> 0.6111
γ BRL, γ FWD/BWD	> 0.3625	> 0.0875	> 0.8875	> 0.5889

Table 5.3: Optimized selection of π^0. Four types of events can be distinguished by the θ angle distribution of the photon clusters: $\theta < 0.55$ corresponds to the FWD, $0.55 < \theta < 2.25$ the BRL and $2.25 < \theta$ the BWD regions.

energies of all reconstructed charged tracks and neutral clusters in the event, measured in the center-of-mass frame, excluding neutrinos and other undetected particles.
In our analysis, however, no significant excess is observed in these regions, likely due to differences in the analyzed phase space compared to previous τ studies. Nonetheless, we employ these variables to suppress Bhabha events in regions of higher thrust and visible energy, where MC simulations tend to overestimate their contribution, as shown in Fig. 5.4. Since the MC

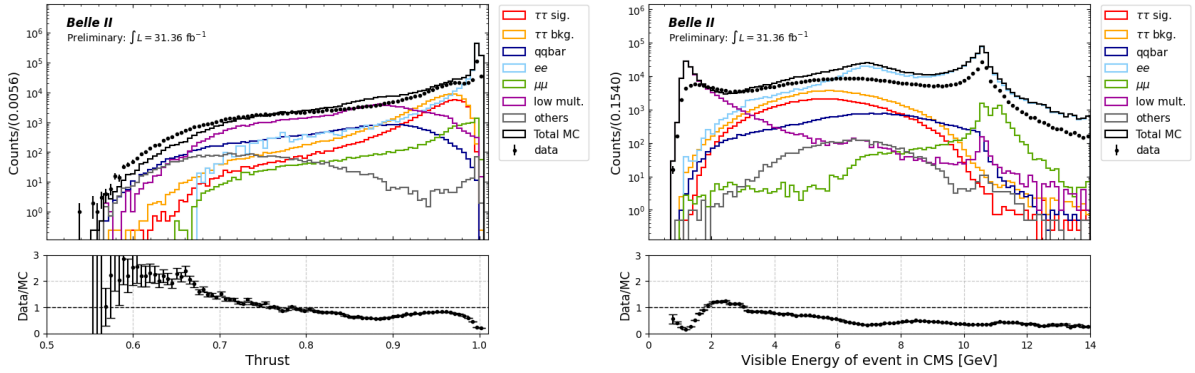

Figure 5.4: Features after the online selection. Only events from Experiment 22, along with the corresponding MC, are shown in the plot.

overestimation is very localised, removing it completely with some additional preselection cuts is possible.
All the *pre-selection criteria* aim to suppress peaking background structures. The analysis is conducted separately for two cases: the electron channel (1 electron on the tag side) and the muon channel (1 muon on the tag side). While results are presented separately for the two channels, the same variables and pre-selection criteria are applied, except for differences in the PID requirement. Preselection cuts are shown in Fig. 5.5, 5.6, 5.7 and 5.8 (Only experiment 22 is used for plotting) and each variable is plotted sequentially after applying the previous cuts. A summary of the applied cuts is provided below:

- $0.9 <$ thrust < 0.995
- 2.5 GeV $<$ visibleEnergyOfEventCMS $<$ 10 GeV
- The K^0_S transverse momentum has to be between 0.2 and 4.5 GeV/c.

- The transverse momentum of the leading track from K^0_S has to be more than 0.25 GeV/c.
- The transverse momentum of the charged track in the signal hemisphere has to be more than 0.1 GeV/c.
- The momentum of the track in the tag hemisphere in CMS has to be less than 4.6 GeV/c.
- The invariant mass of the system $K^0_S + \pi$ has to be between 0.7 and 1.3 GeV.
- The K^0_S's significance of distance has to be more than 10.
- The number of reconstructed photons in the signal hemisphere has to be less than 5.
- The number of photons coming from π^0 decays in the signal hemisphere has to be less than 5.
- The angle between the momentum of each daughter pion and K^0_S (in K^0_S frame) has to be between 0.15 and 3 radiants.
- The K^0_S flight distance has to be more than 0.2 cm.
- The polar angle of the charged pion in the signal hemisphere has to be between 0.35 and 2.6 radians.

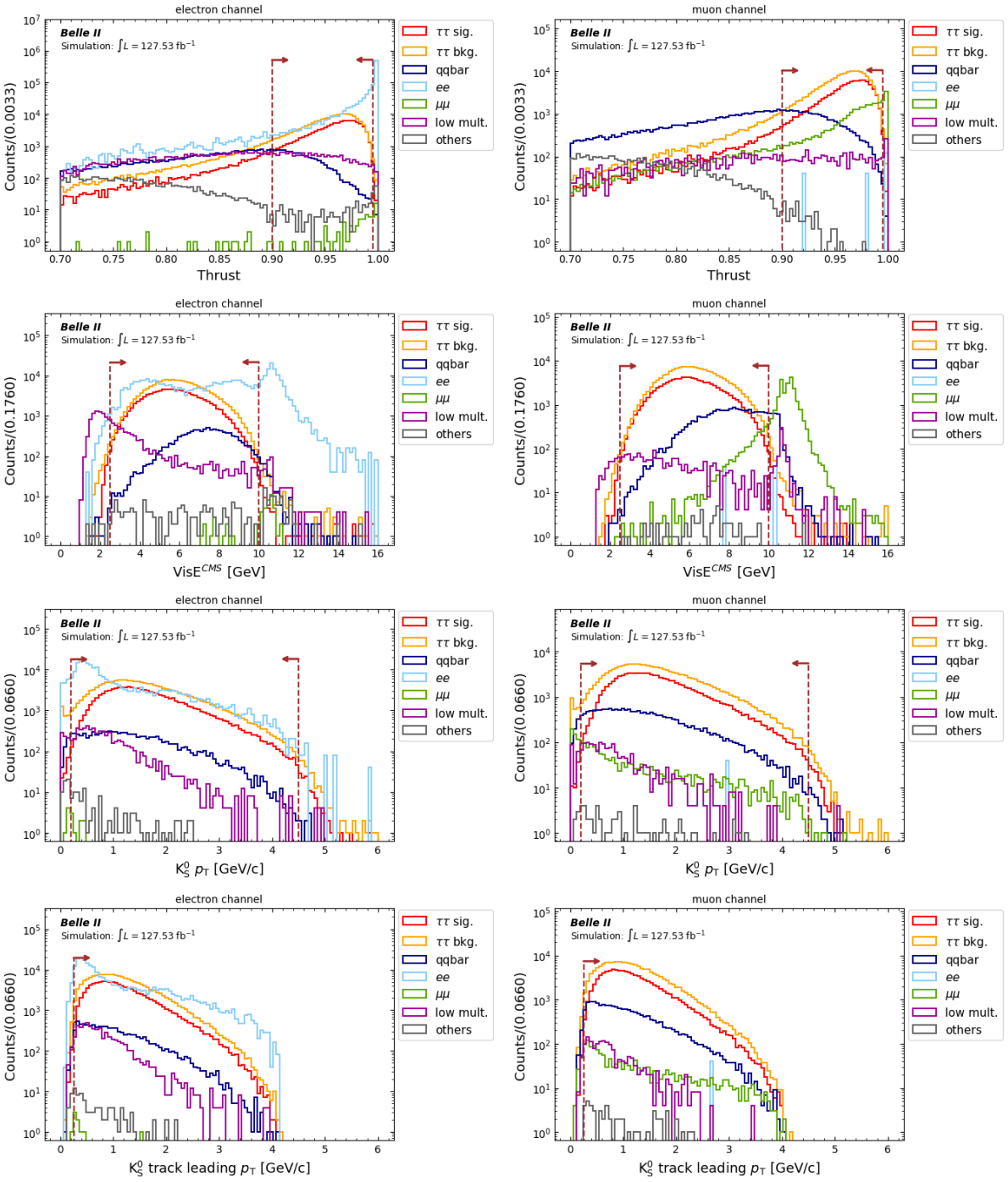

Figure 5.5: On the left (right) the electron (muon) channel variables are reported, starting from the top distributions of thrust, visible energy of event in CMS, K^0_S transverse momentum and the transverse momentum of the leading track from K^0_S are shown. The signal is always reported in red.

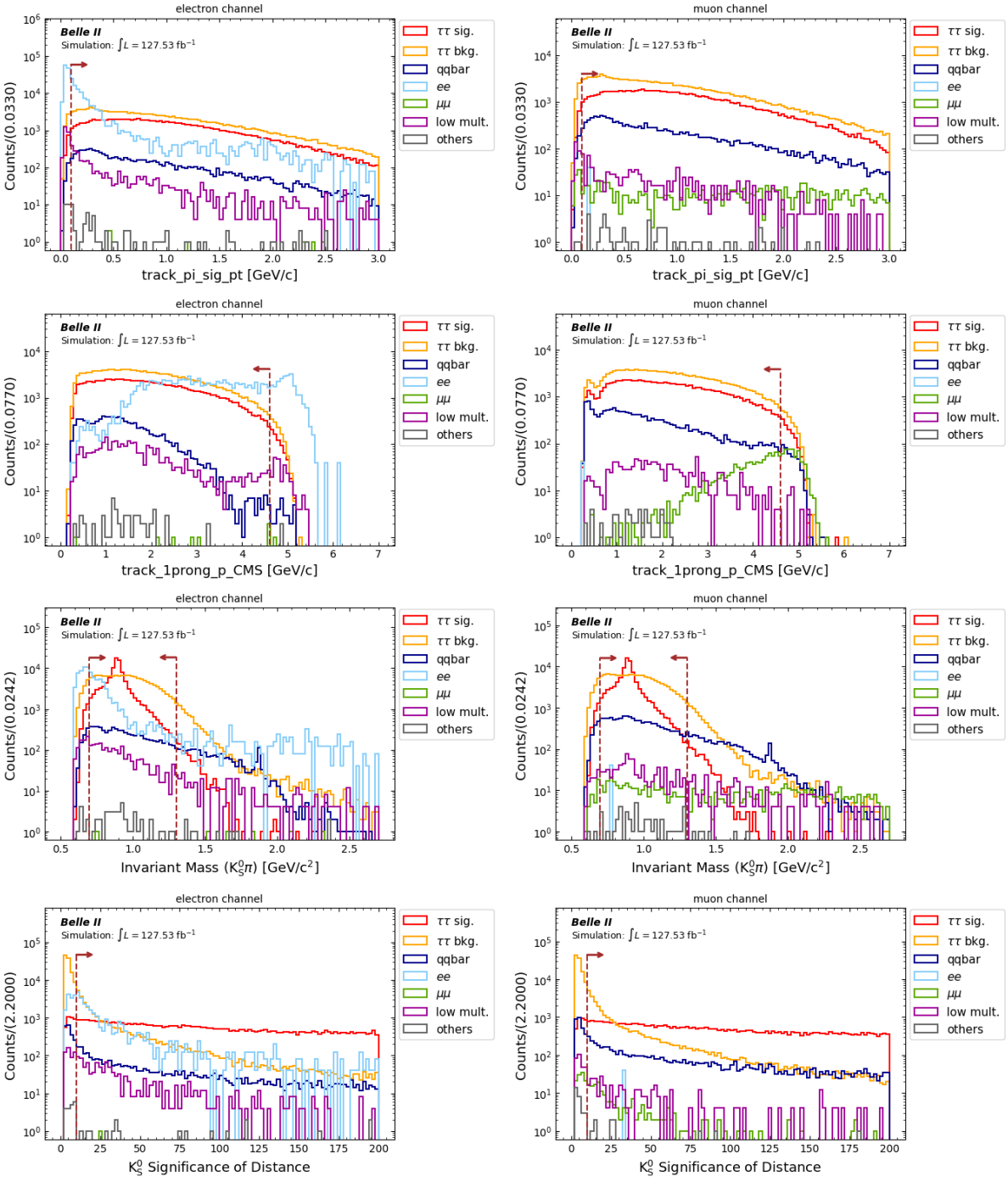

Figure 5.6: On the left (right) the electron (muon) channel variables are reported, starting from the top distributions of the transverse momentum of the charged pion in the signal hemisphere, the momentum of the track in the tag hemisphere, the invariant mass of the system K^0_S and the K^0_S's significance of distance are shown. The signal is always reported in red.

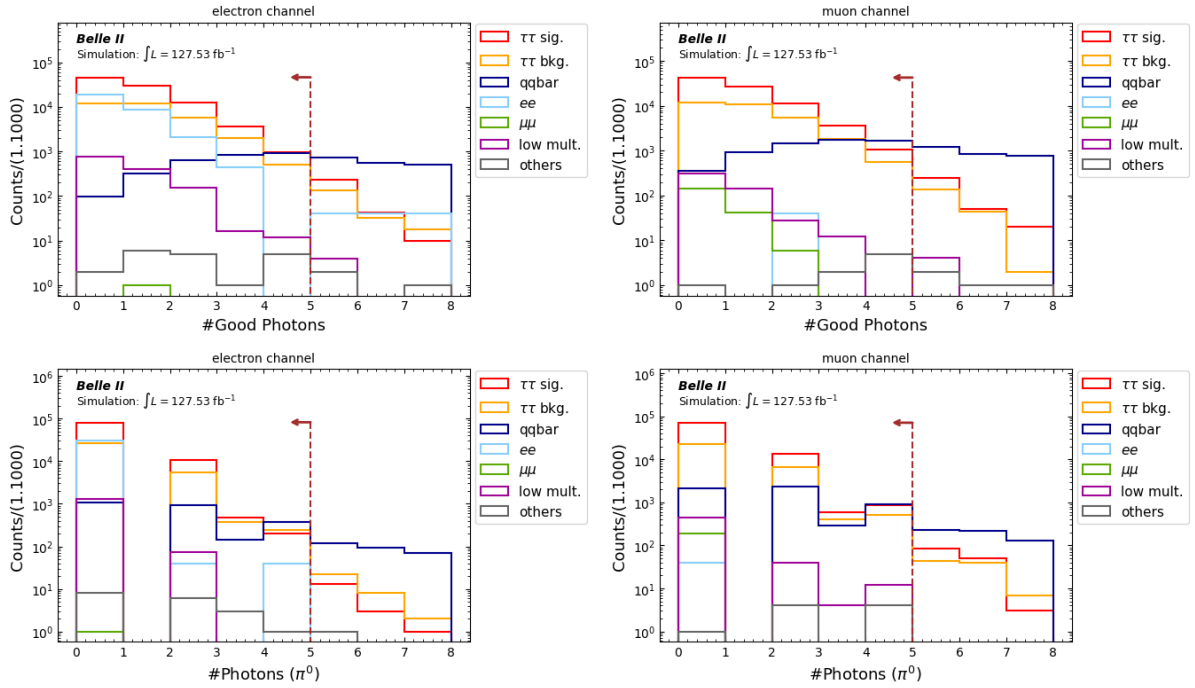

Figure 5.7: On the left (right) the electron (muon) channel variables are reported, starting from the top distributions of the number of reconstructed photons in the event, the number of photons coming from π^0 decay. The signal is always reported in red.

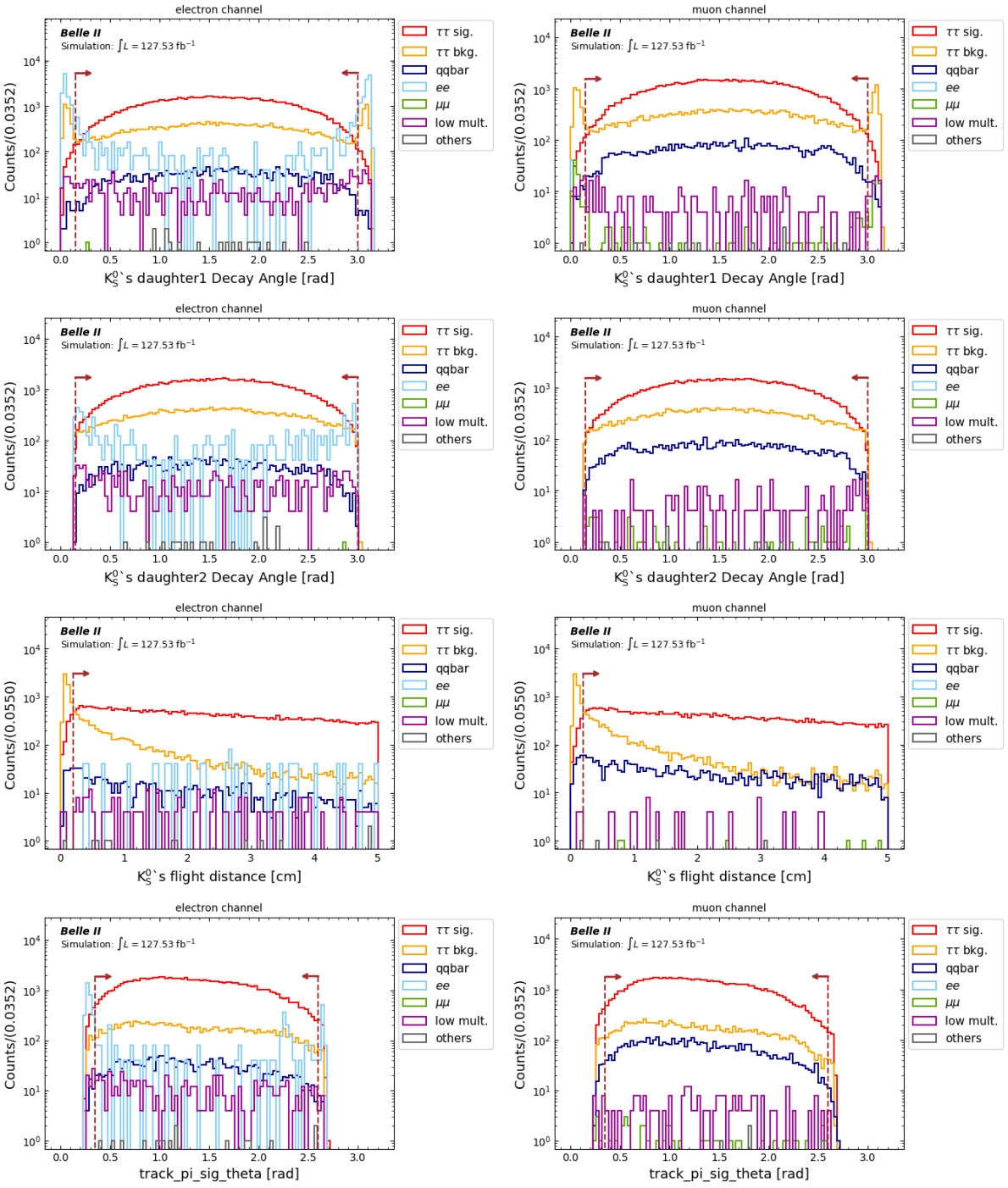

Figure 5.8: On the left (right) the electron (muon) channel variables are reported, starting from the top distributions of the angle between the momentum of each daughter pion and K^0_S (in the K^0_S rest frame), the K^0_S flight distance, and the polar angle of the charged pion in the signal hemisphere are shown. The cut requirements are always reported in red.

To further suppress the remaining low-multiplicity processes, we apply a two-dimensional cut based on the polar angle of the missing momentum and the missing mass squared of the event in the CMS frame. The details of the two-dimensional cuts are presented in Fig. 5.9.

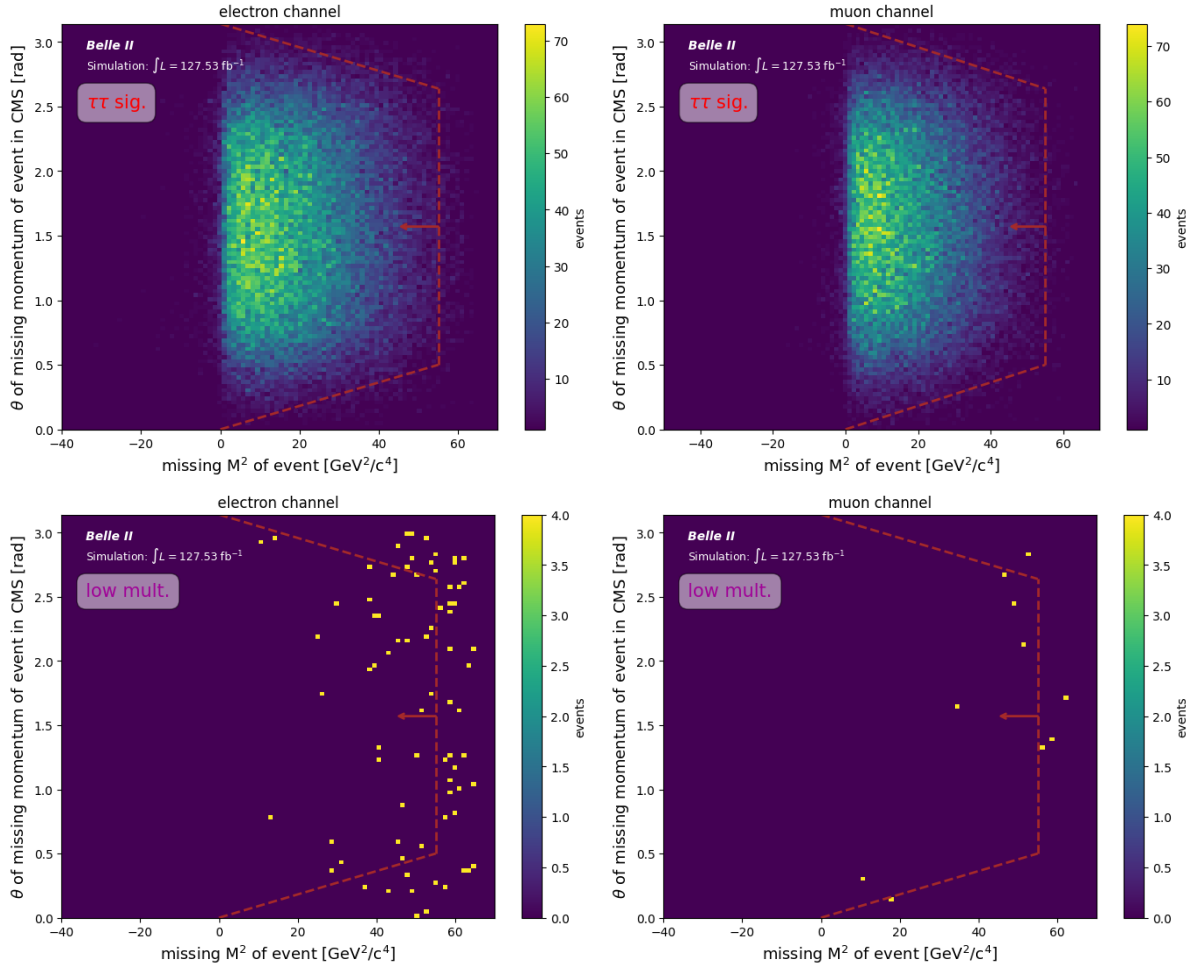

Figure 5.9: The 2-dimensional cuts on the missing mass squared versus the polar angle of the missing momentum in the center-of-mass frame. The top row presents these cuts for the τ-pair signal sample, while the bottom row shows the cuts for the low-multiplicity sample. On the left (right), the electron (muon) channel is displayed.

5.5.3 Trigger Selection

As discussed in Section 3.5, the Belle II trigger system plays a crucial role in selecting events of interest while suppressing backgrounds and handling the high interaction rates at SuperKEKB. For this analysis, we primarily utilize trigger lines based on the ECL information, which provide high efficiency for low-multiplicity final states containing neutral particles such as photons. Charged particle triggers from the CDC are also considered and used as reference triggers to cross-check and validate the performance of the ECL-based triggers.
The ECL triggers with the highest efficiency are the hie + lml0-13, named according to the official Belle II trigger nomenclature:

- `hie`

  - total ECL energy > 1 GeV
  - no ECL Bhabha veto signal

- `lml0` (prescaled since experiment 20, not used)
  - $N_{\text{cluster}} \geq 3$, one with $E_{\text{lab}} \geq 300$ MeV
  - $1 \leq \theta_{\text{id}} \leq 17 \equiv 12.4^\circ < \theta_{\text{lab}} < 154.7^\circ$
  - not an ECL 3D Bhabha
- `lml1`
  - at least one cluster with $E_{\text{CM}} \geq 2$ GeV, $4 \leq \theta_{\text{id}} \leq 14 \equiv 32.2^\circ < \theta_{\text{lab}} < 124.6^\circ$
- `lml2`
  - at least one cluster with $E_{\text{CM}} \geq 2$ GeV, $\theta_{\text{id}} = 2, 3, 15$ or $16 \equiv 18.5^\circ < \theta_{\text{lab}} < 32.2^\circ$ or $124.6^\circ < \theta_{\text{lab}} < 139.3^\circ$
  - not an ECL 3D Bhabha
- `lml4`
  - at least one cluster with $E_{\text{CM}} \geq 2$ GeV, $\theta_{\text{id}} = 1$ or $17 \equiv 12.4^\circ < \theta_{\text{lab}} < 154.7^\circ$
  - not an ECL 3D Bhabha
- `lml6`
  - only one cluster with $E_{\text{CM}} \geq 1$ GeV, $4 \leq \theta_{\text{id}} \leq 15 \equiv 32.2^\circ < \theta_{\text{lab}} < 128.7^\circ$
  - no other cluster with $E_{\text{lab}} \geq 300$ MeV anywhere
- `lml7`
  - only one cluster with $E_{\text{CM}} \geq 1$ GeV, $\theta_{\text{id}} = 2, 3$ or $16 \equiv 18.5^\circ < \theta_{\text{lab}} < 31.9^\circ$ or $128.7^\circ < \theta_{\text{lab}} < 139.3^\circ$
  - no other cluster with $E_{\text{lab}} \geq 300$ MeV anywhere
- `lml8`
  - two clusters with $170^\circ < \Delta\phi_{CM} < 190^\circ$ and $E_{\text{lab}} > 250$ MeV
  - no other cluster with $E_{\text{CM}} \geq 2$ GeV anywhere
- `lml9`
  - two clusters with $170^\circ < \Delta\phi_{CM} < 190^\circ$
  - one cluster with $E_{\text{lab}} > 250$ MeV, the other with $E_{\text{lab}} < 250$ MeV
  - no other cluster with $E_{\text{CM}} \geq 2$ GeV anywhere
- `lml10`
  - two clusters with $160^\circ < \Delta\phi_{CM} < 200^\circ$ and $160^\circ < \Sigma\theta_{CM} < 200^\circ$

  - no other cluster with $E_{\text{CM}} \geq 2$ GeV anywhere

- `lml12` (tighter selection of lml0)
  - $N_{\text{cluster}} \geq 3$, one with $E_{\text{lab}} > 500$ MeV
  - $2 \leq \theta_{\text{id}} \leq 16 \equiv 18.5^\circ < \theta_{\text{lab}} < 139.3^\circ$
  - not an ECL 3D Bhabha

- `lml13`
  - only one cluster with $E_{\text{CM}} \geq 0.5$ GeV, $6 \leq \theta_{\text{id}} \leq 11$
  - no other cluster with $E_{\text{lab}} \geq 300$ MeV anywhere

Where the variable θ_{id} is an identifier used to categorize the polar angle in the lab frame θ_{lab} of the cluster into discrete angular bins. Specifically, the full range of the polar angle is divided into 16 segments, and $\theta_{\text{id}} \in \{1, 2, \ldots, 16\}$ indicates which segment the particle falls into. This binning facilitates angular-dependent analysis by simplifying the continuous variable θ_{lab} into a manageable discrete index.
All the listed trigger bits, except for `lml0`, `lml1`, `lml2`, `lml12` and `lml13`, were not prescaled and active during the entire data-taking period. `lml0`, `lml1` and `lml2` have a prescale of 10 since part of experiment 20, which corresponds to a significant fraction of the entire dataset. Instead, `lml12` and `lml13` were not active before experiment 10.
At least one of the mentioned trigger bits is required to be active in data and MC.

5.5.3.1 Trigger efficiency

Trigger efficiencies are studied using orthogonal trigger lines, CDC-related trigger (`stt`, `ffo`, `fyo`, `fso` and `ffy`), as follows:

$$\epsilon_{\text{ECL-triggers}} = \frac{\text{(CDC ref-triggers) and (ECL-triggers)}}{\text{CDC ref-triggers}} \tag{5.5}$$

$$\epsilon_{\text{CDC-triggers}} = \frac{\text{(ECL-triggers) and (CDC-triggers)}}{\text{ECL-triggers}} \tag{5.6}$$

The CDC trigger lines are defined as follows:

- `stt` (only active since experiment 17)
  - Number of Neuro 3D tracks ≥ 1
  - $|z| < 15$ cm
  - $p > 0.7$ GeV
  - Not an ECL 3D Bhabha

- `ffo` (prescale 100 since experiment 17)
  - number of full 2D tracks ≥ 2
  - $r - \phi$ opening angle $> 90^\circ$
  - Not an ECL 3D Bhabha

- `fyo` (only active since experiment 12)
  - number of full 2D tracks ≥ 1
  - Number of Neuro 3D tracks ≥ 1
  - $r - \phi$ opening angle $> 90°$
  - Not an ECL 3D Bhabha
- `fso` (only active since experiment 12 and prescale 100 since experiment 17)
  - number of full 2D tracks ≥ 1
  - number of reduced 2D tracks ≥ 1
  - $r - \phi$ opening angle $> 90°$
  - not an ECL 3D Bhabha
- `ffy`
  - number of full 2D tracks ≥ 2
  - Number of Neuro 3D tracks ≥ 1
  - Not an ECL 3D Bhabha

In Fig. 5.10 we show the efficiency of each of the aforementioned ECL trigger bits in data and the logical `OR` combination used as the final trigger selection. The efficiency is shown for the e-channel and the μ-channel after applying all the pre-selection criteria. We also want to examine the CDC trigger bits used to define the reference sample. The CDC triggers efficiency is shown in Fig. 5.11 for the e-channel and the μ-channel separately. The experiment dependence of the efficiency for the logical OR of the ECL (CDC) triggers is shown in Fig. 5.12 (5.13) for the e-channel and μ-channel separately. The horizontal lines show the trigger efficiencies in TSIM, which are in good agreement for all the run periods. The overlayed (grey) histogram shows the event yields for each experiment number. After reconstruction and preselection, the relative trigger efficiency on data (MC) is 99.0% (98.1%) for the electron channel and 89.7% (89.9%) for the muon channel. Given the excellent agreement between the data and the simulated trigger efficiency, no additional correction is applied to the MC yields. Potential systematic uncertainties related to the trigger will be discussed in Chapter 6.

5.5.4 Data-MC correction factors

To achieve good agreement between data and MC simulation, several correction factors must be applied to the Belle II MC samples. These corrections compensate for differences in detector response, reconstruction efficiencies, and particle identification performance that are not perfectly modeled in the simulation. Examples include corrections for tracking efficiency, PID efficiencies for charged pions and kaons, and photon reconstruction efficiencies. Applying these data-driven corrections ensures a more accurate estimation of signal yields and background contributions.

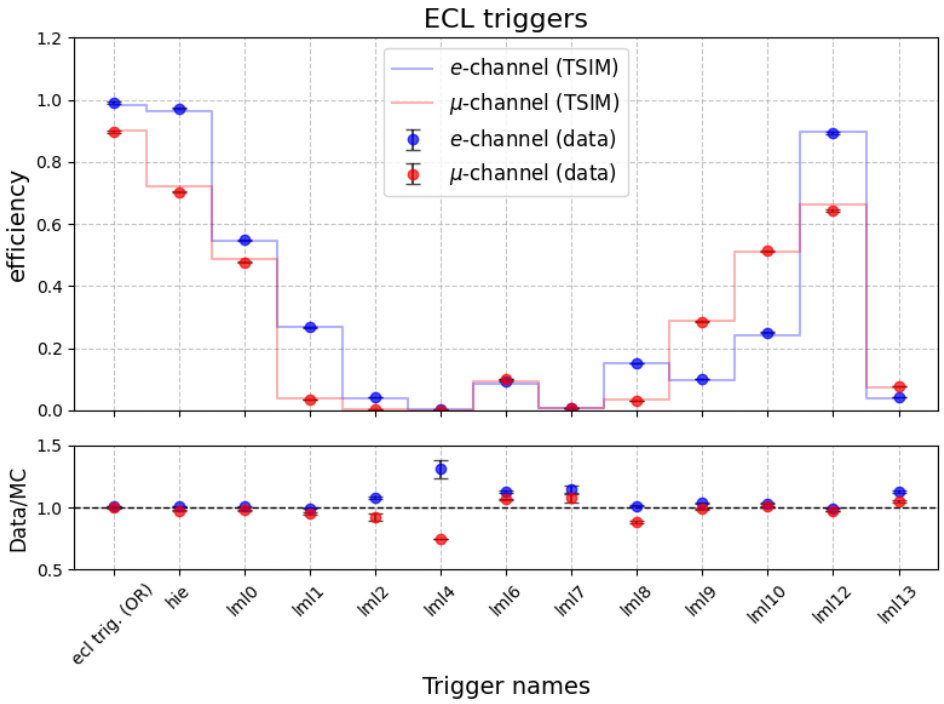

Figure 5.10: The trigger efficiency for the logical OR (first bin) and all ECL trigger bits in data, both for the e-channel (blue) and the μ-channel (red). The overlayed histogram shows the trigger efficiencies in TSIM. The bottom plot show the data/MC ratio.

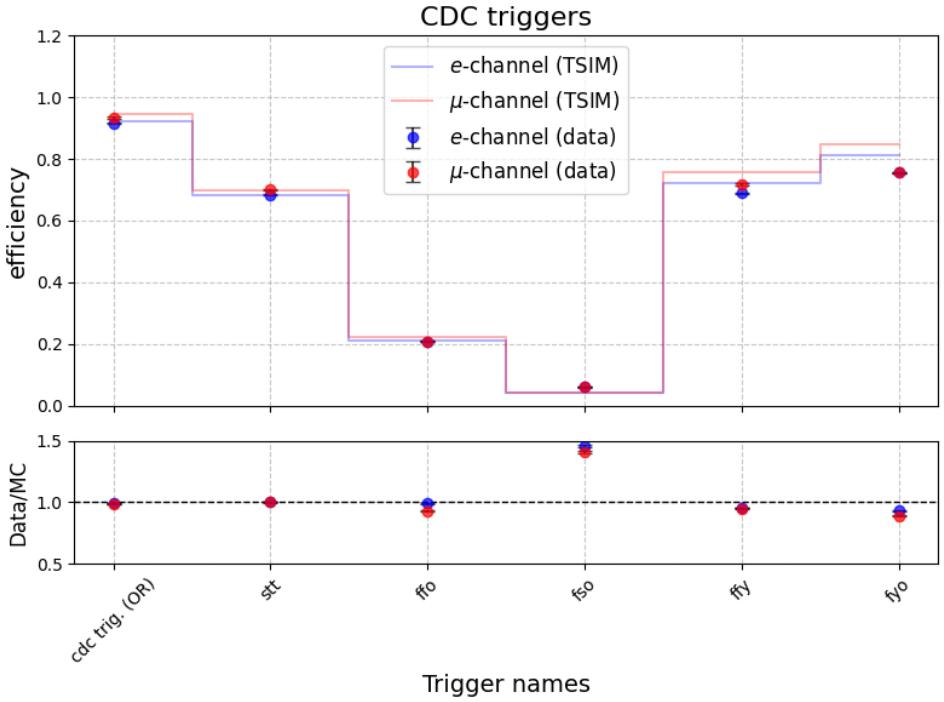

Figure 5.11: The trigger efficiency for the logical OR (first bin) and all CDC trigger bits in data, both for the e-channel (blue) and the μ-channel (red). The overlayed histogram shows the trigger efficiencies in TSIM. The bottom plot show the data/MC ratio.

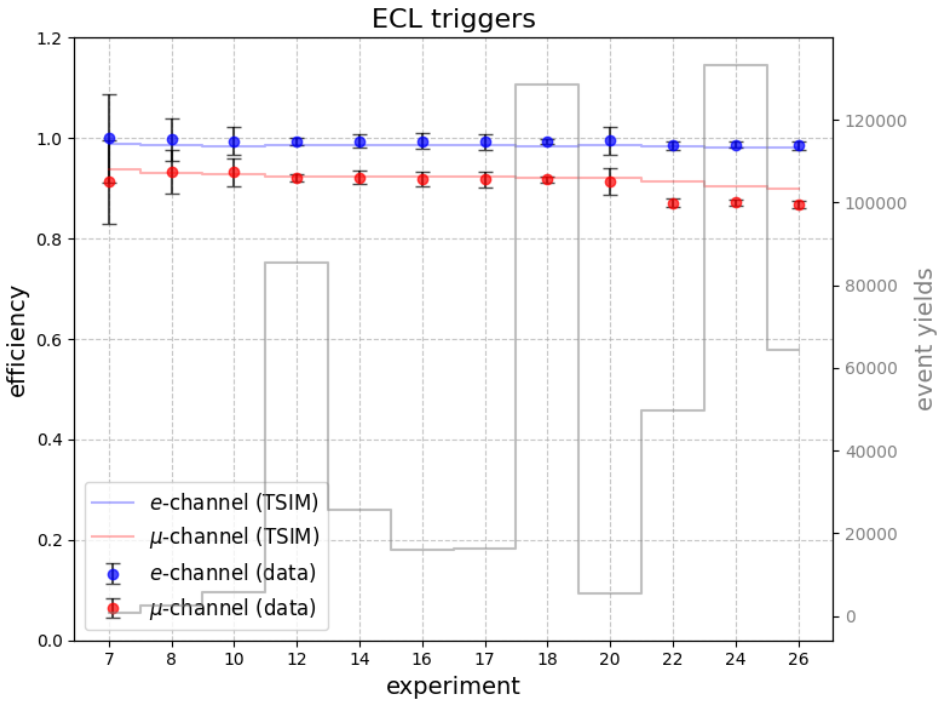

Figure 5.12: The trigger efficiency of the logical OR of the ECL trigger bits in data, split according to experiment number, both for the e-channel (blue) and the μ-channel (red). The overlayed (grey) histogram shows the event yields in the respective bins, and the horizontal lines show the trigger efficiencies in TSIM.

5.5.4.1 Lepton Identification Weights

Lepton identification variables play an important role in this analysis, specifically applied offline to the 1-prong tag-side track. As discussed in Section 5.5.1, electron and muon identification are performed using particle identification (PID) variables based on boosted decision trees (BDT) or likelihood methods, with a selection cut of 0.99 applied for both lepton species. As detailed in Section 3.7.1, data-driven correction weights derived from official lepton identification performance studies are applied to the simulation to account for differences between data and Monte Carlo.

Table 5.4 summarizes the application of these correction factors for various tag-side particle hypotheses, identified via MC truth matching.

5.5.4.2 Kaon ID cut

As explained in Section 5.2, the decay $\tau^- \to K^- K^0_S(\geq 0\pi^0)\nu_\tau$ will also be regarded as a signal decay; however, it will be suppressed by a charged kaon PID veto. The charged kaon PID veto is in place because the sign of the CP asymmetry expected from the $\tau^- \to K^- K^0_S(\geq 0\pi^0)\nu_\tau$ will be opposite to that of $\tau^- \to \pi^- K^0_S(\geq 0\pi^0)\nu_\tau$. This will result in a dilution of the overall CP asymmetry.

We apply a kaon ID veto at a threshold of 0.1. According to the official recommended procedure, corrections must be computed specifically for the cut applied to the sample, and the

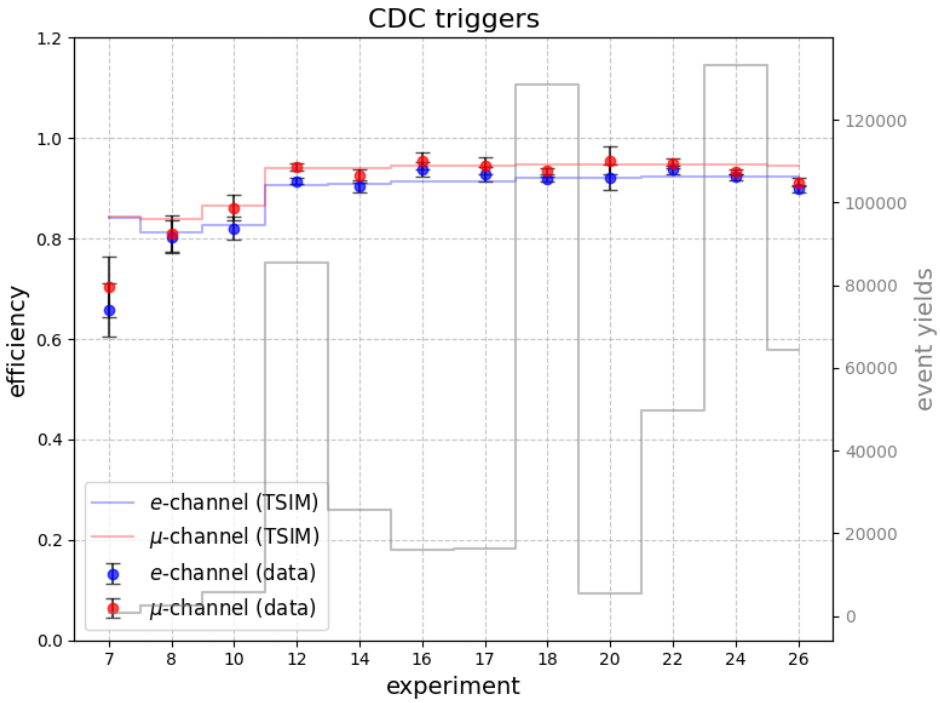

Figure 5.13: The trigger efficiency the logical OR of the CDC trigger bits in data, split according to experiment number, both for the e-channel (blue) and the μ-channel (red). The overlayed (grey) histogram shows the event yields in the respective bins, and the horizontal lines show the trigger efficiencies in TSIM.

e-channel			
t = e	t = π	t = K	t != [e, π, K]
lepton_elID_eff	lepton_elID_fake_pi	lepton_elID_fake_K	1
μ-channel			
t = μ	t = π	t = K	t != [μ, π, K]
lepton_muID_eff	lepton_muID_fake_pi	lepton_muID_fake_K	1

Table 5.4: Application of leptonID corrections for the various cases of tag-side particles, where t stands for tag-side track.

corresponding weights should be obtained using the official tool, named Systematics Framework [41], provided in basf2.

5.5.5 Preselection results

The event yields and fractions, after all preselection criteria for electron and muon tagged samples and all corrections in place, are presented in Tables 5.5 and 5.6 respectively.
At this stage of the analysis, the signal purity is 82.58% and 83.56% for the electron and muon channel respectively. Purity is defined as

$$\mathrm{p} = \frac{N_{\mathrm{sig}}}{N_{\mathrm{sig}} + N_{\mathrm{bkg}}}, \tag{5.7}$$

Type	Events	% MC
Data	216258 ± 465	
MC	213754 ± 347	100
Signal	176513 ± 211	82.58 ± 0.17
$\tau^- \to \pi^- K^0_S(\geq 0\pi^0)\nu_\tau$	137000 ± 186	64.09 ± 0.14
$\tau^- \to K^- K^0_S(\geq 0\pi^0)\nu_\tau$	6883 ± 42	3.22 ± 0.02
$\tau^- \to \pi^- K^0 \bar{K}^0(\geq 0\pi^0)\nu_\tau$	32630 ± 90	15.27 ± 0.05
Background	37240 ± 276	17.42 ± 0.13
τ background	26297 ± 81	12.30 ± 0.04
ee	6816 ± 260	3.19 ± 0.12
$q\bar{q}$	3213 ± 30	1.50 ± 0.01

Table 5.5: Number of events and fraction in MC for electron channel after preselection criteria and data/MC corrections. Errors are statistical only. MC has been scaled to data luminosity. Only main background contributions are shown

Type	Events	% MC
Data	176093 ± 420	
MC	183597 ± 212	100
Signal	153410 ± 192	83.56 ± 0.14
$\tau^- \to \pi^- K^0_S(\geq 0\pi^0)\nu_\tau$	117496 ± 168	64.00 ± 0.12
$\tau^- \to K^- K^0_S(\geq 0\pi^0)\nu_\tau$	6132 ± 38	3.34 ± 0.02
$\tau^- \to \pi^- K^0 \bar{K}^0(\geq 0\pi^0)\nu_\tau$	29803 ± 85	16.23 ± 0.05
Background	30188 ± 90	16.44 ± 0.05
τ background	23363 ± 75	12.72 ± 0.04
$q\bar{q}$	6078 ± 42	3.31 ± 0.02

Table 5.6: Number of events and fraction in MC for muon channel after preselection criteria and data/MC corrections. Errors are statistical only. MC has been scaled to data luminosity. Only main background contribution details are shown.

where N_{sig} is the number of selected signal events and N_{bkg} is the number of background events. The background is mainly dominated by the τ background in both channels, where one τ decays into final states different from the signal decay $\tau^- \to h^- K^0_S \nu_\tau(\geq 0\pi^0)$, but can mimic the signal due to similar particle content or reconstruction ambiguities. For example, τ decays with additional kaons or pions, or with different neutral particle multiplicities can contaminate the sample if misidentified. Besides this, smaller backgrounds arise from QED processes such as e^+e^- scattering and from continuum $q\bar{q}$ hadronic events, which occasionally produce similar final states through hadronization or misidentification. The signal efficiency is defined as

$$\varepsilon_{\text{sig}} = \frac{N_{\text{sig}}}{2 \cdot \mathcal{B}_{\text{sig}} \cdot \mathcal{B}_{\text{tag}} \cdot N_{\tau\tau}}, \tag{5.8}$$

with $\mathcal{B}_{\text{sig}}$ being the branching fraction of the signal τ decays, $\mathcal{B}_{\text{tag}}$ the total branching fraction of the tag side τ decays and $N_{\tau\tau}$ the total number of generated τ-pair events. Only the final efficiency values after the full event selection are reported in Table 5.13.

5.5.6 Background suppression

To suppress the dominant background contributions from $\tau^+\tau^-$, $q\bar{q}$, and, in the electron tag channel, e^+e^- processes, we employ a MVA technique. These backgrounds remain significant after the preselection criteria and can closely mimic the signal topology. The MVA is trained to exploit subtle differences in event kinematics and topology between signal and background in order to enhance signal purity.
Multivariate analysis methods using classification machine learning algorithms aim to recognize patterns in data for classification. During the learning phase, these methods develop a recognition algorithm that can subsequently be applied to similar datasets. The output, often referred to as a classifier, represents the classification of events as a continuous value between 0 and 1.
To accomplish this, three key inputs are required: datasets of events for training and testing the MVA method, features that characterize these events, and computational settings specific to the chosen method, known as hyperparameters.
Several methods can be considered. For this analysis, we opted for a Boosted Decision Tree (BDT) from the `LightGBM` implementation [81]. A distinctive feature of this BDT is that the decision trees are grown leaf-wise rather than level-wise. Instead of setting a maximum depth, the maximum number of leaves is defined as a hyperparameter.
We opted for a two-step BDT approach, allowing the MVA to focus on a specific type of background at each step. For both steps, we divide the sample into one test and one training part, and decided to split as 25% and 75% respectively.
The hyperparameters are first set to default as to mitigate the overtraining effects that can occur if the BDT method is too specific. As a second step, we decide to optimize the hyperparameters using the library `Optuna` [82]. As the optimized hyperparameters yielded poorer performance than the default configuration, the default settings were retained.
The BDT selection is relying on distribution shapes defined by the features that are used as input. As we aim at providing the BDT with features that describe real data as accurately as possible, we have to feed the BDT with weights that translate the luminosity of each sample, but also all the corrections (refer to Section 5.5.4) applied offline. Therefore, we ensure that the selection trained on MC will be as reproducible on data as possible.
For the first step of the two-step BDT, we used event-based variables to discriminate the $q\bar{q}$ and ee backgrounds from $\tau\tau$ (background + signal) sample. This first-step BDT was performed separately for the electron and muon channels, as it was shown that this approach produces better results than the combined case. This is likely because the primary non-$\tau\tau$ background contributions differ between the two channels, making a dedicated BDT for each tagged sample more effective.
The 7 features that are considered as input of the first step BDT method are detailed in Table 5.7. Their distributions are displayed in Fig. 5.14 and 5.15 respectively for the electron an muon channel.

The receiver operating characteristics (ROC) curve illustrates graphically the classification ability of a BDT [83]. More precisely, it is the area under the curve (AUC), normalised to unity, that assesses this measurement. An excellent classification has an AUC close to 1, while a poor one has an AUC close to 0. The AUC value of 0.5 represents a classification made randomly.

Implementation	Feature	Description
`thrust`	thrust	mathematically defined in Eq. 5.1, corresponds to the measurement of the collimation or alignment of final-state particles produced in a collision
`visibleEnergyOfEvent_CMS`	$E^{\mathrm{CM}}_{\mathrm{visible}}$	visible energy in the CMS
`missingMass2OfEvent`	m^2_{missing}	missing mass squared
`missingMomentumOfEventCMS`	$p^{\mathrm{CM}}_{\mathrm{missing}}$	missing momentum in the CMS
`missingMomentumOfEventCMS_theta`	$\theta^{\mathrm{CM}}_{\mathrm{missing}}$	polar angle of the missing momentum in the CMS
`track_1prong_p`	$p_{\text{1-prong}}$	momentum of the track in the tag side
`track_1prong_theta`	$\theta_{\text{1-prong}}$	polar angle of the track in the tag side

Table 5.7: Features used as input of the first-step BDT

In our case, we obtain an AUC equal to 0.917 and 0.931 for the electron and muon channel respectively, as represented in Fig. 5.16. Overtraining, often called overfitting, occurs when the complexity of a model is so high that it reproduces every single feature of the specific data set used for training, and therefore computes a not necessarily reproducible fit. Some BDTs are more likely to experience over-training, but the general consensus is that simplified models can prevent this issue during the training phase. The application of the BDT on a test set allows a verification of its reproducibility. If a notable difference arises in the comparison of the BDT performance on the test and training sets, it indicates that overtraining is occurring. In this analysis, as shown in Fig. 5.17, the BDT response distributions for the training and test sets are in good visual agreement. No such discrepancies are observed, indicating that overtraining is not evident within the statistical precision of the samples used. The BDT output distributions are shown in Fig. 5.18. The selection of an optimal cut on the BDT output is essential. One approach involves evaluating the Figure Of Merit (FOM) with varying penalty factors on the background, but this method exclusively considers the statistical aspects of the sample and does not account for systematic uncertainties. o address this, a scan over a range of BDT output cut values was performed. For each value, we assessed the signal efficiency and the background composition using MC truth information. Additionally, we carried out a preliminary estimation of systematic uncertainties associated with each cut value, including contributions from background modeling, particle identification, and reconstruction effects. The final cut was selected to ensure a favorable trade-off between high signal purity and manageable systematic uncertainty, forming the basis for further optimization in the final analysis. Based on these studies, a BDT output threshold of 0.8 was selected and applied for both channels. After applying the cut on the first BDT output, the new number of events and fractions of MC are shown in Table 5.8

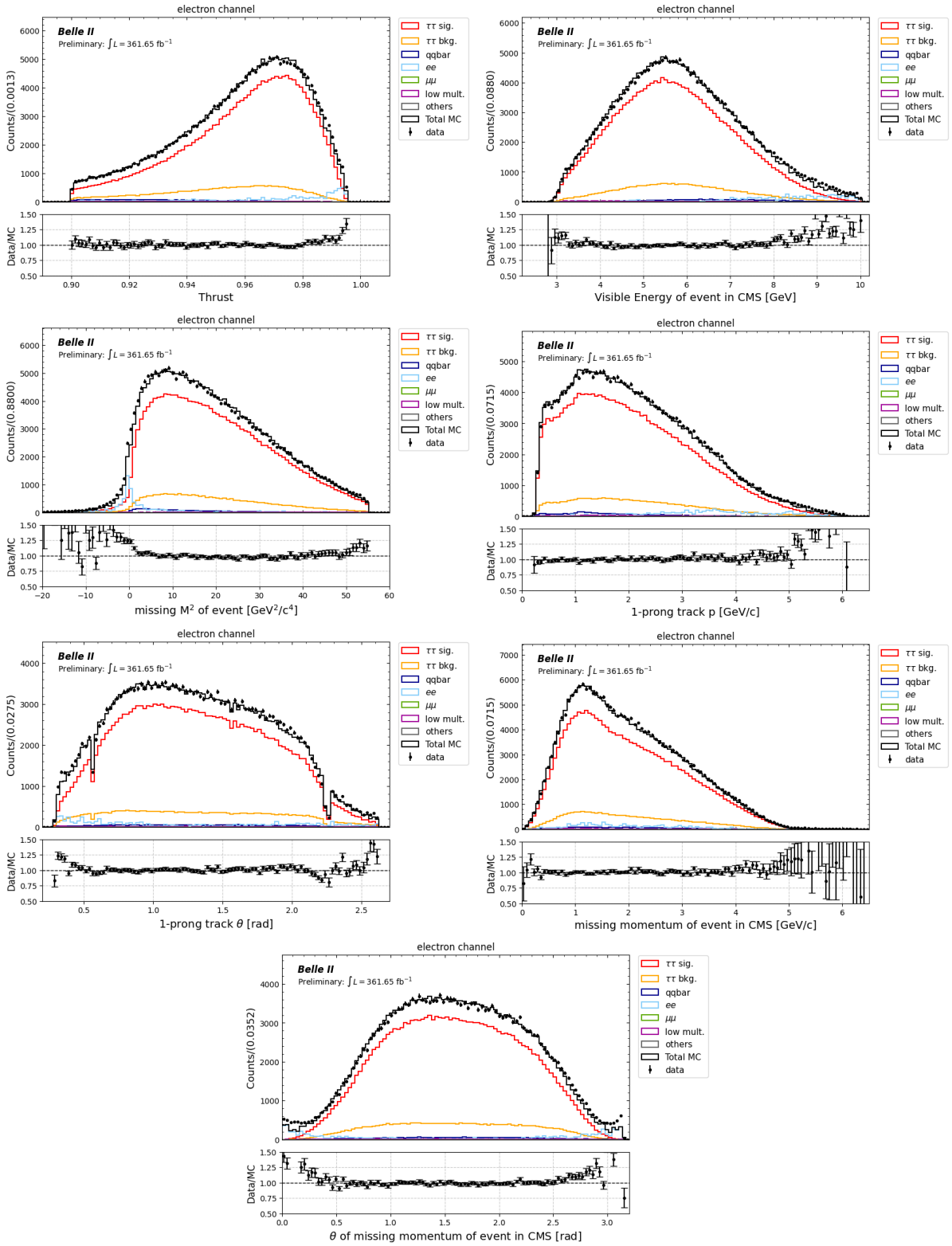

Figure 5.14: Features used as first step BDT input for the electron channel, after the whole preselection and corrections applied, including the use of the LID weights.

and 5.9 for the electron and muon channel respectively.

In the second step of the two-step BDT, we primarily used K^0_S-based variables to discriminate

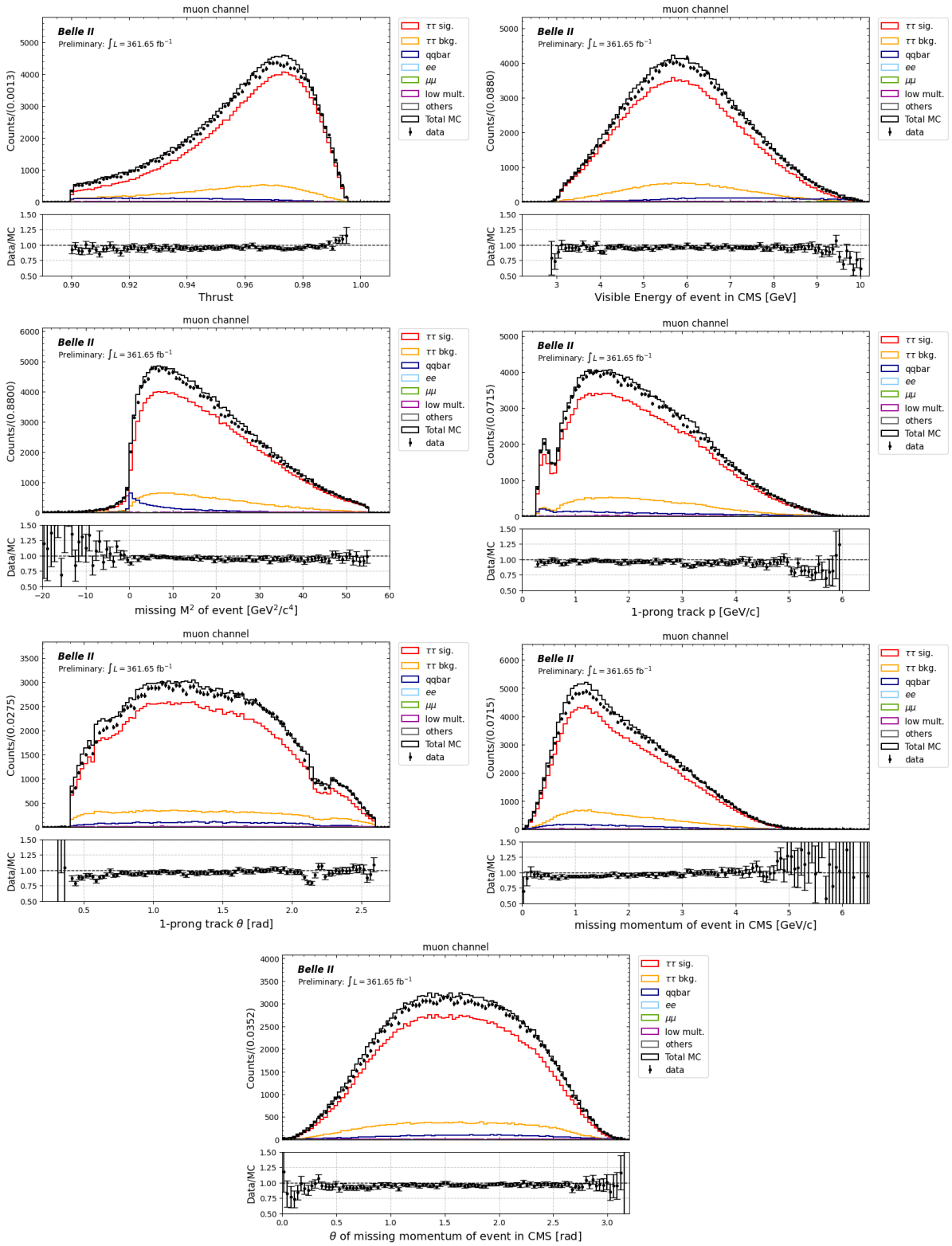

Figure 5.15: Features used as first step BDT input for the muon channel, after the whole preselection and corrections applied, including the use of the LID weights.

the $\tau\tau$ background from the $\tau\tau$ signal decays. The first-step BDT combines the electron and muon channels, as the $\tau\tau$ background is expected to have similar phase-space distributions and features in both channels. This approach also improves the BDT training by increasing the avail-

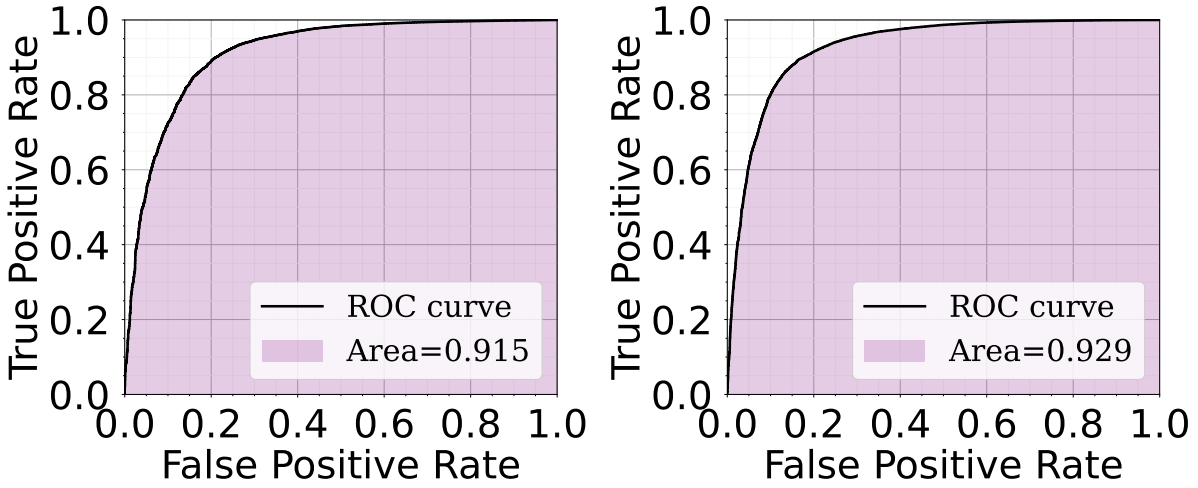

Figure 5.16: ROC curve associated to the first step BDT method employed for the electron (left) and muon (right) channel. The area under the curve (AUC) is equal to 0.917 (electron) and 0.931 (muon).

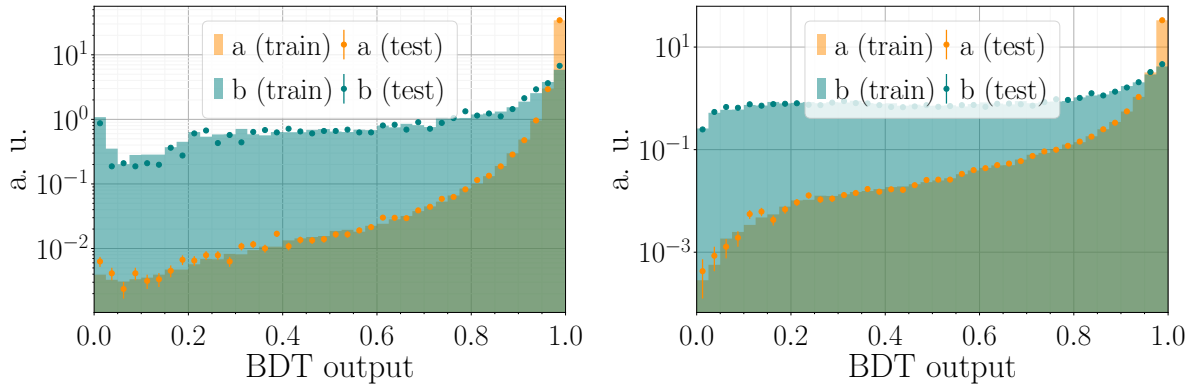

Figure 5.17: Signal (orange) and background (blue) data sets divided into test and training sets for the electron (left) and muon (right) channel. The method is solely trained using the training set, and is applied on the test set to see if the method is reproducible.

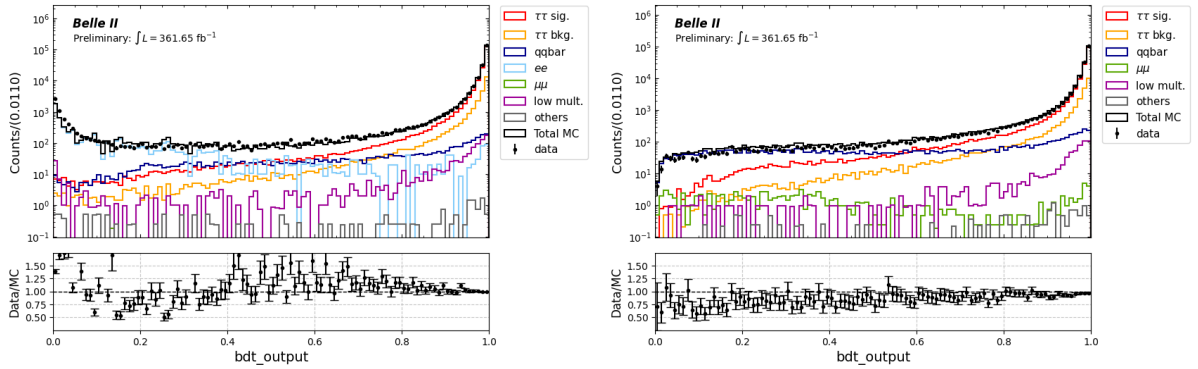

Figure 5.18: First step BDT output distributions for electron (left) and muon (right) channel, in logarithmic y-axis scales.

able statistics. The 28 features that are considered as input of the second step BDT method

Type	Events	% MC
Data	202758 ± 450	
MC	202500 ± 237	100
Signal	174257 ± 209	86.05 ± 0.14
$\tau^- \to \pi^- K^0_S (\geq 0\pi^0)\nu_\tau$	135160 ± 184	66.75 ± 0.12
$\tau^- \to K^- K^0_S (\geq 0\pi^0)\nu_\tau$	6768 ± 41	3.34 ± 0.02
$\tau^- \to \pi^- K^0 \bar{K}^0 (\geq 0\pi^0)\nu_\tau$	32329 ± 90	15.96 ± 0.05
Background	28243 ± 110	13.95 ± 0.06
τ background	25449 ± 80	12.57 ± 0.04
ee	465 ± 68	0.23 ± 0.03
$q\bar{q}$	1581 ± 21	0.78 ± 0.01

Table 5.8: Number of events and fraction in MC for electron channel after first step BDT cut. Errors are statistical only. MC has been scaled to data luminosity. Only main background contribution details are shown

Type	Events	% MC
Data	169134 ± 411	
MC	175517 ± 206	100
Signal	150318 ± 190	85.64 ± 0.15
$\tau^- \to \pi^- K^0_S (\geq 0\pi^0)\nu_\tau$	115006 ± 166	65.52 ± 0.12
$\tau^- \to K^- K^0_S (\geq 0\pi^0)\nu_\tau$	5976 ± 38	3.40 ± 0.02
$\tau^- \to \pi^- K^0 \bar{K}^0 (\geq 0\pi^0)\nu_\tau$	29355 ± 84	16.72 ± 0.05
Background	25199 ± 81	14.36 ± 0.05
τ background	22306 ± 73	12.71 ± 0.04
$q\bar{q}$	2328 ± 25	1.33 ± 0.01

Table 5.9: Number of events and fraction in MC for muon channel after first step BDT cut. Errors are statistical only. MC has been scaled to data luminosity. Only main background contribution details are shown.

are detailed in Table 5.10. Their distributions are displayed in Fig. 5.19 and for the combined electron an muon channel.

Implementation	Feature	Description
`track_kshort_p`, `track_kshort_pt`, `track_kshort_theta`	$p_{K^0_S}$, p_{t,K^0_S}, $\theta_{K^0_S}$	momentum, transverse momentum and polar angle of the K^0_S
`track_pi_kshort_p`, `track_pi_kshort_pt`, `track_pi_kshort_theta`	$p_{\pi(\mathrm{sig})}$, $p_{t,\pi(\mathrm{sig})}$, $\theta_{\pi(\mathrm{sig})}$	momentum, transverse momentum and polar angle of the prong track in the signal side
`kshort_track1_p`, `kshort_track1_pt`, `kshort_track1_theta`	p_{track1}, $p_{t,\mathrm{track1}}$, θ_{track1}	momentum, transverse momentum and polar angle of the first track (positive/negative charged track with highest momentum for positive/negative events) coming from K^0_S decay
`kshort_track2_p`, `kshort_track2_pt`, `kshort_track2_theta`	p_{track2}, $p_{t,\mathrm{track2}}$, θ_{track2}	momentum, transverse momentum and polar angle of the second track (negative/positive charged track for postive/negative events) coming from K^0_S decay
`kshort_track_leadpt`, `kshort_track_subpt`	$p_{t,\mathrm{lead}}$, $p_{t,\mathrm{sub}}$	leading and subleading transverse momentum of the two tracks coming from K^0_S decay
`track_kshort_significanceOfDistance`, `track_kshort_flightDistance`, `track_kshort_distance`	$S^{\mathrm{distance}}_{K^0_S}$, $d^{\mathrm{flight}}_{K^0_S}$, $d^{\mathrm{3D}}_{K^0_S}$	significance of distance, flight distance and 3D distance between the IP and the K^0_S decay vertex.
`track_kshort_daughter1DecayAngle`, `track_kshort_daughter2DecayAngle`	$\theta_{K^0_S-track1}$, $\theta_{K^0_S-track2}$	angle in the K^0_S's rest frame between the reverted CMS momentum vector and the direction of the i-th daughter
`track_kshort_cosHelicityAngleMomentum`	$\cos\theta^p_h$	cosine of the angle between the line defined by the momentum difference of the two daughters in the frame of the K^0_S and the momentum of the K^0_S in the lab frame.

Implementation	Feature	Description
`kshort_track1_dr`, `kshort_track1_dz`, `kshort_track2_dr`, `kshort_track2_dz`	dr_{track1}, dz_{track1}, dr_{track2}, dz_{track2}	absolute value of the distance to the point-of-closest-approach (POCA) in the $r-\phi$ plane and POCA in the z direction with respect to IP for the i-th track coming from K^0_S decay

Table 5.10: Features used as input of the second-step BDT

The ROC curve and the comparison of BDT performance on the test and training sets are presented in Fig. 5.20. In this case as well, no significant differences are observed between the training and test sets. Second step BDT output distribution is shown in Fig. 5.21 where a cut at 0.95 is chosen maximizing the following FOM:

$$\text{FOM} = \frac{N_{\text{sig}}}{\sqrt{N_{\text{sig}} + 100 N_{\text{bkg}}}} \tag{5.9}$$

After applying the cut on the first BDT output, the new number of events and fractions of MC are shown in Table 5.11 and 5.12 for the electron and muon channel respectively.

Type	Events	% MC
Data	142149 ± 377	
MC	145797 ± 192	100
Signal	143966 ± 190	98.74 ± 0.18
$\tau^- \to \pi^- K^0_S (\geq 0\pi^0)\nu_\tau$	113525 ± 169	77.86 ± 0.15
$\tau^- \to K^- K^0_S (\geq 0\pi^0)\nu_\tau$	3905 ± 31	2.68 ± 0.02
$\tau^- \to \pi^- K^0 \bar{K}^0 (\geq 0\pi^0)\nu_\tau$	26536 ± 82	18.20 ± 0.06
Background	1831 ± 26	1.26 ± 0.02
τ background	746 ± 14	0.51 ± 0.01
$q\bar{q}$	857 ± 16	0.59 ± 0.01

Table 5.11: Number of events and fraction in MC for electron channel after second step BDT cut. Errors are statistical only. MC has been scaled to data luminosity. Only main background contribution details are shown

After the full selection the signal purity is 98.76% and 98.35% for the electron and muon channel respectively. For completeness, the signal efficiency is evaluated both for the A_1 contribution alone and for the combined $A_1 + A_2 + A_3$ scenario. The corresponding values are summarized in Table 5.13. In Chapter 6 and 7 possible effects of the selection on the measured asymmetry will be discussed.

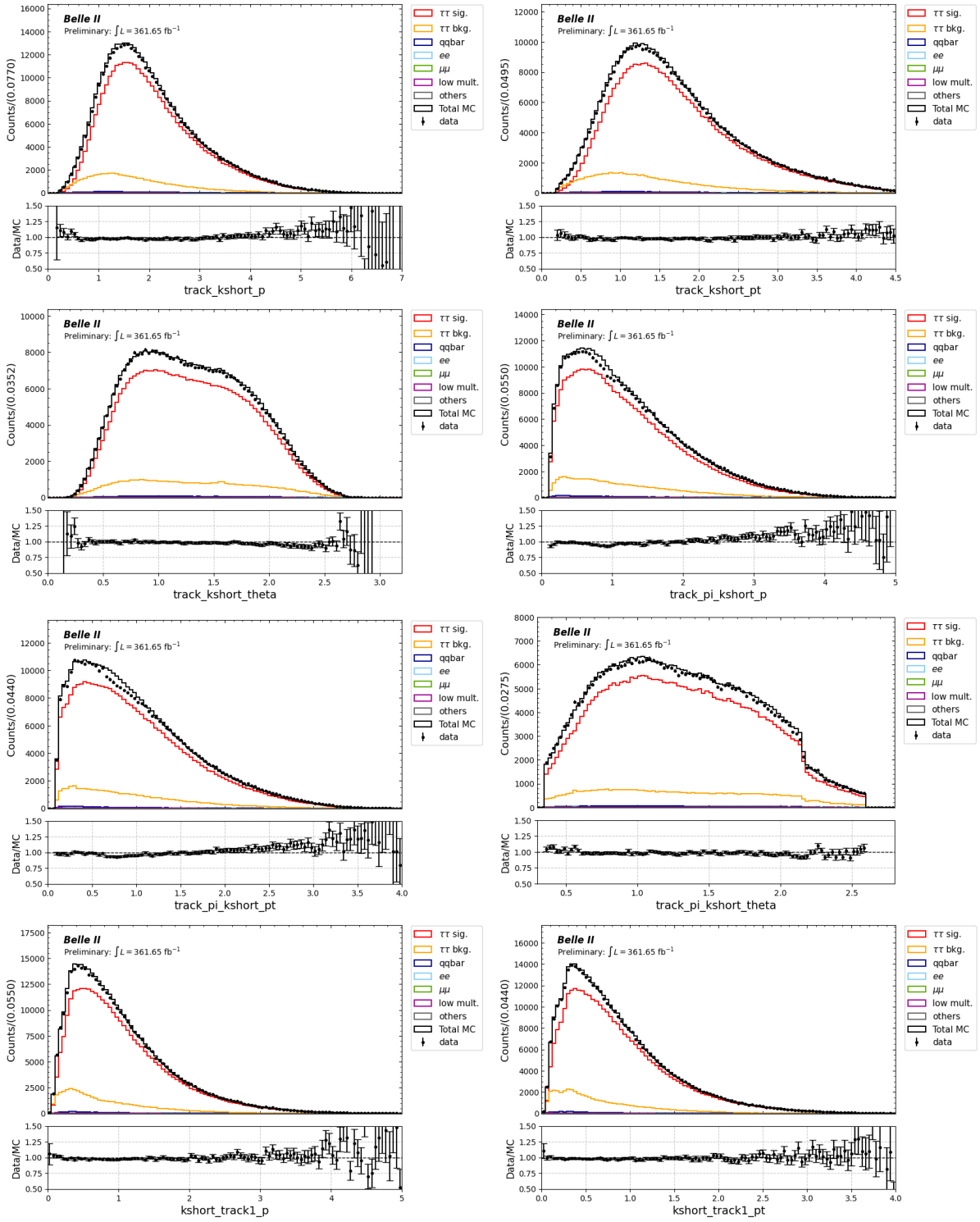

Figure 5.19: Features used as second step BDT input for the combined electron and muon channel, after the preselection, corrections and first step BDT cut applied, including the use of the LID weights (1/3).

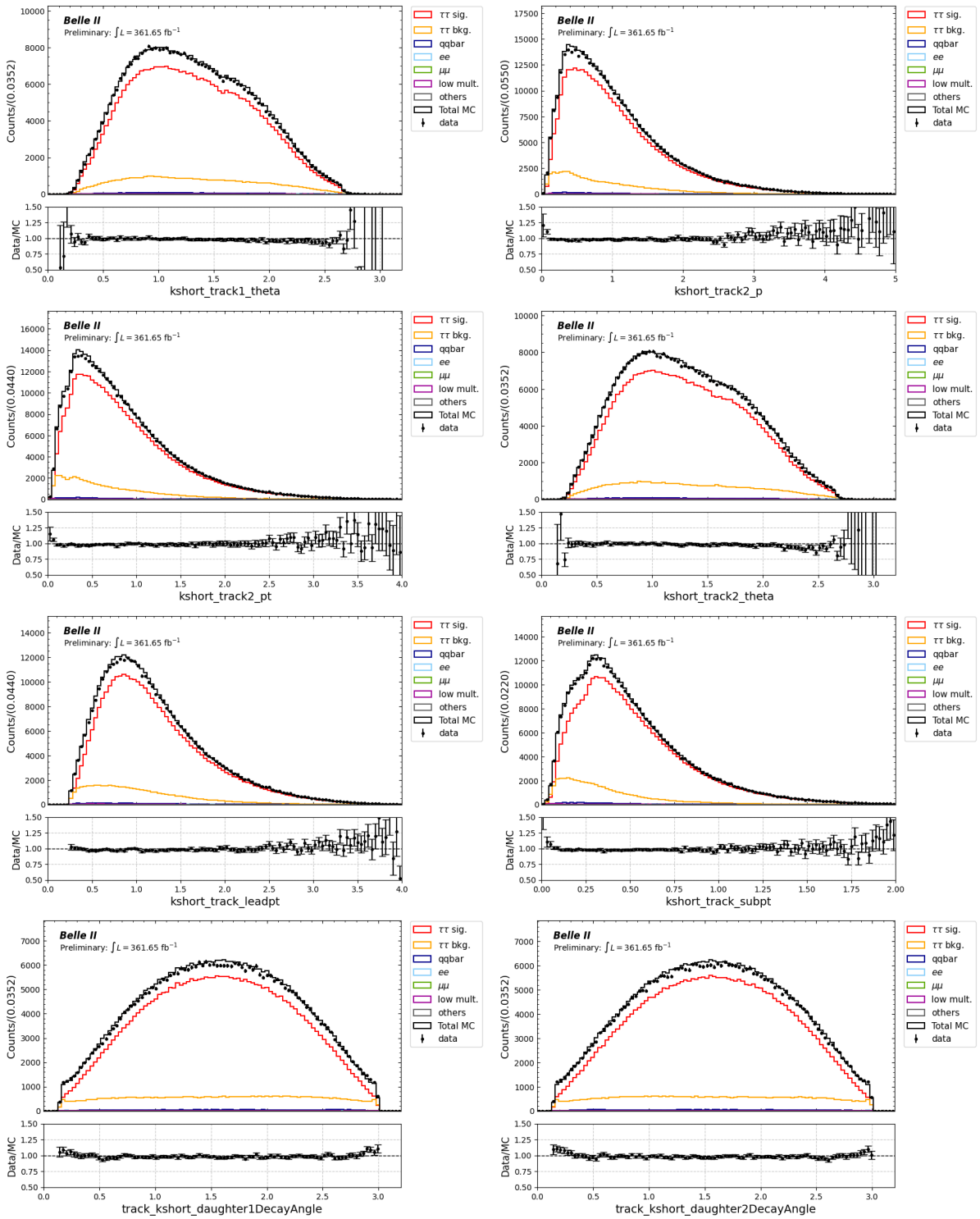

Figure 5.19: Features used as second step BDT input for the combined electron and muon channel, after the preselection, corrections and first step BDT cut applied, including the use of the LID weights (2/3).

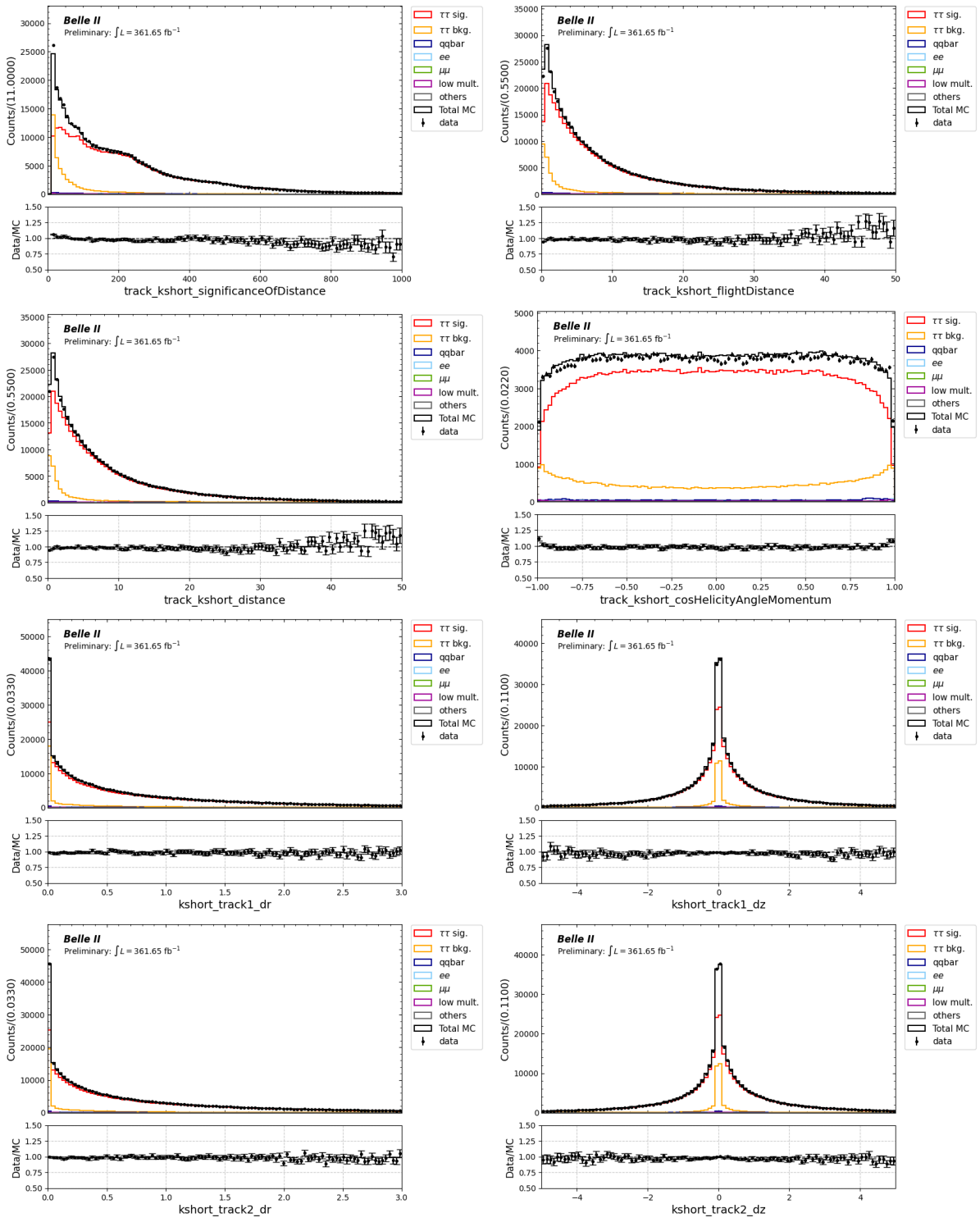

Figure 5.19: Features used as second step BDT input for the combined electron and muon channel, after the preselection, corrections and first step BDT cut applied, including the use of the LID weights (3/3).

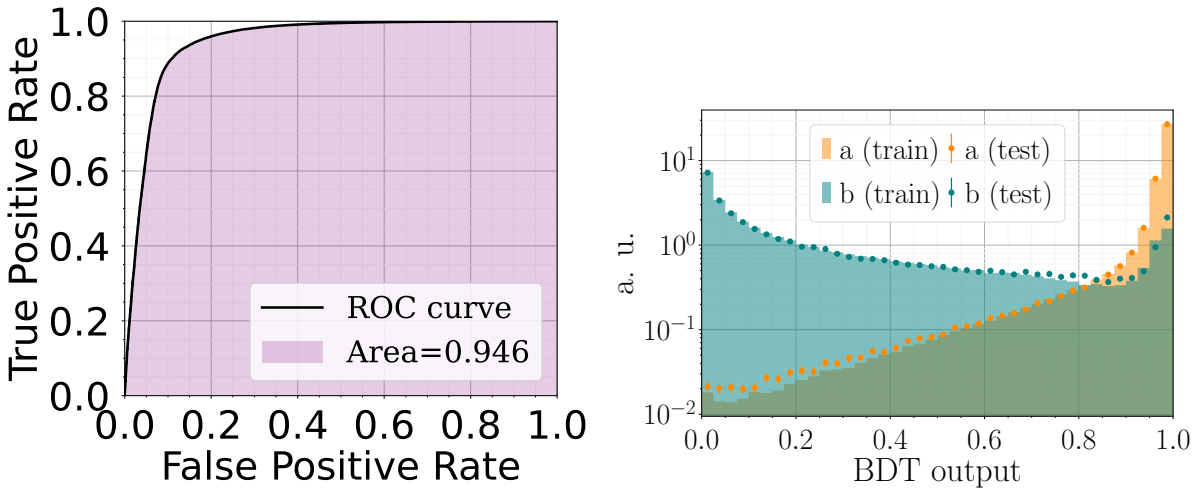

Figure 5.20: On the left, ROC curve associated to the second step BDT method employed for the combined electron and muon tagged sample. The area under the curve (AUC) is equal to 0.947. On the right, signal (orange) and background (blue) data sets divided into test and training sets. The method is solely trained using the training set, and is applied on the test set to see if the method is reproducible.

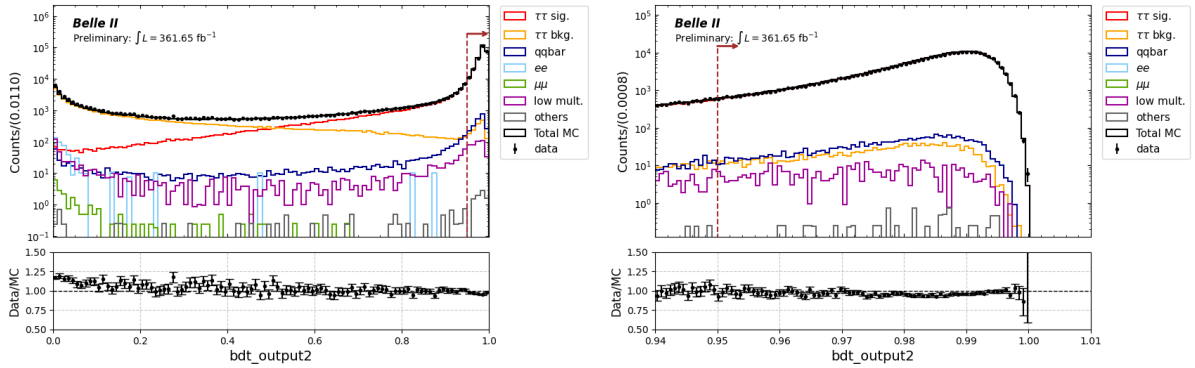

Figure 5.21: On the left, the distribution of the second-step BDT output for the combined electron and muon tagged sample is shown, with a logarithmic y-axis scale covering the full range. On the right, the same distribution is zoomed in on the cut region. The data-MC agreement is nearly perfect. The cut requirement is reported in red

Type	Events	% MC
Data	119950 ± 346	
MC	126872 ± 175	100
Signal	124753 ± 173	98.32 ± 0.19
$\tau^- \to \pi^- K^0_S (\geq 0\pi^0)\nu_\tau$	97232 ± 153	76.63 ± 0.16
$\tau^- \to K^- K^0_S (\geq 0\pi^0)\nu_\tau$	3459 ± 29	2.73 ± 0.02
$\tau^- \to \pi^- K^0 \bar{K}^0 (\geq 0\pi^0)\nu_\tau$	24077 ± 76	18.98 ± 0.07
Background	2125 ± 26	1.68 ± 0.02
τ background	657 ± 13	0.52 ± 0.01
$q\bar{q}$	1285 ± 19	1.01 ± 0.01

Table 5.12: Number of events and fraction in MC for muon channel after second step BDT cut. Errors are statistical only. MC has been scaled to data luminosity. Only main background contribution details are shown.

Decay	Tag	ϵ[%]
A_1	e	7.69
A_1	μ	6.75
A_1	$e + \mu$	7.23
$A_1 + A_2 + A_3$	e	7.01
$A_1 + A_2 + A_3$	μ	6.21
$A_1 + A_2 + A_3$	$e + \mu$	6.60

Table 5.13: Signal efficiencies for different tag modes. Efficiencies are reported separately for the A_1 component and the combined $A_1 + A_2 + A_3$ signal.

Chapter 6

Analysis Method

Measurements of charge-parity-violating decay-rate asymmetries (A_{CP}) are a fundamental goal of the Belle II physics program. In the case of $\tau^{\pm} \to \pi^{\pm} K^0_S \nu_\tau$ decays, A_{CP} is extracted from the difference in the number of reconstructed decay candidates for positive and negative τ leptons. These observed yield asymmetries (A_{raw}) are influenced not only by genuine CP violation but also by various instrumental and physical effects that can introduce charge-dependent biases.
After the selection of signal candidates, the extraction of a genuine CP asymmetry requires careful treatment of these effects, as they can mimic or dilute the true asymmetry. Since A_{CP} is derived from the charge asymmetry between τ^+ and τ^- decays, it is essential to disentangle the genuine CP-violating contribution from other asymmetry sources.
This chapter describes the studies performed to evaluate and correct for the following key contributions:

- **Detection asymmetry**: Arising from charge-dependent reconstruction efficiencies in tracking, particle identification, and K^0_S reconstruction.
- **Neutral kaon-induced asymmetry**: Due to the difference in nuclear interaction cross sections between K^0 and $\bar{K}^0$ in the detector material, which affects the reconstructed K^0_S yield and introduces an apparent asymmetry unrelated to CP violation.
- **Background-induced asymmetries**: From physical or instrumental asymmetries in background processes that may bias the raw asymmetry or dilute the signal.

These corrections are essential to ensure that the final measured asymmetry reflects a potential signal of CP violation in τ decays. Each of these components is discussed in detail in the subsequent sections.

6.1 Raw asymmetry

The yield asymmetry for this analysis can be decomposed into five contributions, as

$$A^{\text{data}}_{\text{raw}}(\tau^{\pm} \to \pi^{\pm} K^0_S \nu) = \frac{N(\tau^+ \to \pi^+ K^0 \bar{\nu}) - N(\tau^- \to \pi^- \bar{K}^0 \nu)}{N(\tau^+ \to \pi^+ K^0 \bar{\nu}) + N(\tau^- \to \pi^- \bar{K}^0 \nu)} \tag{6.1}$$

$$= A_{\text{det}}(\pi^+/\pi^-) + A_{\text{trigger}} + A_{\text{det}}(\text{tag}) + A_{FB} + A(K^0/\bar{K}^0), \tag{6.2}$$

where:

- $A_{\text{det}}(\pi^+/\pi^-)$ is the detection asymmetry of the charged particle candidate in the signal hemisphere and is defined as:

$$A_{\text{det}}(\pi^+/\pi^-) = \frac{\epsilon(\pi^+) - \epsilon(\pi^-)}{\epsilon(\pi^+) + \epsilon(\pi^-)}, \tag{6.3}$$

  where $\epsilon(\pi^+)$ and $\epsilon(\pi^-)$ are the efficiencies to detect and reconstruct a π^+ and a π^-. Differences between $\epsilon(\pi^+)$ and $\epsilon(\pi^-)$ can arise due to two main factors: asymmetries in the detector design and differences in the material interaction rates of particles and their corresponding antiparticles. It is important to note that the actual detection asymmetry highly depends on the particle's kinematics.

- A_{trigger} is the asymmetry due to the different trigger efficiency values for the decay $\tau^+ \to \pi^+ K^0 \bar{\nu}$ and $\tau^- \to \pi^- \bar{K}^0 \nu$.

- $A_{\text{det}}(\text{tag})$ is defined as:

$$A_{\text{det}}(\text{tag}) = \frac{\epsilon(l^+) - \epsilon(l^-)}{\epsilon(l^+) + \epsilon(l^-)}, \tag{6.4}$$

  where $\epsilon(l^+)$ and $\epsilon(l^-)$ are the efficiencies to detect and reconstruct the positive and negative lepton in the tag hemisphere.

- A_{FB} is the forward-backward asymmetry, which arises from the interference between photon and Z^0 boson exchange in the $e^+e^- \to \tau^+\tau^-$ process. The τ^- tends to be emitted in the direction of the incoming electron (forward hemisphere), while the τ^+ tends to go in the direction of the incoming positron (backward hemisphere). If the detector is not perfectly symmetric, this leads to a charge-dependent effect that can contribute to the raw asymmetry.

- $A(K^0/\bar{K}^0)$ represents the asymmetry introduced by the kaon system, defined as:

$$A(K^0/\bar{K}^0) = \frac{\epsilon(K^0) - \epsilon(\bar{K}^0)}{\epsilon(K^0) + \epsilon(\bar{K}^0)}, \tag{6.5}$$

  where $\epsilon(K^0)$ and $\epsilon(\bar{K}^0)$ are the detection efficiencies for K^0 and $\bar{K}^0$, respectively. This asymmetry accounts for effects such as CP violation in the decay $K^0 \to \pi^+\pi^-$, as well as the differing interaction rates (including absorption) of K^0 and $\bar{K}^0$ with the detector material. Additionally, the effects of mixing, CP violation, and absorption interfere due to coherent forward scattering. Therefore, the neutral kaon asymmetry can be expressed as the sum of these three effects:

$$A(K^0/\bar{K}^0) = A_{CP}(K^0/\bar{K}^0) + A_{\text{abs.}}(K^0/\bar{K}^0) + A_{\text{int.}}(K^0/\bar{K}^0). \tag{6.6}$$

  Here, $A_{CP}(K^0/\bar{K}^0)$ is the effect we aim to measure in this analysis. The other contributions included in $A(K^0/\bar{K}^0)$ must be corrected for. While smaller than the asymmetries in charged particle detection, these effects represent a correction that cannot be neglected.

Since our signal sample is made up of multiple decay channels ($\tau^\pm \to \pi^\pm K^0_S \nu(\geq 0\pi^0)$, $\tau^\pm \to K^\pm K^0_S \nu(\geq 0\pi^0)$ and $\tau \to \pi^\pm K^0 \bar{K}^0 \nu(\geq 0\pi^0)$), the decomposition of the raw asymmetry can be applied to each of them.

The decomposition of the raw asymmetry for the $\tau^{\pm} \to K^{\pm}K^0_S\nu$ and $\tau^{\pm} \to \pi^{\pm}K^0_S\nu$ channels is structurally identical, with the only difference being the detection asymmetry associated with the charged hadron. In the $\tau^{\pm} \to \pi^{\pm}K^0_S\nu$ decay, the relevant term is $A_{\text{det}}(\pi^+/\pi^-)$, while for the $\tau^{\pm} \to K^{\pm}K^0_S\nu$ decay it becomes $A_{\text{det}}(K^+/K^-)$, defined as:

$$A_{\text{det}}(K^+/K^-) = \frac{\epsilon(K^+) - \epsilon(K^-)}{\epsilon(K^+) + \epsilon(K^-)}, \tag{6.7}$$

where $\epsilon(K^+)$ and $\epsilon(K^-)$ are the efficiencies to detect and reconstruct a K^+ and a K^-, respectively. All other components of the raw asymmetry decomposition—such as trigger and tag-side asymmetries, forward-backward asymmetry, and the $K^0/\bar{K}^0$ asymmetry—remain unchanged between the two decay channels.
Similarly, the raw asymmetry decomposition for $\tau^{\pm} \to \pi^{\pm}K^0\bar{K}^0\nu$ is identical to that of $\tau^{\pm} \to \pi^{\pm}K^0_S\nu$, except that the $A(K^0/\bar{K}^0)$ term becomes negligible, as the effects from K^0 and $\bar{K}^0$ cancel each other out. Furthermore, neutral pions do not introduce any additional asymmetry in any of the signal decays. To measure the CP violation asymmetry (A_{CP}), it is necessary to compute and account for corrections to all relevant terms.

6.2 Detection asymmetry

While the presence of CP violation manifests as differences in the decay rates of τ^+ and τ^-, additional asymmetries can arise from the detector's non-identical response to positively and negatively charged particles. These detection-induced asymmetries originate not only from charge-dependent tracking efficiencies and particle identification performance but also from physical effects, such as the forward-backward production asymmetry, that interact with the detector's asymmetric acceptance and geometry. Together, these effects can introduce a bias in the observed charge asymmetry that must be carefully evaluated and corrected.
This section describes the procedure used to quantify the detection asymmetry, relying on control samples selected to resemble the signal topology without containing CP-violating effects. By isolating and subtracting these instrumental contributions, we ensure the measured asymmetry reflects only genuine sources of CP violation.

6.2.1 Particle passage through matter

While traversing the detector, different types of particles experience different types of interactions [7]

- **Bremsstrahlung:** A charged particle loses kinetic energy when it is deflected by another charged particle. The energy is released in the form of photons. The amount of so-called bremsstrahlung depends on the rest mass and the velocity of the deflected particle. The geometry of the detector requires that some of the light charged particles (electrons and positrons) are ultra-relativistic, and bremsstrahlung is the dominant contribution of energy loss. For particles with mass M heavier than the electron m_e, the bremsstrahlung is not relevant as it is suppressed by a factor of $(m_e/M)^2$. The amount of energy loss is quantified by the radiation length of a specific material, X_0. The energy of an electron after traversing

a distance x in that material is given by

$$E_e(x) = E_0 e^{-\frac{x}{X_0}} \ , \tag{6.8}$$

where E_0 is the initial energy. As an example, the radiation length of aluminium is about 65 cm. Bremsstrahlung recovery is used in reconstruction software to "recover" emitted photons and improve energy resolution.

- **Ionisation:** Heavy charged particles lose energy due to single collisions with electrons in the material. Atoms are either ionised or excited by the interactions. The mean rate of energy loss, $-\langle \mathrm{d}E/\mathrm{d}x \rangle$, is described by the Bethe-Bloch formula

$$\left\langle \frac{\mathrm{d}E}{\mathrm{d}x} \right\rangle \simeq \frac{Kz^2}{\beta^2} \left[ln \left(\frac{2m_e c^2 \beta^2 \gamma^2 T_{\max}}{I^2} - \beta^2 \right) \right] \ , \tag{6.9}$$

where, $K \simeq 0.307$ MeV $\cdot$ cm^2/g is a constant, z is the charge of the particle (in units of e), $\beta = \frac{v}{c}$, $T_{\max}$ is the max energy transfer in a single collision and I is the mean excitation potential of the material (in eV). Typical values for detector material are a few MeV energy loss per cm. Thus, heavy charged particles have to traverse large amounts of material to lose significant energy. As muons only interact electromagnetically, they can traverse the whole detector.

- **Multiple scattering:** Charged particles can also be deflected by the electromagnetic field of nuclei. A sequence of Coulomb scatterings is called multiple scattering. The angular dispersion can be modelled as a Gaussian. Multiple scattering does not change the charged particle's energy but changes the initial flight direction and, thus, affects the momentum resolution of the tracking system.

- **Hadronic interactions:** Charged and neutral hadrons can also interact strongly with nuclei. The nuclear collision length, λ_T, is the typical length before hadrons scatter elastically or inelastically with nuclei in the material. The rate of collisions, $\mathrm{d}N/\mathrm{d}x$, per travelled length, x, is given by

$$\frac{\mathrm{d}N}{\mathrm{d}x} = \frac{-x}{\lambda_T} = -\sigma_T n x \ . \tag{6.10}$$

It can also be expressed by the cross section, σ_T, multiplied with the number density, n, of the scattering material. The nuclear interaction length, λ_I, is larger as it excludes elastic and quasi-elastic from its definition. The tracking resolution can be impacted by multiple scattering and energy loss, especially for low-momentum hadrons. PID techniques (such as $\mathrm{d}E/\mathrm{d}x$, Cherenkov radiation, and calorimeter profiles) are used to identify hadrons and distinguish them from other particles like electrons and muons.

These interactions between particles and detector material affect the likelihood that charged particles are successfully reconstructed, and crucially, can differ for positively and negatively charged particles due to their distinct interaction cross sections and scattering behaviors.

6.2.2 Detection asymmetries of charged hadrons

The efficiencies, $\epsilon(h^+)$ and $\epsilon(h^-)$, to reconstruct a positively- or negatively-charged particle, $h^\pm$, with momentum $\vec{p}$ are given by

$$\epsilon(h^\pm, \vec{p}) = \frac{N_{\text{rec}}(h^\pm, \vec{p})}{N_{\text{created}}(h^\pm, \vec{p})} \ , \tag{6.11}$$

where it is assumed that the particles are produced within the acceptance of the detector. As discussed, one source of inefficiency is interactions with the material. Other sources of inefficiency, which are related to the reconstruction of events or which are specific to the Belle II detector, are discussed in Chapter 7. In the case discussed here, the reconstruction efficiency is reduced by the material interaction as

$$\epsilon(h^\pm, \vec{p}) = \frac{N_{\text{created}}(h^\pm, \vec{p}) e^{-\frac{d}{\lambda_T(h^\pm, \vec{p})}}}{N_{\text{created}}(h^\pm, \vec{p})} = e^{-\frac{d}{\lambda_T(h^\pm, \vec{p})}} \ , \tag{6.12}$$

where $\lambda_T(h^\pm, \vec{p})$ is the nuclear collision length of particle $h^\pm$ with momentum $\vec{p}$ and d is the flight length in the material. Here, it is assumed that the trajectory of a particle cannot be reconstructed by the tracking system if a particle scatters elastically and inelastically. Thus, the nuclear collision length is an interesting quantity.
The difference in the reconstruction efficiencies of positive and negative particles to detect a charged particle $h^\pm$ with momentum $\vec{p}$ is the detection asymmetry. It is defined as

$$a_D(h^+)(\vec{p}) \equiv \frac{\epsilon(h^+, \vec{p}) - \epsilon(h^-, \vec{p})}{\epsilon(h^+, \vec{p}) + \epsilon(h^-, \vec{p})} \ . \tag{6.13}$$

Integrated asymmetries are denoted with capital A:

$$A_D(h^+) \equiv \frac{\epsilon(h^+) - \epsilon(h^-)}{\epsilon(h^+) + \epsilon(h^-)} \ . \tag{6.14}$$

The detection asymmetry depends on the kinematics of a particle. The measured asymmetry of a multi-body final state contains the effects of several particles. This is discussed in the following.

6.2.3 Detection asymmetry definition

We define detection asymmetry as the combined effect of all detector-related factors. In our case, detection asymmetry is expressed as:

$$A_D \equiv A_{\text{det}}(\pi^+/\pi^-) + A_{\text{trigger}} + A_{\text{det}}(\text{tag}) + A_{FB}, \tag{6.15}$$

which allows the raw data asymmetry for the decay $\tau^\pm \to \pi^\pm K^0_S \nu$ to be written as:

$$A^{\text{data}}_{\text{raw}}(\tau^\pm \to \pi^\pm K^0_S \nu) = A_D + A(K^0/\bar{K}^0). \tag{6.16}$$

The effects included in the detection asymmetry are all correlated, making them difficult to compute and isolate independently.

6.2.4 Simulation of the raw asymmetry

The Belle II Monte Carlo (MC) simulation does not account for kaon asymmetry effects, such as CP violation, absorption, or interference. This is supported by two observations:

- We generated 2 billion MC $\tau\tau$ events without including detector simulation, ensuring that no detector-related asymmetry effects were introduced. Asymmetries for each signal decay channel were calculated based on event counts. Table 6.1 summarizes the results, showing the number of positive and negative events along with the computed asymmetries. All observed asymmetries are statistically consistent with zero, as expected in the absence of CP violation in the MC simulation.

- Absorption effects, which arise from differences in interaction cross sections between K^0 and $\bar{K}^0$ with detector material, are also excluded. In the TauolaBelle2 framework, $\tau\tau$ decays involving neutral kaons directly produce the mass eigenstates K^0_S and K^0_L, rather than the flavor eigenstates K^0 and $\bar{K}^0$. Consequently, differences in nuclear interaction rates between K^0 and $\bar{K}^0$ are not introduced. A decay chain diagram for one of the signal decay channels, derived from the MCParticle list, is shown in Fig. 6.1.

Mode	MC mode number	τ^+	τ^-	Asymmetry(%)
$\tau \to \pi K^0_S \nu_\tau$	226	8340432	8345154	-0.028 ± 0.024
$\tau \to \pi K^0_S \pi^0 \nu_\tau$	126	3795400	3794234	0.015 ± 0.036
$\tau \to \pi K^0_S \pi^0 \pi^0 \nu_\tau$	30	261688	261178	0.098 ± 0.138
$\tau \to K K^0_S \nu_\tau$	228	1477542	1477370	0.006 ± 0.058
$\tau \to K K^0_S \pi^0 \nu_\tau$	124	1494826	1493146	0.056 ± 0.057
$\tau \to \pi K^0_S K^0_L \nu_\tau$	123	2150756	2150466	0.007 ± 0.048
$\tau \to \pi K^0_S K^0_L \pi^0 \nu_\tau$	36	646886	646328	0.043 ± 0.088
$\tau \to \pi K^0_S K^0_S \nu_\tau$	121	467500	468060	-0.06 ± 0.10
$\tau \to \pi K^0_L K^0_L \nu_\tau$	122	466880	467676	-0.09 ± 0.10

Table 6.1: Computed asymmetries for generated MC $\tau\tau$ events, without including the detector simulation. The table shows the number of positive and negative events, the MC mode number, and the calculated asymmetry for each signal decay channel.

Hence, the signal MC raw asymmetry decomposition can be written as

$$A^{\mathrm{MC}}_{\mathrm{raw}}(\tau^\pm \to \pi^\pm K^0_S \nu) = A_{\mathrm{det}}(\pi^+/\pi^-) + A_{\mathrm{trigger}} + A_{\mathrm{det}}(\mathrm{tag}) + A_{FB} = A_D \tag{6.17}$$

6.2.5 $\tau \to 3$-prong control sample

The previous discussion has demonstrated that simulation signal samples can be used to determine detection asymmetry. However, as will be elaborated in the following sections, discrepancies between MC and data charge asymmetries may occur due to inaccuracies in simulating the number of CDC hits in the Belle2 detector. To address this issue, the tracking group generally recommends applying a data-driven correction using a control channel.
For this purpose, the $\tau \to 3$-prong decay channel was selected. See Fig. 6.3 for the schematic of

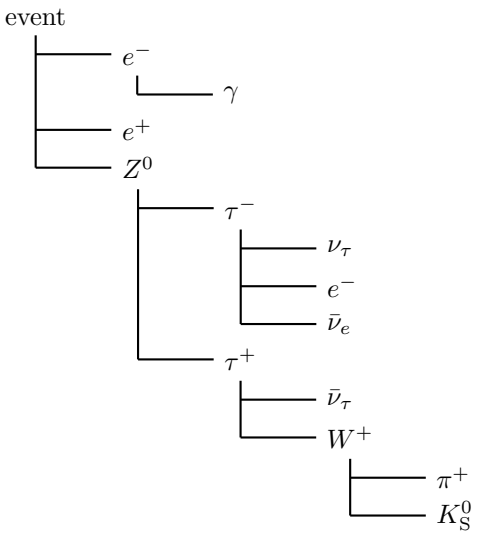

Figure 6.1: Decay chain diagram as generated by TauolaBelle2 for the $\tau^+ \to \pi^+ K^0_S \nu$ decay (signal). The other τ lepton decay to electron (tag).

the topology. In fact, the decomposition of the raw asymmetry for this channel, both in data and MC, reflects the same effects observed in the signal.

$$\begin{aligned} &A_{\text{raw}}^{\text{MC/data}}(\tau^\pm \to \pi^\pm\pi^\mp\pi^\pm\nu) = \\ &= A_{\text{det}}(\pi^+/\pi^-) + A_{\text{trigger}} + A_{\text{det}}(\text{tag}) + + A_{FB} + A_{\text{det}}(\pi^-/\pi^+) + A_{\text{det}}(\pi^+/\pi^-) = \\ &= A_D + A_{\text{det}}(\pi^-/\pi^+) + A_{\text{det}}(\pi^+/\pi^-) \end{aligned} \tag{6.18}$$

The last two additional terms account for the detection efficiencies of the extra pions. These terms are expected to cancel out when the two pions are subjected to similar kinematic constraints.

The strength of this method lies in the fact that the individual components of the detection asymmetry do not need to be known, as the correction for all three terms can be computed simultaneously.

To validate this data-driven correction, we exploit the signal simulation features discussed in the previous Section 6.2.4, and compare the signal and control simulation raw asymmetry. A sketch of the strategy is illustrated in Fig. 6.2.

However, it is generally expected that detection asymmetries depend on the kinematic distributions of the involved particles. Therefore, the kinematic distributions of both the reconstructed signal and control samples must be identical, ensuring that no residual effects from spurious asymmetries remain in A_D. The procedure for equalizing the slightly different momentum distributions of the two channels is a crucial part of the analysis.

As a first step, we used the same reconstruction used in the signal sample to the control sample, as it is described in Section 5.5.1, with slight modifications to account for differences between the two channels. These modifications were carefully chosen to preserve the validity of the control sample while aligning its kinematic properties with those of the signal sample:

- We require 0 number of K^0_S in the signal hemisphere, defined as in the stdKshorts list. This is necessary to avoid additional CP violation effect that may affect the charge asymmetry of the control sample.

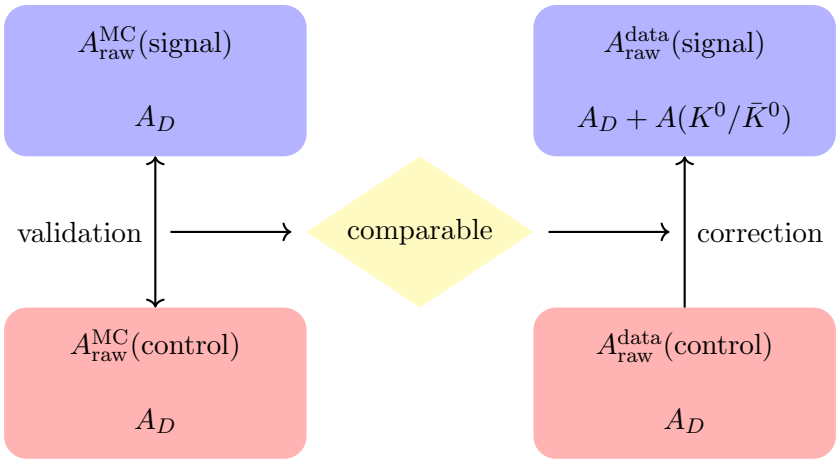

Figure 6.2: Flowchart for detection asymmetry determination and validation.

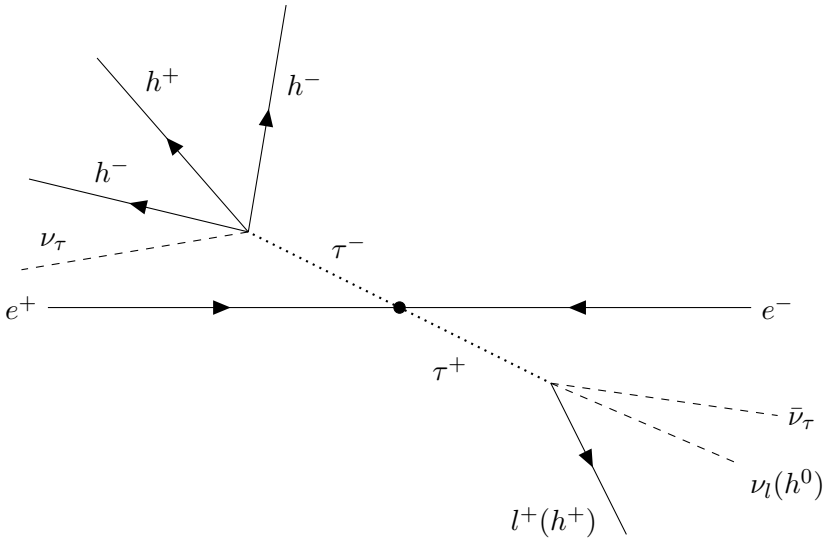

Figure 6.3: Schematic view of the control decay event topology.

- All the charged particle candidate in the signal hemisphere and the 1-prong track have to be "good tracks".

As a second step, the same preselection criteria described in Section 5.5.2 are applied. However, in this case, events are required to have zero K_S^0, and therefore all cuts involving K_S^0-based variables are excluded from the preselection. For clarity, a summary of the applied cuts is provided below:

- $0.9 <$ thrust < 0.995
- 2.5 GeV $<$ visibleEnergyOfEventCMS $<$ 10 GeV
- The K_S^0 transverse momentum has to be between 0.2 and 4.5 GeV/c.
- The momentum of the track in the tag hemisphere in CMS has to be less than 4.6 GeV/c.
- The invariant mass of the system $K_S^0 + \pi$ has to be between 0.7 and 1.3 GeV.
- The number of reconstructed photons in the event has to be less than 5.

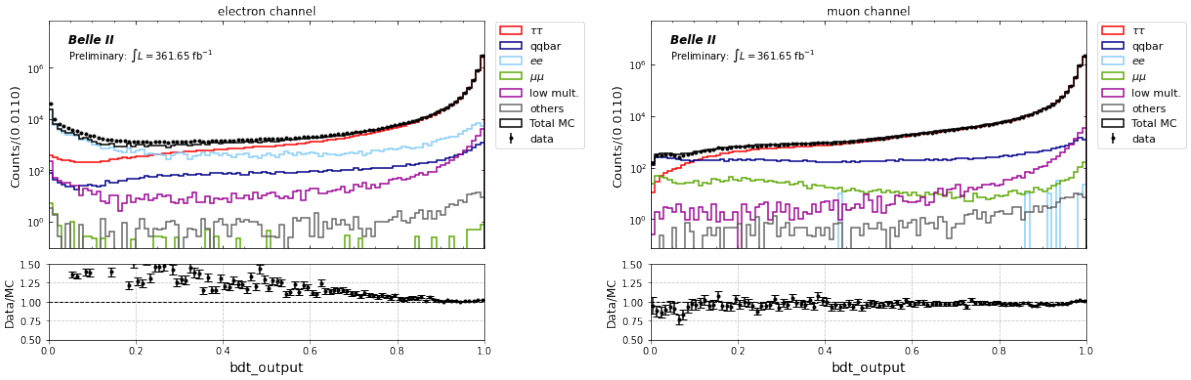

Figure 6.4: BDT output distributions for the electron (left) and muon (right) channel, in logarithmic y-axis scales.

- The number of photons coming from π^0 decays has to be less than 5.

Similar to the signal channel, we apply the same trigger selection and identical cuts on the lepton identification variables to ensure consistency in the trigger asymmetry A_{trigger} and the tag particle asymmetry $A_{\text{det}}(\text{tag})$. These selections and cuts are described in Sections 5.5.3 and 5.5.4.1, respectively. Corrections for the lepton identification variables are computed and applied following the same procedure as in the signal channel.
As the last step, we apply the first step of the two-step BDT trained on the signal sample to achieve a phase space as similar as possible to the signal channel and suppress the background. The second step of the two-step BDT cannot be applied since it is trained on K^0_S-based variables that are not present in the control channel.
BDT output distributions are shown in Fig. 6.4. The cut value of 0.8, as applied in the signal channel, was also chosen here. After applying the cut to the BDT output, Table 6.2 and 6.3 present the number of events and MC fractions for the electron and muon tagged samples separately.

Type	Events	% MC
Data	4518268 ± 2126	
MC	4421268 ± 1231	100
$\tau\tau$	4360905 ± 1046	98.63 ± 0.04
$\tau \to 3\pi(\geq 0\pi^0)\nu_\tau$	4198756 ± 1027	94.97 ± 0.04
$\tau \to K\pi\pi(\geq 0\pi^0)\nu_\tau$	114779 ± 170	2.59 ± 0.01
$\tau \to$ others	47370 ± 110	1.07 ± 0.01
Background	60381 ± 649	1.37 ± 0.02
ee	41868 ± 639	0.95 ± 0.01
low. mult.	10928 ± 105	0.25 ± 0.01
$q\bar{q}$	7491 ± 47	0.17 ± 0.01

Table 6.2: Number of events and fraction in MC for electron channel after the cut on the BDT output on the control channel. Errors are statistical only. MC has been scaled to data luminosity. Only main background contribution details are shown

Type	Events	% MC
Data	3773127 ± 1942	
MC	3732698 ± 952	100
$\tau\tau$	3710504 ± 945	99.41 ± 0.04
$\tau \to 3\pi(\geq 0\pi^0)\nu_\tau$	3602747 ± 932	96.52 ± 0.04
$\tau \to K\pi\pi(\geq 0\pi^0)\nu_\tau$	98503 ± 154	2.64 ± 0.01
$\tau \to$ others	9254 ± 51	0.25 ± 0.01
Background	22194 ± 115	0.59 ± 0.01
$q\bar{q}$	11374 ± 54	0.30 ± 0.01
low. mult.	10083 ± 98	0.27 ± 0.01

Table 6.3: Number of events and fraction in MC for muon channel after the cut on the BDT output on the control channel. Errors are statistical only. MC has been scaled to data luminosity. Only the main background contribution details are shown.

6.2.6 Control sample reweighting

With the selection criteria applied as described in the previous section, we can assume that both A_{trigger} and $A_{\text{det}}(\text{tag})$ contribute equally to the raw asymmetry in both the signal and control samples. However, a residual asymmetry may still arise from $A_{\text{det}}(\pi^+/\pi^-)$ due to the kinematic differences between the two samples. Assuming that $A_{\text{det}}(\pi^+/\pi^-)$ can be parameterized as a function of the pion's momentum and polar angle, the control sample events are reweighted by assigning each event a weight based on the ratio of the signal distribution to the control distribution for these two kinematic variables. This ensures that the reweighted control sample mimics the kinematic characteristics of the signal sample.

Before reweighting, one of the three pions in the control decay channel must be selected for extracting the ratio, while simultaneously ensuring that the remaining two pions are subject to similar kinematics.

This is achieved by calculating the invariant mass of the two $\pi^+\pi^-$ pairs and designating the pair with the invariant mass closest to the ρ^0 peak as the "extra pions". The kinematic distributions of these extra pions, shown in Fig. 6.5, confirm that this approach remains effective, even in the absence of a ρ^0 resonance in the decay chain. Since our signal sample encompasses multiple decay channels, the control sample weights, w_{control}, are computed as a weighted sum of the individual weights $w_i(p, \theta)$, as described in Eq. 6.19. The weights are combined using the MC fractions, f_i, of each decay channel in the signal sample. Each weight $w_i(p, \theta)$ is based on the ratio of the simulated (MC) kinematic distributions for the corresponding signal and control decay channels, ensuring the control sample reproduces the same raw asymmetry decomposition. Unitary weights are assigned to background samples.

$$w_{\text{control}}(p, \theta) = \sum_i w_i(p, \theta) f_i \tag{6.19}$$

A one-to-one correspondence between each signal and control decay channel used to extract the individual weights is shown in Table 6.4 and the MC fractions used for the weighted sum are

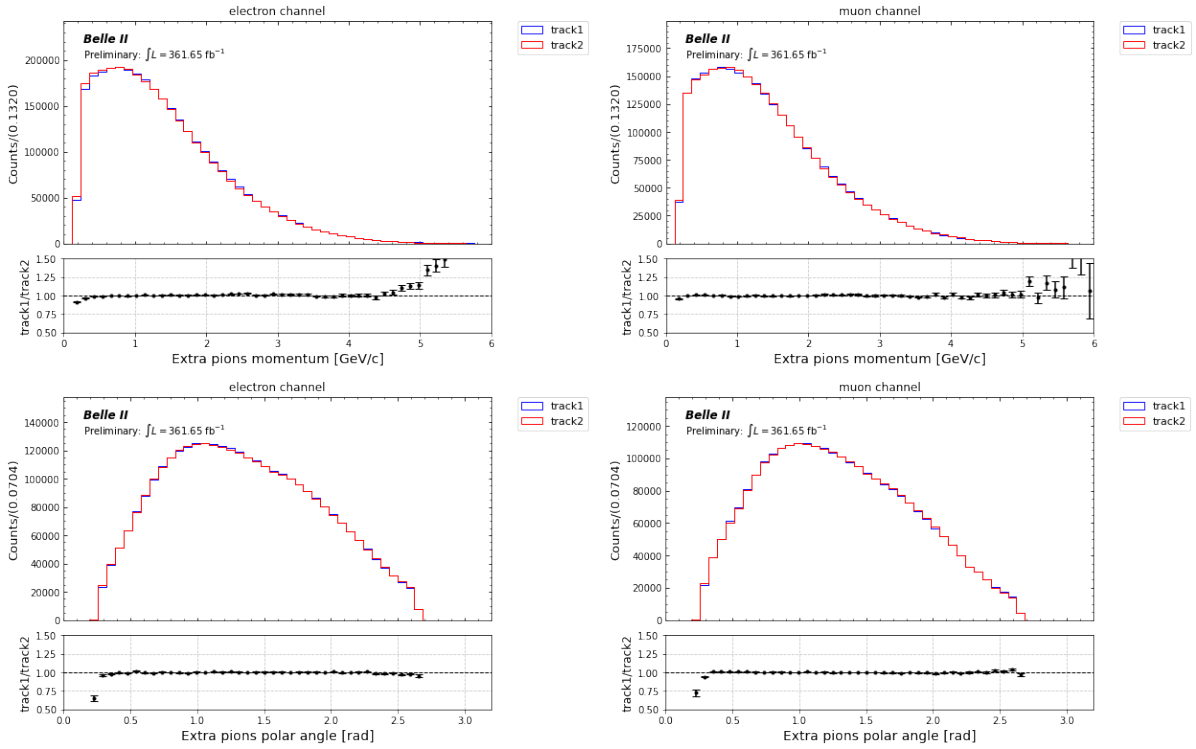

Figure 6.5: Data comparison of momentum (above) and polar angle (below) distributions for the two extra pions (track1 and track2) in the electron (left) and muon (right) case.

listed in Table 6.5.

Signal	Control	Raw asymmetry decomposition
$\tau \to \pi K^0_S \nu$	$\tau \to \pi\pi\pi$	$A^{det}(\pi^+/\pi^-) + A^{trigger} + A^{det}(\text{tag})$
$\tau \to \pi K^0_S \nu\pi^0$	$\tau \to \pi\pi\pi\pi^0$	$A^{det}(\pi^+/\pi^-) + A^{trigger} + A^{det}(\text{tag})$
$\tau \to \pi K^0_S \nu 2\pi^0$	$\tau \to \pi\pi\pi 2\pi^0$	$A^{det}(\pi^+/\pi^-) + A^{trigger} + A^{det}(\text{tag})$
$\tau \to K K^0_S \nu$	$\tau \to K\pi\pi$	$A^{det}(K^+/K^-) + A^{trigger} + A^{det}(\text{tag})$
$\tau \to K K^0_S \nu\pi^0$	$\tau \to K\pi\pi\pi^0$	$A^{det}(K^+/K^-) + A^{trigger} + A^{det}(\text{tag})$
$\tau \to \pi K^0 \bar{K}^0 \nu$	$\tau \to \pi\pi\pi$	$A^{det}(\pi^+/\pi^-) + A^{trigger} + A^{det}(\text{tag})$
$\tau \to \pi K^0 \bar{K}^0 \nu\pi^0$	$\tau \to \pi\pi\pi\pi^0$	$A^{det}(\pi^+/\pi^-) + A^{trigger} + A^{det}(\text{tag})$

Table 6.4: Signal and corresponding control decay channels with matching raw asymmetry decomposition.

To get these individual weights with enough precision, MC samples have been produced for each specific decay. For each decay mode 10 millions signal MC events were generated and reconstructed. All the control and signal sample distributions are shown in Fig. 6.6 and Fig. 6.7.

6.2.7 Detection asymmetry results

The detection asymmetry is compared between the signal and control Monte Carlo (MC) samples as part of the validation procedure, following the reweighting of the control sample. The results

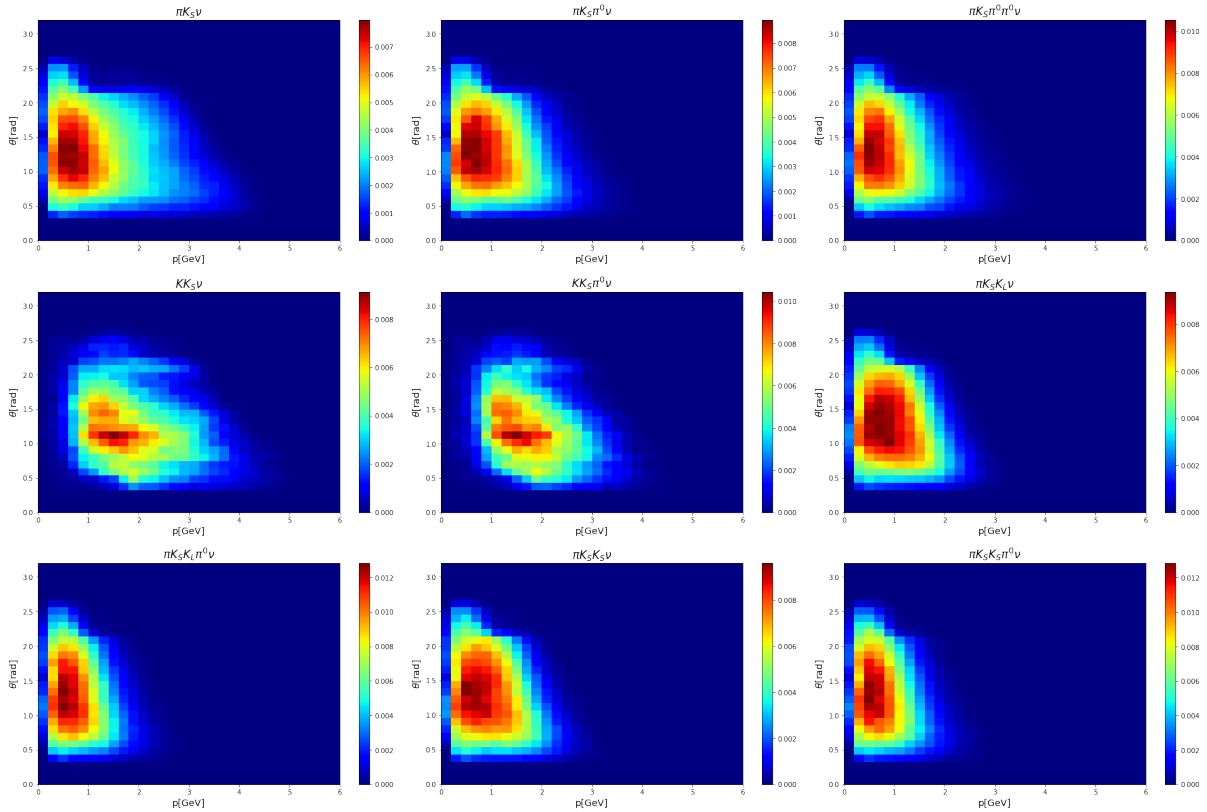

Figure 6.6: 2D normalized distributions of momentum and polar angle for the prompt track in the signal channels.

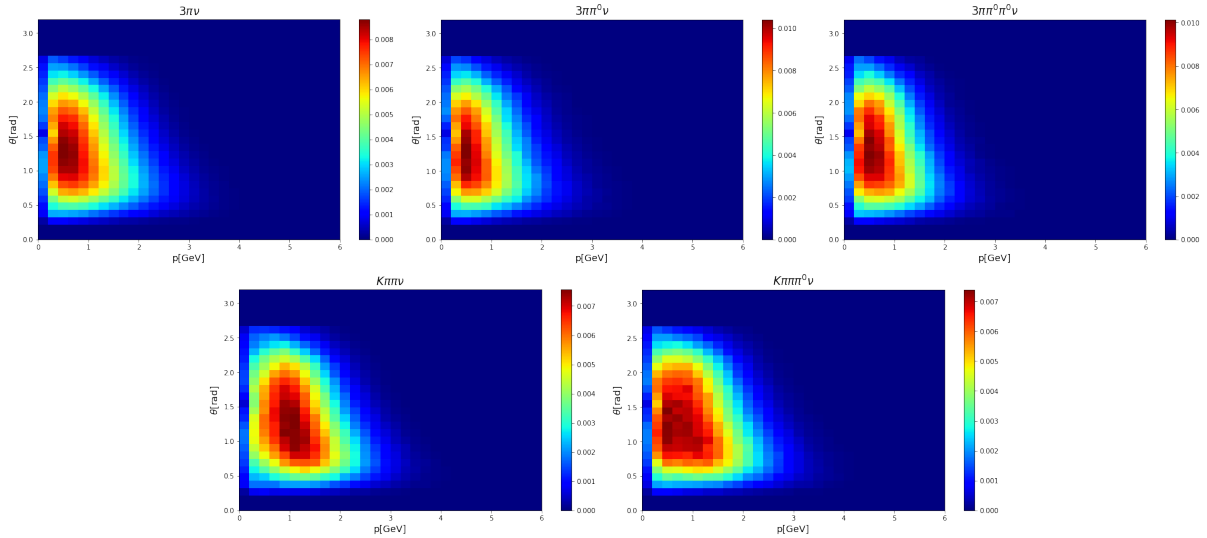

Figure 6.7: 2D normalized distributions of momentum and polar angle for the prompt track in the control channels.

Decay channel	fraction (e-channel) [%]	fraction (μ-channel) [%]
$\tau \to \pi K^0_S \nu$	53.23	50.76
$\tau \to \pi K^0_S \pi^0 \nu$	23.36	24.49
$\tau \to \pi K^0_S \pi^0 \pi^0 \nu$	1.27	1.37
$\tau \to K K^0_S \nu$	1.3	1.28
$\tau \to K K^0_S \pi^0 \nu$	1.38	1.45
$\tau \to \pi K^0_S K^0_L \nu$	13.44	13.85
$\tau \to \pi K^0_S K^0_L \pi^0 \nu$	2.92	3.14
$\tau \to \pi K^0_S K^0_S \nu$	1.75	1.91
$\tau \to \pi K^0_S K^0_S \pi^0 \nu$	0.1	0.1

Table 6.5: Signal decay modes MC fractions in signal sample.

for the electron and muon channels are given by:

$$e\text{-tag}: \quad A^{\mathrm{MC}}_{\mathrm{raw}}(\text{signal}) = (-1.79 \pm 0.07)\% \qquad A^{\mathrm{MC}}_{\mathrm{raw}}(\text{control}) = (-1.80 \pm 0.03)\% \tag{6.20}$$

$$\mu\text{-tag}: \quad A^{\mathrm{MC}}_{\mathrm{raw}}(\text{signal}) = (-0.45 \pm 0.09)\% \qquad A^{\mathrm{MC}}_{\mathrm{raw}}(\text{control}) = (-0.49 \pm 0.03)\% \tag{6.21}$$

The excellent agreement between signal and control MC samples in both the electron and muon channels demonstrates that the kinematic reweighting has been successfully applied and validates the procedure. The same reweighting procedure is applied to the control sample in data to extract the detection asymmetry correction.

$$A^{\mathrm{data}}_{\mathrm{raw}}(\text{control}) = (-1.33 \pm 0.05)\% \quad \text{for the electron tag} \tag{6.22}$$

$$A^{\mathrm{data}}_{\mathrm{raw}}(\text{control}) = (-0.33 \pm 0.06)\% \quad \text{for the muon tag} \tag{6.23}$$

The measured values above are taken as the final detection asymmetry correction to be applied in Eq. 6.1. The discrepancy between data and MC asymmetry is a well-established phenomenon in Belle II and originates from differences in the reconstruction efficiency of positive and negative tracks between data and simulation. All uncertainties quoted above are purely statistical.
This concludes the evaluation of the detection asymmetry. The next section addresses the correction for the asymmetry induced by the K^0–$\bar{K}^0$ interaction with detector material.

6.3 Neutral Kaon asymmetry

The neutral kaon candidates are reconstructed in the CP eigenstate $\pi^+\pi^-$. As the mass eigenstate K^0_S is not a CP eigenstate, the decay $K^0_S \to \pi^+\pi^-$ is CP-violating. Additionally, K^0 and $\bar{K}^0$ mesons have different absorption rates in the detector material, equivalent to charged kaons. The effects of mixing, CP violation, and absorption interfere due to coherent forward scattering [84]. Thus, the time evolution of neutral kaons while traversing the Belle II detector is modeled, and the contribution of the neutral kaon asymmetry $A(K^0/\bar{K}^0)$ to the raw asymmetry $A^{raw}(\tau^\pm \to \pi^\pm K^0_S \nu)$ is determined.

6.3.1 Asymmetry formalism

For the rest of the note the convention $\hbar = c = 1$ is used to simplify the formulas.
Following the arguments of Section 2.3.1, the effective Schroedinger equation of neutral kaon mixing in vacuum can be written as

$$i\frac{d}{dt}\begin{pmatrix}|K^0(t)\rangle\\|\bar{K}^0(t)\rangle\end{pmatrix}_{\text{vac}} = \left(\mathbf{M} - \frac{i}{2}\mathbf{\Gamma}\right)\begin{pmatrix}|K^0(t)\rangle\\|\bar{K}^0(t)\rangle\end{pmatrix}_{\text{vac}} \tag{6.24}$$

where $\mathbf{M}$ and $\mathbf{\Gamma}$ are hermitian matrices describing mixing and decay of K^0 and $\bar{K}^0$ mesons. The eigenstates of $(\mathbf{M} - \frac{i}{2}\mathbf{\Gamma})$ are the known K^0_{S} and K^0_{L} states. They are given as

$$|K^0_{\text{S}}\rangle = \frac{1}{\sqrt{2(1+|\epsilon|^2)}}\left[(1+\epsilon)\,|K^0\rangle + (1-\epsilon)\,|\bar{K}^0\rangle\right], \tag{6.25}$$

$$|K^0_{\text{L}}\rangle = \frac{1}{\sqrt{2(1+|\epsilon|^2)}}\left[(1+\epsilon)\,|K^0\rangle - (1-\epsilon)\,|\bar{K}^0\rangle\right], \tag{6.26}$$

where ϵ is the parameter describing CP violation in kaon mixing. The lifetime of the neutral kaon is large enough that they can transverse significant amounts of material before they decay. The interaction of K^0 and $\bar{K}^0$ mesons with matter can be written as:

$$i\frac{d}{dt}\begin{pmatrix}|K^0(t)\rangle\\|\bar{K}^0(t)\rangle\end{pmatrix}_{\text{nuc}} = \begin{pmatrix}\chi & 0\\0 & \bar{\chi}\end{pmatrix}\begin{pmatrix}|K^0(t)\rangle\\|\bar{K}^0(t)\rangle\end{pmatrix}_{\text{nuc}}, \tag{6.27}$$

where the complex numbers χ and $\bar{\chi}$ are related to the interaction of K^0 and $\bar{K}^0$ mesons with matter. The real part of χ describes phase shifts (dispersion) and the imaginary part describes absorption in the material. Equations 6.24 and 6.27 are combined to account coherently for the effects of mixing, CP violation and absorption. The full equation of neutral kaons in matter is given by

$$i\frac{d}{dt}\begin{pmatrix}|K^0(t)\rangle\\|\bar{K}^0(t)\rangle\end{pmatrix} = \left(\mathbf{M} - \frac{1}{2}\mathbf{\Gamma} + \chi\right)\begin{pmatrix}|K^0(t)\rangle\\|\bar{K}^0(t)\rangle\end{pmatrix}. \tag{6.28}$$

Eq. 6.28 is neither diagonal in the K^0 and $\bar{K}^0$ basis nor in the K^0_{S} and K^0_{L} basis. Therefore, K^0_{S} and K^0_{L} states are no longer mass eigenstates and transitions between the two states are possible. This effect has been known as *regeneration* since 1955 [85]. It is used in neutral kaon experiments as it allows to *regenerate* K^0_{S} mesons from a pure K^0_{L} beam by sending the beam through material. In the context of this analysis it is a nuisance.
Eq. 6.28 assumes that the regeneration is the coherent combination of the effects from mixing, CP violation and absorption. However, whether the regeneration process is coherent or incoherent depends on the density and the size of the medium and on the kaon momentum [86]. For ~ 1 Gev momentum and in the precise forward direction, the length at which two scattering centres can still interfere fully coherently is ~ 10 cm, which corresponds to approximately two mean decay lengths. Hence, to a good approximation, regeneration in Belle II occurs only coherently and this is what assumed in the following.
The time evolution of an arbitrary neutral kaon state, $\tilde{\Psi}$, in matter in the K^0_{S} and K^0_{L} basis is

then given by the following equations [87, 88]

$$|\tilde{\Psi(t)}\rangle = \alpha_{\rm L}(t)\,|K^0_{\rm L}\rangle + \alpha_{\rm S}(t)\,|K^0_{\rm S}\rangle \quad \text{with} \tag{6.29}$$

$$\alpha_{\rm L}(t) = e^{-i\Sigma\cdot t}\left[\alpha_{\rm L}(0)\cos(\Omega t) - i\frac{\alpha_{\rm S}(0)\Delta\lambda + \alpha_{\rm S}(0)\Delta\chi}{2\Omega}\sin(\Omega t)\right], \tag{6.30}$$

$$\alpha_{\rm S}(t) = e^{-i\Sigma\cdot t}\left[\alpha_{\rm S}(0)\cos(\Omega t) + i\frac{\alpha_{\rm S}(0)\Delta\lambda - \alpha_{\rm L}(0)\Delta\chi}{2\Omega}\sin(\Omega t)\right], \tag{6.31}$$

where the complex constants $\Omega \equiv \frac{1}{2}(\lambda_{\rm L} + \lambda_{\rm S} + \chi + \bar{\chi})$ describe mixing and absorption. They are given by the masses, $m_{L,S}$, decay widths, $\Gamma_{\rm L,S}$, of the $K^0_{\rm L}$ and $K^0_{\rm S}$ states and the absorption coefficient χ ($\bar{\chi}$) of K^0 ($\bar{K}^0$) states by means of

$$\Delta\lambda = \lambda_{\rm L} - \lambda_{\rm S} = \Delta m - \frac{i}{2}\Delta\Gamma = (m_{\rm L} - m_{\rm S}) - \frac{i}{2}(\Gamma_{\rm L} - \Gamma_{\rm S}), \tag{6.32}$$

$$\Delta\chi = \chi - \bar{\chi} = -\frac{2\pi N}{m}\Delta f = -\frac{2\pi N}{m}(f - \bar{f}), \tag{6.33}$$

where N is the scattering density of the material, m the kaon mass, and f and $\bar{f}$ are the forward scattering amplitudes.
The imaginary part of Δf is related to the total cross section via the optical theorem:

$$\sigma_{\rm tot} = \frac{4\pi}{p}{\rm Im}f, \tag{6.34}$$

where p is the momentum of the neutral kaon. Similar to charged kaons, K^0 and $\bar{K}^0$ interaction cross section depends on momentum, p, of neutral kaons and on the number of nucleons, A, in the target. It is taken from Reference [89, 90] as

$$\Delta\sigma(\bar{K}^0 N) = \sigma(\bar{K}^0 N) - \sigma(K^0 N) = \frac{A^{0.758}\Delta\sigma(K^- p)}{1 + 1.252e^{1.841 p^{K^-}\,({\rm GeV}/c)}}{\rm mb} \tag{6.35}$$

where $\Delta\sigma(K^- p) \equiv \sigma(K^- p) - \sigma(K^+ p)$ and p^{K-} is the momentum of K^-. This formula is obtained assuming isospin symmetry of nuclear interaction, $\sigma(\bar{K}^0 n) \cong \sigma(K^- p)$ and $\sigma(K^0 p) \cong \sigma(K^+ n)$. These assumptions allow us to compute $\Delta\sigma(\bar{K}^0 N)$ in the low-momentum range down to 1 GeV/c and below.
The real and imaginary part of Δf need to be known. The phase of Δf has been determined in [89, 91] to be $\arg\Delta f = (-124.7 \pm 0.8)^\circ$.
The formalism of Equations 6.29 to 6.35 includes two effects. First, the incoherent absorption and elastic scattering of K^0 and $\bar{K}^0$ states is given by ${\rm Im}(\Delta f)$. This effect is equivalent to the case of charged kaons. Second, the term ${\rm Re}(\Delta f)$ describes a dispersion (relative phase shifts) of K^0 and $\bar{K}^0$ states. Both effects lead to a mixing of $K^0_{\rm L}$ and $K^0_{\rm S}$ states.
At production, the flavour of the K^0 meson is defined. A K^0 state is produced in the decay of a τ^+ and a $\bar{K}^0$ state in the decay of a τ^-. The two pure states at production are given in the $K^0_{\rm L}$ and $K^0_{\rm S}$ basis as

$$|K^0\rangle = \frac{\sqrt{1+|\epsilon|^2}}{2}\frac{1}{1+\epsilon}\left[|K^0_{\rm L}\rangle + |K^0_{\rm S}\rangle\right], \tag{6.36}$$

$$|\bar{K}^0\rangle = \frac{\sqrt{1+|\epsilon|^2}}{2}\frac{1}{1-\epsilon}\left[|K^0_{\rm L}\rangle - |K^0_{\rm S}\rangle\right], \tag{6.37}$$

Parameter	Value
Δm	$(0.5293 \pm 0.0009) \times 10^{10} \hbar s^{-1}$
$\tau_S \equiv 1/\Gamma_S$	$(0.8954 \pm 0.0004) \times 10^{-10} s$
$\tau_L \equiv 1/\Gamma_L$	$(5.116 \pm 0.021) \times 10^{-8} s$
m	$(497.614 \pm 0.024)\mathrm{MeV}/c^2$
$\arg(\Delta f)$	$(-124.7 \pm 0.8)^\circ$
$\lvert\epsilon\rvert$	$(2.228 \pm 0.011) \times 10^{-3}$
$\phi_{+-} \equiv \arg\epsilon$	$(43.51 \pm 0.05)^\circ$
$\Delta\sigma(\bar{K}^0 N)$	$A^{0.758\pm0.003}\Delta\sigma(K^- p)\left[1 + 1.252e^{-1.841 p^{K^-}(\mathrm{GeV}/c)}\right]^{-1}$ mb

Table 6.6: Values of the parameters used to compute neutral kaon asymmetry [7, 89–91].

which defines the initial amplitudes $\alpha_{L,S}(0)$ at $t = 0$ for the initial K^0 and $\bar{K}^0$ states.
The considered final state $\pi^+\pi^-$ is a CP-even eigenstate, $CP\,|\pi^+\pi^-\rangle = |\pi^+\pi^-\rangle$. The mass eigenstates K^0_L and K^0_S are no pure CP eigenstates. They can be written in terms of CP-even eigenstate, K^0_1, and the CP-odd eigenstate, K^0_2, as

$$|K^0_L\rangle = \frac{1}{\sqrt{1+|\epsilon|^2}}\left(|K^0_2\rangle + \epsilon\,|K^0_1\rangle\right), \tag{6.38}$$

$$|K^0_S\rangle = \frac{1}{\sqrt{1+|\epsilon|^2}}\left(|K^0_1\rangle + \epsilon\,|K^0_2\rangle\right). \tag{6.39}$$

Using Eq. 6.38 yields that the decay rate of an arbitrary state $\tilde{\Psi}$, defined in Eq. 6.29, to a CP-even final state is proportional to

$$|\alpha_S(t) + \epsilon\alpha_L(t)|^2 \tag{6.40}$$

at a given time t. the time dependent asymmetry is then defined as

$$a_{K^0/\bar{K}^0}(t) = \frac{\Gamma(K^0_{t=0} \to \pi^+\pi^-)(t) - \Gamma(\bar{K}^0_{t=0} \to \pi^+\pi^-)(t)}{\Gamma(K^0_{t=0} \to \pi^+\pi^-)(t) + \Gamma(\bar{K}^0_{t=0} \to \pi^+\pi^-)(t)} \tag{6.41}$$

where $\Gamma(K^0_{t=0} \to \pi^+\pi^-)(t)$ is the time-dependent decay rate of an initial K^0 state and $\Gamma(\bar{K}^0_{t=0} \to \pi^+\pi^-)(t)$ is the time-dependent decay rate of an initial $\bar{K}^0$ state. The time imtegrated asymmetry is given by

$$A_{K^0/\bar{K}^0} = \frac{\int_0^\infty \epsilon(t)\left[\Gamma(K^0_{t=0} \to \pi^+\pi^-)(t) - \Gamma(\bar{K}^0_{t=0} \to \pi^+\pi^-)(t)\right] dt}{\int_0^\infty \epsilon(t)\left[\Gamma(K^0_{t=0} \to \pi^+\pi^-)(t) + \Gamma(\bar{K}^0_{t=0} \to \pi^+\pi^-)(t)\right] dt} \tag{6.42}$$

where $\epsilon(t)$ is the decay time integrated acceptance of K^0_S mesons. All parameters used in the calculation are given in Table 6.6. The decay time acceptance is treated separately as it depends on the K^0_S sample in data.

6.3.2 Asymmetry computation

The material in our detector is not homogeneously distributed. There are several detection layers with different materials and vacuum or air in between. Therefore, the flight path of a

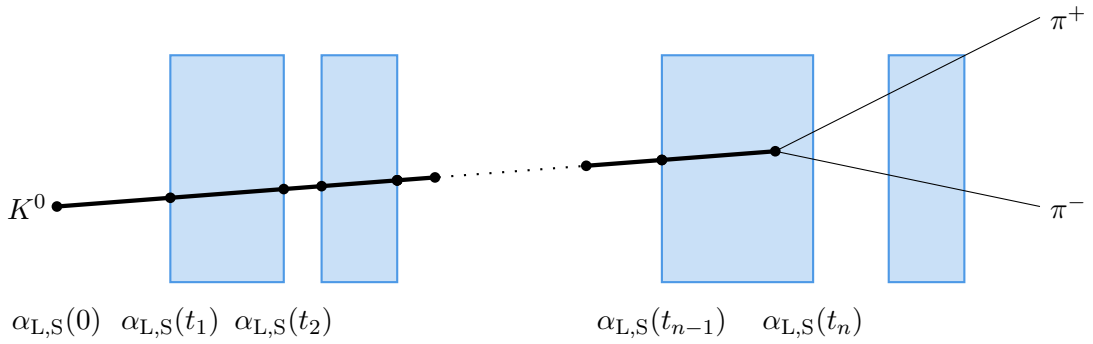

Figure 6.8: The flight path of a neutral kaon through detector material. The iterative procedure to obtain the amplitudes $\alpha_{\mathrm{L,S}}$ is depicted. In this simplified picture the blue boxes can have a different density ρ and number of nucleons A.

particle is divided into sections, see Fig. 6.8. The detector geometry as it is implemented in the event simulation and reconstruction is used. The amplitudes $\alpha_{\mathrm{L,S}}(t_n)$ are calculated for a time difference $t_n - t_{n-1}$ with the start values $\alpha_{\mathrm{L,S}}(t_{n-1}) = \alpha_{\mathrm{L,S}}(0)$ according to Eq. 6.29:

$$\alpha_{\mathrm{S}}(t_n) = \alpha_{\mathrm{S}}(t_n - t_{n-1}) \quad \text{with} \quad \alpha_{\mathrm{L,S}}(0) = \alpha_{\mathrm{L,S}}(t_{n-1}), \tag{6.43}$$

$$\alpha_{\mathrm{L}}(t_n) = \alpha_{\mathrm{L}}(t_n - t_{n-1}) \quad \text{with} \quad \alpha_{\mathrm{L,S}}(0) = \alpha_{\mathrm{L,S}}(t_{n-1}). \tag{6.44}$$

the iterative calculation of α_{S} and α_{L} is performed with initial K^0 and $\bar{K}^0$ states for the flight path of every K^0_{S} candidate in our data sample. The usage of K^0_{S} candidates selected in data takes automatically the decay-time acceptance of reconstructed K^0_S decays into account. The expected time-integrated asymmetry of a K^0_{S} sample is then given as

$$A_{K^0/\bar{K}^0} = \frac{1}{N} \sum_{j=1}^{N} a_j(t_j), \tag{6.45}$$

where N is the number of K^0_{S} candidates in the sample and $a_j(t_j)$ is the expected asymmetry of candidate j with decay time t_j according to Eq. 6.10. The decay time t_j is extracted from the K^0_{S} flight distance d and momentum p using relativistic time-distance relation formula

$$t_j = \frac{d m_{\mathrm{S}}}{pc} \tag{6.46}$$

6.3.3 Computation workflow

The software comprises two primary components. The first component generates a ray at the interaction point, employing a Geant4 simulation of the Belle II detector. This ray is aligned with the neutral kaon's direction within the sample, simulating the kaon's flight path through the detector. Along this trajectory, the component calls the `GetDensity` and `GetMassOfMolecule` methods from the `G4Material` class to access the density and atomic mass of materials encountered along the path. These material properties are sampled along the kaon's trajectory, providing detailed material characterization. An example of this scan, focused on the beampipe region, is shown in Fig. 6.9. The second component uses the information retrieved by the first part of the code to perform the computation using the formulas in Section 6.3.1.

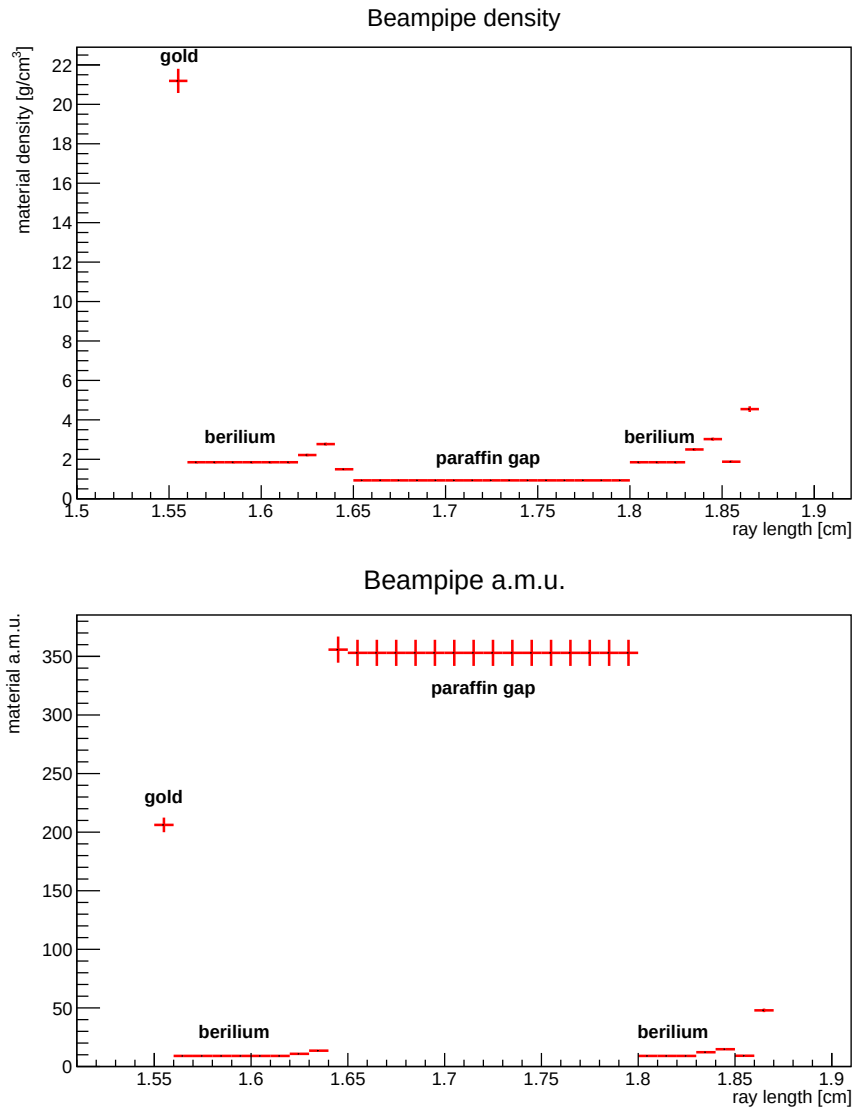

Figure 6.9: Density and atomic mass profile of the beampipe along the ray path for a sample event with $\theta = 140°$ and $\phi = 0°$. For compound materials, the molecular mass is used.

An example of the time-dependent asymmetry computation for one single event is shown in Fig. 6.10. The three different contribution to the total asymmetry, CP violation, absorption and interference can be computed separately by making the following changes to the equations in Section 6.3.1

- To isolate CP violation from other effects, we set the absorption term to zero by taking $\Delta\chi = 0$. This modifies equations 6.30 and 6.31 as follows:

$$\alpha_{\mathrm{L}}(t) = e^{-i\Sigma\cdot t}\left[\alpha_{\mathrm{L}}(0)\cos(\Omega t) - i\frac{\alpha_{\mathrm{L}}(0)\Delta\lambda}{2\Omega}\sin(\Omega t)\right], \tag{6.47}$$

$$\alpha_{\mathrm{S}}(t) = e^{-i\Sigma\cdot t}\left[\alpha_{\mathrm{S}}(0)\cos(\Omega t) + i\frac{\alpha_{\mathrm{S}}(0)\Delta\lambda}{2\Omega}\sin(\Omega t)\right] \tag{6.48}$$

- To isolate the absorption term from other effects, the CP violation parameter is set to zero, $\epsilon = 0$. Under this condition, the neutral kaon flavor eigenstates can be decomposed

into mass eigenstates as follows:

$$|K^0\rangle = \frac{1}{2}\left[|K_{\rm L}^0\rangle + |K_{\rm S}^0\rangle\right] \tag{6.49}$$

$$|\bar{K}^0\rangle = \frac{1}{2}\left[|K_{\rm L}^0\rangle - |K_{\rm S}^0\rangle\right] \tag{6.50}$$

The decay rate of an arbitrary state, as derived in the general case in Eq. 6.40, will now be proportional to:

$$\Gamma \propto |\alpha_S(t)|^2 \tag{6.51}$$

- The contribution of the interference term is obtained by subtracting the CP violation and absorption terms, calculated as described above, from the total asymmetry.

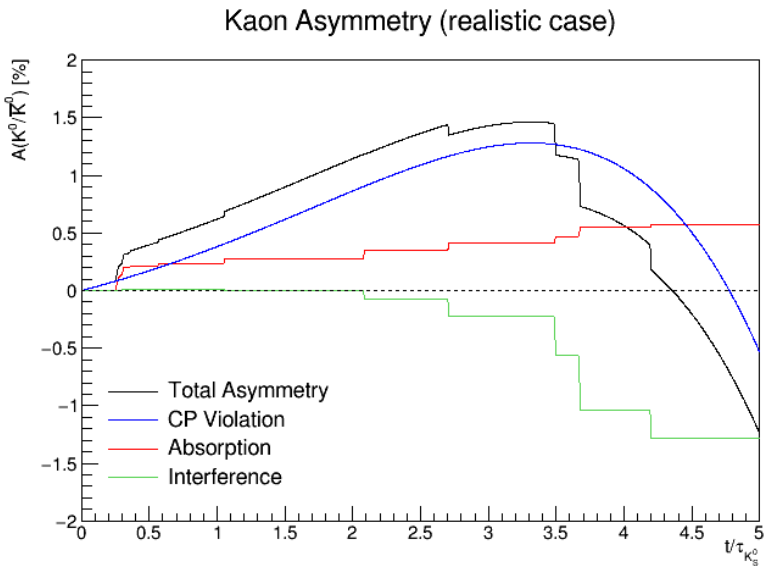

Figure 6.10: Time-dependent neutral kaon asymmetry for small $K_{\rm S}^0$ decay times, highlighting the contributions from CP violation, absorption, and interference. At small decay times the asymmetries due to absorption and CP violation increase linearly with time for small decay times. Both have the same order of magnitude and same sign. The interference term has little effect below 2 $\tau_{\rm S}$, while for larger decay time it significantly affects the asymmetry.

The decomposition in the three terms can be useful for selectively correcting specific components of the neutral kaon asymmetry. For our case, only the interference and absorption contributions to the total integrated asymmetry are computed and applied to correct data raw asymmetry as

$$A_{\rm abs}(K^0) = \frac{1}{N}\sum_{j=1}^{N} a_{j(\rm abs.)}(t_j) \tag{6.52}$$

$$A_{\rm int}(K^0) = \frac{1}{N}\sum_{j=1}^{N} a_{j(\rm int.)}(t_j) \tag{6.53}$$

In Table 6.7 the calculated asymmetries are shown for electron and muon tag separately. These values account for the various decay channels included in our signal sample, where the asymmetry is above or below zero depending on whether the K^0 ($\bar{K}^0$) is produced from a τ^+ (τ^-) or τ^-

Sample	$A_{\text{abs}}[\%]$	$A_{\text{int}}[\%]$
e-tag	$0.1085 \pm 0.0003(\text{stat.})^{+0.0053}_{-0.0053}(\text{syst.})$	$-0.0003 \pm 0.0002(\text{stat.})^{+0.0001}_{-0.0001}(\text{syst.})$
μ-tag	$0.1063 \pm 0.0003(\text{stat.})^{+0.0059}_{-0.0048}(\text{syst.})$	$-0.0005 \pm 0.0001(\text{stat.})^{+0.0001}_{-0.0001}(\text{syst.})$

Table 6.7: The calculated absorption (A_{abs}) and interference (A_{int}) asymmetry (K^0) including systematic uncertainty due to the uncertainty on the material budget

(τ^+) decay. The quoted systematic uncertainty assigned to this calculation comes from the knowledge of the detector material budget. This is known to an accuracy of about 5%. The uncertainties on the remaining input values are negligible in comparison, see Table 6.6. Hence, the relative systematic uncertainty stays at about 5%.

6.3.4 Correction applied to the data raw asymmetry

From Table 6.7, the contribution of the interference to the integrated asymmetry can be neglected, as most of the events lie within the $< 2\tau_{\text{S}}$ decay time region.
The neutral kaon asymmetry correction factor due to absorption applied to the data raw asymmetry is found to be

$$A_{\text{abs}}(K^0) = (0.108 \pm 0.005)\% \quad \text{for the electron tag} \tag{6.54}$$

$$A_{\text{abs}}(K^0) = (0.106 \pm 0.006)\% \quad \text{for the muon tag} \tag{6.55}$$

6.3.5 Validation

To ensure the accuracy and reliability of the developed code, it is essential to validate its performance using representative data samples. This validation process helps verify that the code functions as expected under different conditions and produces correct results. For this purpose, two different control samples, $D^{\pm} \to K^0_{\text{S}}\pi^{\pm}$ and $D^0 \to K^0_{\text{S}}\pi^+\pi^-$, are used. These decays reflect the typical scenarios the code is expected to handle.
The neutral kaon asymmetry depends on the reconstructed decay times of the K^0_{S} candidates, as discussed in the previous section. In order to test the code, the raw asymmetry is determined in bins of this quantity for the two samples and compared with the predicted asymmetry in a given bin. The raw and the predicted asymmetries are shown as function of the K^0_{S} decay time in Fig. 6.11 for the two samples. The raw asymmetries have contributions from the $D^{\pm}$ production and the pion detection asymmetry, while the neutral kaon asymmetry vanishes for zero decay time. This overall offset is taken into account by shifting the prediction by the averaged difference of raw and predicted asymmetry. Only differences in the shape are of interest here.
The raw asymmetry follows the predicted downward trend in both samples. The p values are 0.65 and 0.06 for K^0_{S} candidates in $D^{\pm} \to K^0_{\text{S}}\pi^{\pm}$ and $D^0 \to K^0_{\text{S}}\pi^+\pi-$ decays, respectively, and show that the predicted asymmetries agree well with the data.

6.4 Background subtraction

In order to compare the measured decay-rate asymmetry with the SM prediction, we need to subtract the background events from the data. The backgrounds are predicted by the Monte

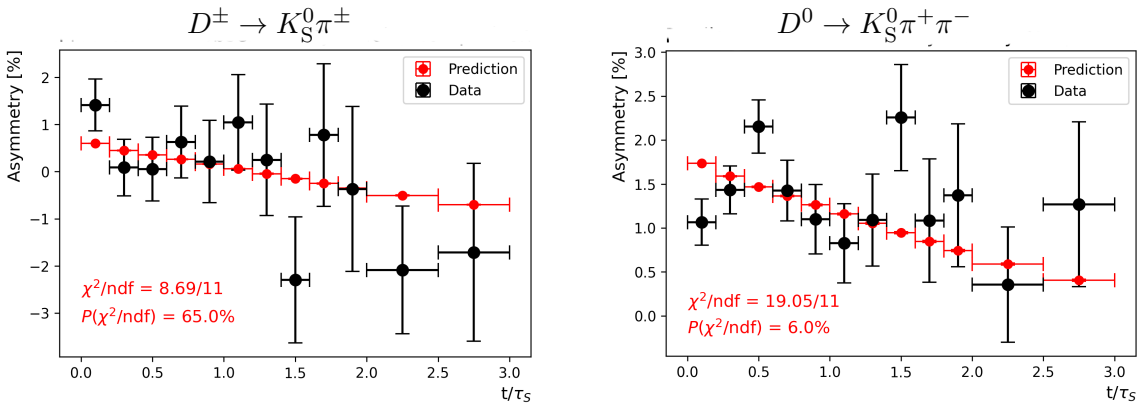

Figure 6.11: The raw asymmetry of $D^{\pm} \to K^0_S \pi^{\pm}$ and $D^0 \to K^0_S \pi^+ \pi-$ candidates and the predicted $A_{K^0/\bar{K}^0}$ as function of the K^0_S decay times. The predicted asymmetry is shifted by the average difference of measured and predicted asymmetry, to account for spurious detection and production asymmetries. The p-value for the hypothesis that predicted and observed asymmetry have the same slope is given.

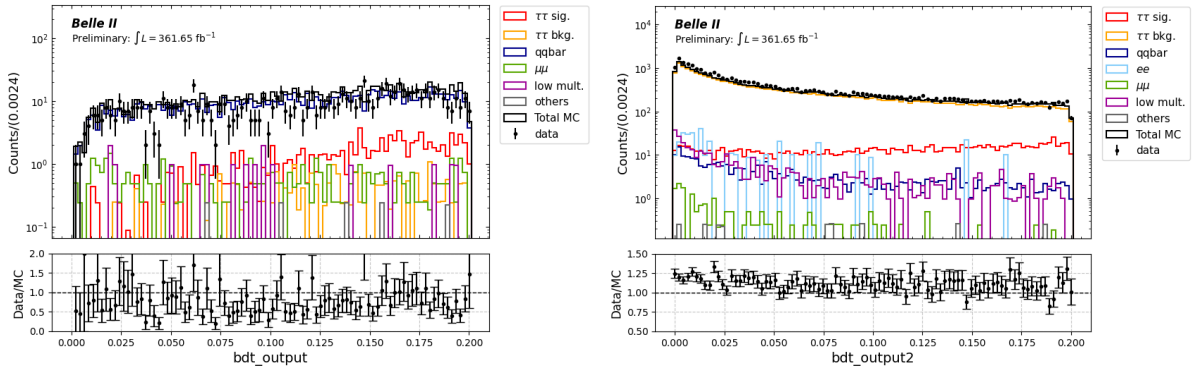

Figure 6.12: Left: Output of the first-step BDT for the muon-tagged sample in the rejected region (0–0.2), where the $q\bar{q}$ background dominates. Right: Output of the second-step BDT for the combined sample in the rejected region (0–0.2), where the $\tau\tau$ background contribution prevails.

Carlo to be dominated by $q\bar{q}$ events with a smaller component from other τ decays (see Table 5.11 and 5.12 for the Monte Carlo prediction). The accuracy of the background prediction of the Monte Carlo is checked by comparing the number of data and MC events in the rejected regions (0-0.2) of the two-step BDT. The first-step BDT output in the muon channel is used to compare data and MC predictions for the $q\bar{q}$ background contribution, while the second-step BDT output is used for the $\tau\tau$ background contribution. The data-to-MC ratios observed in these control regions indicate discrepancies, especially in the overall normalization. To account for this, a yield correction factor is derived from the data/MC ratio in the respective control regions and applied to the Monte Carlo background prediction. This correction ensures a more accurate subtraction of the background contributions in the signal region. The background is then subtracted by

computing an asymmetry correction factor through the formula

$$A_{\text{bkg}} = \sum_i f_i \times A_i \tag{6.56}$$

where f_i and A_i are the fractions and the asymmetries of the i-th background contribution predicted by MC. The correction is found to be

$$A_{\text{bkg}} = (0.019 \pm 0.013)\% \qquad \text{for the electron tag,} \tag{6.57}$$

$$A_{\text{bkg}} = (-0.014 \pm 0.016)\% \qquad \text{for the muon tag,} \tag{6.58}$$

where the errors are statistical.

6.5 Blinding Procedure

To prevent experimenter bias during the analysis, a blinding strategy was employed. This consisted of applying a hidden random offset to the final CP asymmetry computed from data. The offset was constant across all checks and visualizations, such that all comparisons (e.g., consistency checks across variables as detailed in the next Chapter) remained valid, but the absolute value of the measured asymmetry was concealed.
This blinding offset is going to be removed once the full analysis procedure, including all corrections and systematic uncertainty evaluations, was finalized and approved. Therefore, no decision in the analysis workflow was influenced by the actual value of the measured asymmetry.

Chapter 7

Systematic Uncertainties and Consistency Checks

7.1 Systematic uncertainties

In any precision measurement, a careful assessment of systematic uncertainties is essential to ensure the robustness and reliability of the result. Systematic uncertainties arise from imperfect knowledge of the detector response, modeling of background processes, and external inputs, among other sources.
This chapter summarizes the evaluation of all relevant systematic uncertainties affecting the measurement of the CP asymmetry in $\tau^{\pm} \to \pi^{\pm} K^0_S \nu$ decays. Each contribution is quantified and discussed in detail to provide a comprehensive understanding of their impact on the final result.

7.1.1 Detection Asymmetry

The systematic uncertainty associated with the detection asymmetry correction is taken as the statistical uncertainty on the measured correction itself, as quoted in Eq. 6.22. This is justified by the fact that the procedure is validated in Monte Carlo, and the observed data–MC discrepancy is a known and stable feature in Belle II. No additional uncertainty is assigned beyond the statistical precision of the correction.

7.1.2 Neutral kaon asymmetry

The systematic uncertainty associated with the neutral kaon asymmetry correction arises solely from the material budget uncertainty, which is known to an accuracy of approximately 5%, and the statistical uncertainty, as quoted in Eq. 6.54. The uncertainties in the other input values used in the computation are negligible by comparison (see Table 6.6).
To evaluate the material budget uncertainty, we adjust the detector material density (as recorded in the first part of the code) by $\pm 5\%$, and calculate the difference between the resulting values and the central value.

7.1.3 Background subtraction

The systematic uncertainty on the decay-rate asymmetry due to the background subtraction is computed using the statistical error on the background correction factor and the uncertainty in the data/MC agreement extracted from the BDT region < 0.2 where background dominates. Uncertainties in the data/MC agreement are propagated to find the corresponding uncertainty. The total background is varied within this uncertainty and the maximum change in the value of the background correction factor asymmetry was taken as the systematic error. The systematic error due to the data/MC agreement is found to be 0.009% and 0.006% for the electron and muon tagged sample respectively. The total systematic error on the decay-rate asymmetry due to the background subtraction is estimated to be 0.017% for both the electron and muon tagged sample.

7.1.4 Selection uncertainties

We used the $\tau \to 3-$ prong control sample to correct for any detector related and charge dependent selection effect. Most of the selection cuts applied to the signal were also used for the control sample. By comparing the raw asymmetries in the signal and control MC samples, any residual charge dependence in the selection criteria would be revealed as a significant difference between the two asymmetries. Since the signal and control MC asymmetries are found to be in good agreement (Eq. 6.20), no additional systematic uncertainty due to selection biases is assigned.

7.1.5 Track efficiency

Within the Belle II collaboration, tracking efficiency corrections are available; however, these corrections are currently provided without differentiation by particle type or charge. Recent studies have investigated the possibility of charge-dependent tracking efficiency corrections, but these are not yet mature enough for use in this analysis.
Furthermore, the detection asymmetry correction described previously already accounts for tracking efficiency effects, including charge-dependent differences and variations between particle types present in the event. Therefore, no additional systematic uncertainty related to track efficiency corrections is assigned.

7.1.6 Impact of the tag track PID

The LID efficiency corrections applied in this analysis are charge-dependent, reflecting known differences in the detector response to positively and negatively charged leptons. Since the control sample uses the same tag track PID criteria as the signal sample, any charge-dependent PID effects are present in both. Therefore, these effects are already accounted for within the detection asymmetry correction derived from the control sample. As a result, no additional systematic uncertainty related to tag track PID is assigned.

7.1.7 $q\bar{q}$ and $\tau\tau$ background asymmetry

Since both the $q\bar{q}$ and $\tau\tau$ background constitutes a few percentage of the total sample, their impact on the overall charge asymmetry is limited. Moreover the statistical error on the asymmetry value from MC prediction was already taken into account in the evaluation of the systematic error of the background subtraction. We do not assign any additional systematic uncertainty due to these background asymmetries.

7.1.8 Forward-backward asymmetry

The production of $\tau^+\tau^-$ events has a slight forward-backward asymmetry (A_{FB}). This could manifest into an asymmetry if there is difference in the selection efficiency between the forward and backward regions of the detector.
The A_{FB} is also present in the control sample and the nominal MC sample. The error associated with A_{FB} is already accounted for and thus not listed as an extra source of systematic error.

7.1.9 MC predictions and branching fractions

The decay-rate asymmetry, after subtracting the background, applying the neutral kaon interaction correction and the detection asymmetry correction, still includes the other τ decays with K^0_S in the final state. Specifically, the decay-rate asymmetry is diluted due to $\tau^- \to K^- K^0_S \nu_\tau$ and $\tau^- \to \pi^- K^0 \bar{K}^0 \nu_\tau$ decays. The measured asymmetry A is related to the signal asymmetry A_1 and the remaining background asymmetries A_2 and A_3 by:

$$\begin{aligned} A &= \frac{f_1 A_1 + f_2 A_2 + f_3 A_3}{f_1 + f_2 + f_3} \\ &= \left(\frac{f_1 - f_2}{f_1 + f_2 + f_3} \right) A_{SM} \end{aligned} \tag{7.1}$$

where f_1, f_2 and f_3 are the fractions of $\tau^- \to \pi^- K^0_S (\geq 0\pi^0)\nu_\tau$, $\tau^- \to K^- K^0_S (\geq 0\pi^0)\nu_\tau$, and $\tau^- \to \pi^- K^0 \bar{K}^0 (\geq 0\pi^0)\nu_\tau$ in the total selected sample, shown in Tables 5.11 and 5.12. Within the SM, $A_1 = -A_2 = A_{SM} = (0.33 \pm 0.01)\%$ because the K^0_S in $\tau^- \to \pi^- K^0_S (\geq 0\pi^0)\nu_\tau$ is produced via a K^0, whereas the K^0_S in $\tau^- \to K^- K^0_S (\geq 0\pi^0)\nu_\tau$ is produced via a $\bar{K}^0$. Furthermore, $A_3 = 0$ in the SM because the asymmetries due to the K^0 and $\bar{K}^0$ will cancel each other. To compare the measured asymmetry A with the theoretical prediction, it must be scaled by the dilution factor:

$$\frac{f_1 - f_2}{f_1 + f_2 + f_3} \tag{7.2}$$

The uncertainty on this factor accounts for statistical uncertainties from the Monte Carlo predictions and uncertainties in the branching fractions, with the latter being dominant. The relevant branching fractions and their uncertainties are listed in Table 7.1. We get the following values for the dilution factor in the e-tag and μ-tag sample respectively:

$$e\text{-tag} : 0.76 \pm 0.02 \qquad \mu\text{-tag} : 0.75 \pm 0.03. \tag{7.3}$$

7.1.10 Summary of systematic uncertainties

Table 7.2 summarizes the main systematic uncertainties considered in this analysis. The individual contributions have been evaluated as described in the previous sections. The total

Decay	TauDecayMode2	BF
$\tau^- \to \pi^- K^0_S \nu_\tau$	226	0.004192 ± 0.000069
$\tau^- \to \pi^- \pi^0 K^0_S \nu_\tau$	126	0.001909 ± 0.000065
$\tau^- \to \pi^- 2\pi^0 K^0_S \nu_\tau$	30	0.000131 ± 0.000113
$\tau^- \to K^- K^0_S \nu_\tau$	228	0.000743 ± 0.000017
$\tau^- \to K^- \pi^0 K^0_S \nu_\tau$	124	0.000750 ± 0.000035
$\tau^- \to \pi^- K^0_S K^0_L \nu_\tau$	123	0.001081 ± 0.000241
$\tau^- \to \pi^- \pi^0 K^0_S K^0_L \nu_\tau$	36	0.000325 ± 0.000119
$\tau^- \to \pi^- K^0_S K^0_S \nu_\tau$	121	0.000235 ± 0.000006
$\tau^- \to \pi^- \pi^0 K^0_S K^0_S \nu_\tau$	34	0.000018 ± 0.000002

Table 7.1: Signal decay modes with their PDG2020 τ branching fractions and the corresponding mode identifiers used in the τ-pair MC.

systematic uncertainty is obtained by combining all contributions in quadrature. This overview provides a concise reference to the relative impact of each source on the measurement.

Source	**Uncertainty (%)**	
	e-tag	μ-tag
Detector Uncertainty	0.05	0.06
$K^0 - \bar{K}^0$ Nuclear Interaction	0.01	0.01
Background	0.02	0.02
Total	0.05	0.06

Table 7.2: Systematic Uncertainties

7.2 Consistency checks

The asymmetry and the related main corrections were checked as a function of these four variables:

- Experiment number (time period);
- K^0_S polar angle;
- K^0_S momentum;
- K^0_S flight distance;

7.2.1 Experiment Number

To ensure the robustness of the measurement, it is essential to verify that the extracted CP asymmetry and its associated corrections remain stable throughout the data-taking period. This is assessed through a series of consistency checks performed as a function of the experiment number, which represents the chronological order of data collection.

Detection asymmetry correction The detection asymmetry correction is evaluated in bins of experiment number and compared between the signal and control Monte Carlo (MC) samples. As shown in the left panel of Fig. 7.1, the results for both electron- and muon-tagged events are stable and compatible with the integrated correction, represented by the colored band. The agreement between signal and control samples in each bin remains within 1σ, supporting the reliability of the control sample for the correction extraction.

Neutral kaon asymmetry correction Fig. 7.1 (right) presents the neutral kaon asymmetry correction as a function of experiment number. The observed values show no significant deviations or trends across the data-taking period. Minor fluctuations are consistent with expected variations in the material budget and detector conditions over time, and remain well within statistical uncertainties.

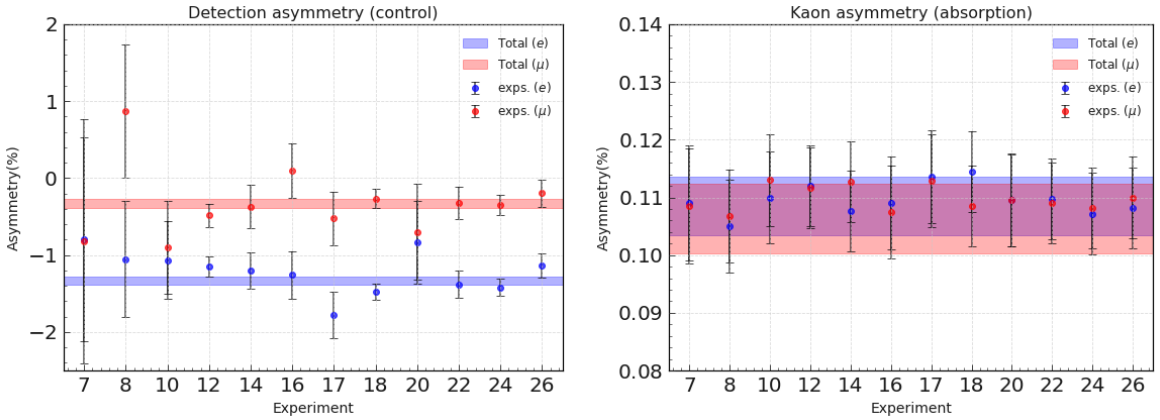

Figure 7.1: Detection asymmetry correction (left) and neutral kaon asymmetry correction (right) as a function of the experiment number. The integrated values are indicated by the colored bands.

Background modeling The MC composition of τ and $q\bar{q}$ backgrounds is checked across all experiment number bins. The fractional yields are found to be stable within statistical uncertainties, confirming that no significant variations in the background composition occurred throughout the data-taking period. Consequently, the background correction and dilution factors are taken from the integrated MC sample without introducing a time dependence.

Stability of the raw asymmetry The blinded A_1 asymmetry, after applying all relevant corrections, is scanned as a function of experiment number. The results, shown in Fig. 7.2, are consistent across all bins with the integrated asymmetry value for both tagging channels. A common random shift is applied to preserve the blinding. These findings support the stability of the measurement and the absence of time-dependent systematic effects.

7.2.2 K^0_S polar angle

To verify the stability of the measurement and corrections across different kinematic regions, we study the A_1 asymmetry as a function of the K^0_S polar angle. This is important because

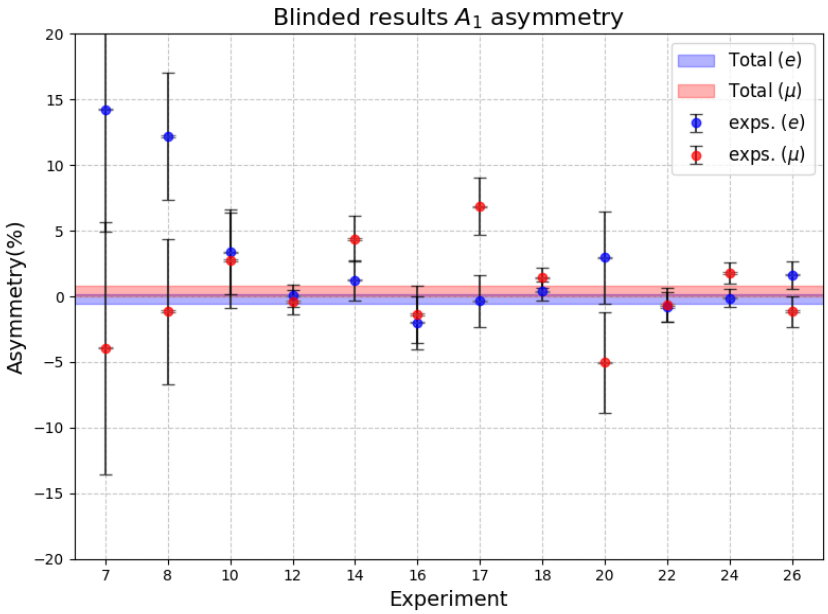

Figure 7.2: Blinded A_1 asymmetry results for electron (blue) and muon (red) tag samples in bins of experiment number. The integrated asymmetry is indicated by the colored band.

detector acceptance, material effects, and reconstruction efficiencies vary with polar angle and could bias the asymmetry measurement if not properly corrected.
The total sample is divided into four bins of K^0_S polar angle (in radians) with approximately uniform statistics:

$$[0, 0.89], \quad [0.89, 1.26], \quad [1.26, 1.67], \quad [1.67, 3.14] \tag{7.4}$$

Detection asymmetry correction The MC detection asymmetry is compared between signal and control samples for each bin. Since the control sample does not contain a K^0_S, it is not binned, and the full control sample is used for each bin to reduce statistical uncertainty. After applying pion reweighting on the control sample, the MC asymmetry comparison is shown in Fig. 7.3.
A significant discrepancy between control and signal MC is observed in the first and last bins, attributed to differing τ polar angle distributions in the control and signal samples. These distributions affect the forward-backward asymmetry and thus the detection asymmetry. Fig. 7.4 shows the normalized τ polar angle (in CMS) distributions for each K^0_S polar angle bin, highlighting the shape differences responsible for the discrepancy.
To mitigate this, the τ polar angle distribution in the control sample is reweighted to match the signal distribution before recalculating the MC detection asymmetry. The reweighted MC asymmetry comparison is shown in Fig. 7.5. This reweighting is not necessary for the integrated sample but improves consistency in the binned analysis.

Neutral kaon asymmetry correction The neutral kaon asymmetry correction is evaluated in bins of K^0_S polar angle and shown in Fig. 7.6. Larger corrections appear in the forward region due to increased material interactions, consistent with expectations.

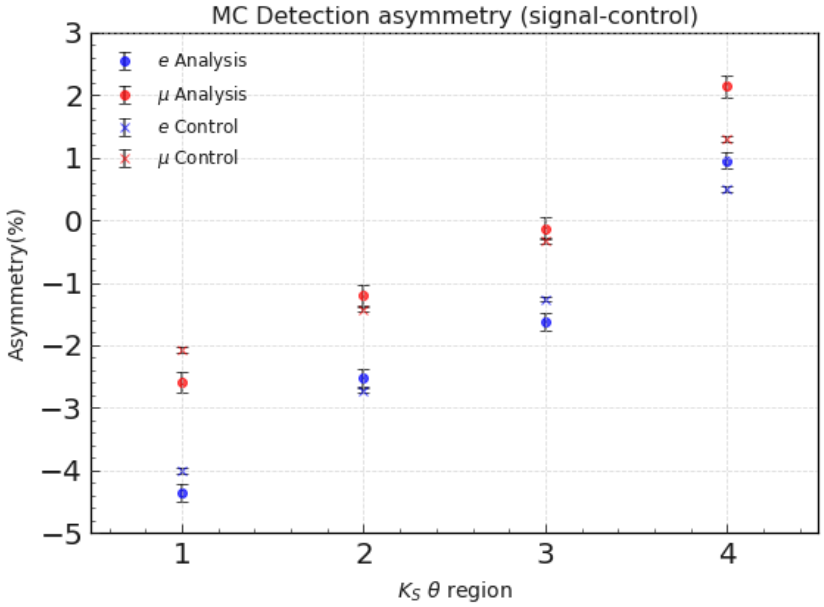

Figure 7.3: MC detection asymmetry in signal (circle) and control (cross) samples for electron (blue) and muon (red) tags as a function of K^0_S polar angle.

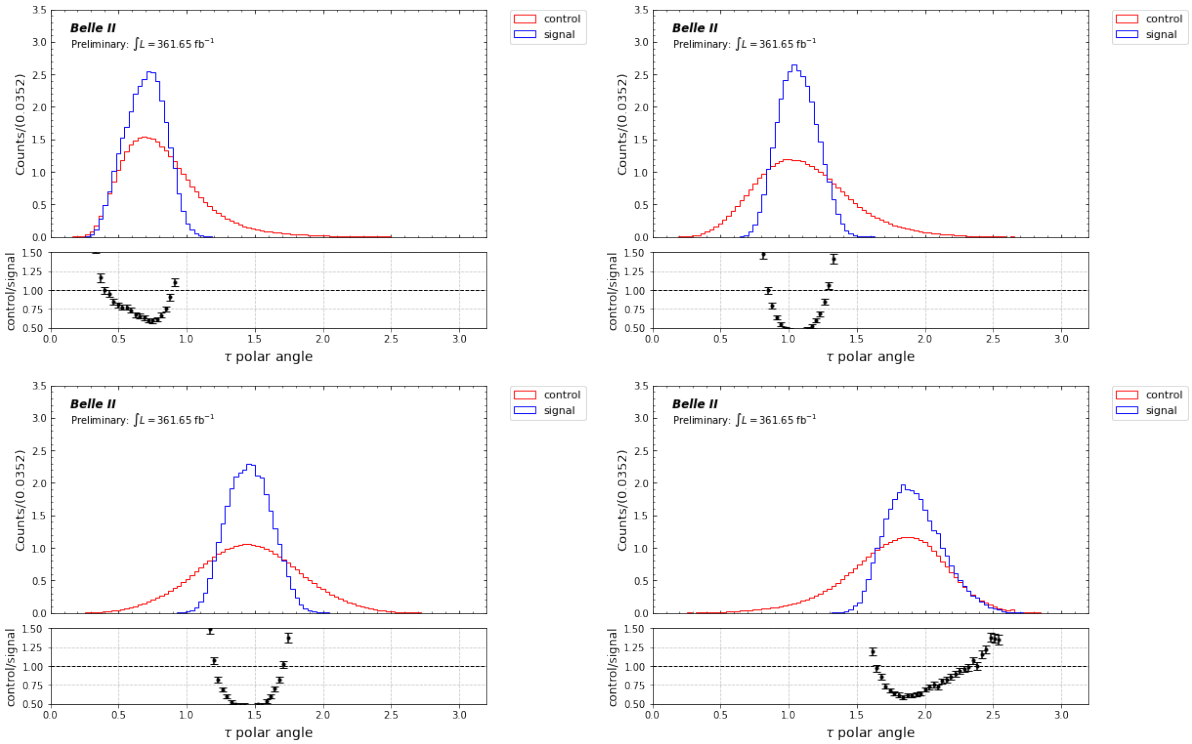

Figure 7.4: τ polar angle (in CMS) distribution for each K^0_S polar angle bin. The control sample is shown in red and the signal sample in blue, normalized to unit area.

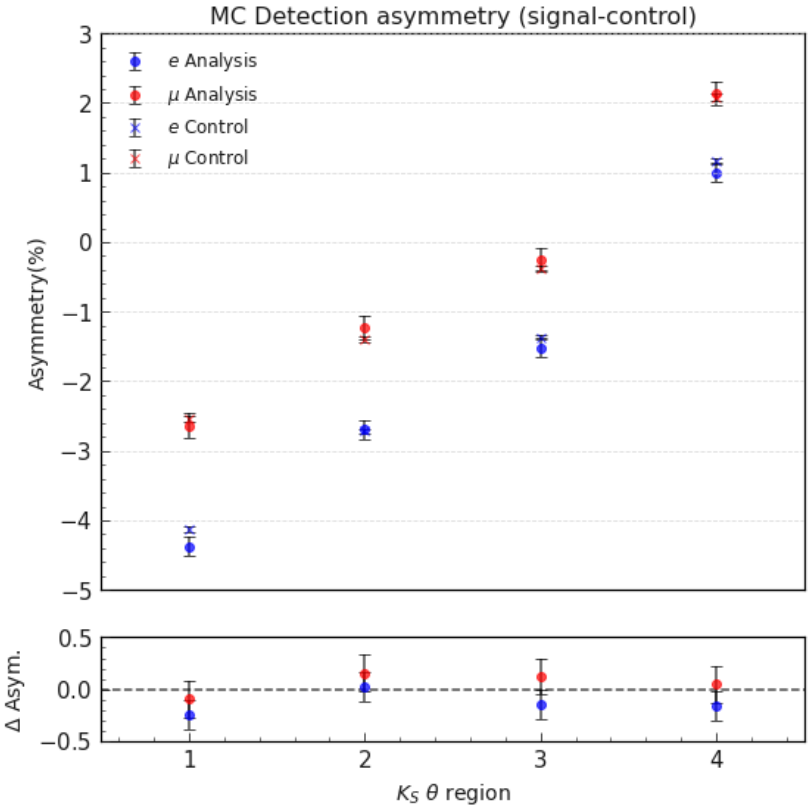

Figure 7.5: MC detection asymmetry in signal (circle) and control (cross) samples for electron (blue) and muon (red) tags after the τ polar angle reweighting.

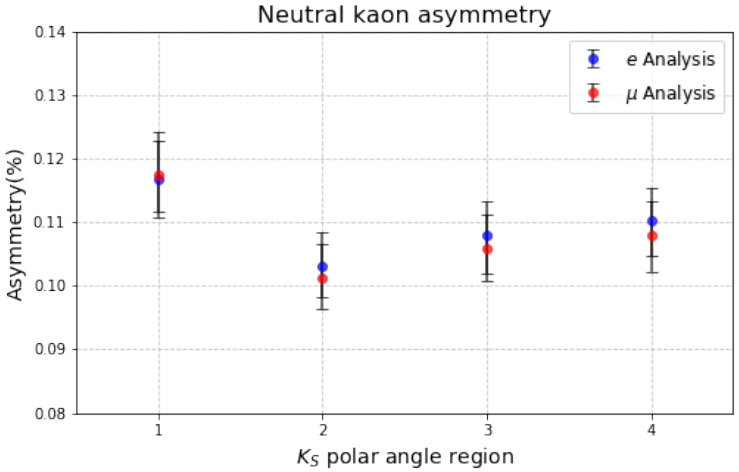

Figure 7.6: Neutral kaon asymmetry correction for electron (blue) and muon (red) tag samples as a function of K^0_S polar angle.

Background correction validation The data/MC yield ratios for τ and $q\bar{q}$ backgrounds are evaluated in each bin, as shown in Fig. 7.7. The corrections are stable across bins and consistent with the integrated sample values.

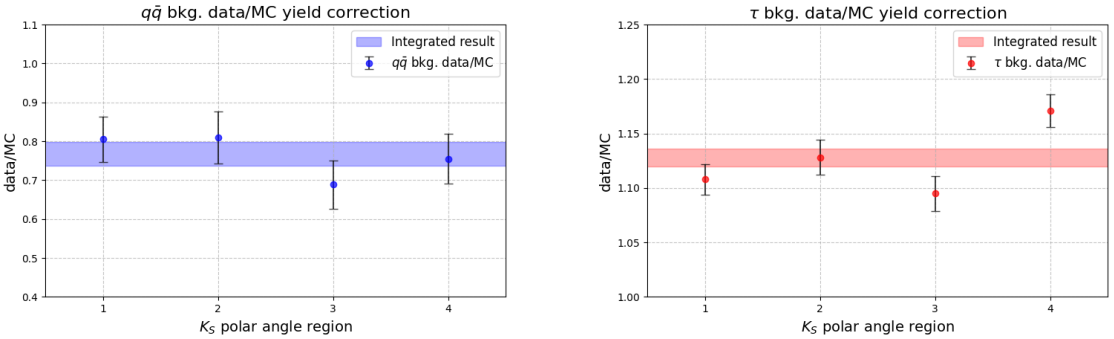

Figure 7.7: $q\bar{q}$ (left) and τ (right) background data/MC yield correction as a function of K^0_S polar angle. These corrections are applied in the background subtraction.

Final asymmetry check After applying all corrections, the blinded A_1 asymmetry is computed in each bin and shown in Fig. 7.8. The results are consistent across bins and agree with the integrated sample value.

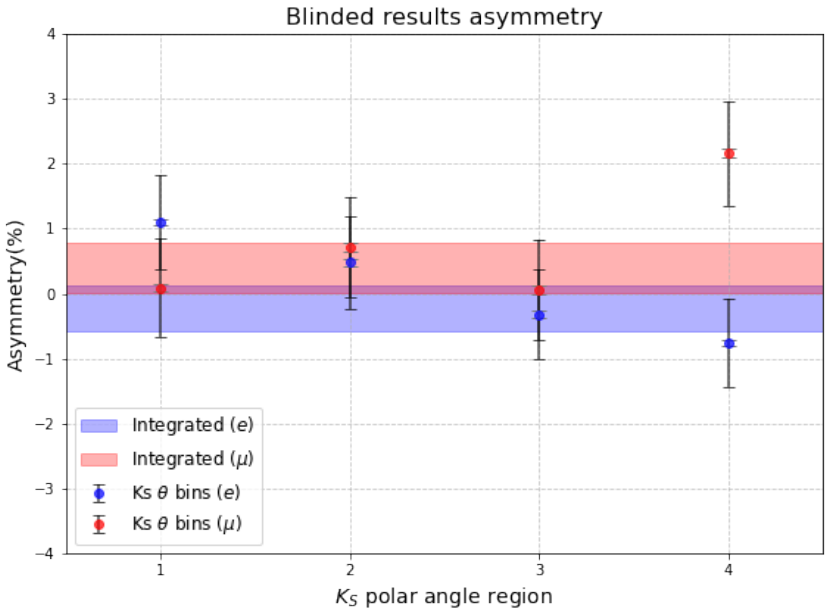

Figure 7.8: Blinded A_1 asymmetry results for electron (blue) and muon (red) tag samples in bins of K^0_S polar angle. The colored band shows the integrated sample asymmetry.

7.2.3 K^0_S momentum

Studying the stability of the asymmetry measurement as a function of the K^0_S momentum (in GeV) is crucial because the detector response, material interactions, and reconstruction efficiencies can depend strongly on particle momentum. These effects can introduce momentum-dependent biases if not properly corrected, potentially impacting the accuracy of the measured asymmetry.
The total sample is divided into four bins of K^0_S momentum, chosen to yield approximately uniform statistics:

$$[0, 1.42], \quad [1.42, 1.93], \quad [1.93, 2.64], \quad [2.64, 7.20] \tag{7.5}$$

Detection asymmetry correction The MC detection asymmetry is compared between signal and control samples in each momentum bin. Because the control sample does not contain a true K^0_S, a pseudo momentum is constructed by summing the momenta of extra pions to apply the same binning scheme. The detection asymmetry comparison is shown in Fig. 7.9.

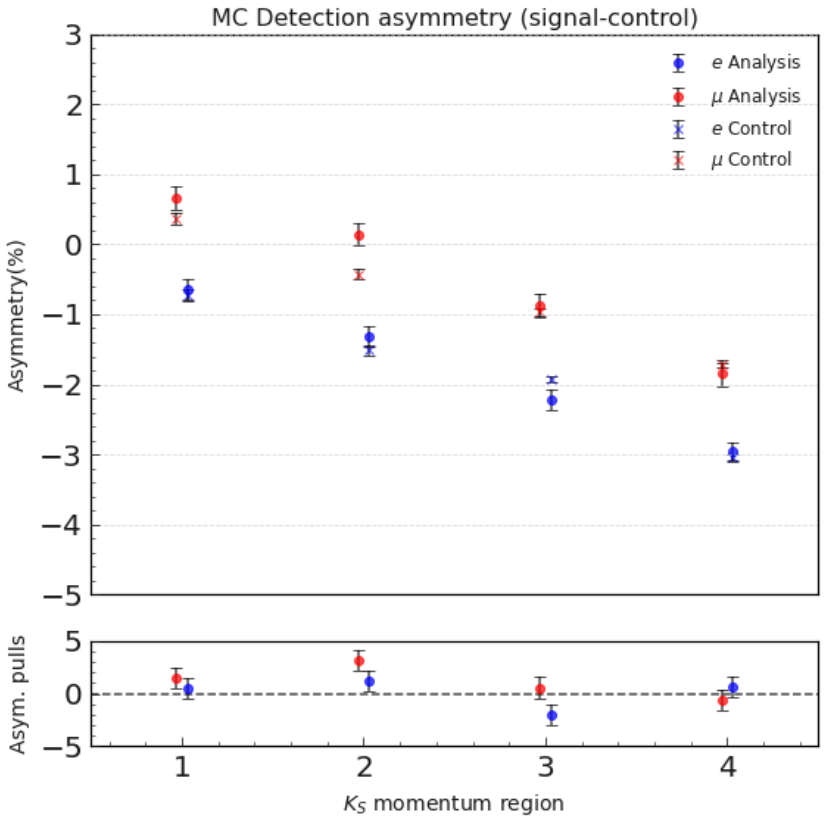

Figure 7.9: MC detection asymmetry in signal (circle) and control (cross) samples for electron (blue) and muon (red) tags as a function of K^0_S momentum. The lower panel shows the pull values indicating the significance of differences.

The τ polar angle distributions between signal and control samples are also checked and found to be consistent across bins. Unlike the polar angle case, no additional τ reweighting is needed here, and it has been verified that applying such reweighting does not significantly alter the asymmetries.

The pull values in the lower subplot of Fig. 7.9 show that the differences between signal and control detection asymmetries remain within 2σ in nearly all bins, indicating good agreement within statistical uncertainties.

Neutral kaon asymmetry correction The neutral kaon asymmetry correction is recalculated in bins of K^0_S momentum, shown in Fig. 7.10. The shape of the correction follows the expected behavior from Eq. 6.35, where the asymmetry originates from the difference in neutral kaon production cross sections (K^0 versus $\bar{K}^0$) and scales inversely with kaon momentum.

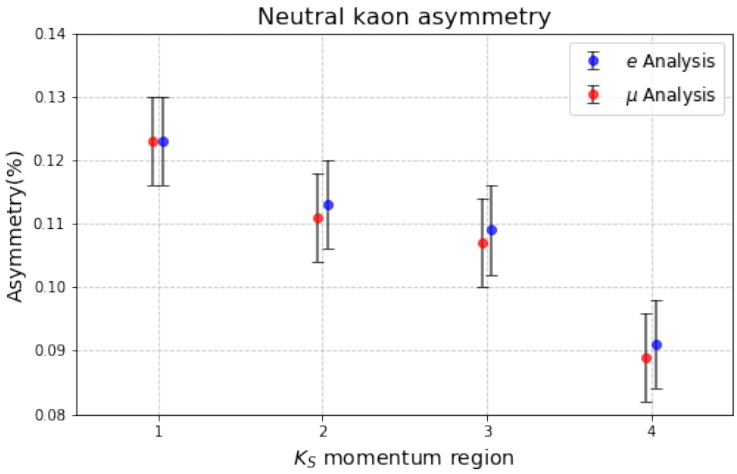

Figure 7.10: Neutral kaon asymmetry correction for electron (blue) and muon (red) tag samples as a function of K^0_S momentum.

Background correction validation The background yield corrections for $q\bar{q}$ and τ backgrounds are evaluated as a function of K^0_S momentum, as shown in Fig. 7.11. These corrections ensure that any momentum-dependent biases in background estimation are properly accounted for in the final measurement.

Asymmetry stability Because the relative contributions of the asymmetry components A_1, A_2, and A_3 vary significantly with momentum, the dilution factors are recalculated in each bin. The blinded A_1 asymmetry results as a function of K^0_S momentum are shown in Fig. 7.12. The asymmetry values are mutually consistent across bins and agree with the integrated measurement, confirming the robustness of the corrections.

7.2.4 K^0_S flight distance

Examining the asymmetry as a function of the K^0_S flight distance is motivated by the fact that longer-lived K^0_S mesons traverse more detector material, which can impact the reconstruction efficiency and the probability of interactions. These effects may introduce systematic biases if

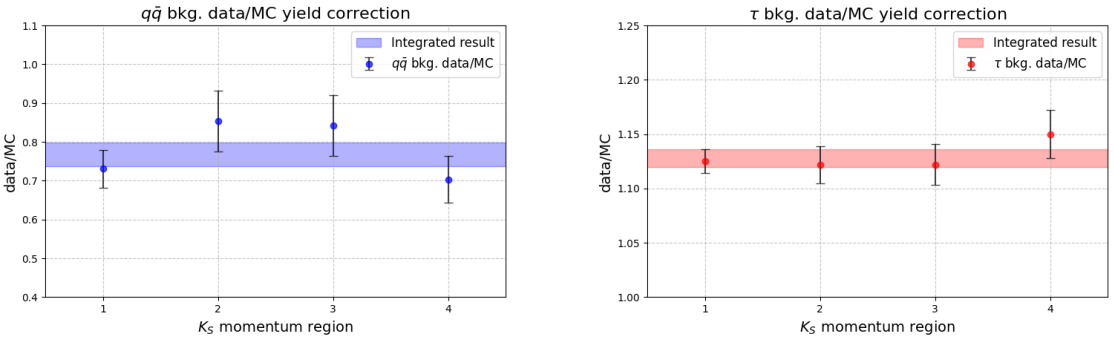

Figure 7.11: $q\bar{q}$ (left) and τ (right) background data/MC yield corrections as a function of K^0_S momentum. These corrections are applied in the background subtraction for data.

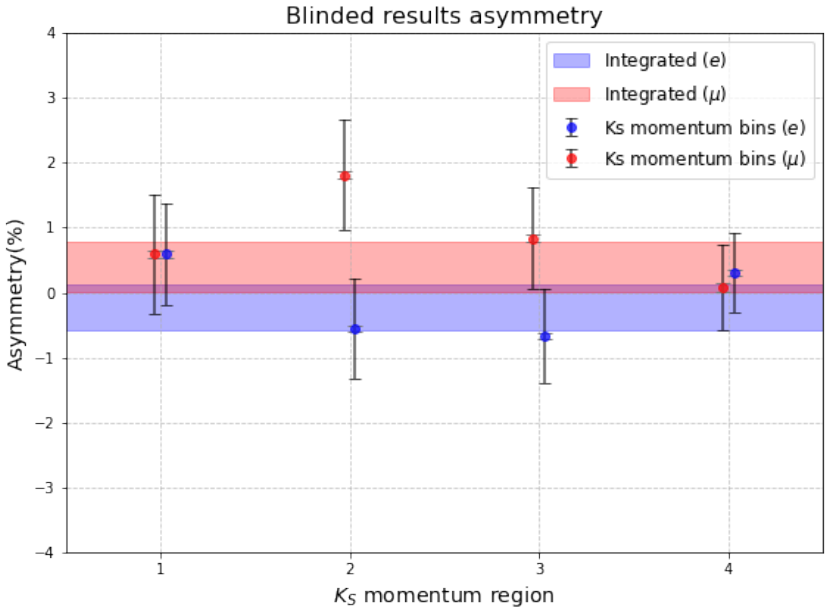

Figure 7.12: Blinded A_1 asymmetry results for electron (blue) and muon (red) tag samples in bins of K^0_S momentum. The colored band shows the integrated sample asymmetry.

not properly modeled, particularly in the context of CP violation where decay time dependencies are expected.
The full data sample is divided into four bins of K^0_S flight distance (in cm), chosen to yield roughly uniform statistics:

$$[0, 3], \quad [3, 6.5], \quad [6.5, 13], \quad [13, 300] \tag{7.6}$$

Detection asymmetry correction The MC detection asymmetry is compared between signal and control samples across bins of K^0_S flight distance, as shown in Fig. 7.13. The results indicate good agreement between the two samples for both electron- and muon-tagged events. The pull distribution (shown in the lower panel of the figure) further confirms that any discrepancies are within statistical uncertainties.

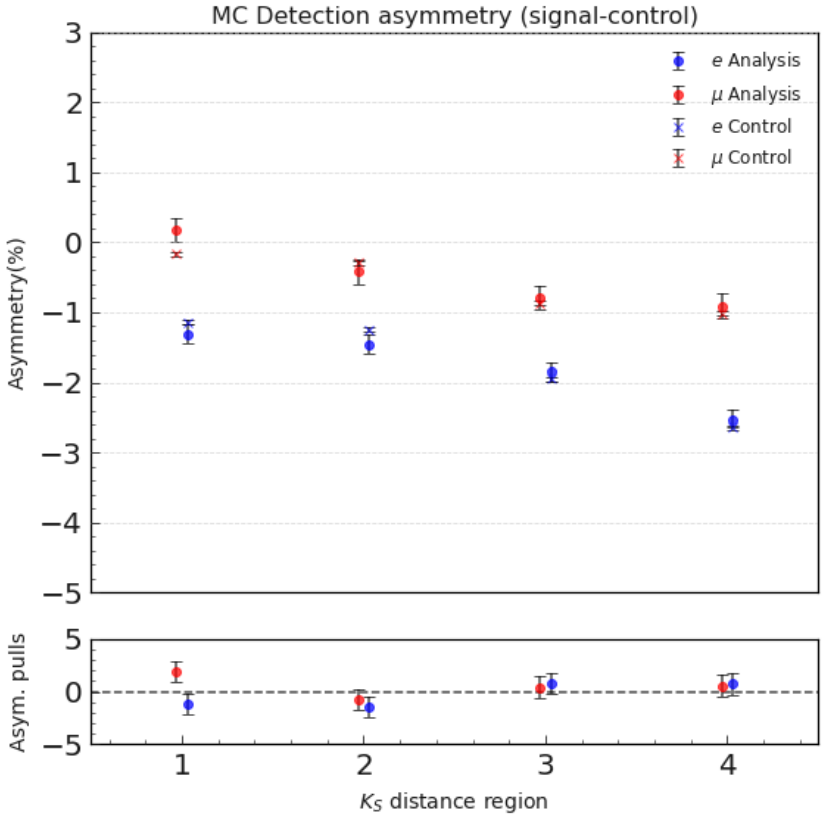

Figure 7.13: MC detection asymmetry in signal (circle) and control (cross) samples for electron (blue) and muon (red) tags as a function of K^0_S flight distance. The lower panel displays the pull values for each bin.

Neutral kaon asymmetry correction The correction for the neutral kaon asymmetry is evaluated as a function of K^0_S flight distance, shown in Fig. 7.14. The shape of the correction reflects the increasing amount of detector material traversed at larger flight distances, which affects the relative interaction rates of K^0 and $\bar{K}^0$ mesons. This behavior is consistent with expectations from material-induced asymmetries.

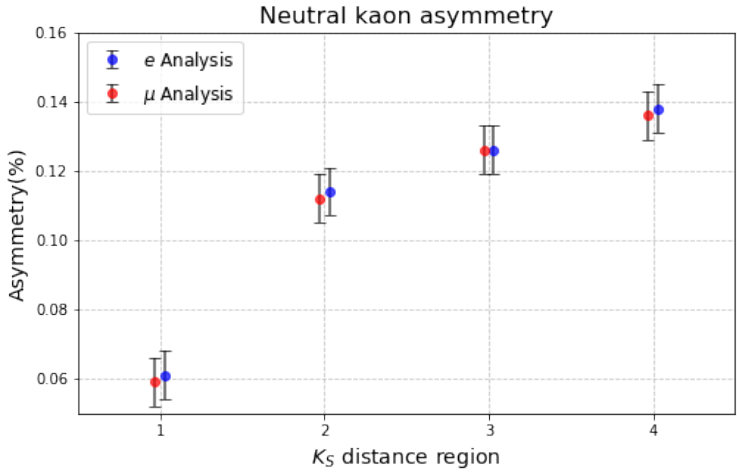

Figure 7.14: Neutral kaon asymmetry correction for electron (blue) and muon (red) tag samples as a function of K^0_S flight distance.

Background correction validation The background data/MC yield corrections for $q\bar{q}$ and τ backgrounds are evaluated in each flight distance bin and shown in Fig. 7.15. These corrections are found to be consistent with the corresponding values for the integrated sample, indicating no significant flight distance dependence in the background modeling.

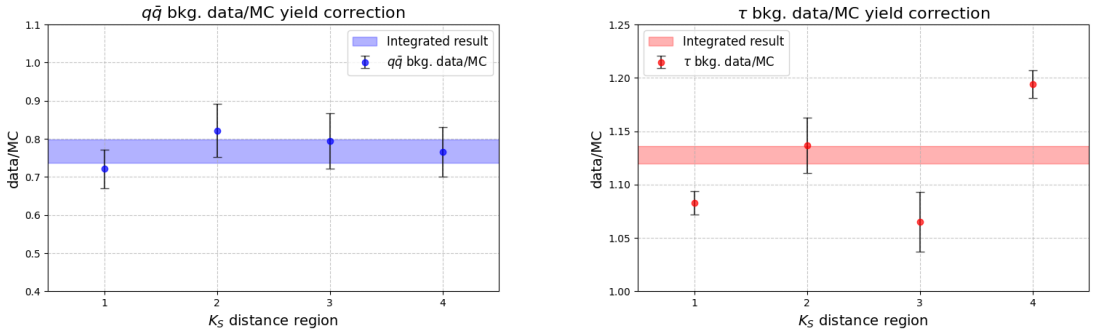

Figure 7.15: $q\bar{q}$ (left) and τ (right) background data/MC yield corrections as a function of K^0_S flight distance.

Asymmetry stability The A_1 CP asymmetry is re-evaluated in bins of K^0_S flight distance, with blinded results presented in Fig. 7.16. While the asymmetry is theoretically expected to increase with flight distance due to its correlation with the K^0_S decay time, this trend is not clearly visible in the data, primarily due to the limited statistical precision in each bin. Nevertheless, the asymmetry values remain compatible with the integrated result within uncertainties.

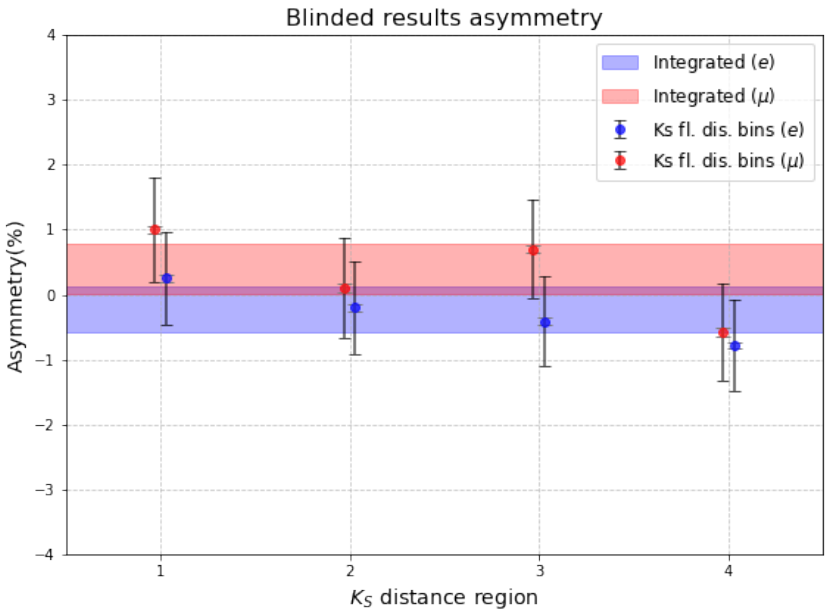

Figure 7.16: Blinded A_1 asymmetry results for electron (blue) and muon (red) tag samples in bins of K^0_S flight distance. The integrated sample asymmetry is indicated by the colored band.

Chapter 8

A_3 Asymmetry Paper

It is known that CP violation intrinsic to the neutral kaon system can influence decays with K^0 or K^0_S in the final state. This effect depends on the experimental setup and the applied cuts. The measured time-integrated CP asymmetry is influenced by the experimental detection efficiency as a function of both the energy in the lab frame and the decay time of the kaon. This implies a non-vanishing CP asymmetry for the decay channel $\tau \to \pi K_S K_L \nu_\tau$. A theoretical prediction for this asymmetry and its experimental relevance is discussed in this Chapter. The content presented in this Chapter is the result of a collaborative effort between the analysts of the main analysis and the theoretical team. Please note that all the results discussed here are still under review and have not yet been made public. Therefore, these findings should be considered preliminary and should not be regarded as final or definitive.

8.1 Introduction

In the main analysis, the total measured asymmetry includes background contributions from other τ decays, particularly those involving two kaons:

$$A_2 = \frac{\Gamma(\tau^+ \to K^+ K_S \bar{\nu}_\tau) - \Gamma(\tau^- \to K^- K_S \nu_\tau)}{\Gamma(\tau^+ \to K^+ K_S \bar{\nu}_\tau) + \Gamma(\tau^- \to K^- K_S \nu_\tau)} \tag{8.1}$$

$$A_3 = \frac{\Gamma(\tau^+ \to \pi^+ K_L K_S \bar{\nu}_\tau) - \Gamma(\tau^- \to \pi^- K_L K_S \nu_\tau)}{\Gamma(\tau^+ \to \pi^+ K_L K_S \bar{\nu}_\tau) + \Gamma(\tau^- \to \pi^- K_L K_S \nu_\tau)} \tag{8.2}$$

These two decays have an impact on the overall asymmetry measurement since the SM asymmetry A_1 from $\tau^- \to K^- K_S \nu_\tau$ is equal and opposite to the $\tau^- \to \pi^- K_S \nu_\tau$ asymmetry ($A_1 = -A_2$). This is beacuse the K_S in the $\tau^- \to \pi^- K_S \nu_\tau$ mode is produced by a $\bar{K}^0$ whereas the K_S in the $\tau^- \to K^- K_S \nu_\tau$ mode is produced by a K^0. The asymmetry A_3 from $\tau^- \to \pi^- K^0 \bar{K}^0 \nu_\tau$ mode is expected to be zero, which in turn dilutes the overall asymmetry. This work aims to refine the theoretical prediction of the A_3 asymmetry.
A theoretical estimation for the CP asymmetry A_1 was first provided in [5]

$$A_1 \simeq 2\Re(\epsilon) \simeq 3.3 \times 10^{-3}, \tag{8.3}$$

where ϵ is the CP violation measure in neutral kaon mixing. Later, in [92], this prediction was reviewed showing the importance of the $K_L - K_S$ interference term in the computation of the decay rate asymmetry. It was shown that the CP asymmetry ratio A_1 depends on the decay

time of the kaon, and in particular, on the experimental cuts.
To understand the importance of the experimental cuts we define the experimental measure asymmetry

$$A_{Exp,P} = \frac{\int_0^\infty dt[f_P(t)\Gamma(t) - \bar{f}_P(t)\bar{\Gamma}(t)]}{\int_0^\infty dt[f_P(t)\Gamma(t) + \bar{f}_P(t)\bar{\Gamma}(t)]} \tag{8.4}$$

to be the CP asymmetry in the case where the neutral kaon decays into $\pi^+\pi^-$. Here, Exp label the fact that we refer to the experimental measured asymmetry, t is the time in the kaon rest frame, P is a subscript that indicates the process from which the kaons originate, and f_P and $\bar{f}_P$ is the efficiency function discussed in detailed below. The rates,

$$\Gamma(t) = \Gamma(K^0(t) \to 2\pi), \qquad \bar{\Gamma}(t) = \Gamma(\bar{K}^0(t) \to 2\pi), \tag{8.5}$$

are defined as the decay rate for K^0 and $\bar{K}^0$ as a function of the decay time t in the kaon's reference frame.
As pointed out in [92], the decay rate CP asymmetry $A_{Exp,P}$ defined in Eq. 8.4, depends on the function, f_P, that encodes the experimental reconstruction efficiency parameterized by the $K_S \to \pi\pi$ decay time t.
In this work, we extend the analysis presented in [92] about the rule of the efficiency function $f_P(t)$ and its application for realistic experiments. The dependence of $f_P(t)$ on the energy, momentum, and decay time distributions of the kaons emitted in the specific process P is discussed. In particular this work concentrates on the $\tau \to \pi K_S K_L \nu_\tau$ decay mode. It originated from the $\tau \to \pi K^0 \bar{K}^0 \nu_\tau$ decay where the kaon and anti-kaon ended up decaying as a K_S and K_L. In an ideal experiment, the time-integrated asymmetry due to K^0 and $\bar{K}^0$ cancel each other between the K_S and the K_L decays. We show that the time and energy dependence of the reconstruction efficiency makes $A_3 \neq 0$ in a realistic experiment.
The importance of such background in the main analysis is then discussed. This implies that for the anticipated precision of the A_1 analysis, it is safe to assume $A_3 = 0$ as the errors introduce by it is negligible compared to other sources of error.

8.2 Efficiency function

The efficiency function $f_P(t)$ in Eq. 8.4 is defined in the kaon rest frame. Yet, what set it, is the lab frame, that is the detector and how things are processed. In general, there is an efficiency function in the lab frame that depends on the energy, momentum, whether the particle is a K^0 or $\bar{K}^0$, and other aspects of the event. Thus, a laboratory frame efficiency function $F(L, E, X_P)$ is defined, which gives the reconstruction efficiency of the experiment as a function of the decay length L, energy E, and any other relevant parameters collected in the multivariable symbol X_P. In order to get the efficiency function in the kaon rest frame $F_P(t)$, we need to boost it from the lab frame to the kaon rest frame. Obtaining the general result is complicated as it depends on many parameters, but a reasonable approximation can be made: F is only a function of the decay length and energy in the lab frame, that is $F(L, E)$. This function can be written as $F(\beta\gamma t, E)$, where the kaon rest frame decay time t and the lab frame energy of the kaon E is used instead. Under that assumption, the efficiency function is parameterized by the kaon decay

time t in its rest frame:

$$f_P(t) = \int dE\ S_P(E) F(\beta\gamma t, E) \tag{8.6}$$

Here $S_P(E)$ is the kaon energy spectrum in the lab frame. Eq. 8.6 explicitly shows the dependence of the reconstruction efficiency $f_P(t)$ on the energy distribution of the kaon, which depends on the specific process P. As a consequence, using Eq. 8.4, the CP asymmetry will also be dependent on the process P that originated the $K_{\rm S}$ in final state.

8.3 CP Violation for decays with two neutral kaons

The energy dependence of the cuts makes the CP asymmetry ratio in Eq. 8.2, non-vanishing. In terms of the kaon interaction eigenstates created, we are looking at the process $\tau \to \pi K^0 \bar{K}^0 \nu_\tau$, where the $K^0\bar{K}^0$ are identified as a $K_{\rm S}$ and $K_{\rm L}$. Here as $K_{\rm S}$ is identified by a $\pi\pi$ system in final state. Experimentally, $K_{\rm L}$ is missing in the final detection due to its long lifetime. This makes A_3 a background to the A_1 measure.

For an ideal experiment without cuts and perfect efficiency, A_3 is zero. The reason is that since both K^0 and $\bar{K}^0$ are produced, the probability to have a $\pi\pi$ system in final state, is the same for the τ^+ and the τ^- decay. In a realistic experiments the cuts generate an asymmetry. In particular, this happens because of the energy distribution dependence of the efficiency function. This is due to the fact the kaon interaction eigenstates K^0 and $\bar{K}^0$ are produced with different energy spectrum in the τ decay. Thus, a more energetic K^0 has different probability to emerge from a τ^+ or a τ^-. As a consequence, the experimental cuts can create a difference in the sample of K^0 and $\bar{K}^0$ coming from τ^+ and τ^-.

To write this in formulas, let's assume that K^0 and $\bar{K}^0$ are emitted with a different energy spectra in the $\tau^\pm \to \pi^\pm K^0 \bar{K}^0 \nu_\tau$ process. We define $S^\pm_{K^0}(E)$ and $S^\pm_{\bar{K}^0}(E)$ to be the normalized energy spectra of the K^0 and the $\bar{K}^0$ emitted in the decay of the $\tau^\pm$ in the laboratory frame. If $F(L, E)$ is the reconstruction efficiency in the laboratory frame, then the kaon's frame efficiency function for the K^0 and $\bar{K}^0$ emitted by the $\tau^\pm$ are

$$f^\pm_{K^0} = \int dE\ S^\pm_{K^0}(E) F(\beta\gamma t, E) \tag{8.7}$$

$$f^\pm_{\bar{K}^0} = \int dE\ S^\pm_{\bar{K}^0}(E) F(\beta\gamma t, E) \tag{8.8}$$

To simplify the notation we define:

$$R^\pm_X = \int dt f^\pm_X(t)\Gamma(t) \tag{8.9}$$

$$\bar{R}^\pm_X = \int dt f^\pm_X(t)\bar{\Gamma}(t) \tag{8.10}$$

where $X = K^0, \bar{K}^0$. In the case of $\tau^\pm \to \pi^\pm K^0 \bar{K}^0 \nu_\tau$ the total rate to have a $K_{\rm S}$ in final state is $R^\pm_{K^0} + \bar{R}^\pm_{\bar{K}^0}$. Thus, the asymmetry A_3 that we measure is:

$$A_3 = \frac{\left[R^+_{K^0} + \bar{R}^+_{\bar{K}^0}\right] - \left[R^-_{K^0} + \bar{R}^-_{\bar{K}^0}\right]}{\left[R^+_{K^0} + \bar{R}^+_{\bar{K}^0}\right] + \left[R^-_{K^0} + \bar{R}^-_{\bar{K}^0}\right]} \tag{8.11}$$

This expression can be simplified with some manipulation assuming that there is no direct CP violation the decay of the $\tau^{\pm}$, that is $S^{\pm}_{K^0}(E) = S^{\mp}_{\bar{K}^0}(E)$, which means that the energy spectrums of K^0 and $\bar{K}^0$ are the opposite in τ^+ and τ^- decay. As a consequence $R^{\pm}_{K^0}(E) = R^{\mp}_{\bar{K}^0}(E)$ and $\bar{R}^{\pm}_{K^0}(E) = \bar{R}^{\mp}_{\bar{K}^0}(E)$. In that case we get

$$A_3 = \frac{\left[R^+_{K^0} - \bar{R}^-_{\bar{K}^0}\right] - \left[R^-_{K^0} - \bar{R}^+_{\bar{K}^0}\right]}{\left[R^+_{K^0} + \bar{R}^-_{\bar{K}^0}\right] + \left[R^-_{K^0} + \bar{R}^+_{\bar{K}^0}\right]} = \frac{\left[R^+_{K^0} - \bar{R}^+_{K^0}\right] - \left[R^+_{\bar{K}^0} - \bar{R}^+_{\bar{K}^0}\right]}{\left[R^+_{K^0} + \bar{R}^-_{K^0}\right] + \left[R^+_{\bar{K}^0} + \bar{R}^+_{\bar{K}^0}\right]} \tag{8.12}$$

We note that the first and the second terms in numerator recall the experimentally measured asymmetry A_ϵ given in Eq. 8.4 for the $S^+_{K^0}(E)$ and the $S^+_{\bar{K}^0}(E)$ energy distributions respectively,

$$A_{\epsilon,K^0} = \frac{\left[R^+_{K^0} - \bar{R}^+_{K^0}\right]}{\left[R^+_{K^0} + \bar{R}^-_{K^0}\right]}, \qquad A_{\epsilon,\bar{K}^0} = \frac{\left[R^+_{\bar{K}^0} - \bar{R}^+_{\bar{K}^0}\right]}{\left[R^+_{\bar{K}^0} + \bar{R}^+_{\bar{K}^0}\right]} \tag{8.13}$$

If in Eq. 8.12 we use the approximation that $S^{\pm}_{K^0} \simeq S^{\pm}_{\bar{K}^0}$, that is when the two energy spectra for K^0 and $\bar{K}^0$ are similar, we get a simpler expression

$$A_3 \simeq \frac{1}{2}\left[A_{\epsilon,K^0} - A_{\epsilon,\bar{K}^0}\right] \ . \tag{8.14}$$

Eq. 8.14 gives the total asymmetry observed in an experiment. We note that $A_3 \neq 0$ is due to the fact that K^0 and $\bar{K}^0$ are emitted with different energy spectrum $S^{\pm}_{K^0}(E) \neq S^{\pm}_{\bar{K}^0}(E)$ in the decay of the τ. As a consequence, the dependence of the rest frame efficiency $f_P(t)$ on the energy spectrum, Eq. 8.6, makes the asymmetries due to K^0 and $\bar{K}^0$ not cancel. Indeed, if $f^{\pm}_{K^0}(t) = f^{\pm}_{\bar{K}^0}(t)$ we would have $A_{\epsilon,K^0} = A_{\epsilon,\bar{K}^0}$, that is $A_3 = 0$. Moreover, it is important to note that, while A_1 is a physical asymmetry (in the sense that it would exist even in an ideal experiment with perfect efficiency $F(L,E) = f_P(t) \equiv 1$), $A_3 \neq 0$ is a consequence of the limited reconstruction efficiency of the experiment.

8.4 Belle II analysis A_3 estimate

The aim of this work is to give an upper bound on the asymmetry A_3 to show that it can be safely neglected in experimental analysis. To do so a simplified toy model for the process $\tau \to \pi K^0 \bar{K}^0 \nu_\tau$ was developed. Working in the hadronic reference frame, it is assumed that, in the production of the three mesons, an intermediate K* resonance is produced [93, 94]:

$$m_{K^*} = 0.892 \text{ GeV} \qquad \Gamma_{K^*} = 0.050 \text{ GeV} \ . \tag{8.15}$$

The details of the toy model generation are omitted here; however, it is important to emphasize that this model is not intended to provide realistic predictions of the physical differential rate. Instead, it serves as an extreme scenario, featuring distinct energy distributions for K_0 and $\bar{K}^0$, in order to establish an upper bound on the experimental value of A_3.

8.4.1 Experimental efficiency function

To compute the asymmetry A_3, it is necessary to account for the reconstruction efficiency $F(L,E)$. As discussed in Section 8.2, this is equivalent to determining the reconstruction efficiency as a function of the decay time in the kaon rest frame and the kaon energy in the lab

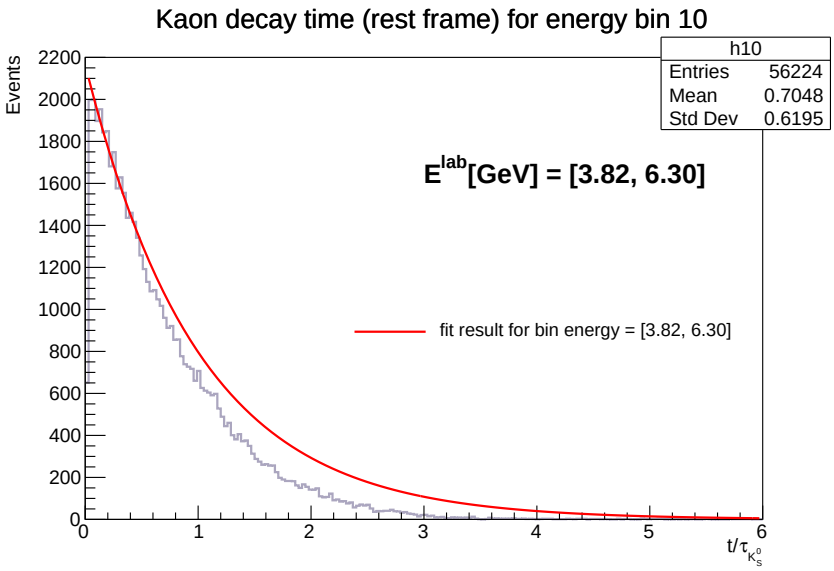

Figure 8.1: Exponential fit of the decay time distribution in the most energetic bin.

frame, $F(t, E)$. The key strategy is to exploit the fact that only the relative reconstruction efficiency is required, thereby avoiding the more complex task of computing the absolute efficiency, which would demand precise knowledge of the number of produced events as a function of L and E.

To extract the two-dimensional efficiency function $F(t, E)$, the kaon energy distribution before the reconstruction and the simulation of the detector is divided into ten bins of equal statistics, ordered such that the energy increases progressively across the bins. The energy ranges for the bins are (in GeV): [0.55, 1.23], [1.23, 1.47], [1.47, 1.68], [1.68, 1.90], [1.90, 2.14], [2.14, 2.42], [2.42, 2.76], [2.76, 3.20], [3.20, 3.82]. For each energy bin, the corresponding decay time distribution in the kaon rest frame is computed. The decay time t_{rest} is derived from the flight distance d and the kaon momentum in the lab frame $p_{K^0_S}$, using the relation:

$$t_{rest} = \frac{d}{\gamma\beta c} = \frac{d\, m_{K^0_S}}{p_{K^0_S}\, c} \tag{8.16}$$

To extract the relative reconstruction efficiency for each energy bin, a reference decay time distribution is required. This reference is obtained from the most energetic bin by fitting its decay time distribution with an exponential function:

$$f(t) = N_0\, e^{-t/\tau_{K^0_S}}. \tag{8.17}$$

The fit is performed in the low decay-time region, where the reconstruction efficiency is expected to be highest. In this fit, only the normalization parameter N_0 is left free, while the lifetime $\tau_{K^0_S}$ is fixed to its known value. The result of the fit is shown in Fig. 8.1. The resulting reference distribution is then compared to the decay time distributions of the other energy bins, as illustrated in Fig. 8.2. The relative reconstruction efficiency in each energy bin E_i is then obtained by taking the ratio between the corresponding decay time distribution and the

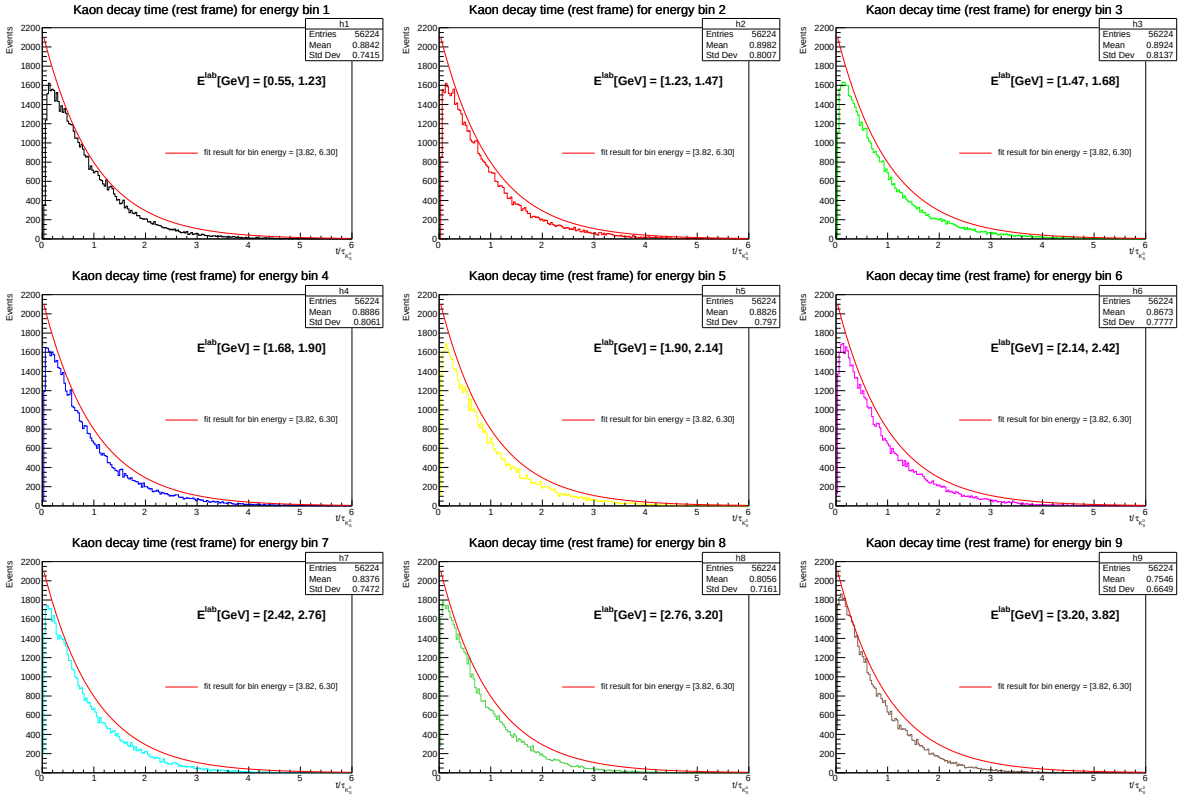

Figure 8.2: Reference distribution (red line) comparison with decay time distribution for different kaon's energy bin.

reference. This ratio is modeled using a piecewise function defined over two time intervals:

$$f(t)_{E_i} = \begin{cases} (\alpha + \beta e^{-\gamma t})^{\delta}, & \text{if } t < p \\ at^2 + bt + c, & \text{if } t \geq p \end{cases} \tag{8.18}$$

where p denotes the switching point between the two regimes and is treated as a fit parameter. The results are shown in Fig. 8.3 Due to statistical limitations and the inadequacy of the model at large decay times, and specifically beyond five K^0_S lifetimes, the reconstruction efficiency is assumed to be zero in that region.

8.4.2 A_3 upper bound

From the toy model, the spectrum in Fig 8.4 for K^0 and $\bar{K}^0$ in the τ rest frame is obtained. This spectrum is then boosted to the lab reference frame. For the case of Belle II we assume the lab frame in the case of an asymmetric electron-positron collider with invariant mass $\sqrt{s}|_{e^+e^-} = 10.58$ GeV, and that all this energy is used for the $\tau^+\tau^-$ production. The asymmetry is defined by the different energies of the colliding particles: 4 GeV and 7 GeV. We then get an upper bound on the asymmetry coefficient A_3 measured in the experiment:

$$A_3 < \frac{1}{2}\sum_{i=1}^{10}\left(\int_{\Delta E_i} f_{K^0}(E)A_1(E)dE - \int_{\Delta E_i} f_{\bar{K}^0}(E)A_1(E)dE\right) . \tag{8.19}$$

Numerically, is found:

$$A_3 < 9.2 \times 10^{-5} \simeq 0.03 \times 2\Re(\epsilon) . \tag{8.20}$$

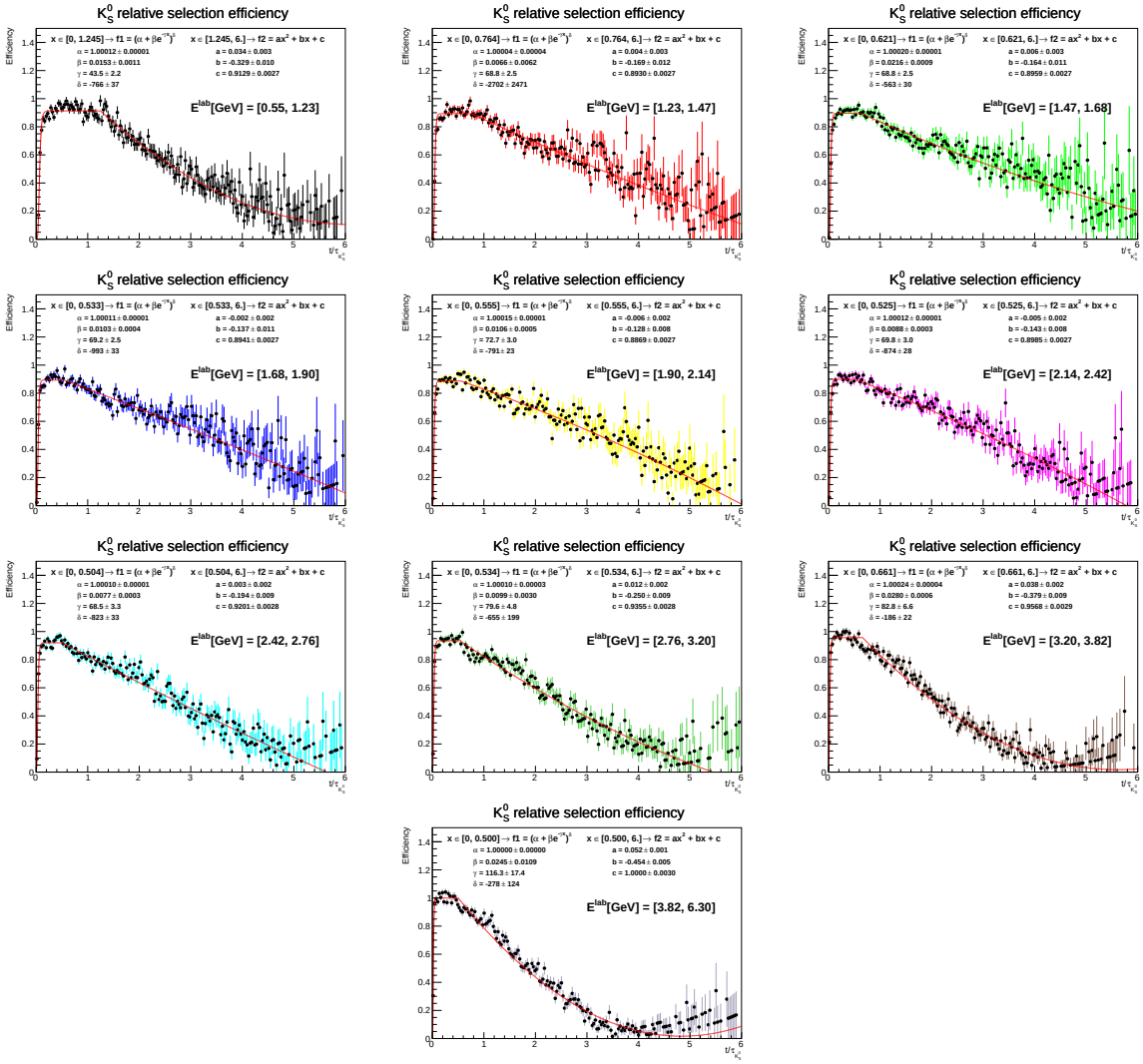

Figure 8.3: Relative reconstruction efficiencies as a function of the kaon's decay time for each energy bin.

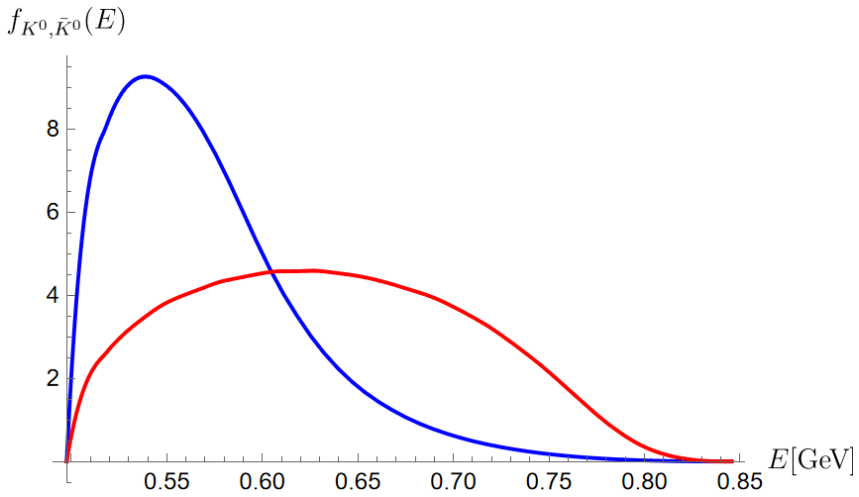

Figure 8.4: Normalized energy distribution function for K^0 (red line) and $\bar{K}^0$ (blue line) in the τ rest frame in the case of a simplified model for the interaction with the exchange of a K^* resonance [93,94]. In particular, this model is a limit case in which the spectrum of the two kaons is more different (leading to an upper bound value for the asymmetry A_3). The distribution functions are computed as the normalized differential rate as a function of the energy of the kaons.

8.5 Conclusion

In this work, we derive theoretical predictions for the CP asymmetry in the decay of the τ lepton into two neutral kaons. We demonstrate that the energy dependence of the reconstruction efficiency renders the decay channel $\tau \to \pi K_L K_S \nu_\tau$ CP-violating. A theoretical prediction for the CP asymmetry A_3 is provided, which depends on both the reconstruction efficiency function and the kaon energy spectrum produced in the decay. The efficiency function, parameterized by the decay time and energy of the kaons, $F(t, E)$, is obtained from the results of the main analysis. An upper bound on the experimental value of the asymmetry is found, $A_3 < 9.2 \times 10^{-5}$. Based on this, it can be concluded that the CP asymmetry is sufficiently small to be considered negligible in the context of the main analysis.

Chapter 9

Conclusion

9.1 Final results and discussion

In summary, we measure the CP asymmetry in $\tau^- \to \pi^- K^0_S \nu_\tau (\geq 0\pi^0)$ decays using the full LS1 dataset collected by Belle II. The signal sample contains approximately 262×10^3 decays, including contributions from $\tau^- \to K^- K^0_S \nu_\tau$ and $\tau^- \to \pi^- K^0 \bar{K}^0 \nu_\tau$ modes. The analysis is performed separately for electron-tagged ($\sim 142 \times 10^3$ events) and muon-tagged ($\sim 120 \times 10^3$ events) samples.

Three main corrections are applied to extract the genuine CP asymmetry. The detection asymmetry correction accounts for differences in the interaction of charged particles with detector material and is derived using $\tau^- \to \pi^-\pi^+\pi^-\nu_\tau$ decays. The neutral kaon asymmetry correction removes effects due to the different nuclear interaction cross-sections of K^0 and $\bar{K}^0$. Background-related asymmetries are corrected using estimates for $q\bar{q}$ and τ background yields based on MC and data control regions. All corrections are validated across relevant kinematic variables and over the full data-taking period.

The blinded CP asymmetry, obtained after background subtraction, corrections for neutral kaon interactions and detection asymmetries is:

$$A = (\text{xxx} \pm 0.27\ (\text{stat}) \pm 0.06\ (\text{syst}))\% \quad (\text{e-tag sample}) \tag{9.1}$$

$$A = (\text{xxx} \pm 0.29\ (\text{stat}) \pm 0.07\ (\text{syst}))\% \quad (\mu\text{-tag sample}) \tag{9.2}$$

where the first uncertainty is statistical and the second is systematic. To isolate the genuine CP-violating component A_1 coming from the $\tau^- \to \pi^- K^0_S \nu_\tau (\geq 0\pi^0)$, a dilution factor is applied to remove the contributions from the A_2 and A_3 terms, following the relation:

$$A_1 = \left(\frac{f_1 + f_2 + f_3}{f_1 - f_2} \right) A. \tag{9.3}$$

This relation assumes $A_1 = -A_2$ and $A_3 = 0$, as predicted by the SM. For $A_3 = 0$, a dedicated paper, currently in preparation (to which the author has contributed), investigates the validity of this assumption from an experimental perspective.

At the time of writing, the unblinding procedure has not yet been initiated. The analysis is currently under review by the Belle II internal review committee. The final CP asymmetry values will only be revealed after the completion of this review process and formal approval for

unblinding. For completeness, the expected format of the final results, once unblinded, is as follows:

$$A_{CP}(\tau^- \to \pi^- K^0_S \nu_\tau \ (\geq 0\ \pi^0)) = (\text{xxx} \pm 0.35\ (\text{stat}) \pm 0.07\ (\text{syst}))\% \quad \text{(e-tag sample)} \tag{9.4}$$

$$A_{CP}(\tau^- \to \pi^- K^0_S \nu_\tau \ (\geq 0\ \pi^0)) = (\text{xxx} \pm 0.38\ (\text{stat}) \pm 0.09\ (\text{syst}))\% \quad (\mu\text{-tag sample}) \tag{9.5}$$

$$A_{CP}(\tau^- \to \pi^- K^0_S \nu_\tau \ (\geq 0\ \pi^0)) = (\text{xxx} \pm 0.26\ (\text{stat}) \pm 0.06\ (\text{syst}))\% \quad \text{(combined)} \tag{9.6}$$

The results obtained from the two tagging methods are combined assuming uncorrelated systematic errors. This result achieves a precision comparable to that of the previous measurement reported by the BaBar collaboration [14].
The comparison of the unblinded result to the SM prediction of $A_{\text{SM}} = (0.33 \pm 0.01)\%$ and its corresponding statistical significance will be performed after full unblinding.

9.1.1 Preliminary results from 10% unblinding

A preliminary unblinding was performed on 10% of the dataset to assess the expected sensitivity of the analysis and verify the stability of the methodology. The measured CP asymmetries for the electron-tagged, muon-tagged, and combined samples are summarized in Table 9.1.

Observable	**Electron tag**	**Muon tag**	**Combined Sample**
Observed A_{CP} [%]	$-0.01 \pm 1.1 \pm 0.07$	$0.88 \pm 1.22 \pm 0.09$	$0.39 \pm 0.82 \pm 0.06$
SM Prediction [%]	0.30 ± 0.01	0.30 ± 0.01	0.30 ± 0.01
Significance	-0.28σ	0.47σ	0.11σ
p-value	0.78	0.64	0.91

Table 9.1: Measured CP asymmetry in $\tau^- \to \pi^- K^0_S \nu_\tau (\geq 0\pi^0)$ from 10% unblinded data. Uncertainties are statistical and systematic, respectively.

The significance is calculated with respect to the Standard Model prediction, corrected by the Belle II experimental K^0_S reconstruction efficiency [92], of $A_{\text{SM}} = (0.30 \pm 0.01)\%$ [**?**], using:

$$S = \frac{|A_{CP}^{10\%} - A_{\text{SM}}|}{\sqrt{\sigma^2_{\text{stat}} + \sigma^2_{\text{syst}} + \sigma^2_{\text{SM}}}}, \tag{9.7}$$

with the corresponding p-values obtained from the standard normal distribution. In all three channels, the results are consistent with the SM prediction within the current statistical uncertainties. It is emphasized that these results are preliminary and based on only 10% of the full dataset. The final results will be based on the full unblinded sample, pending approval by the Belle II internal review committee.

9.2 Conclusion and outlook

This work has presented a search for CP violation in τ decays through the measurement of the decay-rate asymmetry A_1 between $\tau^+ \to \pi^+ K^0_S \bar{\nu}\tau (\geq 0\pi^0)$ and $\tau^- \to \pi^- K^0_S \nu_\tau (\geq 0\pi^0)$. Using a dataset corresponding to 362 fb^{-1} of integrated luminosity collected by the Belle II experiment,

the blinded asymmetry was measured to be:

$$A_{CP} = (\text{xxx} \pm 0.26\ (\text{stat}) \pm 0.06\ (\text{syst}))\%. \tag{9.8}$$

This result provides a new measurement of A_1 with a precision comparable to that achieved by the BaBar collaboration. The total uncertainty is dominated by the statistical component, with systematic effects carefully evaluated and kept subdominant. A major challenge in this analysis was the presence of background modes that closely mimic the signal decay. Addressing this required detailed multi-channel corrections to ensure accurate extraction of the asymmetry. Looking forward, the prospects for further improvement in this measurement are highly promising.

In particular, a measurement of the A_2 asymmetry – associated with $\tau^- \to K^- K^0_S \nu_\tau$ decays – could be achieved relatively straightforwardly by inverting the kaon particle identification criteria used in the A_1 selection. Preliminary studies indicate that this strategy could allow the A_2 component to be isolated efficiently. A direct measurement of A_2 would provide an important cross-check to the Standard Model prediction and further clarify the origin of any observed CP-violating effects in τ decays at BABAR.

In the longer term, the most effective path to reducing the uncertainties in this measurement is through the accumulation of more data. Increased statistics will not only reduce the statistical uncertainty directly but also improve the precision of systematic corrections, particularly those related to detection asymmetries, by enlarging the size of relevant control samples.

Bibliography

[1] L. T. X.H̃e, *Spontaneous CP Violating Phase as the Phase in PMNS Matrix*, Eur. Phys. J. C **71** (2011) .

[2] N. Cabibbo, *Unitary Symmetry and Leptonic Decays*, Phys. Rev. Lett. **10** (1963) 531.

[3] M. Gell-Mann and A. Pais, *Behavior of Neutral Particles under Charge Conjugation*, Phys. Rev. **97** (1955) 1387.

[4] K. Kleinknecht, *Uncovering CP Violation: Experimental Clarification in the Neutral K Meson and B Meson Systems*, Springer (2003) .

[5] I. I. Bigi and A. I. Sanda, *A 'known' CP asymmetry in τ decays*, Physics Letters B **625** (2005) 47.

[6] A. Pich, *Tau Lepton physics: theory overview*, Nuclear Physics B - Proceedings Supplements **55** (1997) 3.

[7] Particle Data Group, R. L. Workman *et al.*, *Review of Particle Physics*, PTEP **2022** (2022) 083C01.

[8] A. Stahl, *Physics with Tau Leptons*, Springer (2000) .

[9] A. Pich, *Precision tau physics*, Progress in Particle and Nuclear Physics **75** (2014) 41.

[10] H. Nunokawa, S. Parke and J. W. F. Valle, *CP violation and neutrino oscillations*, Progress in Particle and Nuclear Physics **60** (2008) 012102.

[11] D. Delepine, G. Faisel and S. Khalil, *Supersymmetric R parity violation and CP asymmetry in semileptonic τ decays*, Phys. Rev. D **77** (2008) 016003.

[12] D. Kimura, K. Y. Lee, T. Morozumi, and K. Nakagawa, *Direct CP violation in hadronic τ decays*, Nuclear Physics B - Proceedings Supplements **189** (2009) 84.

[13] M. Bischofberger *et al.* (Belle Collaboration), *Search for CP Violation in $\tau^{\pm} \to K^0_S \pi^{\pm} \nu_\tau$ Decays at Belle*, Phys. Rev. Lett. **107** (2011) 131801.

[14] J. P. Lees *et al.* (BABAR Collaboration), *Search for CP violation in the decay $\tau^- \to \pi^- K^0_S (\geq 0\pi^0) \nu_\tau$*, Phys. Rev. D **85** (2012) 099904.

[15] W. Altmannshofer *et al.*, *The Belle II physics book*, PTEP **2019** (2019) 123C01, Erratum ibid. **2020** (2020) 029201, `arXiv:1808.10567`.

[16] K. Akai, K. Furukawa, and H. Koiso, *SuperKEKB collider*, Nucl. Instrum. Methods Phys. Res. A **907** (2018) .

[17] K. Abe *et al.*, *Observation of* $B \to K^* l^+ l^-$, Phys. Rev. Lett. **91** (2001) 261601.

[18] K. Abe *et al.*, *Observation of Large CP Violation in the Neutral B Meson System*, Phys. Rev. Lett. **87** (2001) 091802.

[19] Ed. A. J. Bevan, B. Golob, Th. Mannel, S. Prell, and B. D. Yabsley, *The physics of the factories*, Eur. Phys. J. **C74** (2014) 3026, arXiv:1406.6311.

[20] K. Akai, K. Furukawa, and H. Koiso, *SuperKEKB collider*, Nucl. Instrum. Meth. **A907** (2018) 188, arXiv:1809.01958.

[21] Belle II collaboration, *On Resonance, Continuum, Cosmics*, https://software.belle2.org/development/sphinx/online_book/fundamentals/02-datataking.html, note = Accessed: 2025-05-02, 2025.

[22] E. Ganiev, *Measurement of the branching fraction, longitudinal polarization fraction, and charge-parity violating asymmetry in* $B^+ \to \rho^+ \rho^0$ *decays at Belle*, PhD thesis, Univeristy of Trieste, Sept. 2021.

[23] O. Yukiyoshi *et al.*, *Accelerator design at SuperKEKB*, Progress of Theoretical and Experimental Physics **2013** (2013) .

[24] Belle II collaboration, T. Abe, *Belle II Technical Design Report*, arXiv:1011.0352.

[25] M. Bertemes, G. Inguglia, and C. Schwanda. , *Search for dark sector physics and performance of the Belle II detector in final state events with muons and large missing energy.*, PhD thesis, Vienna, Technische Universität Wien, 2021.

[26] H. Ye *et al.*, *Commissioning and performance of the Belle II pixel detector*, Nucl. Instrum. Methods Phys. Res. A **987** (2021) 164875.

[27] J. Kemmer and G. Lutz, *New detector concepts*, Nucl. Instrum. Methods in Phys. Res. A **255** (1987) 365.

[28] H. Ye *et al.*, *Commissioning and performance of the Belle II pixel detector*, Nucl. Instrum. Methods in Phys. Res. A **987** (2021) .

[29] Belle-II SVD, K. Adamczyk *et al.*, *The design, construction, operation and performance of the Belle II silicon vertex detector*, JINST **17** (2022) P11042, arXiv:2201.09824.

[30] N. Taniguchi (Belle II Collaboration), *Central Drift Chamber for Belle-II*, J. Instrum. **12** (2017) C06014.

[31] Belle II Tracking Group, V. Bertacchi *et al.*, *Track finding at Belle II*, Comput. Phys. Commun. **259** (2021) 107610, arXiv:2003.12466.

[32] J. Fast (Belle II TOP Group), *The Belle II imaging Time-of-Propagation (iTOP) detector*, Nucl. Instrum. Methods Phys. Res. A **876** (2017) 145.

[33] K. Inami, *MCP-PMT development for Belle-II TOP counter*, Phys. Procedia **37** (2012) 683.

[34] K. Kojima (Belle II TOP Group), *The operation and performance of the TOP detector at the Belle II experiment*, Proc. Sci. **398** (2022) .

[35] S. Nishida *et al.*, *Aerogel RICH for the Belle II forward PID*, Nucl. Instrum. Methods Phys. Res. A **766** (2014) 28.

[36] S. Korpar (Belle II ARICH Group), *A 144-channel HAPD for the Aerogel RICH at Belle II*, Nucl. Instrum. Methods Phys. Res. A **766** (2014) 145.

[37] Yonenaga *et al.*, *Performance evaluation of the aerogel RICH counter for the Belle II spectrometer using early beam collision data*, Prog. Theor. Exp. Phys. **2020** (2020) .

[38] I. Adachi *et al.*, *Detectors for extreme luminosity: Belle II*, Nucl. Instrum. Methods Phys. Res. A **907** (2018) 46.

[39] T. Aushev *et al.*, *A scintillator based endcap KL and muon detector for the Belle II experiment*, Nucl. Instrum. Methods Phys. Res. A **789** (2015) 134.

[40] Belle II Framework Software Group, T. Kuhr *et al.*, *The Belle II Core Software*, Comput. Softw. Big Sci. **3** (2019) 1, `arXiv:1809.04299`.

[41] Belle II collaboration, *Belle II Analysis Software Framework (basf2)*, `https://doi.org/10.5281/zenodo.5574115`.

[42] S. Skambraks *et al.*, *A 3D track finder for the Belle II CDC L1 trigger*, J. Phys. : Conf. Ser. **1525** (2020) 012102.

[43] S. Bähr *et al.*, *The Neural Network First-Level Hardware Track Trigger of the Belle II Experiment*, Nucl. Instrum. Methods Phys. Res. A **1073** (2025) 170279.

[44] Belle II collaboration, *Luminosity*, `https://www.belle2.org/research/luminosity`, 2024. Accessed: 2025-02-27.

[45] F. Abudinén and *et al.* (Belle II Collaboration), *Measurement of the integrated luminosity of the Phase 2 data of the Belle II experiment*, Chinese Physics C **44** (2020) .

[46] B. Aubert *et al.*, *Measurement of the total width, the electronic width, and the mass of the Υ(10580) resonance*, Physical Review D **72** (2005) 032005.

[47] S. Jadach, B. F. L. Ward, and Z. Wąs, *The precision Monte Carlo event generator KK for two-fermion final states in e^+e^- collisions*, Comput. Phys. Commun. **130** (2000) 260, `arXiv:hep-ph/9912214`.

[48] S. Jadach, B. F. L. Ward, and Z. Was, *Coherent exclusive exponentiation for precision Monte Carlo calculation*, Phys. Rew. D. **63** (2001) .

[49] S. Banerjee *et al.*, *Monte Carlo Event Generator updates, for tau pair events at Belle II energies*, 2021. doi: https://doi.org/10.48550/arXiv.2111.05914.

[50] O. Shekhovtsova *et al.*, *Resonance chiral Lagrangian currents and τ decay Monte Carlo*, Phys. Rev. D **86** (2012) 113008.

[51] M. Chrzaszcz *et al.*, *TAUOLA of τ lepton decays—framework for hadronic currents, matrix elements and anomalous decays*, Computer Physics Communications **232** (2018) 220.

[52] I. M. Nugent *et al.*, *Resonance Chiral Lagrangian Currents and Experimental Data for $\tau^- \to \pi^-\pi^-\pi^+\nu_\tau$*, Phys. Rev. D **88** (2013) 093012.

[53] E. Barberio, B. van Eijk, and Z. Wąs, *PHOTOS: A universal Monte Carlo for QED radiative corrections in decays*, Comput. Phys. Commun. **66** (1991) 115.

[54] T. Sjöstrand *et al.*, *An Introduction to PYTHIA 8.2*, Comput. Phys. Commun. **191** (2015) 159, `arXiv:1410.3012`.

[55] G. Balossini *et al.*, *Matching perturbative and parton shower corrections to Bhabha process at flavour factories*, Nuclear Physics B **758** (2006) 227.

[56] G. Balossini *et al.*, *Photon pair production at flavour factories with per mille accuracy*, Physics Letters B **663** (2009) 209.

[57] C. M. C. Calame *et al.*, *The BABAYAGA event generator*, Nuclear Physics B - Proceedings Supplements **131** (2004) 48.

[58] C. M. C. Calame, *The BABAYAGA event generator*, Physics Letters B **520** (2001) 16.

[59] C. M. C. Calame *et al.*, *Large angle Bhabha scattering and luminosity at flavor factories*, Nuclear Physics B **584** (2000) 459.

[60] F. A. Berends, P. H. Daverveldt, and R. Kleiss. , *Radiative corrections to the process $e^+e^- \to e^+e^-\mu^+\mu^-$*, Nuclear Physics B **253** (1985) 421.

[61] F. A. Berends, P. H. Daverveldt, and R. Kleiss. , *Complete lowest-order calculations for four-lepton final states in electron-positron collisions*, Nuclear Physics B **253** (1985) 441.

[62] F. A. Berends, P. H. Daverveldt, and R. Kleiss. , *Monte Carlo simulation of two-photon processes: II: Complete lowest order calculations for four-lepton production processes in electron-positron collisions*, Computer Physics Communications **40** (1986) 285.

[63] S. Uehara, *TREPS: A Monte-Carlo Event Generator for Two-photon Processes at e^+e^- Colliders using an Equivalent Photon Approximation*, 2013. doi: https://doi.org/10.48550/arXiv.1310.0157.

[64] GEANT4 collaboration, S. Agostinelli *et al.*, *GEANT4: A simulation toolkit*, Nucl. Instrum. Meth. **A506** (2003) 250.

[65] M. Milesi, J. Tan and P. Urquijo, *Lepton identification in Belle II using observables from the electromagnetic calorimeter and precision trackers*, EPJ Web of Conferences **245** (2020) 06023.

[66] T. V. Dong *et al.*, *Calibration and alignment of the Belle II central drift chamber*, Nucl. Instrum. Methods in Phys. Res. A **930** (2019) 132.

[67] S. Shimazaki *et al.*, *Front-end electronics of the Belle II drift chamber*, Nucl. Instrum. Methods in Phys. Res. A **735** (2014) 193.

[68] O. Frost, *A local tracking algorithm for the central drift chamber of Belle II*, Master's thesis, Karlsruhe Institute of Technology (KIT), 2013. `https://publish.etp.kit.edu/record/21906`.

[69] M. Nadler and R. Frühwirth, *Robust track fitting in the Belle II inner tracking detector*, Journal of Physics: Conference Series **396** (2012) 022037.

[70] J. Rauch and T. Schlüter, *GENFIT — a Generic Track-Fitting Toolkit*, Journal of Physics: Conference Series **608** (2015) 012042.

[71] R. Veenhof, *Garfield, a drift-chamber simulation program*, Conf. Proc. C **9306149** (1993) 66.

[72] P. A. Zylaet *et al.* (Particle Data Group)Prog. Theor. Exp. Phys. **2020**, 083C01 (2020) .

[73] Belle II collaboration, *basf2 light-2303-iriomote documentation*, `https://software.belle2.org/light-2303-iriomote/sphinx/online_book/basf2/various_additions.html`, 2024. Accessed: 2025-05-02.

[74] Belle II collaboration, *Belle II Software Documentation*, `https://software.belle2.org/release-06-00-10/sphinx/index.html`, 2023. Accessed: 2025-05-02.

[75] S. Jadach et al. Comput. Phys. Commun. **130** (2000) 260.

[76] S. Jadach et al. Phys. Rev. D **63** (2001) 113009.

[77] M. Chrzaszcz *et al.* Comput. Phys. Commun. **232** (2018) 220.

[78] S. Banerjee and A. Pathak, *Update of TAUOLA Monte Carlo for Belle II software*, BELLE2-NOTE-PH-2020-055 (2020).

[79] T. Sjostrand, S. Mrenna and P. Z. Skands, *PYTHIA 6.4 Physics and Manual*, JHEP **05** (2006) 026.

[80] Z. Gruberová, Z. Dolezal, P. Rados and A. Rostomyan, *Study of the τ lepton decays at the Belle II experiment*, BELLE2-MTHESIS-2021-007. (2021).

[81] M. Corporation, *LightGBM*, `https://lightgbm.readthedocs.io/en/latest/pythonapi/lightgbm.LGBMClassifier.html`, 2024. Accessed: 2024-12-13.

[82] T. Akiba, S. Sano, T. Yanase, T. Ohta, and M. Koyama, *Optuna: A Next-generation Hyperparameter Optimization Framework*, in *Proceedings of the 25th ACM SIGKDD International Conference on Knowledge Discovery and Data Mining.*, 2019.

[83] S. Narkhede, *Understanding AUC - ROC Curve*, `https://towardsdatascience.com/understanding-auc-roc-curve-68b2303cc9c5`.

[84] *Propagation of neutral kaons in matter*, in *Neutral Kaons*, vol. 153 of *Springer Tracts in Modern Physics*. Springer, Berlin, Heidelberg, 1999. doi: 10.1007/BFb0109538.

[85] A. Pais and O. Piccioni, *Note on the decay and absorption of the θ^0*, Phys. Rev. **100** (1955) 1487.

[86] K. Kleinknecht, *K_L-K_S regeneration*, Fortsch. Phys. **21** (1973) 57.

[87] M. L. Good, *Relation between scattering and absorption in the Pais-Piccioni phenomenon*, Phys. Rev. **106** (1957) 591.

[88] W. Fetscher, P. Kokkas, P. Pavlopoulos, T. Schietinger, and T. Ruf, *Regeneration of arbitrary coherent neutral kaon states: A new method for measuring the $K^0 - \bar{K}^0$ forward scattering amplitude*, Z. Phys. **C72** (1996) 543.

[89] A. Gsponer *et al.* , *Precise coherent K_S^0 regeneration amplitudes for C, Al, Cu, Sn and Pb nuclei from 20 to 140 GeV/c and their interpretation*, Phys. Rev. Lett. **42** (1979) 13.

[90] B. R. Ko, E. Won, B. Golob, P. Pakhlov, *Effect of nuclear interactions of neutral kaons on CP asymmetry measurements*, Phys. Rev. D **84** (2011) .

[91] R. A. Briere and B. Winstein, *Determining the phase of a strong scattering amplitude from its momentum dependence to better than 1°: The example of kaon regeneration*, Phys. Rev. Lett **75** (1995) 402.

[92] Y. Grossman and Y. Nir, *CP Violation in $\tau^\pm \to \pi^\pm K_S \nu$ and $D^\pm \to \pi^\pm K_S$: The Importance of $K_S - K_L$ Interference*, J. High Energ. Phys. **2012** (2012) .

[93] R. Decker *et al.*, *Tau decays into three pseudoscalar mesons*, Zeitschrift für Physik C Particles and Fields **58** (1993) 445–451.

[94] M. Finkemeier and E. Mirkes, *Tau decays into kaons*, Zeitschrift für Physik C Particles and Fields **69** (2014) 243–252.

Acknowledgements

First and foremost, I would like to express my heartfelt gratitude to my supervisors, Armine Rostomyan and Alberto Martini, for their exceptional guidance and unwavering support throughout my PhD journey. Their door was always open-both literally and figuratively-and I could always count on their readiness to answer questions, provide feedback, and offer encouragement, no matter how busy they were. Their steadfast belief in me and their continuous mentorship have been invaluable.

To the individuals who, although not present day-to-day, played a pivotal role in enabling my PhD journey: your support, whether through essential advice, institutional assistance, or timely opportunities, made a lasting difference. I am particularly grateful to Kerstin Tackmann and Krisztian Peters for their help in making this path possible.

To my family, thank you for your unconditional love, endless patience, and belief in me. Your support has been the foundation upon which all of this stands.

To my colleagues and the entire DESY Belle II group, thank you for the stimulating discussions, collaborative spirit, and shared experiences that made the workplace not only productive but also enjoyable. I truly value the intellectual exchange we shared.

Lastly, I am grateful to my friends for being a source of motivation, laughter, and balance during these years. Your presence, whether near or far, made this journey richer and more meaningful.

Thank you all.

Declaration on oath

I hereby declare and affirm that this doctoral dissertation is my own work and that I have not used any aids and sources other than those indicated.
If electronic resources based on generative artificial intelligence (gAI) were used in the course of writing this dissertation, I confirm that my own work was the main and value-adding contribution and that complete documentation of all resources used is available in accordance with good scientific practice. I am responsible for any erroneous or distorted content, incorrect references, violations of data protection and copyright law or plagiarism that may have been generated by the gAI.

Hamburg, 21 May 2025

Date

Signature of doctoral candidate